ASIER IGLESIAS SANCHEZ | Methodology for assessing the in-service behaviour of glass plates considering the effect of residual stresses

Mondragon Unibertsitatea

DOCTORAL THESIS

METHODOLOGY FOR ASSESSING THE IN-SERVICE BEHAVIOUR OF GLASS PLATES CONSIDERING THE EFFECT OF RESIDUAL STRESSES

Primer Plano de vidrio templado roto. Chungking. DepositPhotos. ID: 64038943

ASIER IGLESIAS SANCHEZ | Arrasate-Mondragón, 2022

Mondragon Unibertsitatea
Goi Eskola Politeknikoa
Faculty of Engineering

METHODOLOGY FOR ASSESSING THE IN-SERVICE BEHAVIOUR OF GLASS PLATES CONSIDERING THE EFFECT OF RESIDUAL STRESSES

ASIER IGLESIAS SANCHEZ

11/01/2022

DOCTORATE IN MECHANICAL ENGINEERING AND ELETRICAL ENERGY

METHODOLOGY FOR ASSESSING THE IN-SERVICE BEHAVIOUR OF GLASS PLATES CONSIDERING THE EFFECT OF RESIDUAL STRESSES

Thesis presented in

MONDRAGON UNIBERTSITATEA

for achieving the doctoral degree in

MECHANICAL ENGINEERING AND ELECTRICAL ENERGY

Presented by

ASIER IGLESIAS SANCHEZ

Directed by

DR. JON ANDER ESNAOLA
DR. MANEX MARTINEZ

In ARRASATE-MONDRAGON

The 11/01/2022

Acknowledgements

Lehenik eta behin, mila esker nire zuzendariei, Manex eta Jon Ander, urte hauetan tesia garatzeko emandako aholkuengatik, erakutsitako guztiagatik eta bereziki, niregan jarritako konfiantzagatik.

Bigarrenik, eskerrak eman nahi nioke Iñigo Llavoriri ere, egunerokotasunean sortzen ziren arazoei aurre egiten laguntzeko beti prest egoteagatik.

Bestaldetik, eskerrak eman nahi nizkioke doktorando gelan (eta machining-eko departamentuan) nirekin urte hauek partekatu dituzten lagun guztiei. Antolatu ditugun afariez gain, bertan izandako elkarrizketak eta laguntzak ezinbestekoak izan dira tesi hau gauzatzeko. Eskerrik asko!

Agradecer profundamente a Miguel Muñiz Calvente y Alfonso Fernández Canteli, al igual que a los técnicos de laboratorio de la Universidad de Oviedo, por su amabilidad durante mi breve pero intensa estancia allí. Muchas gracias por estar siempre dispuestos a colaborar y aprender. Del mismo modo, eskerrik asko a los investigadores y técnicos de laboratorio de Mondragon Unibertsitatea que me han ayudado durante estos años.

Eskerrik asko también a mis amigos y amigas, y en particular a ti, Ainhoa, por animarme en los momentos más difíciles, y poder disfrutar con vosotros los ratos libres que dejaba la tesis. Mila esker!

Por último, agradecer a mi familia, en especial a mis padres, Jose y Maite, sin cuyo esfuerzo no me podría haber aventurado en esta experiencia.

MILA ESKER GUZTIOI!!!

Abstract

The structural performance of glass mainly depends on the surface quality and the residual stress state. Surface damage produced during the manufacturing process or subsequent handling, might lead to the presence of microscopic flaws on the surface. The opening or propagation of these microscopic flaws reduce the strength of glass. For this reason, glass is most often tempered before being employed as a structural material. Tempering techniques bring about non-uniform heat transfer rates, which lead to non-homogeneous residual stresses, having a direct impact on the structural behaviour of components. Moreover, once glass is ready to use, its fracture behaviour tends to present significant differences between measured strength values. This results in the need for extensive experimental work, especially if non-uniform residual stresses need to be considered. Thus, this thesis presents a numerical methodology to predict the in-service behaviour of glass plates subjected to bending loads considering the residual stresses developed as a result of non-uniform cooling processes.

First, a numerical methodology based on a Fluid-Structure Interaction (FSI) one-way approach is proposed to consider the influence of non-uniform cooling techniques on the residual stress development during the thermal tempering process. Results show that local flow phenomena during heat treatment process play a vital role in residual stress development in glass plates. In line with this approach, efforts were made to reduce the computational time of the involved calculations. For this purpose, the influence of volumetric radiation and the viscoelastic behaviour of glass were analysed. As a result, a decrease of around 87% of the computational time with respect to the initially proposed procedure was achieved. The results were in good agreement with both, experimental measurements in laboratory case studies and an industrial tempering case study published in the literature.

Secondly, a statistical-numerical procedure to predict the failure probability of structural glass components is presented. To this end, statistical assessment based on the Generalised Local Model (GLM) was carried out. Bending loads, which may result from the effect of wind, snow or the weight of pedestrians, are considered the main loads acting on structural glass plates. Therefore, plates exhibiting different residual stress conditions subjected to bending loads were analysed. The most striking observation to emerge from the analysis was the transferability between the failure cumulative functions of annealed and tempered glass, with the latter exhibiting different residual stress patterns. A master Primary Failure Cumulative Damage Function (PFCDF) was also calculated by jointly assessing the results of the experimental tests. This enables a more reliable prediction of the fracture behaviour of annealed and tempered glass. Overall, average relative differences between the predicted and experimental data were below 10%. Finally, particularly noteworthy was the scatter band of the experimental results. Given this spread, statistical evaluation can be considered essential for designing or assessing structural pre-stressed components.

Laburpena

Gainazalaren kalitateak eta beiraren tentsio-egoerak eragin zuzena dute bere portaera estrukturalean. Fabrikazio edo ondorengo manipulazio prozesuen zehar beiraren gainazalean gertatzen diren kontaktu ugariek pitzadura mikroskopikoak sor ditzakete. Pitzadura horiek irekitzeak edo hedatzeak beiraren erresistentzia murrizten du. Hori dela eta, beira material estruktural gisa erabili ahal izateko, sarritan tenple izeneko tratamendu termikoa aplikatzen zaio. Hala eta guztiz ere, tenple teknikek bero transferentzia ez uniformeak eragiten dituzte. Horren ondorioz, portaera estrukturalean eragin zuzena duten hondar-tentsio ez uniformeak sortzen dira. Horrez gain, behin beira erabiltzeko prest dagoenean, bere frakturako portaerak dispertsio handia erakusten du neurtutako indar balioen artean. Horrek kanpaina esperimental handiak ezinbestekoak izatea eragiten du, batez ere hondar-tentsio ez uniformeak kontutan hartu behar badira. Gauzak horrela, tesi honetan tenplaketan sortutako hondar-tentsioak kontuan hartuz, makurdura kargen eraginpean dauden beirazko plaken portaera estrukturala aurreikusteko metodologia numeriko bat aurkezten da.

Tenpleko hozketa ez uniformeak hondar-tentsioetan duten eragina kontsideratzeko, Fluido-Estruktura Interakzioan (FSI ingelesezko siglen arabera) oinarritzen den modelizazioa proposatzen da. Gauzak horrela, tratamendu termikoen zehar gertatzen diren fluxu fenomeno lokalak hondar-tentsioen sorreran eragin handia dutela erakutsi da. Aldi berean, kalkuluen kostu konputazionala murrizteko teknikak proposatzen dira. Horretarako, radiazio bolumetrikoaren eta beiraren portaera biskoelastikoaren eragina aztertzen da. Lortutako aurkikuntzek hasiera baten proposatutako prozeduraren kostu konputazionalarekiko %87-ko murrizketa bat suposatu dute. Azkenik, lortutako emaitzak, bai laborategiko emaitza esperimentalekin, bai bibliografian oinarritutako kasu industrial batekin bat datozela egiaztatu da.

Bestalde, beirazko pieza estrukturalen hutsegitea aurreikusteko modelo estatistiko-numeriko bat aurkezten da. Horretarako, Modelo Lokal Orokortuan (GLM ingelesezko siglen arabera) oinarritutako ebaluazio estatistikoa egin da. Beirazko plaka estrukturaletan eragiten duten karga nagusienak haizea, elurra edo oinezkoen pisuaren ondorioz sortutakoak dira. Hori dela eta, makurdura kargen eraginpean dauden eta tentsio egoera ezberdinak aurkezten duten plakak aztertu dira. Egindako analisitik, behaketarik harrigarriena izan da suberatutako eta tenplatutako plaken hutsegite-funtzioen transferigarritasuna frogatzea. Aldi berean, egindako kanpaina esperimentalaren ebaluazio bateratuak PFCDF (ingelesetik *Primary Failure Cumulative Damage Function*) orokor bat kalkulatzea ahalbidetu du, beiraren haustura portaeraren aurreikustea fidagarriagoa eginez. Orokorrean, %10-eko bataz besteko diferentzia erlatiboa lortu da aurreikusitako emaitzaren eta datu esperimentalen artean. Azkenik, bereziki aipagarria izan da emaitza esperimentalen dispertsio banda. Hau ikusita, funtsezkoa kontsideratu da ebaluazio estatistikoa gauzatzea beirazko pieza estrukturalak diseinatzeko edo aztertzeko.

Resumen

El comportamiento estructural del vidrio depende principalmente de la calidad superficial y del estado tensional. Los múltiples contactos que ocurren en la superficie durante el proceso de fabricación, o posterior manipulación, pueden provocar la generación de grietas microscópicas en ella. La apertura o propagación de dichas grietas reduce la resistencia del vidrio. Por esta razón, el temple es una práctica común para poder emplear el vidrio como material estructural. Las técnicas de temple resultan en robos de calor no-uniformes en la superficie, lo cual genera tensiones residuales no-homogéneas, que influyen de manera directa en el comportamiento estructural. Además, una vez el vidrio esta listo para su uso, su comportamiento a fractura muestra una gran dispersión en lo que a la medición de resistencia última se refiere. Por esta razón, su caracterización requiere grandes campañas experimentales, más aún si se desea considerar la distribución no uniforme de las tensiones. Por lo tanto, esta tesis presenta una metodología numérica para predecir el comportamiento en servicio de placas de vidrio sometidas a flexión teniendo en cuenta las tensiones residuales generadas durante el temple.

A tal objeto, se propone un modelo basado en la Interacción Fluido-Estructura (FSI por sus siglas en inglés) para considerar la influencia de enfriamientos no uniformes en la generación de tensiones residuales durante el proceso de temple. Los resultados muestran que los fenomenos locales del fluido refrigerante influyen de manera notable en la generación de tensiones. Del mismo modo, se proponen técnicas para reducir el coste computacional de los cálculos requeridos. Para ello, se han analizado los fenomenos de radiación volumétrica y viscoelasticidad del material. Los hallazgos obtenidos suponen una reducción del coste computacional de en torno al 87 % respecto al proceso numérico propuesto inicialmente. Finalmente, los resultados obtenidos han sido acordes con lo observado experimentalmente, tanto en ensayos de laboratorio como en un caso industrial publicado en bibliografía.

Por otra parte, se presenta un modelo estadístico-numérico para predecir la fractura de componentes estructurales de vidrio. Para ello, se ha realizado una evaluación estadística basada en el Modelo Local Generalizado (GLM por sus siglas en inglés). Las cargas principales que actúan sobre el vidrio estructural pueden ser debidas al efecto del viento, nieve o el peso de transeúntes. Por esta razón, se han analizado placas sometidas a flexión. La observación más relevante ha sido la confirmación de la transferibilidad de los resultados de placas recocidas y templadas. Del mismo modo, la evaluación conjunta de los datos experimentales ha permitido el cálculo de la PFCDF (del inglés *Primary Failure Cumulative Damage Function*) maestra, habilitando así una predicción más fiable del comportamiento a fractura del vidrio. En general, la diferencia relativa promedio entre las predicciones y las mediciones experimentales ha sido de un 10 %. Finalmente, la dispersión observada en los resultados experimentales es digna de mención. Dada esta circunstancia, la evaluación estadística se considera esencial para poder diseñar o analizar componentes de vidrio que ostentan tensiones residuales.

Contents

List of Figures

List of Tables

Glossary

a_λ	Spectral absorption coefficient [1/m]
C	Photoelastic constant [TPa^{-1}]
$c_{\mathrm{p,g}}$	Specific heat of glass [J/kgK]
D	Jet diameter [m]
e	Internal energy [J]
e_{g}	Glass thickness [m]
$\boldsymbol{e}$	Deviatoric strain tensor
$\vec{F}$	External body force [N]
$F_{\max}$	Maximum experimental force [N]
G_{s}	Shear relaxation modulus [MPa]
GP	Generalised parameter
$\vec{g}$	Gravitational acceleration [$\mathrm{m/s}^2$]
H	Jet-to-plate distance [m]
H_{act}	Activation energy [J/mol]
I	Iteration number
I_λ	Spectral radiative intensity [$\mathrm{W/m}^2$]
$I_{\mathrm{b},\lambda}$	Spectral blackbody intensity [$\mathrm{W/m}^2$]
K	Stress intensity factor [MPa $\mathrm{m}^{1/2}$]
K_2	Bending constant
K_{b}	Bulk modulus [MPa]
k	Turbulent kinetic energy
$k_{\mathrm{th,g}}$	Thermal conductivity of glass [W/mK]
$k_{\mathrm{th,f}}$	Thermal conductivity of the fluid [W/mK]
L	Plate length [m]
M_{p}	Response function of a given property
P_{f}	Probability of failure
$P_{\mathrm{f,global}}$	Global probability of failure
P_{s}	Probability of survival
$P_{\mathrm{s,global}}$	Global probability of survival
p	Static pressure [Pa]
$\dot{q}$	Generated volumetric heat [$\mathrm{W/m}^3$]
$\mathrm{R_g}$	Universal gas constant [$\mathrm{J/K \cdot mol}$]
r_1	Radius of load ring [m]
r_2	Radius of support ring [m]
$r_{3,\mathrm{m}}$	Mean radius of square plate [m]
$\vec{r}$	Position vector
$\vec{s}$	Direction vector
$\vec{s'}$	Scattering direction vector
S_{eq}	Equivalent size
S_{h}	Sources of energy
S_{ref}	Reference size
T	Temperature [K]
T_0	Initial quenching temperature [K]
T_{B}	Reference temperature [K]
T_{f}	Fictive temperature [K]
T_{g}	Glass transition temperature [K]
t	Time [s]
t_0	Initial time [s]
t_∞	Steady-state time [s]
t_{cri}	Critical time [s]
$\vec{v}$	Velocity [m/s]
v_τ	Friction velocity [m/s]
x_{jet}	Distance between jets [m]
y	Distance from the wall [m]
y^+	Wall Y plus

Greek Letters

α_{g}	Solid glass expansion coefficient [K^{-1}]
α_{l}	Liquid glass expansion coefficient [K^{-1}]
β	Shape parameter
β_{beam}	Laser beam angle
δ	Scale parameter
δ_{eq}	Equivalent scale parameter
δ_{opt}	Optical retardation
δ_{k}	Kronecker delta
$\boldsymbol{\varepsilon}$	Strain tensor
ε	Turbulence dissipation rate
ε_{I}	Iterative relative difference
$\varepsilon_{\mathrm{th}}$	Thermal strain
λ	Location parameter
μ	Dynamic viscosity of the fluid [$\mathrm{Pa} \cdot \mathrm{s}$]
μ_{g}	Dynamic viscosity of glass [$\mathrm{Pa} \cdot \mathrm{s}$]
ν	Poisson's ratio
ξ	Scaled time
ρ	Density of the fluid phase [$\mathrm{kg/m^3}$]
ρ_{g}	Density of glass [$\mathrm{kg/m^3}$]
$\boldsymbol{\sigma}$	Stress tensor [MPa]
σ	Residual stress [MPa]
σ_0	Parallel stress component [MPa]
σ_{90}	Perpendicular stress component [MPa]
σ_{eq}	Equivalent stress [MPa]
σ_{max}	Maximum principal stress [MPa]
σ_{rad}	Radial stress [MPa]
σ_{tan}	Tangential stress [MPa]
σ_{sc}	Scattering coefficient
$\boldsymbol{\tau}_{\mathrm{v}}$	Viscous stress tensor
τ_{w}	Wall shear stress
Φ	Phase function
ϕ	Shift factor
ω	Turbulence specific dissipation rate
Ω	Solid angle [°]

Acronyms

AA	Annealed glass
AT	Asymmetrically tempered glass
ATHD20	Asymmetrically tempered glass at short jet-to-plate distance
ATHD40	Asymmetrically tempered glass at large jet-to-plate distance
CAE	Computer Aided Engineering
CDR	Coaxial Double Ring
CFD	Computational Fluid Dynamics
DIC	Digital Image Correlation
DNS	Direct Numerical Simulation
DOM	Discrete Ordinates Method
EFCDF	Experimental Failure Cumulative Damage Function
EVM	Eddy Viscosity Model
FEA	Finite Element Analysis
FEM	Finite Element Method
FSI	Fluid-Structure Interaction
GEKO	Generalised $k-\omega$
GLM	Generalised Local Model
GP	Generalised Parameter
HD20	Short jet-to-plate distance tempered test
HD40	Large jet-to-plate distance tempered test
HTC	Heat Transfer Coefficient
LEFM	Linear Elastic Fracture Mechanics
LES	Large-Eddy Simulation
PFCDF	Primary Failure Cumulative Damage Function
PIA	Principle of Independent Action
RANS	Reynolds-Averaged Navier-Stokes
RS	Residual stress
RSM	Reynolds-Stress Model
RTE	Radiative Transfer Equation
SCALP	Scattered Light Polariscope
SIF	Stress Intensity Factor
SST	Shear Stress Transport
ST	Symmetrically tempered glass
STHD20	Symmetrically tempered glass at short jet-to-plate distance

STHD40	Symmetrically tempered glass at large jet-to-plate distance
XFEM	eXtended Finite Element Method

Chapter 1

Introduction

Mechanically strong, optically transparent and chemically inert. These features have made glass a suitable choice for several technological and engineering applications, covering a wide range of industries, such as construction, transportation, packaging or the solar photovoltaic sector. Moreover, the demand for tempered flat glass is expected to grow during the forthcoming years, as observed in Figure 1.1.

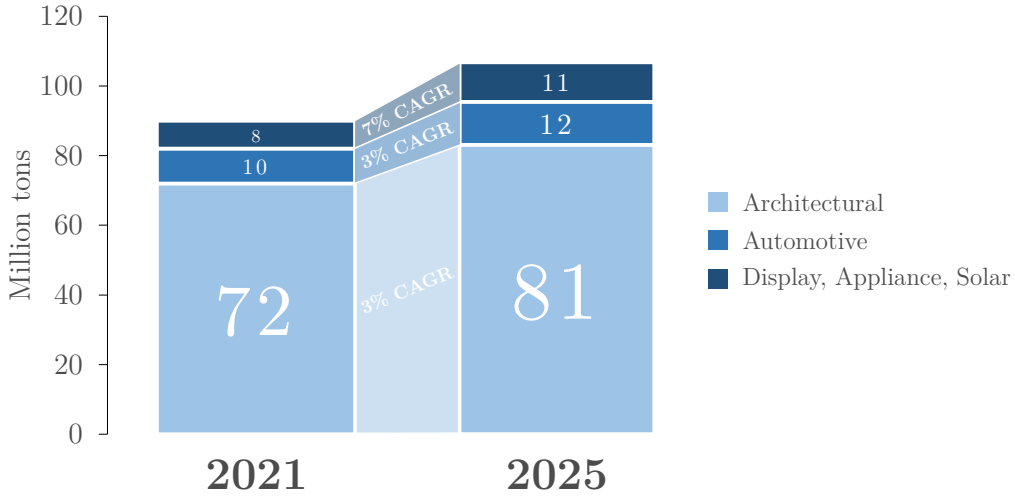

Figure 1.1: Tempered flat glass demand forecasted by segments and the expected compound annual growth rate (CAGR) [1].

Numerous glass applications derive from the combination of load bearing capacity with the recent trend to achieve transparency and lightness. Therefore, large surface glass components have become ubiquitous, mainly in the automotive sector, such as windshields or sunroofs, and in the architectural sector, where windows, façades or even full glass structures have exponentially seduced the architects [2, 3].

Meanwhile, the glass industry is trying to reduce the weight of its glass components in order to decrease the cost of the raw material, the energy employed to heat and produce it, as well as the cost of transportation and the amount of material to recycle [4]. This weight diminution is achieved by reducing the thickness of the material. However, this operation also implies the obtention of a weaker product.

The structural performance of glass depends on several factors, being the surface quality and the residual stress state two of the most influential ones [5]. In this sense, bending loads are considered the main loads acting on structural glass plates. These loads may result from the effect of wind and snow on buildings and vehicles, or the ones generated during the assembly processes, such as, installations of windows on their frame or sunroofs in the car structure. The theoretical tensile strength of glass is supposed to be ample for withstanding these external loads, as it can be as much as 14 GPa [6]. Nevertheless, the surface damage produced during the manufacturing process as well as subsequent handling, cutting, or usage, lead to the presence of microscopic flaws on the surface. Thus, in practical or everyday applications, ordinary glass does not exhibit pristine condition and it might also be broken at loads as little as 7 MPa [7, 8]. The reason for this lies on the tendency of these microscopic flaws to propagate, particularly if the area is subjected to tensile loading.

Historically, glass was annealed in order to reduce or eliminate the tensile residual stresses developed during the manufacturing process [9]. Nevertheless, with the aim of developing compressive stresses on the surface and use glass as a structural material, the tempering process is most often applied. There exist two types of tempering processes: the chemical tempering and the thermal tempering [7]. Both processes consist on developing a superficial compressive stress with the intention of strengthening glass [8, 10, 11]. However, as the chemical tempering implies a higher cost due to the specific equipment needed and a lower depth of layer, which refers to the thickness of the compressive stress layer in the material, the thermal tempering becomes a more efficient method [12].

During the thermal tempering, glass is heated to a uniform temperature at which it is fluid enough to relax internal stresses and rigid enough to avoid important deformations. Subsequently, different cooling techniques might be applied to chill the hot glass specimen. Air is the quintessential cooling technique employed to rapidly cool and strengthen the material due to its associated low cost [13, 14]. Nevertheless, some other techniques such as spray mist cooling, solid contact cooling or gaseous media like steam might also be used.

In general, the design and control of a tempering process have relied on trial and error tests or on experience based judgements. In an effort to produce high quality and large durable components, the control of the process is crucial. Likewise, fracture characterisation have been grounded on huge experimental programs due to the brittle behaviour of glass. Lately, the development of computer aided engineering (CAE) tools have aided engineers to calculate and design structural components by means of numerical simulation. In this context, two main factors need to be accounted for designing lightweight structural glass components, namely, the residual stress state and the microscopic flaw distribution on the surface.

Residual stress prediction

Two aspects are distinguished when it comes to residual stress calculation in glass components: the structural or material field and the heat transfer modelling.

The material modelling and the origin of residual stresses in glass have been deeply studied in literature [15–17]. Similarly, heat transfer modelling was found to be a key factor in the prediction of residual stresses in glass as they are largely influenced by the thermal history of the components [13, 18–20]. During the glass tempering process, where large heat transfer rates are obtained, the heat transfer mechanisms involved refer to conduction, convection and radiation. Conduction is usually well understood as it is characterised by the thermal conductivity of the material [21]. Regarding convection phenomena, the definition of constant and uniform heat transfer coefficients (HTCs) has been a commonly adopted approach due to its associated low computational cost [19, 22–25]. Recently, an alternative approach was proposed to calculate residual stresses on a glass moving plate [26]. The authors employed time-constant but spatially different HTC distributions to analyse the effect of different jet configurations.

These simplified approaches to model the jet cooling of parts are not exclusively adopted within the glass industry but also within the heat treatment modelling of metals [27]. Some works defined and implemented spray heat transfer correlations into a numerical code that related the HTC to the surface temperature to predict the cooling curve of spray quenched aluminium components [28–30]. Other investigations, modelled the multiphase spray cooling process for step shafts by constant HTCs depending on the shaft diameter [31]. This same approach was also used to simulate the spray quenching process of steel forged shafts [32, 33].

One of the main limitations of the numerical modelling of heat treatment processes is to assume homogeneous and constant HTCs. Local flow phenomena during cooling play a far more vital role in the residual stress development distribution of glass [34]. Additionally, several authors highlighted that more knowledge about the control of the heat treatment process was needed as they observed high variations not only in the residual stress state of individual specimens, but also among specimens of the same batch [35, 36].

Finally, radiation in semi-transparent media also gains special relevance. Indeed, it can play a vital role in the temperature variation over time as it helps to redistribute the heat through the component [37, 38]. According to Siegel, this fact might have a direct impact on residual stress development during the manufacturing or heat treatment processes [39]. Lately however, some authors stated that the contribution of radiation decreased as the cooling rate increased [20, 40]. Even though, as works focused on this topic relied on 1D calculations, its importance and effect on the spatial residual stress distribution was not clarified yet.

Surface microscopic flaws

By and large, the compressive stress layer originated in the heat treatment process may hamper crack propagation, but when components are subjected to large loadings, brittle materials are unable to redistribute these stresses and catastrophic failure is bound to happen. In other words, glass becomes very sensitive to local stress concentrations due to the lack of local yielding of the material. Accordingly, cracking occurs. Figure 1.2 illustrates a crack reaching the tensile stress region at the core of the material, that is, propagating beyond the depth of layer, resulting in the spontaneous fracture of the component.

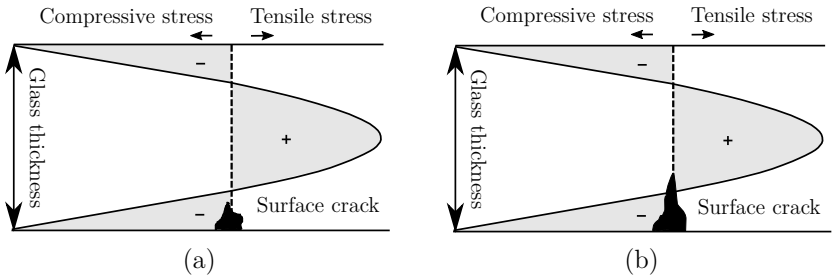

Figure 1.2: Residual stress distribution of a tempered glass pane through the thickness: (a) with a surface flaw smaller than the depth of layer, and (b) with a surface flaw larger than the depth of layer. Adapted from [11].

For this reason, prediction of the in-service behaviour of glass becomes a paramount matter to prevent its structural collapse. Several approaches can be found in the literature to deal with this issue. Due to its ease of implementation, calculations based on allowable stresses or safety factors can be observed in certain design guides or standards, such as the German technical guideline or the prEN 13474 standard [41, 42]. Nevertheless, the presence of cracks on the surface developed during the manufacturing process, prompted the use of probabilistic assessments. In this sense, the Weibull distribution is reported to be the most widely used statistical approach for representing the fracture strength of brittle materials [43–45]. Different variants of the Weibull model can be noticed, such as the bi-parametric or three-parametric implementation. Based on this model and experimental data, some works performed direct statistical assessment of annealed and tempered glass panes [11, 46, 47]. Nonetheless, these evaluations only allowed to predict the specific case studied, that is, the exact analysed component without varying the geometry or load acting on it. An additional drawback regarding failure analysis of glass refers to the required large experimental work due to the presence of defects randomly distributed on its surface. Moreover, if non-uniform residual stresses are to be considered, the total effort required in the laboratory increases significantly. Lately, phenomenological models have also gained traction [48]. These models describe the fracture behaviour of the material based on empirical observations. As a result, they enabled to adopt a multi-scale approach by considering the micro and macro scale in the design of structural components. Another common approach to study the structural integrity of glass components relates to the formulation based on fracture mechanics. Glass is considered a perfect elastic material at room temperature, hence, Linear Elastic Fracture Mechanics (LEFM) is usually adopted for analysing the influence of defects on this material. In this context, Irwin identified the so-called Stress Intensity Factor (SIF), K, to characterise the material brittleness or fracture toughness [49, 50]. These developments gave rise to analytical formulations for investigating the influence of cracks.

Lately however, their application to complex problems has been outdated by numerical methods [51]. In this regard, the calculation of the SIFs based on the eXtended Finite Element Method (XFEM) or the Finite Element Method (FEM) have become a common practice, particularly for modelling surface scratches [52, 53]. Nevertheless, these numerical methods become unfeasible if the whole population of microscopic flaws on the glass surface are to be considered.

1.1 Motivation

Controlling the cooling down process of structural parts is a cumbersome task owing to the simultaneous appearance of different physics, turning the heat treatment process into a multiphysic problem. In this context, computational fluid dynamics (CFD) becomes a powerful tool to predict the temperature distribution over the heat treated component [26, 54]. Nonetheless, the performed investigations not only emphasised the need to control heat transfer during tempering, but also mentioned shortages regarding the numerical modelling, such as, the complexity of modelling the interaction of multiple impingement jets and the large amount of computational resources required. For this reason, efficient 3D numerical procedures to control the heat treatment process remains a challenge.

With respect to the in-service behaviour, analytical formulations as well as numerical methods can be implemented for studying the structural integrity of glass components in the presence of cracks. Nevertheless, the physical representation of surface microcracks by numerical methods such as the FEM or XFEM becomes unfeasible. Additionally, a significant experimental effort is required to statistically analyse the fracture behaviour of pre-stressed glass. This fact emphasises the need to develop an efficient numerical-probabilistic tool to predict the failure probability of heat treated components.

In summary, the strength of glass is highly influenced by the surface damage and the residual stress state. Owning to its brittle behaviour, the tensile strength of glass is limited because of the existence of surface flaws. As a result, glass is prone to brittle fracture and a probabilistic assessment becomes relevant to prevent its catastrophic failure. Similarly, a representative prediction of the residual stress pattern remains essential to analyse the in-service behaviour of the designed parts. The performance of glass during in-service operations, generally subjected to bending loads, e.g. wind load, may differ depending on the residual stress pattern in the component. It is therefore of great importance to develop a predictive model to determine the tempered state of glass and its in-service behaviour when components are subjected to external loads.

1.2 Objectives

The main objective of this research is to provide a numerical methodology to predict the in-service behaviour of glass plates subjected to bending loads considering the residual stresses developed during the glass cooling process.

With the view to achieving the main objective, the following sub-objectives are stated:

- **Sub-objective 1:** to develop a computationally efficient numerical procedure to consider the influence of non-uniform cooling techniques on the residual stress development during the heat treatment process of glass components.
- **Sub-objective 2:** to validate the developed numerical methodology by laboratory tempering tests and an industrial tempering case study.
- **Sub-objective 3:** to develop a cost-effective statistical-numerical procedure to predict the failure probability of glass components subjected to bending loads and accounting for non-uniform residual stress distributions.
- **Sub-objective 4:** to validate the developed statistical-numerical procedure by laboratory bending tests of glass plates exhibiting distinct residual stress patterns.

Therefore, the novelty of the proposed methodology lies in the development of a numerical procedure to predict the in-service behaviour of glass components accounting for the residual stresses developed during the heat treatment process.

1.3 Dissertation outline

This dissertation has been divided in two main chapters, as presented in Figure 1.3.

Chapter 2 introduces the numerical methodology based on Fluid-Structure Interaction (FSI) to predict the non-uniform residual stress distributions during the glass tempering process. Firstly, a literature review encompassing the current approaches to predict residual stresses are analysed. Similarly, the main shortcomings regarding numerical modelling are identified. Then, the fundamentals of the physics involved in the tempering process and the followed experimental operations in the current heat treatment procedures are addressed. Afterwards, the FSI numerical methodology to consider the interaction between the fluidic, thermal and mechanical fields is delineated. Nevertheless, due to the associated high computational cost, different computational cost reduction techniques are considered in order to propose a modified FSI procedure and give response to **Sub-objective 1**. With the aim of validating the proposed modified procedure, laboratory specimens under controlled conditions are tested. Subsequently, an additional case study is considered for verifying the model under industrial conditions. As a result, **Sub-objective 2** is addressed.

Chapter 3 shares a similar layout. In this case, it focuses on the in-service behaviour of the component after the manufacturing or heat treatment process, that is, it deploys the findings of the preceding chapter. In the first place, a literature review summarising the statistical nature of glass

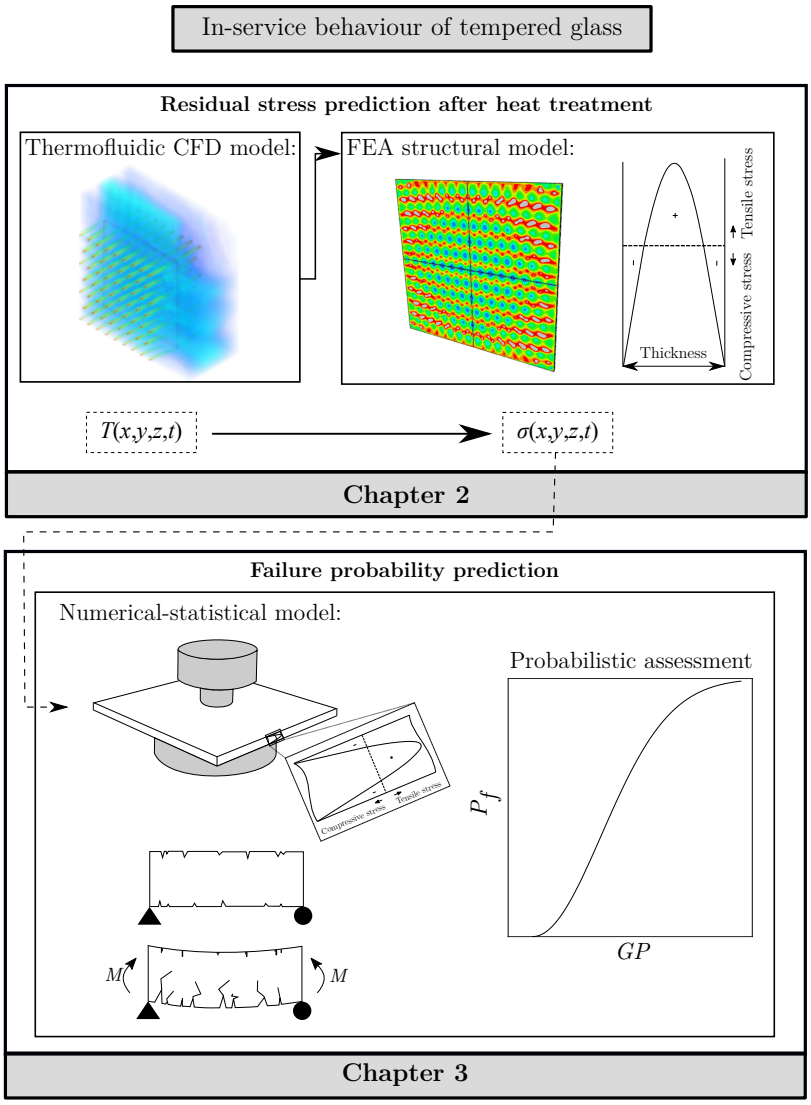

Figure 1.3: Overview of the research methodology.

strength, the experimental testing methods and the fracture modelling of glass is presented. Thereafter, the fundamentals supporting the performed statistical assessment are delineated. At this point, the methodology to predict the failure of tempered glass components is described. This way, the needs of **Sub-objective 3** are fulfilled. Likewise, a discussion of the obtained results is done by comparing them to the performed experimental work. This way, **Sub-objective 4** is also addressed.

Finally, **Chapter 4** comprises the main conclusions of the thesis and suggestions for future work are also made.

Chapter 2

Numerical methodology based on Fluid-Structure Interaction to predict residual stresses during tempering

2.1 Introduction

In recent years, the glass industry has been working to reduce the weight of the final product so as to decrease the cost in raw materials and/or the energy required to heat and produce the glass. Weight reduction is usually achieved by reducing the thickness of the material, however this can also result in a weaker component. In parallel to this, customers are moving towards the use of large area glass components with the aim of achieving lightness and transparency. Nevertheless, glass exhibits brittle fracture behaviour and, unlike ductile materials, is prone to collapsing from local stress concentrations. For this reason, glass is most often heat treated before using it as a structural material.

Thermal tempering is the most effective and efficient method to enhance the load bearing capacity and strength of glass workpieces [7, 8, 10]. The degree of temper depends on the initial temperature of the glass sample and the cooling rate used during the tempering process [13, 18–20]. However, as residual stresses develop due to the thermal gradient between the surface and the centre of the material, cooling strategies leading to appropriate tempering remain limited [12, 13, 55]. The standard thermal tempering process is generally composed of air nozzle arrays for cooling the glass components. This technology may result in non-uniform cooling distributions on the glass surface which have a direct impact on the structural and aesthetic features of heat treated components [35, 56, 57]. To date, the design and control of tempering processes have relied on trial and error tests or experience based judgements and options for improving these approaches are limited [58]. As a result, numerical methods have gained significant traction.

New environmental laws and the growing competition have reduced the profit margin on glass industry, making it necessary to perform a more comprehensive optimisation of the production cycle [59]. This fact greatly emphasises the need to control the cooling process during heat treatment and reduce the stress variabilities and optical anisotropies that may arise. Therefore, the development of a methodology based on numerical analysis is necessary to better understand the physical phenomena involved and reduce the need for complex and time-consuming experimental tests.

In this chapter a FSI numerical methodology to calculate the non-uniform residual stresses developed during the tempering process is presented. To this end, the different types of structural glass, current heat treatment procedures, state-of-the-art modelling of tempering, and residual stress characterisation techniques are explained in the literature review. In the section that follows, the proposed methodology is presented and the numerical procedure is described in detail.

With the aim of validating the proposed FSI methodology, two different case studies are modelled. First, a validation procedure based on laboratory case studies characterised by symmetrical single-jet cooling is presented. Here, the defined laboratory case studies, the corresponding numerical models and the followed experimental procedure are explained. Then, the proposed FSI numerical methodology is validated by the experimental laboratory results and challenge of the high computational cost is also addressed. A sensitivity analysis to analyse the influence of specific process uncertainties and modelling parameters on the residual stress development is also carried out.

Once the proposed numerical procedure is validated by laboratory data, the performed procedure is extended to an industrial case study, where multiple nozzle arrays are employed. In this way, the validity of the performed hypotheses and their implementation in an industrial environment are demonstrated. Figure 2.1 depicts an overview of the steps carried out in this project.

Finally, the main conclusions of the analysis are summarised.

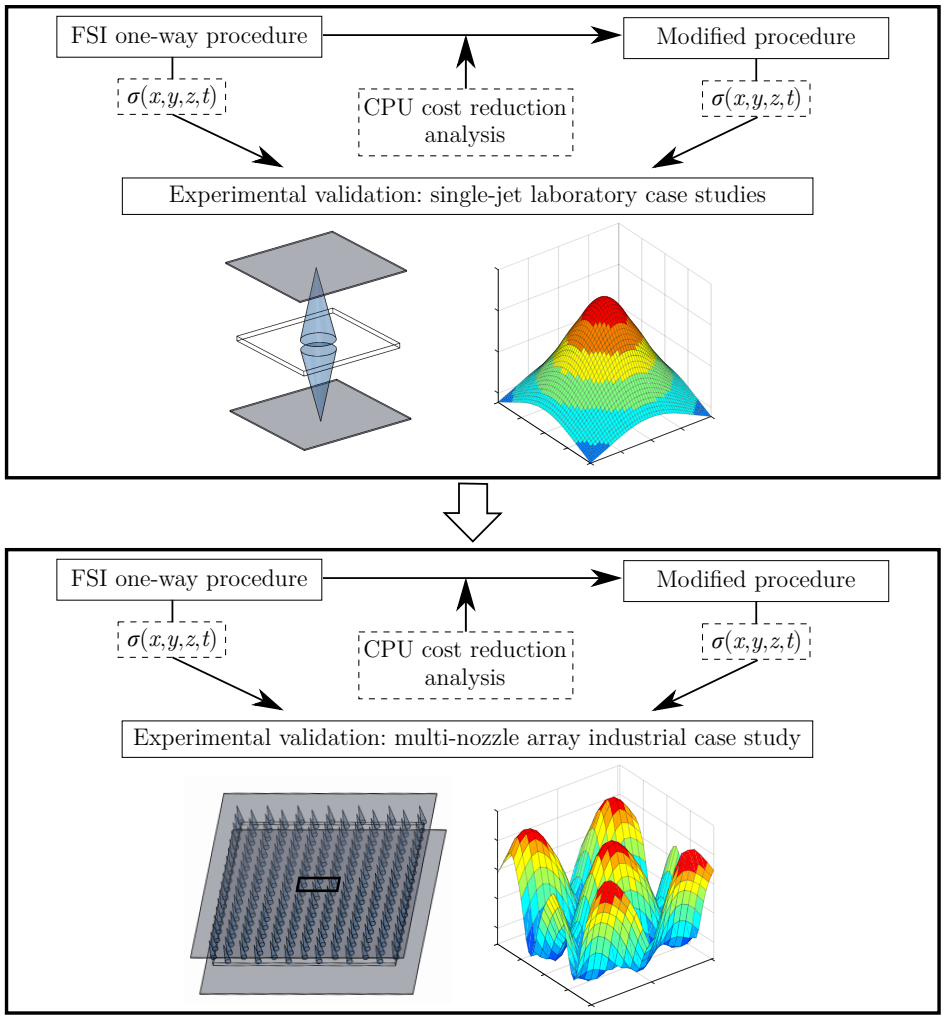

Figure 2.1: Overview of the study to estimate the residual stress pattern in glass components.

2.2 Literature review

This section summarises the state of the art of glass tempering. Firstly, the different types of structural glass are outlined. Secondly, the current experimental procedure for heat treating glass is analysed. The thermo-mechanical behaviour of the material and the various numerical approaches to predict residual stresses in glass are then discussed. Finally, the main residual stress characterisation techniques to ensure the required part quality are reviewed.

2.2.1 Structural glass

The most common and least expensive glass type is soda-lime-silica glass [2, 60, 61]. Beverage bottles and containers, lenses and mirrors, lightbulbs, window panes and façades are all made from this material [62]. Through out this thesis the term glass is used for the soda-lime-silica glass family. Despite its brittle nature, properties of heat treated glass can be similar to those of ductile materials, such as aluminium (see Table 2.1).

Table 2.1: Properties of glass and aluminium [63].

	Annealed glass	**Tempered glass**	**Aluminium**
Strength [MPa]	7-28	59-150	130
Young's modulus [GPa]	70	70	70
Density [kg/m^3]	2500	2500	2700
Thermal expansion coefficient [K^{-1}]	9.1	9.1	24
Poisson's ratio	0.23	0.23	0.33

An additional problem related to glass is breakage, which may produce sharp fragments and cause injuries. As a result, there exits different glass processing methods to accomplish the safety and strength requirements needed for structural applications.

Annealed glass

During its forming process, glass is subjected to a rapid cooling that results in the development of residual stresses. The main reason why glass is annealed is to relax or reduce the previously developed residual stresses. Non-annealed or poorly annealed glass may break easily during handling or show poor mechanical resistance under any thermal or mechanical load. Thus, annealing is usually applied to increase the durability of the material and to obtain a high degree of homogeneity of the refraction index [64].

Nowadays, the annealing process is continuously applied on the production line, where residual stresses are relaxed by cooling the material under controlled conditions until room temperature.

Tempered glass

Generally, introduction of compressive stresses into the surface is the most cost-effective way to strengthen glass. Compression closes small existing cracks present from the manufacturing process. This fact lead to a larger ultimate strength of the material, which can be as much as 4 to 5 times higher than the one of annealed glass.

In order to achieve high durability, the depth case, which refers to the depth of the compressive layer in thermally tempered parts, must be greater than the size of any surface defect. Some typical flaws reach 1–10 μm, even though, the size of the flaws is widely distributed and there might be larger flaws around 100 μm [8].

The commercial strengthened glass market is mainly dominated by the chemical and thermal tempering processes. On the one hand, during chemical tempering an alkali-containing glass is immersed in a bath containing a molten alkali salt such as potassium nitrate (KNO_3). This process takes place at temperatures around 370 – 450 °C. In the case of soda-silica glass, the larger potassium ions replaced the host sodium ions, creating a compressive stress layer that increases glass strength. The main advantages of this process are the achievement of large surface compressive stresses, the ability to temper thin plates even down to 100 μm, and the ability to strengthen irregular geometry products as long as the surface can be contacted by the molten salt [7, 10, 12]. Nevertheless, the main drawback of this process is the cost due to the specific equipment needed and the large process duration [8, 12]. Some other disadvantages are the limitation to certain types of glass and the associated low depth of layer (< 100 μm).

During the thermal tempering, glass is heated to a uniform temperature at which it is fluid enough to relax internal stresses and rigid enough to avoid large deformations due to its own weight. Air jets are usually employed for chilling the material from a temperature above the glass transition temperature. The surface of the part cools more rapidly than the core, and at a certain point the surface will behave as an elastic solid, whilst the interior still remains in a viscous state. The coefficient of thermal expansion of the liquid glass is about three times higher than the solid glass, resulting in a contraction mismatch during the rapid cooling. When the surface is cooled down to ambient temperature, the core continues to cool and contract leading to a compression stress state on the surface [8, 12]. Consequently, a balancing tensile stress is developed in the midplane of the component, resulting in a parabolic stress distribution through the thickness of the part.

Thermal tempering is a very efficient method to handle flaws as it creates a large case depth, being nearly a 20% of the wall thickness [7, 10]. However, limitations arise for thicknesses down to 2-3 mm [12]. Additionally, when the stresses exceed the tensile strength or when a crack propagates into the tensile zone, glass breaks spontaneously into small fragments due to the release of the high strain energy of the material [8, 10, 65]. Because of this large internal strain energy, all fabrication altering the stress distribution, such as, cutting, edge-working, or drilling of holes must be performed prior to the heat treatment process [8, 66]. Similarly, tempered glass tends to fracture into blunt and small fragments reducing the risk of injuries. Therefore, tempered glass is habitually used as safety glazing, such as in shower enclosures, roofs or in applications where significant resistance against wind pressure, thermal stress or both, is needed.

Heat strengthened glass

The heat strengthening process is very similar to thermal tempering, but the cooling is less severe, hence, it brings about a lower glass strength. As lower compressive stresses are achieved, heat strengthened glass does not show the same fracture pattern as tempered glass and it breaks into large pieces resembling the breakage mode of annealed glass [8, 63]. Through out this thesis, the term tempered glass is used for heat treated glass, even if certain standards define a specific uniform compressive stress value to attain such condition [67].

Laminated glass

Laminated glass consists on layering two or more sheets using an adhesive foil. The glass sheets might consist of annealed, heat strengthened, fully tempered, or a combination of them, albeit annealed sheets are the most commonly used [66]. The interlayer is usually made of thermoplastic polymer PVB (Polyvinyl Butyral) because it almost completely blocks ultraviolet radiation and produces high sound insulation [9, 10, 63, 68]. The structural behaviour is determined by the ability of the interlayer to transfer shear between the glass panes [69]. When one glass sheet is broken, the fragments remained stuck to the interlayer making it suitable for safety applications. Laminated glass is on average more expensive than tempered glass as it is thicker, and thus, heavier. Moreover, as different glass types can be combined, it is convenient to analyse them independently before joining them into a laminated glass structure.

2.2.2 Thermal tempering procedures

During the thermal tempering, glass is heated to a uniform temperature at which it is fluid enough to relax internal stresses and rigid enough to avoid large deformations due to its own weight. Heating by radiation rather than by convection is preferred as smaller thermal gradients are generated within the part due to the volumetric feature of radiation in glass [70].

Regarding the initial quenching temperature, previous research findings showed its large influence on residual stress development. Narayanaswamy proved that for a specific cooling rate, as the initial quenching temperature was increased, the achievable degree of temper increased until a plateau was reached [18]. A similar conclusion was obtained in this aspect by Aronen & Karvinen and Agboka et al., who showed that as initial temperature increased, the maximum surface tensile stresses developed at the onset of cooling decreased for different glass thicknesses [20, 71]. This fact highlights the risk of in-process breakage of glass during cooling. The authors stated that for high convection coefficients, initial temperature lower than 650 °C could lead to breakage of the specimen. They also concluded that the breakage of the specimen could be prevented if the tempering was initiated from a relatively high temperature ($T_0 \approx$ 700 - 750 °C). The reason for this may be the contraction and relaxation phenomenon of glass. If tempering is performed from a relatively low temperature close to the glass transition range, the surface rapidly cooled and the warmer region, namely, the core, restrain the surface contraction putting it under tensile stresses. Nonetheless, if the initial temperature is high, the midplane is too soft to restrain the initial surface contraction and tensile residual stresses do not occur. At such high initial temperatures, however, components may exhibit large deformations or warpage due to the low viscosity of the material. Thus, heat treaters are forced to quench the part from lower initial temperatures even if this imply a smaller degree of temper and the development of tensile residual stresses at the beginning of the process. Therefore, the uniformity of the temperature distribution along the whole glass surface becomes a major concern to prevent in-process fracture during quenching.

Historically, different cooling strategies have been adopted to quench glass. First attempts regarded to water immersion quenching. However, the use of water provided excessive cooling rates bringing about the breakage of glass during cooling. Furthermore, immersion quenching generally shows different boiling regimes during cooling, resulting in a complex temperature dependent phenomenon [72, 73]. Consequently, this technique resulted in an excessive and non-uniform cooling making it an inadequate candidate for glass tempering [13]. Afterwards, liquids with moderate heat transfer capability, such as, mixture of oils and greases, molten salts or low melting metals like tin, were used. Nonetheless, even these type of liquids needed to be preheated to decrease their cooling power, becoming a potential hazard for the operators who quench the red-hot glass into the preheated oil. Additionally, quenching by solid contact was also investigated. This technique consisted on pressing glass between two cold metal plates reducing the distortion produced by liquid quenching. However, chill cracks arose on the surface as a consequence of the large heat transfer between glass and metal. It was in the 20^{th} century when not only the shape but also the surface finish was preserved by cooling glass by impinging air jets. Thermal tempering by air jets can be directly performed on the production line without reheating the workpieces that have been made. Nevertheless, the common industrial procedure consist on heating the already manufactured part [14, 74–78].

Overall, the standard tempering process for flat glass consists of an horizontal process where the glass moves on ceramic rollers [79]. With the aim of achieving an homogeneous heat extraction, oscillation by moving the glass forwards and backwards over the rollers is also a common approach [26, 56]. For this purpose, air quenching has become the dominant cooling technique employed in industry. The use of air nozzle arrays involves smaller costs compared to immersion quenching, no production of toxic or combustible gases and greater process flexibility.

Nevertheless, air quenching encompasses several challenges within the heat treating industry. As the need to reduce the weight of the components became popular, the thickness of tempered glass decreased. Consequently, as the HTC is approximately inversely proportional to the glass thickness, higher values were required to fully temper glass (see Figure 2.2).

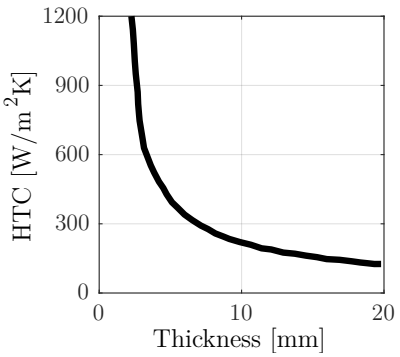

Figure 2.2: The required HTC to temper glass as a function of thickness, adapted from [6] and [14].

Accordingly, the required air power to temper glass is strongly dependent on the thickness of the component to be quenched (see Figure 2.3).

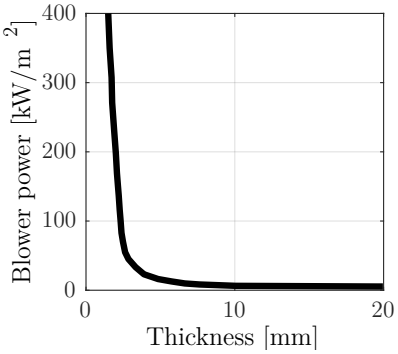

Figure 2.3: Blower power required to fully temper glass as a function of thickness, adapted from [14].

Consequently, the air blower costs could represent a significant amount of the entire glass forming and tempering plant costs. As a result, other novel cooling techniques that enable lower manufacturing costs and similar or higher heat transfer rates, such as mist cooling, are emerging [80–83].

2.2.3 Thermal tempering modelling

With the view to modelling the thermal tempering process of glass, different features need to be taken into account. Firstly, the constitutive model of the material at high temperature needs to be addressed. Then, different residual stress modelling approaches are reviewed. In this context, the material behaviour and residual stresses are shown to be strongly dependent on temperature and the temperature history of the material. Therefore, understanding of heat transfer mechanisms, such as convection modelling and radiation in semi-transparent, becomes a paramount matter for predicting and controlling residual stresses of heat treated glass.

Material constitutive model

The material constitutive model of glass is grounded on two main mechanisms that are involved in the residual stress development during tempering: the viscoelastic stress relaxation and the structural relaxation phenomena.

1) **Viscoelasticity**

   Glass is an amorphous non-crystalline material where silica (SiO_2) is the main component. At room temperature, glass behaves as a linear elastic solid. However, when temperature is increased its mechanical properties change rapidly over a small temperature range, also known as the glass transition temperature, T_g. For this reason, glass is known to exhibit the phenomenon of glass transition [10, 61]. During this transformation stage, the bonds of the material break, denoting the onset of viscoelastic behaviour.

Viscoelastic materials are generally modelled by phenomenological spring and dashpot models, such as the Generalised Maxwell model. In this way, the time dependent linear viscoelastic behaviour of the material is described by means of a differential equation. In 1876 Boltzmann developed a more general model for materials exhibiting multiple relaxation mechanisms [84]:

$$\sigma_{ij}(t) = 2\int_0^t G_{\mathrm{s}}\left(t-t'\right)\frac{\mathrm{d}e_{ij}\left(t'\right)}{\mathrm{d}t'}\mathrm{d}t' + \delta_{\mathrm{k}ij}\int_0^t K_{\mathrm{b}}\left(t-t'\right)\frac{\mathrm{d}\varepsilon_{ii}\left(t'\right)}{\mathrm{d}t'}\mathrm{d}t', \tag{2.1}$$

where σ_{ij} is the stress tensor, t refers to the time, t' is an incremental parameter for time, e_{ij} is the deviatoric strain tensor, ε_{ii} is the trace of the strain tensor and $\delta_{\mathrm{k}ij}$ is the Kronecker's delta. According to the Boltzmann superposition principle, the stress relaxation due to viscoelasticity is characterised by the time dependent shear $G_{\mathrm{s}}(t)$ and bulk $K_{\mathrm{b}}(t)$ modulus. The shear modulus affects to the deviatoric stress while the bulk modulus to the hydrostatic stress. These relaxation modules can be described as a series of exponential functions known as Prony series [85].

In addition to time, temperature has a strong influence on the viscoelastic material properties. The characterisation of the stress relaxation curves implies a hard experimental work to obtain the different relaxation curves under different loads for each temperature. However, in certain cases it is possible to shift the normalised relaxation curves and build a single master relaxation curve based on a reference temperature T_{B}. The materials that are able to relate the time and temperature in this manner are known as thermorheological simple materials, and glass is characterised by this behaviour. For this reason, the relaxation function of glass obtained at an arbitrary temperature can be transformed to another temperature by defining a scaled time ξ instead of the real time t. The scaled time has the dimension of time and is given by the following expression:

$$\xi = \phi(T)t. \tag{2.2}$$

The shift function, $\phi(T)$, which is generally used to scale the real time t, obeys an Arrehnius type law:

$$\ln\phi(T) = \ln\frac{\mu_{\mathrm{g}}\left(T_{\mathrm{B}}\right)}{\mu_{\mathrm{g}}(T)} = \frac{H_{\mathrm{act}}}{\mathrm{R}_{\mathrm{g}}}\left(\frac{1}{T_{\mathrm{B}}} - \frac{1}{T}\right), \tag{2.3}$$

where μ_{g} is the dynamic viscosity of glass, T is an arbitrary temperature, T_{B} the reference temperature, H_{act} is the activation energy and R_{g} is the universal gas constant.

2) **Structural relaxation**

Depending on the rate of heating or cooling, certain glass properties such as density are varied. This variation stems from the structural arrangement of the atoms. In addition, the structural relaxation is deemed as an influential phenomenon during the residual stress development in glass [18]. Based on the mathematical formulation proposed by Narayanaswamy [17], Figure 2.4 shows the volumetric contraction phenomena over the glass transition range. As can be observed, the volumetric contraction varied not only with temperature but also with the applied cooling rate, whereas the thermal contraction remained constant. All the same, it always shows the same shape; it increases with temperature and stabilises beyond the glass transition temperature, T_g.

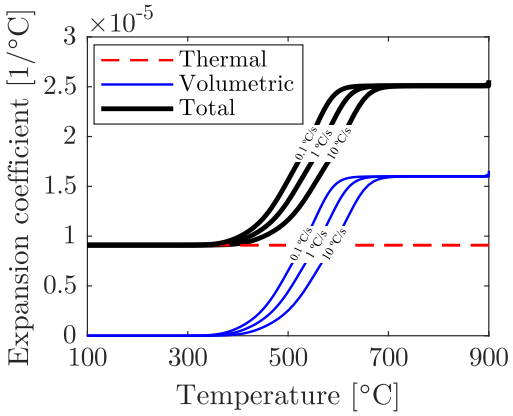

Figure 2.4: Variation of thermal and volumetric expansion coefficients over the glass transition range for different cooling rates: 0.1 °C/s, 1 °C/s, and 10 °C/s; based on [17].

The volumetric contribution to the total contraction coefficient vanishes at a higher temperature with increasing cooling rate. When a low cooling rate was applied, such as 0.01 °C/s, the contribution of the volumetric expansion coefficient vanished at 350 °C, whereas if a higher cooling rate was applied, namely, 10 °C/s, this phenomenon occurred at 400 °C. The latter case had more to do with the cooling rate magnitude that normally occurs during the tempering process. Similarly, Figure 2.5 sets out the variation of normalised volume over the glass transition range when the material is subjected to different cooling rates. As shown here, the higher the applied cooling rate, the higher the volume in the material. As a result, the density of the material became smaller for high cooling rate processes than for a lower cooling rate process. This fact combined with a non-uniform cooling leads to a non-uniform contraction of the material, which is considered as one of the main sources of residual stresses. Additionally, it is possible to observe that almost all the structural arrangement occurred in the glass transition range. However, as glass is an amorphous material, its microstructure continued to rearrange even at lower temperatures.

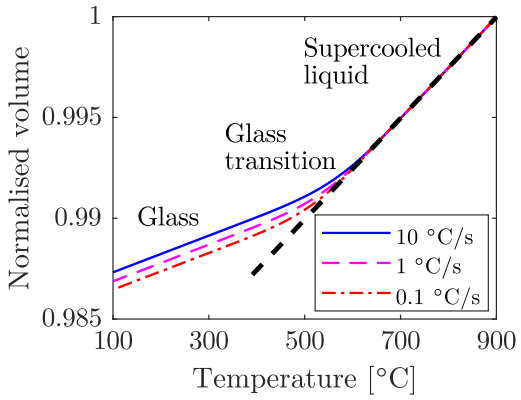

Figure 2.5: Variation of normalised volume over the glass transition range for different cooling rates: 0.1 °C/s, 1 °C/s, and 10 °C/s; based on [17].

With the aim of describing the microstructural state of glass, Tool introduced the concept of fictive temperature, T_f, as a measure of the degree of non-equilibrium glass [86]. In 1971 Narayanaswamy proposed a structural model that accounted for these cooling rate dependent properties [17]. In this regard, a new mathematical statement to determine the fictive temperature was presented. In this way, the fictive temperature was observed to be dependent on the response function $M_\mathrm{p}(t)$, which is obtained experimentally:

$$T_\mathrm{f}(t) = T(t) - \int_0^t M_\mathrm{p}\left(\xi(t) - \xi'(t)\right) \frac{\partial T\left(t'\right)}{\partial t'} \mathrm{d}t. \tag{2.4}$$

When the fictive temperature was found, the thermal strain, ε_th, could be calculated by the next equation:

$$\Delta\varepsilon_{\mathrm{th}ij} = \delta_{\mathrm{k}ij}\Delta\varepsilon_\mathrm{th} = \delta_{\mathrm{k}ij}\left(\alpha_\mathrm{g}\Delta T + \left(\alpha_\mathrm{l} - \alpha_\mathrm{g}\right)\Delta T_\mathrm{f}\right), \tag{2.5}$$

where $\delta_{\mathrm{k}ij}$ is the Kronecker delta and α_l and α_g are the thermal expansion coefficients for the liquid and solid state, respectively.

Residual stress modelling

Two main aspects are distinguished when it comes to residual stress calculation in glass components, namely, the structural or material field and the heat transfer modelling. The material modelling and the origin of residual stresses in glass have been deeply studied in literature. Adams & Williamson described the first analytical equation for uniformly cooled glass sheets [15]. From this point on, additional models for non-uniform cooling processes, such as the tempering process, were proposed [13, 87].

Following the works based on the thermoelastic theory, Lee et al. presented a viscoelastic model to predict not only the final residual stress distribution but also the transient stress distributions [16]. However, the model was not able to fit the experimental data when quenching the material at low quenching temperatures. Narayanaswamy & Gardon [88] improved the thermoviscoelastic model but it was not until 1971 when Narayanaswamy proposed an extension of the viscoelastic model adding the structural relaxation phenomenon of glass [17]. Moreover, this effect was shown to be a meaningful contributor to the residual stress development during the glass cooling process [18]. As a consequence, Nielsen et al. contributed to the calculation of residual stresses in complex glass components by implementing the constitutive material model proposed by Narayanaswamy in a 3D algorithm for finite element analysis [89].

On the other hand, heat transfer modelling is a key factor in the prediction of residual stresses in glass, as they are largely influenced by the thermal history of the components. During the glass tempering process, where large heat transfer rates are obtained, the heat transfer mechanisms involved refer to conduction, convection and radiation. Conduction is usually well understood as it is characterised by the thermal conductivity of the material [21]. Regarding convection phenomena, the definition of constant and uniform HTCs has been a commonly adopted approach due to its associated low computational cost. Daudeville & Carre presented a FEM model to calculate residual stresses in glass plates based on the definition of constant HTCs [19, 22]. Bernard et al. conducted a thermal characterisation in aluminium plates by thermocouples to resemble the heat extraction in glass during tempering [90, 91]. In this manner, they determined the local HTC for different areas of the plate: top surface, edge and hole surface. Nielsen et al. performed a parametric study to observe the influence of geometrical features, such as, plate thickness or hole diameter, on residual stress development near holes [23]. To this end, the authors defined convective HTCs on the glass surface based on the aforementioned study of Daudeville & Carre [22]. Similarly, Pourmoghaddam et al. carried out more exhaustive parametric studies about the behaviour of residual stresses near geometrical discontinuities [24, 25]. They relied on the HTCs obtained by Bernard & Daudeville to perform the thermal calculations [91]. In a more recent work, Pourmoghaddam et al. presented an inverse analysis to determine the needed engine power in order to reach a specific residual stress magnitude by air quenching [92]. The authors performed axisymmetric simulations to calculate the required HTC for the desired degree of temper. Overall, the main shortcoming in the numerical modelling of heat treatment processes is to neglect the local flow phenomena and to approximate it by uniform and constant HTCs over time. Conversely, Mikkonen et al. proposed an alternative approach by using time-constant but spatially different HTC distributions to analyse the effect of different jet configurations on a moving plate [26]. This assumption might enable a further reduction of the computational cost. However, as the transient nature of the turbulent flow is simplified, its influence on the adopted tempering configuration needs to be assessed.

Convection modelling

The defined nozzle geometry and arrangement was reported to have a huge importance on the heat extraction distribution of cooled parts [93]. In fact, the use of multiple nozzle arrays might lead to substantially different flow and heat transfer characteristics than the ones obtained by single jets due to the interaction between neighbouring jets [94, 95]. At short jet-to-plate distances and high jet velocities, the deflected air streams after hitting the surface may meet on the vicinity of the stagnation points and secondary peaks in heat transfer rate can be developed [96]. Conversely, at large nozzle-to-plate distances and small spacings between jets, interaction of the jet flows before reaching the

surface can take place [97]. Consequently, the flow strength might be weakened and smaller heat transfer magnitudes can be achieved. Nevertheless, if the nozzle-to-nozzle distance was increased, the interaction between cores disappeared and the interaction between the deflecting flows of each jet on the surface might foster an upward flow, also known as the 'fountain effect' [97, 98]. Finally, the design of the outflow is known to have a strong influence on the cooling efficiency and effectiveness, as it may determine the strength of crossflow on the surface [75, 94, 99].

All these effects had a direct impact on the residual stress distributions as emphasised by Monnoyer & Lochegnies [34]. Nielsen et al. accomplished residual stress measurements on commercially tempered glass plates with different thicknesses by a portable scattered light polariscope (SCALP) [35]. They concluded that more knowledge about the control of the heat treatment process was needed as they observed high variations not only in the residual stress state of individual specimens, but also among specimens of the same batch. A similar statement was made by Anton et al., who measured the residual stress pattern by SCALP and concluded that highly non-uniform distributions were observed [36]. Likewise, Chen et al. carried out an experimental investigation about the uniformity of residual stresses in tempered glass plates [56]. They concluded that too spaced cooling jets might lead to residual stress inhomogeneity and that oscillation of the glass specimen could improve the cooling flow homogeneity. Last but not least, Mikkonen et al. and Karvinen et al. analysed the importance of heat transfer control on the quality of glass in terms of optical anisotropy [26, 54]. The authors highlighted the use of numerical methods to solve the HTC distributions developed by jet impingement. Thus, flow uniformity becomes a main concern during tempering. However, the assumptions of homogeneous and constant HTCs hinders the consideration of non-uniform cooling distributions. Furthermore, authors generally not only emphasised the need to control heat transfer during tempering, but also mentioned shortages regarding numerical modelling, such as, the complexity of modelling the interaction of multiple impingement jets and the large amount of computational resources required.

Recently, the application of novel cooling techniques, which in turns demand more sophisticated numerical approaches, is becoming popular within the heat treatment industry. With the view to enhancing the quality of the products or reducing the manufacturing costs, new processes, such as, pulsed jets, swirling jets or interrupt quenching techniques encompassing the use of mist cooling might be encountered [100–102]. For this purpose, modelling the turbulent flow and its interaction with the target surface becomes the major challenge for understanding the involved underlying mechanisms and the developed transient boundary layer. In this sense, computational fluid dynamics (CFD) becomes a powerful tool that allows capturing the effect of flow behaviour in the heat exchange along the heat treated surface.

Based on CFD, the fluid phase and heat and mass transfer are modelled by the Navier-Stokes equations, composed of the conservation of mass and the momentum. On the one hand, the continuity equation can be written in partial differential form as follows:

$$\frac{\partial \rho}{\partial t} + \nabla \cdot (\rho \vec{v}) = 0, \tag{2.6}$$

where ρ is the density and $\vec{v}$ is the velocity. The first term represents the mass rate increase in time and the second one the mass flow out of the control volume. On the other hand, conservation of momentum in an inertial or non-accelerating reference frame can be described in partial differential form as follows:

$$\frac{\partial(\rho\vec{v})}{\partial t} + \nabla \cdot (\rho\vec{v}\vec{v}) = -\nabla p + \rho\vec{g} + \mu\nabla^2\vec{v} + \vec{F}. \tag{2.7}$$

The first term on the left side represents the momentum increase rate, and the second term the momentum flux composed of static pressure gradient, gravitational forces, the viscous stress tensor and external body forces, respectively.

Regarding heat transfer analysis, density is no longer constant and an additional fundamental equation is needed to complete the system. This relation is the energy equation given by:

$$\frac{\partial}{\partial t}\left[\rho\left(e + \frac{v^2}{2}\right)\right] + \nabla \cdot \left[\rho\left(e + \frac{v^2}{2}\right)\vec{v}\right] = \nabla \cdot (k_{\mathrm{th,f}}\nabla T + (\boldsymbol{\tau}_{\mathbf{v}} \cdot \vec{v})) - \nabla \cdot (p\vec{v}) + S_{\mathrm{h}}. \tag{2.8}$$

In this equation the bracketed term is the total energy of the flow composed of the internal energy, e, and kinetic energy, $v^2/2$. $k_{\mathrm{th,f}}$ is the thermal conductivity of the fluid and $\boldsymbol{\tau}_{\mathrm{v}}$ the viscous stress tensor. The terms on the right-hand side of the equation represent the energy transfer due to conduction, viscous dissipation and the sources of energy S_{h}, which include the heat generation due to chemical reactions, radiation source terms or heat transfer between the continuous and a discrete phase. In the solid region, the energy equation shows the following form:

$$\frac{\partial T}{\partial t}\rho_{\mathrm{g}}c_{\mathrm{p,g}} = \nabla \cdot (k_{\mathrm{th,g}}\nabla T) + \dot{q}, \tag{2.9}$$

where ρ_{g}, $c_{\mathrm{p,g}}$ and $k_{\mathrm{th,g}}$ are the density, specific heat and conductivity of glass, respectively, and $\dot{q}$ is the volumetric heat generation.

An additional key factor in CFD simulations refers to the modelling of turbulence. Navier-Stokes equations and turbulence modelling are highly non-linear, and hence, numerical methods are used to solve them. The Direct Numerical Simulation (DNS) is the most precise method, followed by the Large-Eddy Simulation (LES) approach, and finally, the Reynolds-Averaged Navier-Stokes (RANS) numerical method is encountered. The computational cost of each method is directly related to its resolution degree. DNS implies a prohibitively high computational cost and it could be considered non-practical for industrial applications. LES requires less computational resources but still demands a very fine grid to solve turbulence scales. Actually, even if RANS is considered to be the lowest accurate method to solve turbulent flows, it has shown an appropriate performance when modelling jet impingement heat transfer applications [100, 103]. Consequently, in the following lines the RANS method is briefly described.

The velocity at a particular point in a turbulent fluid is characterised by a high fluctuating behaviour. The RANS approach decomposes the instantaneous velocity of the flow into the time-averaged and fluctuating components. To do so, it introduces additional unknowns into the Navier-Stokes equations, namely, the so-called Reynolds stresses, which are related to the involved averaged fluctuating velocity components. Two types of closure models exist to solve the unknown additional parameters and close the system of governing equations: the Reynolds-Stress Model (RSM), also known as the seven equations model, and the Eddy Viscosity Model (EVM), which is classified according to the number of equations involved; zero, one or two equation models. The EVM entails a lower computational cost. Moreover, for most industrial applications, two equation turbulence models are generally used.

These models make use of empirically correlated constants to solve the proposed turbulence modelling equations. Among them, the standard $k-\varepsilon$ model is the most widely used model in engineering problems. However, it performs poorly for flows with large pressure gradients, strong separation and high swirling component. Consequently, it usually shows poor results in the stagnation and wall jet regions and it is not recommended for jet impingement applications. In this context, the $k-\omega$ turbulence model has gained popularity as it is considered to be more accurate than $k-\varepsilon$ models for boundary layer flows [104]. Particularly this is the case for the Shear Stress Transport (SST) model. The SST model is a two equation turbulent model where the $k-\omega$ model is employed to solve the boundary layer and the $k-\varepsilon$ model is used to solve the freestream flow in the far field. Additionally, Zuckerman & Lior performed an exhaustive review about turbulence modelling and considered the SST model as one of the most appropriate options to model impinging jets in terms of accuracy and computational cost [100]. Recently however, ANSYS developed a new turbulence model family called Generalised $k-\omega$ (GEKO) model. GEKO is based on the $k-\omega$ model formulation, but with the flexibility to cover a wide range of flow scenarios, such as jet impingement. This way, a better prediction of the round jet expansion is achieved, as conventional models like SST may overpredict the spreading rate of round jets substantially.

Furthermore, when the impinging flow hits the targeted surface, an abrupt change of the flow velocity takes place, resulting in large wall shear stresses and an overprediction of the turbulent kinetic energy on the surface [103]. As a result, an overestimated heat transfer rate may be achieved in the stagnation area on the targeted surface. The Intermittency Transition model with Kato-Launder production limiter was found to deal with this problem [105–107]. This option limits the excessive production of turbulence kinetic energy caused by the high level of shear stress rate in the stagnation regions. Nevertheless, underprediction of heat transfer in the stagnation region have been observed for $H/D > 10$ [108].

In general, the presented turbulence models are based on the assumption that turbulent Reynolds numbers are high enough to neglect viscous effects. Turbulent flows however, are significantly affected by the presence of walls. Near a wall, velocity changes rapidly due to the no-slip condition which results in viscous phenomenon in the immediate vicinity of the wall. This near-wall region is called the viscous boundary layer. As a result, large gradients occur near the impinged wall, and thus, it is crucial to accurately represent the flow in this region. The distance from the wall is measured by the non-dimensional parameter y^+, which is defined by:

$$y^+ = \frac{\rho v_\tau y}{\mu} \tag{2.10}$$

where y is the distance from the wall, μ is the dynamic viscosity of the fluid and v_τ is the friction velocity given by:

$$v_\tau = \sqrt{\frac{\tau_\mathrm{w}}{\rho}} \tag{2.11}$$

where τ_w is the wall shear stress. The turbulence scales developed in the boundary layer are so small that the needed number of cells increases considerably. If the k – ω turbulence model is used, the boundary layer is numerically solved. Consequently, a high quality mesh is needed to properly model the boundary layer and the y^+ value shall not exceed the unity for the first grid cell [104].

Radiation modelling

During glass tempering, not only the convective heat transfer is important, but thermal radiation in semi-transparent media also gains special relevance. In semi-transparent materials the absorption and emission of energy are a bulk rather than a surface phenomena. Thus, it can play a vital role in the temperature calculation as it helps to redistribute the heat through the component [37, 38]. According to Siegel, this fact might have a direct impact on residual stress development during the manufacturing or heat treatment processes [39]. Recently however, some authors stated that the contribution of radiation decreased as the cooling rate increased [20, 40]. Figure 2.6 sets out the larger weight of radiation in the total heat flux extraction as glass becomes thicker during a conventional tempering process.

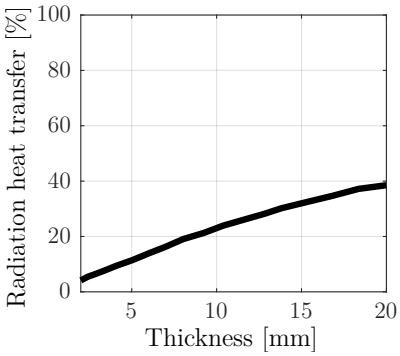

Figure 2.6: Contribution of radiation during quenching from 620 °C as a function of thickness, where the remaining part refers to the forced convection contribution. Adapted from [6].

Even though, as works focused on this topic relied on 1D calculations, its importance and effect on the spatial residual stress distribution was not clarified yet. Thus, being radiation a volumetric phenomenon, it demands specific modelling techniques. Gardon was the one who presented a pioneering thermal model accounting for the volumetric feature of glass radiation, meaning that each element inside the volume of the material was able to emit and absorb energy [70]. As a result, this process tended to homogenise the temperature within the material, while in opaque materials conduction is the only mechanism that enable this heat distribution. Recently, Siedow et al. described three main numerical methodologies to solve the complex mathematical formulation related to the radiative bulk behaviour of glass: the diffusion or Rosseland approximation, methods based on the spherical harmonic expansion (P_N approximation) and the Discrete Ordinates Method (DOM) [109]. Among them, the DOM was considered to be the most accurate one but it also involved a high computational cost [110]. Because of this reason, many authors have neglected the volumetric feature of glass radiation in order to simplify the numerical computation [25, 92]. Other authors included the radiation effect on the defined convective HTC [22, 89]. Bernard et al. proposed an alternative solution based on two radiative fluxes by defining a surface emissivity for the opaque spectral field and a volume emissivity for the semi-transparent wavelength range [90, 91]. Nevertheless, no radiation interaction within the volume was considered. Lately, Siedow et al. and Agboka et al. performed 1D thermomechanical analysis and compared different methods for the computation of radiation in glass [20, 40]. The authors showed in terms of residual stresses that the modified DOM was in better agreement with the experimental

results.

The DOM solves the radiative transfer equation (RTE) by defining a finite number of discrete solid angles. Each angle is defined by a vector direction $\vec{s}$ in the global Cartesian system (x, y, z). This method also allows to model non-grey radiation assuming a grey-band model. As glass exhibits a banded behaviour of this type, a constant spectral absorption coefficient a_λ for each wavelength band can be assumed.

The RTE for a non-grey model and in terms of spectral radiative intensity $I_\lambda(\vec{r}, \vec{s})$ can be written as:

$$\nabla \cdot (I_\lambda(\vec{r}, \vec{s})\vec{s}) + (a_\lambda + \sigma_{\mathrm{sc}})\, I_\lambda(\vec{r}, \vec{s}) = a_\lambda I_{\mathrm{b},\lambda} + \frac{\sigma_{\mathrm{sc}}}{4\pi} \int_0^{4\pi} I_\lambda(\vec{r}, \vec{s})\Phi(\vec{s}, \vec{s}')\mathrm{d}\Omega'. \tag{2.12}$$

In this equation $\vec{r}$ is the position vector, $\vec{s}$ is the direction vector, $\vec{s}'$ is the scattering direction vector and σ_{sc} is the scattering coefficient. The spectral absorption coefficient is denoted by a_λ and $I_{\mathrm{b}\lambda}$ is the black body intensity given by the Planck function. Finally, the phase function and solid angle are represented as Φ and Ω', respectively.

2.2.4 Residual stress characterisation techniques

Residual stresses arise from the resulting large thermal gradients and the inhomogeneous contraction of glass. These stresses can be measured by destructive or non-destructive methods.

Destructive methods analyse the glass fragments to determine the residual stress magnitude of glass parts. Dicing, namely, the ability of glass to break into small pieces, depends on the tensile residual stresses developed in the midplane of the part. A large amount of strain energy is able to reduce the glass fragments into harmless, cubical in shape, with blunt edges and no sharp points pieces. Thus, large fragments are the consequence of insufficiently tempered glass. As a result, heat strengthened glass are usually known as the strongest glass that do not experience dicing. The European standard EN 12150-1 establishes the procedure to be followed to carry out this assessment [111]. Many works studied the relation between glass fragments and residual stresses and relied on the counting of broken fragments to assess the quality of heat treated glassware [35, 102, 112–115]. However, this technique might only be valid for qualitatively assess the degree of temper, as some authors stated that no correlation exists between the local residual stress magnitude and the number of fragments [35, 112].

Among non-destructive measurements, photoelastic measurements based on the polarisation of light are encountered. Glass is optically isotropic, which means that its refractive index is the same in all directions. However, mechanical stresses causes deformations in the glass structure bringing about local changes in the refractive index within the material. This phenomenon is known as optical anisotropy or birefringence. Hence, stressed glass shows different indexes of refraction that coincide with the principal stress axes [116]. Because of this reason, polariscopes are instruments that are able to photoelastically quantified the residual stress pattern in glass components [25, 34, 117–119].

For a quantitative measurement of residual stresses in glass, different methods are reviewed in the literature [120]. Among them, the method based on scattered light photoelasticity used for three-dimensional stress analysis has gained traction during the last decade. Recently, Aben et al. developed a portable measurement equipment which offers the possibility to determine the stress distribution on the surface and through the thickness of glass [112].

The device emits a polarized laser beam at 70° angle from the surface normal, and it records the polarisation change along the light path. The variation in the intensity of the light makes the software possible to calculate the absolute optical retardation at each point along the laser beam. Finally, being the photoelastic constant of soda-lime glass known ($C = 2.7$ TPa^{-1}), the stress is calculated by:

$$\sigma = \frac{1}{C} \cdot \frac{\delta_{\text{opt}}}{\sin^2 \beta_{\text{beam}}}, \tag{2.13}$$

where δ_{opt} is the optical retardation and β_{beam} is the laser beam angle specified by the manufacturer. The measuring accuracy of SCALP alludes to 5% [121]. To avoid refraction of light, a glass prism and a layer of immersion liquid between the prism and the glass panel are employed (see Figure 2.7).

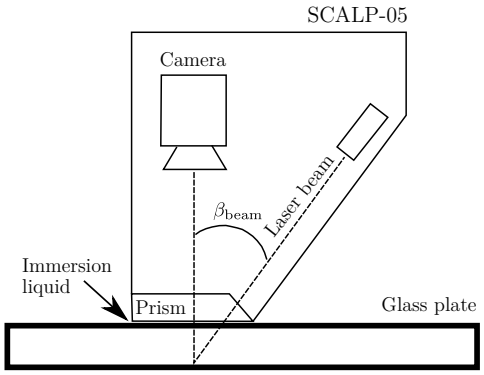

Figure 2.7: Internal mechanism of SCALP-05 adapted from [122].

With the aim of measuring residual stresses in glass components, the SCALP has been widely used by several works in the literature [25, 35, 36, 123, 124].

2.3 Numerical FSI methodology to predict non-uniform residual stress distributions

The proposed methodology presents a FSI based numerical procedure to predict the non-uniform residual stress distributions during the glass tempering process. Firstly, the general FSI one-way based methodology is provided. Subsequently, with the aim of reducing the computational cost of the general FSI procedure, different computational cost reduction techniques are proposed. In this way, a cost-effective modified FSI procedure for calculating residual stresses is presented.

2.3.1 General FSI procedure

One of the main limitations in most works focused on the residual stress prediction during heat treatment processes refers to the definition of constant and uniform HTCs over time. As a result, non-representative residual stress distributions might be achieved. Generally, heat treated components do not show uniform residual stress patterns due to the employed cooling technique, mainly composed of air jet arrays. The influence of a non-uniform cooling however, is generally not considered even if the thermal history of the material is known to play a vital role in residual stress development, especially, in glass components. Therefore, the proposed FSI one-way procedure intends to capture the effect of non-uniform cooling to predict the residual stress magnitude and distribution on heat treated components. The procedure consists of the following steps:

1. **Thermal history calculation:** a CFD model, where the conduction, convection and radiation phenomena are considered, needs to be defined. Here, the material physical, thermal and optical properties as well as the turbulence and radiation models are defined. To this end, the commercial CFD program ANSYS FLUENT is used for carrying out the calculation.

2. **Structural model considering the structural relaxation of glass:** the calculated temperature distribution are transferred into the commercial Finite Element Analysis (FEA) software ABAQUS FEA. The structural model considers the viscoelasticity and structural relaxation phenomena of glass based on the Narayanaswamy model. Its implementation in a 3D algorithm for finite element calculation can be found in the study of Nielsen [85].

3. **Non-uniform RS prediction:** once the part is cooled down to ambient temperature and the complete thermal history is read, the permanent residual stresses are predicted. A 3D geometry model is considered to represent the complete residual stress domain.

Figure 2.8 sets out the overview of the proposed numerical procedure for calculating the non-uniform residual stresses.

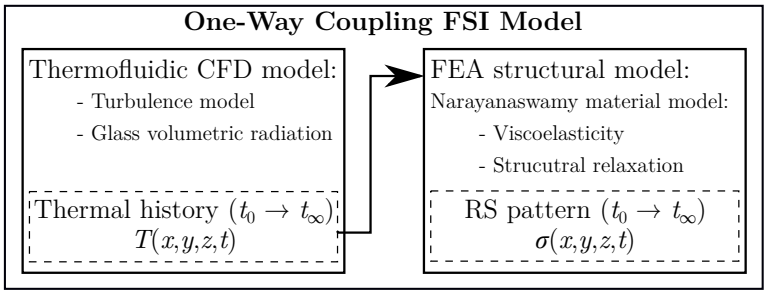

Figure 2.8: Flow chart of the proposed FSI one-way procedure to calculate the residual stress pattern over time.

2.3.2 Computational cost reduction techniques

The present FSI one-way procedure involves a large computational cost mainly due to the radiation phenomenon and the fluid flow computation. Thermal radiation in semi-transparent media gains special relevance, as it becomes a volumetric phenomenon as compared to opaque materials. Nevertheless, it also involves a large computational cost as it depends on many parameters, such as; direction, wavelength, time, thickness of the material, and so forth. According to some authors however, the importance of radiation decreased for low thickness and high cooling rates [6, 40]. Therefore, when low thickness and high cooling rates are combined, radiation might be neglected in order to reduce the computational cost of the model.

In addition to radiation phenomenon, CFD simulations usually imply the use of small time increments, as low as milliseconds, to solve the physics related to turbulence and heat transfer. Consequently, the proposed FSI procedure involves a large computational cost and needs a high amount of computational resources making it unfeasible for an industrial time scale. For this reason, with the aim of further decreasing the computational cost, the mechanisms involved on the residual stress development needed to be understood.

The structural relaxation of glass is known as an important source of residual stresses during the glass cooling process [18]. As shown in Figure 2.4 however, the volumetric feature of glass expansion vanished at 400 °C taking into account the cooling rate magnitudes that are normally involved in the tempering process. At this point, glass is below the T_g and behaves as an elastic solid material, making the volumetric expansion to lose traction. As a result, there might be a critical time, t_{cri}, with its associated critical temperature, where residual stresses are no longer influenced by cooling rate and become independent of thermal history.

Additionally, an alternative to further reduce the computational cost was reported in the literature [26]. This approach simplified the transient calculation of the flow by defining a spatially non-uniform but time constant HTC distribution.

With the view to validating these assumptions and optimising the current FSI one-way procedure for quenching modelling, the influence of each computational cost reduction technique in the final residual stress pattern was evaluated. From this assessment, the following main conclusions were drawn:

- Firstly, the influence of volumetric radiation was found to be negligible when low thickness components were subjected to large heat extractions.
- Secondly, the existence of a critical temperature below which the obtained residual stress pattern was independent from the applied cooling rate was verified.
- Finally, it was found that the use of spatially non-uniform steady HTC could be a cost-effective solution but it could also present some limitations regarding the residual stress pattern when complex transient flow phenomena became of relevance.

2.3.3 Modified FSI procedure

Based on the conclusions drawn from the computational cost reduction analysis, the proposed modified FSI procedure to model low thickness quenching processes encompasses both, a transient CFD simulation without volumetric radiation and a purely thermal model below the critical temperature. This way, a commitment between accuracy and efficiency was sought. The use of a steady HTC could be an additional implementation but the flow nature and its influence should be first addressed. In this regard, Figure 2.9 presents the computational sequence of the proposed modified procedure.

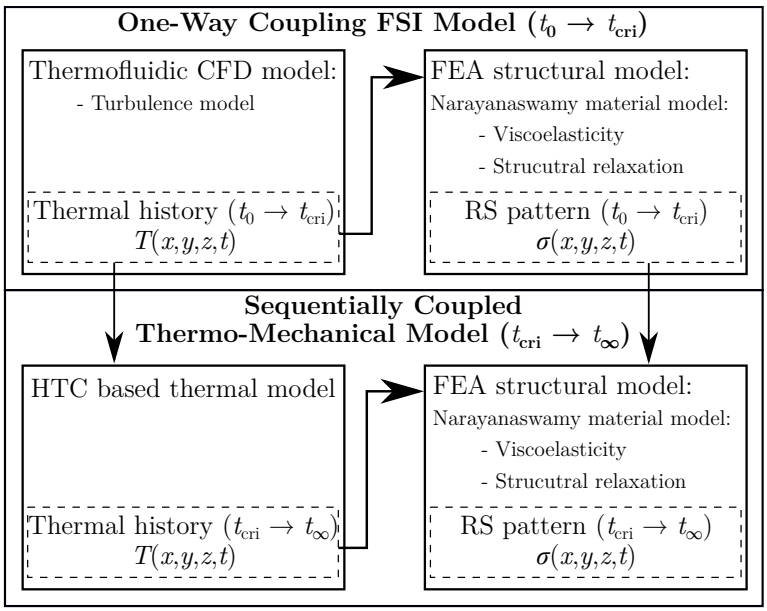

Figure 2.9: Flow chart of the proposed modified procedure to calculate the residual stress pattern over time.

As presented in Figure 2.9, a CFD model without volumetric radiation was defined with the aim of capturing the transient local flow phenomena during the initial stage of the cooling process. However, once the highest temperature in the model was below 400 °C, namely, when the critical time, t_{cri}, was reached, the CFD calculation was interrupted. At this point, the obtained initial thermal history was transferred to a thermal model where a constant in time and spatially uniform HTC was applied. Here, the remaining thermal history until room temperature was calculated. At this point, the steady-state temperature instant, t_∞, is attained. Finally, the complete thermal history was read into the structural model and the non-uniform residual stresses were predicted.

2.4 Validation procedure

In this section, the validation procedure is described. Firstly, the laboratory tests performed under controlled conditions are defined. Next, the defined numerical model is explained. Finally, the experimental procedure for validating the numerical results is described.

2.4.1 Description of case studies

In this section, the laboratory tests performed under controlled conditions are described. Soda lime glass plates were used and hereinafter the term glass refers to the soda-lime-silica glass family. The specimens were of a flat square shape with a nominal length of 90 mm on each side and a nominal thickness of 4 mm. The edges of the plates were polished at the factory.

The as-received condition of the plates, was annealed. Therefore, a tempering process was applied to develop residual stresses. For this purpose, specimens were symmetrically tempered by two air nozzles. In addition, different jet-to-plate distances, H/D, were studied, where H is the distance to the plate and D the nozzle diameter. As a result, two conditions are proposed to experimentally validate the numerical results:

- Symmetrically tempered glass at $H/D = 20$ (STHD20).
- Symmetrically tempered glass at $H/D = 40$ (STHD40).

A frame structure to hold the glass plates in a vertical position was designed and manufactured. To limit the thermal exchange between the glass sample and the supports, rock wool was used in the contact areas. Each contact area was limited to 5-10 mm on the edges of the plate. In this way, a perpendicular flow against the plate was achieved (see Figure 2.10).

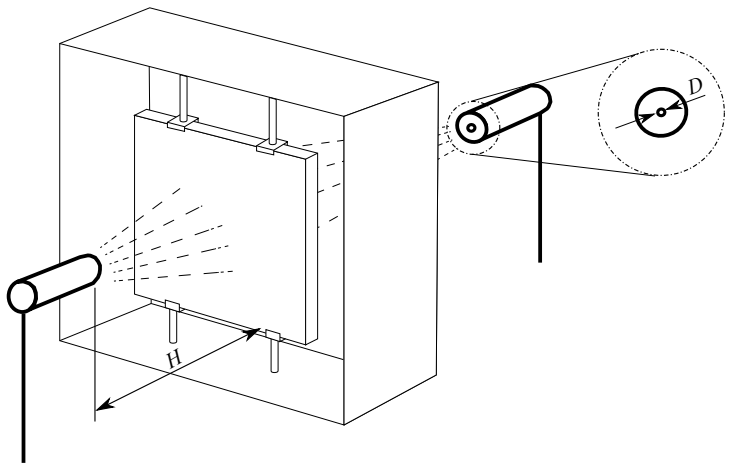

Figure 2.10: The frame designed to symmetrically temper glass plates with single jets.

2.4.2 Single-jet numerical model

In the following lines, the computational model of the performed laboratory tests is described, and the computational fluidic domain, structural domain, and the defined material properties are explained. Then the defined post-processing procedure is shown. Finally, a sensitivity study to analyse the influence of specific parameters on the development of residual stress in the laboratory specimens is presented.

Fluidic computational domain

The fluidic computational domain was composed of the glass plate and its surrounding fluid domain. The inlet section was modelled as a pipe based on the length of the employed nozzles to obtain a fully developed flow at the entry of the domain. To reduce the computational time, a 1/2 model was employed, which was defined by assuming symmetry in the XY plane. Likewise, the computational grid was extended sufficiently far to ensure that no significant pressure gradients normal to any of the boundaries of the computational domain occurred (see Figure 2.11).

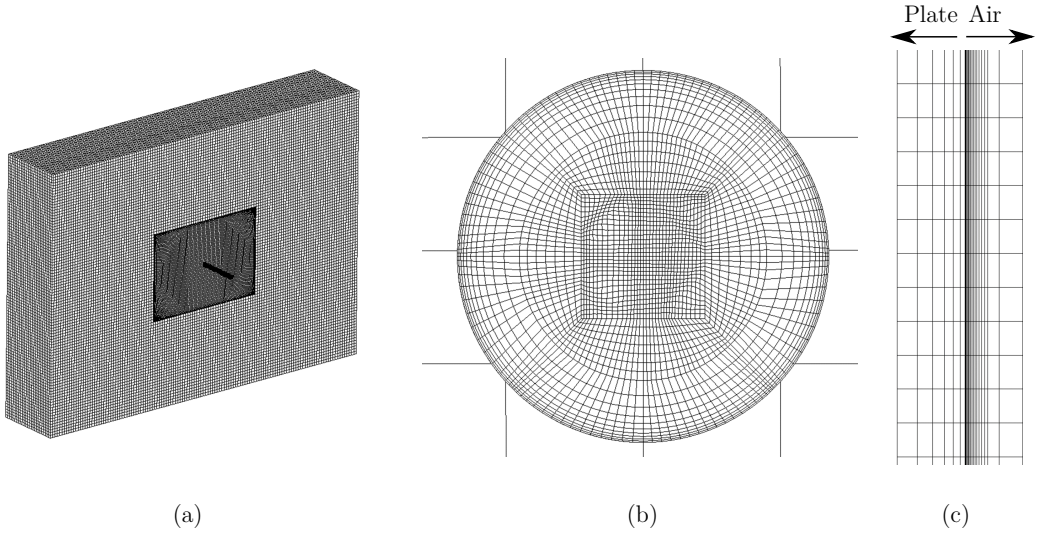

Figure 2.11: Three dimensional computational model: (a) 1/2 symmetry computational domain; (b) mesh discretisation of the inlet domain; and (c) detail of the near wall mesh.

The fluid domain was divided into a central and an external region based on the location of the quenched plate, where finer and coarser meshes were defined, respectively. In this way, multiple refinement processes were carried out in both, the solid and fluid meshes, to appropriately represent the zones where large velocity and thermal gradients occurred. For the fluidic computational grid, an adaptive mesh method based on the velocity gradients of the air flow was employed. The resulting model was composed of 3,667,714 elements. Six hexahedral elements were defined through half the thickness of the plate and a bias factor of four was used to better capture the thermal gradients developed on the surface. A structured hexahedral mesh was built to define the air domain and 16

inflation layers with a first layer thickness of 5 μm were defined near the glass wall to obtain a wall y^+ value in the order of unity. In this way, the velocity and temperature gradients taking place at the boundary layer were captured.

The GEKO turbulence model, and the pressure-based solver were employed. The SIMPLE algorithm was used to solve the pressure and velocity fields and the second order upwind discretisation scheme was selected. The convergence criterion was defined based on the root mean square residuals of each equation. A value below 10^{-4} was considered for the momentum, continuity, and turbulent equations, whereas a value below 10^{-6} was defined for the energy and radiation calculations.

The DOM was used to calculate the volumetric radiation phenomenon in the glass plate, and thus, a grey-banded behaviour was assumed for the absorption coefficient as shown in Table 2.2. With the view to clarifying the influence of volumetric radiation on the residual stress distribution during the glass tempering process, calculations were made with and without considering the effect of radiation.

Finally, after analysing the time step size sensitivity, a Courant number between 1 and 10 was maintained to define the time step size. As for the initial conditions, an initial steady solution using a first-order discretisation scheme to compute the fluid flow was performed. Subsequently, a second-order discretisation scheme was selected and finally, the energy equation was activated by assuming a uniform initial temperature of 650 °C in the plate. Nonetheless, the assumption of a uniform temperature at the onset of the tempering process might not be representative. Thus, the quench delay, which refers to the time period from when the furnace door began to open until the cooling is initiated, must be taken into account. To this end, a preliminary transient calculation to estimate the natural convection and radiation heat transfer until the part was transferred to the tempering unit was performed. As a result, an initial non-uniform temperature distribution in the plate was assumed at the onset of quenching.

Structural computational domain

After the CFD simulation was calculated, a structural analysis was performed by importing the model into the finite element software. The same symmetry conditions and mesh as in the fluidic calculation were used. However, in this case the fluid domain was removed and the numerical model was only composed of the solid glass plate. In accordance with the element type, quadratic full-integration hexahedral elements were defined. The mesh consisted of 48600 elements, composed of six elements through half the thickness.

Material properties

Glass was modelled by the constitutive model described by Narayanaswamy, which accounts for viscoelasticity and structural relaxation phenomena [17]. For this reason, a user-defined subroutine UMAT was used to model the high temperature behaviour of glass. In the present study, the UMAT was built based on the valuable contribution of Nielsen, who presented and validated the model of Narayanaswamy for the glass tempering process in a commercial Finite Element code [85]. Similarly, the material parameters for the exponential series used for viscoelasticity and for the structural response function were based on the data described in the study of Nielsen [89].

The temperature dependent thermal conductivity and specific heat for soda-lime glass were based on data from the literature [22]:

$$k_{\mathrm{th,g}} = 0.741 + 8.58 \cdot 10^{-4} T, \tag{2.14}$$

$$c_{\mathrm{p,g}} = \begin{cases} 1433 + 6.5 \cdot 10^{-3} T & T \geq 850 \text{ K}, \\ 893 + 0.4T - 18 \cdot 10^{-8} T^{-2} & T < 850 \text{ K}. \end{cases} \tag{2.15}$$

Regarding the physical properties, a density of 2470 kg/m^3 for soda-lime glass was defined. In addition to these properties, a grey banded behaviour was assumed for the purposes of modelling the absorption coefficient. Table 2.2 provides the defined absorption coefficient values for each wavelength range. The refractive index was assumed to remain constant at 1.5 for the analysed region of the spectrum based on the work of Nicolau & Maluf [125].

Table 2.2: Absorption coefficient values for specified wavelength bands.

Wavelength [μm]	**Absorption coefficient [1/m]**
0.4 - 1.4	150
1.4 - 2.9	90
2.9 - 4	390

The absorption coefficient sharply increased after 2.9 μm, meaning that the glass became opaque for long wave radiation. With regard to the thermal properties of the cooling fluid, temperature dependent properties of air at ambient pressure were taken into consideration [126]. The specific heat, thermal conductivity and dynamic viscosity of air were defined as a function of temperature, whereas the ideal gas law was used to calculate the density of the air.

Post-processing procedure

The discussion of the post-processing procedure of the results is focused on the experimental temperature and residual stress measurements. Surface local points to validate the temperature variation over time were defined. Figure 2.12 sets out the dashed area for computing the average surface temperature and the defined measurement local points. The central, upper and lower local points aimed to capture

the temperature in the stagnation area and its surroundings. A local point in the dry region, far from the impingement area, was also defined.

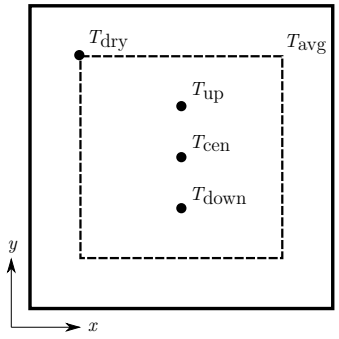

Figure 2.12: The defined average area on the glass surface, and local points for measuring the temperature variation over time.

Table 2.3 reports the four local points as well as their respective coordinates on the 90 x 90 mm surface.

Table 2.3: Local temperature measurement points with the corresponding coordinates.

Description	Nomenclature	Coordinates in mm
Central local temperature	T_{cen}	(45,45)
Upper local temperature	T_{up}	(45,60)
Lower local temperature	T_{down}	(45,30)
Dry region local temperature	T_{dry}	(15,75)

As for the residual stress results, Figure 2.13 illustrates the representative area of analysis.

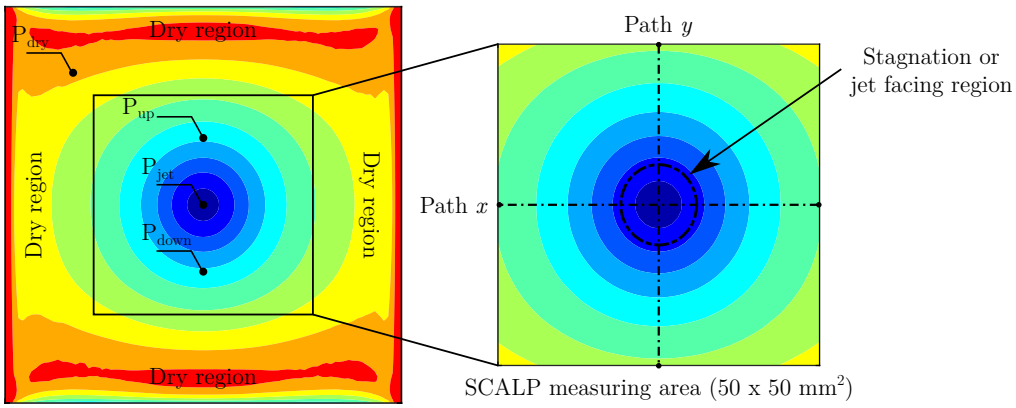

Figure 2.13: Residual stress pattern on the complete glass surface and the area of analysis, in which the stagnation area, dry region and the x and y paths to perform subsequent experimental validations are defined.

As the ordinary residual stress state defined by σ_x and σ_y is influenced by the directional feature of the selected coordinate system, in this thesis the absolute maximum principal stresses were used for the term residual stress. The following post-processing features were proposed to analyse the results:

- Absolute maximum principal stress contours were plotted in the area of analysis to identify the tensile and compressive regions.
- Similar to the local temperature points, control points located in the dry and jet facing areas were established to analyse the variations in residual stress over time. The dry region refers to the area towards the edges of the plate, where the influence of the impingement flow lost traction. The jet facing area or stagnation region refers to the zone where the jet flow collided with the targeted surface.
- Two paths along the x and y directions crossing at the centre of the plate were defined to validate the obtained residual stress magnitudes against experimental measurements.

Sensitivity analysis

The presented numerical methodology entailed uncertainty in many parameters due to the dissimilar physics involved in the glass tempering process. Firstly, the material constitutive model, which incorporates viscoelastic stress relaxation and structural relaxation phenomena, involves discrepancy in several material parameters as these are based on multiple works in the literature [16, 17, 86, 127]. The main reason for this might be due to the highly complex methods to measure certain characteristic parameter values. With this in mind, Daudeville et al. carried out a sensitivity analysis varying mechanical and thermal parameters [22]. The authors observed that variations in the Young's modulus, liquid glass thermal expansion coefficient and the reference temperature for viscoelastic modelling had a significant effect on the magnitude of residual stresses. Additionally, as the composition of glass can differ from manufacturer to manufacturer, Aronen et al. performed a similar uncertainty analysis by varying thermal and mechanical properties [71]. They highlighted that variations in mechanical properties had a greater influence on residual stress calculations and proposed an empirical correlation to take these effects into account.

In general, insights into the sensitivity of parameters of the constitutive material model have been provided by previous researches in the literature, and hence, was considered outside the scope of this thesis.

Thermal modelling, on the other hand, is known to play a role in residual stress development during tempering [18, 20, 71]. Thus, the variation of the initial quenching temperature and the defined jet velocity were considered to be of great interest to observe the influence of these parameters on the final residual stress distribution.

Furthermore, turbulence modelling is known to be a critical step in CFD due to its influence on the flow and heat transfer behaviour of the considered application. As a result, there is no clear agreement in the literature regarding the selection of turbulence models. The Standard $k-\epsilon$ model usually reports poor results in the stagnation and wall jet regions, and thus is not recommended for jet impingement applications. To date, the SST $k-\omega$ model has been considered as one of the most appropriate options for modelling impinging jets in terms of accuracy and computational cost [100]. Additionally, a new turbulence model called Generalized $k-\omega$ (GEKO), which enables a better prediction of the

round jet expansion was identified in the literature [104]. The Intermittency Transition model with Kato-Launder production limiter was also found to be useful for impinging jets at $H/D < 10$ [108]. Therefore, this study assesses the influence of turbulence modelling on residual stress development by analysing the following models: the $k - \omega$ SST, GEKO and GEKO with Intermittency Transition model with Kato-Launder production limiter.

2.4.3 Experimental procedure

The experimental laboratory work to validate the obtained results consisted of carrying out tempering tests of glass plates to achieve different residual stress patterns. Similarly, a fluidic, thermal and residual stress characterisation was proposed during the tests.

Thermal tempering tests

The tempering unit was composed of one DAG PRESTO GOLD nozzle on each side of the plates and connected by flexible air hoses. Each jet had a 3 mm diameter nozzle and the distance between the nozzle exit and the sample was varied from $H/D = 20$ to $H/D = 40$. Higher H/D ratios than the standard tempering process were selected with a view to obtaining a more uniform stress distribution and preventing very localised and large residual stresses in the plate. In the same manner, a flow meter was employed to control the pressure and flow rate and an on/off switch was used to activate the air supply.

A radiation furnace NABERTHERM LH60/14 was employed for the heat treating the samples. Firstly, a temperature control of the heating process was carried out with a National Instruments data acquisition system controlled by LabVIEW. A 4 slot NI cDAQ chassis with a 9213 module was used to record the data from the temperature sensors. To this end, three N-type thermocouples were attached to the glass surface with OMEGA CC high-temperature cement. Then, the furnace was preheated at 650 °C and a heating cycle of 10 minutes was defined based on the thermocouple measurements.

Once the furnace was heated up to 650 °C, glass samples were successively introduced into the furnace. After the defined heating period finished, the frame was transferred to the cooling unit. Five samples were quenched for each jet-to-plate distance to assess experimental reproducibility of the developed residual stresses.

Fluidic characterisation

Turning now to jet flow velocity, pressure measurements with an AEROLAB wake-rake device consisting of 18 total pressure ports were performed (see Figure 2.14). As the device was attached to a three-axes positioning system, measurements were taken at different heights and a jet inlet-velocity of 200 m/s was fitted to the experimental data.

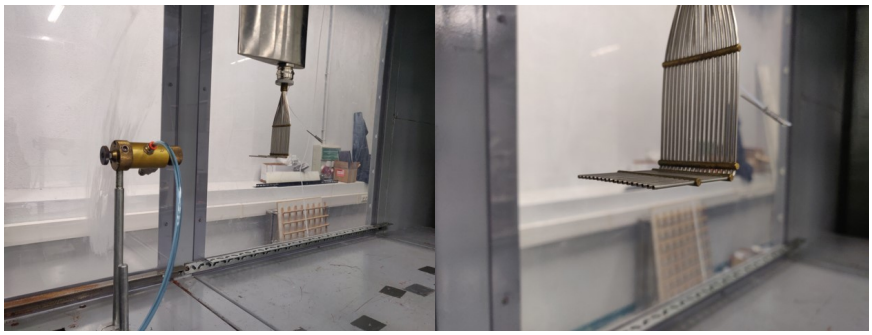

Figure 2.14: Experimental set-up for the fluidic characterisation of the air jets.

Thermal characterisation

Thermography based temperature measurements were also performed with three repetitions per condition. The thermographic camera FLIRT1030Sc recorded the temperature of the plates over time during quenching. Likewise, the high emissivity ceramic coating AREMCO 840-CM, with an emissivity chart provided by the supplier, was used to paint a surface of the plate and record the temperature during cooling. The emissivity of the coating presented an uncertainty range of ±3.5%. As two nozzles were required for cooling down the specimens, the camera was slightly inclined up to 30° to facilitate a full view of the surface of the plate (see Figure 2.15).

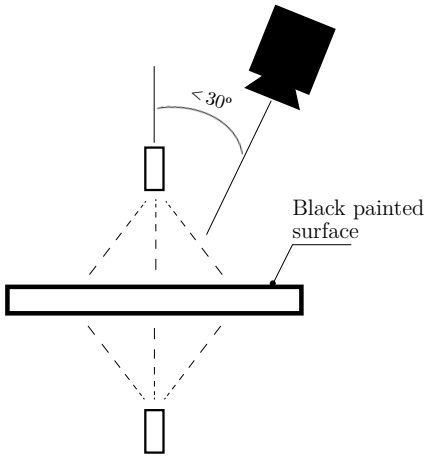

Figure 2.15: Top view of the tempering unit set-up.

The thermographic camera recorded the temperature of the entire surface of the samples, and thus, the temperature variation over time was captured.

Residual stress characterisation

After the tempering process was carried out, non-destructive residual stress measurements were taken. The SCALP-05 developed by GlasStress Ltd. was used to measure the residual stress distribution in the quenched glass plates. This instrument can measure through thickness residual stresses up to 6 mm.

To determine the residual stress magnitudes and distribution on the surface, the SCALP together with a CNC coordinate machine was employed. This provided automated control in the x and y directions. The machine also enabled a rotation around the z axis as two measurements in two perpendicular orientations at the same location were required (see Figure 2.16). Consequently, a parallel stress component σ_0 and, a perpendicular stress component, σ_{90}, were obtained. With this in mind, the following formulations enabled the residual stress calculation in the x and y directions:

$$\sigma_{\mathrm{x}} = \frac{\left(\sigma_0 \cos^2 \beta_{\mathrm{beam}} + \sigma_{90}\right) \sin^2 \beta_{\mathrm{beam}}}{1 - \cos^4 \beta_{\mathrm{beam}}}, \tag{2.16}$$

$$\sigma_{\mathrm{y}} = \frac{\left(\sigma_{90} \cos^2 \beta_{\mathrm{beam}} + \sigma_0\right) \sin^2 \beta_{\mathrm{beam}}}{1 - \cos^4 \beta_{\mathrm{beam}}}. \tag{2.17}$$

Similarly, the equivalent stress, σ_{eq}, or residual stress, σ, could be estimated by:

$$\sigma_{\mathrm{eq}} = \sigma = \sqrt{\sigma_{\mathrm{x}}^2 + \sigma_{\mathrm{y}}^2 - \sigma_{\mathrm{x}}\sigma_{\mathrm{y}}}. \tag{2.18}$$

If measurement points are close to geometrical discontinuities, such as edges, the stress calculations might not be representative due to noise in the raw experimental data. During the measurement process, the edge region was observed to exhibit larger distortion than the central area of the plate. As a result, measurements in this area were distorted due to light scattering at the non-even edge surface. For this reason, the residual stress measurements were limited to an area of 50 x 50 mm. During the CNC measurements, a step size of 1 mm was defined resulting in a total of 2500 measurement points. All specimens were placed into the testing set-up to ensure the same location for each sample (see Figure 2.16).

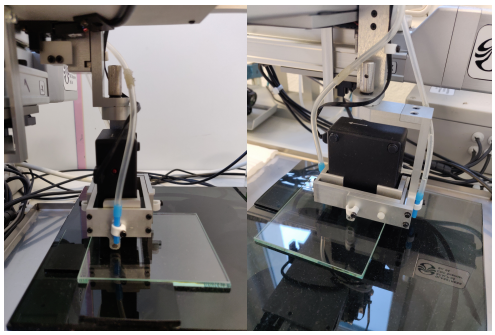

Figure 2.16: SCALP device assembled into the CNC coordinate machine.

Nevertheless, deviations in the location of the stagnation point, namely, the maximum residual stress, were observed in both surfaces of the symmetrically tempered plates. The reason for this may be the positioning of the jets during the set-up, where an angular variation of the jet might lead to a visible misalignment as the jet-to-distance increased. Following the procedure presented in Figure 2.17, these deviations were corrected, and the measured paths were realigned in accordance with the maximum residual stress point.

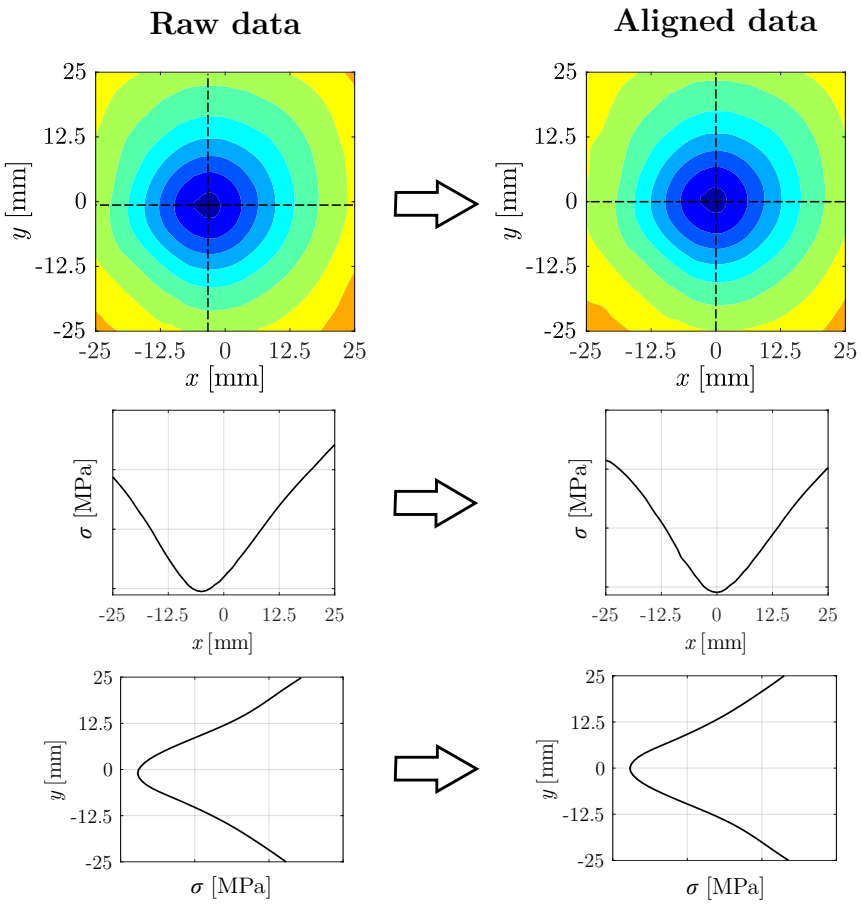

Figure 2.17: Realignment process of the experimentally measured residual stress distribution.

Once the residual stress distributions were aligned, an average was calculated incorporating all the measured distributions. In this way, a comparison with the numerically calculated stress pattern could be made.

2.5 Discussion of the results

This section firstly introduces the numerical model used for the proposed numerical FSI methodology. Then, the obtained results and the different computational cost reduction techniques are assessed. More specifically, the influence of volumetric radiation on the non-uniform residual stress distribution of tempered glass plates, the existence of a critical temperature and the influence of considering a spatially non-uniform steady HTC are investigated. In this way, the validation of the proposed procedure with respect to the complete FSI one-way procedure, which considers the volumetric radiation phenomenon and shows no interruption of the CFD calculation during the cooling process, is done. Once the procedure is validated, a sensitivity analysis to analyse the influence of the initial temperature of the plate, the jet velocity and the turbulence model selection is carried out.

2.5.1 Generalised FSI one-way procedure

Hereafter, the generalised FSI one-way procedure to predict the non-uniform residual stress distribution on glass plates is validated. To this end, first the numerical results are introduced and then, the experimental temperature and residual stress measurements are presented. Finally, the validation of the numerical results is performed.

Numerical results

With the aim of modelling the performed tempering tests, an initial glass plate temperature needed to be defined. The initial temperature distribution of the plate after the heating process might play an important role in the residual stress development, hence, the assumption of a uniform initial temperature might not be representative. For this purpose, the experimental quench delay was measured and considered. In this case, a quench delay of 10 s was observed until the cooling process was initiated. Therefore, assuming a uniform temperature of 650 °C in the furnace, a natural convection stage characterised by a convective HTC of 20 W/m^2K to fit the experimental data was established. Figure 2.18 shows the calculated initial temperature distribution on the surface and through the thickness of the plate after taking the quench delay into account.

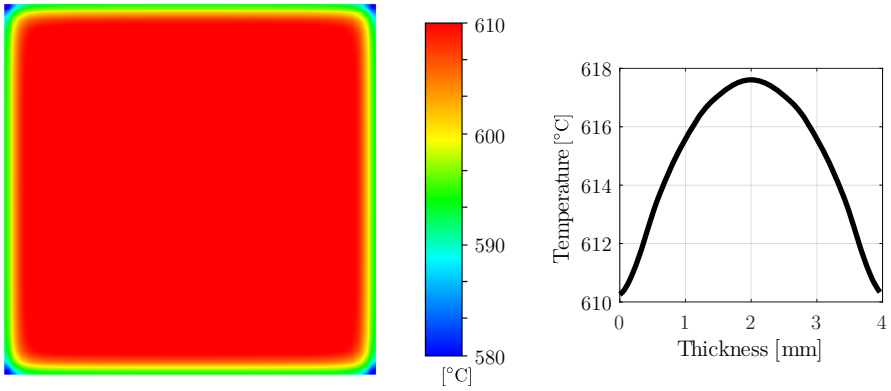

Figure 2.18: Calculated initial temperature distribution after taking the quench delay into account: (a) on the surface, and (b) through the thickness of the plate.

In this stage, as no forced convection was applied, volumetric radiation gained importance not only on extracting heat but also on homogenising temperature through the thickness of the plate. As a result, a parabolic temperature distribution without significant thermal differences between the surface and the core was obtained. Regarding the cooling process, Figure 2.19 shows the calculated temperature variation over the first 15 s of cooling after the quench delay in the local points described in Table 2.3 for symmetrically cooled plates at $H/D = 20$ and $H/D = 40$.

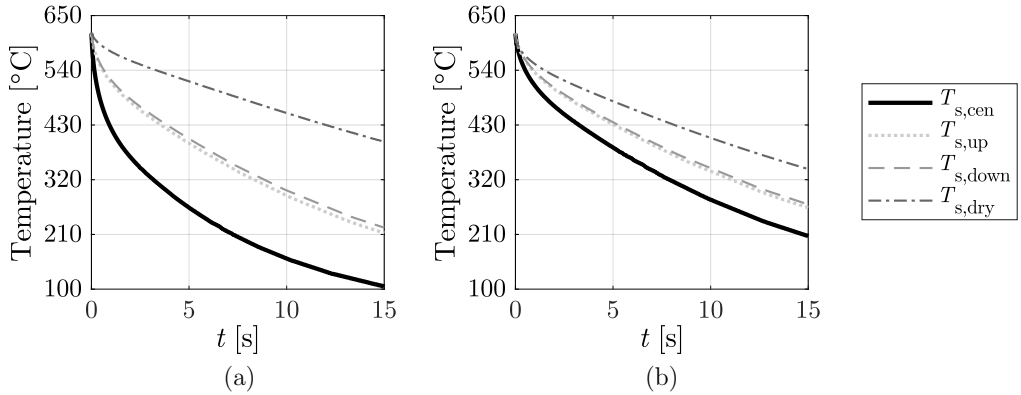

Figure 2.19: Estimated local temperature variations over time for the analysed tempered glass configurations: (a) STHD20, and (b) STHD40.

The plates cooled at a shorter distance exhibited larger temperature differences, due to the dissimilar cooling rates obtained at the defined locations. When the jet-to-plate distance was increased, the speed of the jet flow when arriving at the targeted surface was lower, and hence, a slower but more homogeneous cooling was obtained. The different thermal histories observed in both tempering configurations led to different residual stress distributions as shown in Figure 2.20.

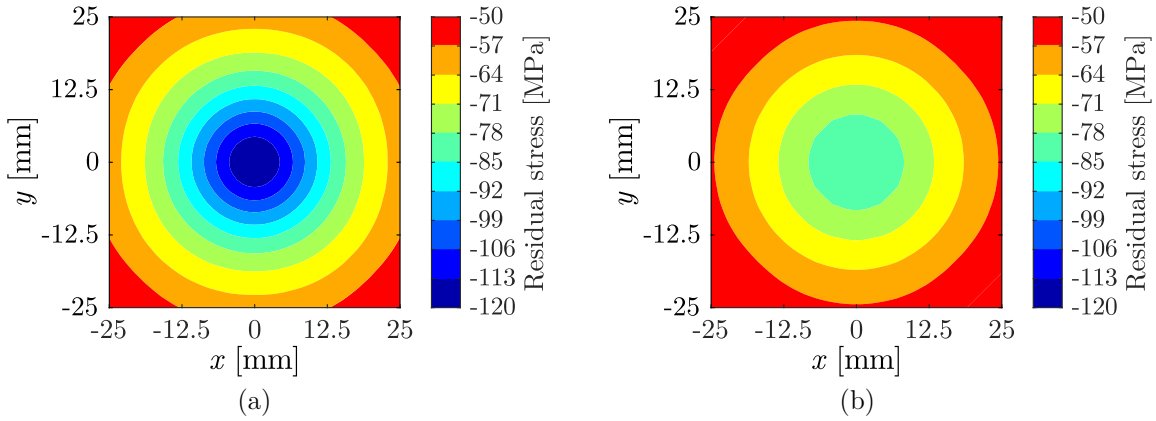

Figure 2.20: Calculated residual stress distributions for the analysed tempered glass configurations: (a) STHD20, and (b) STHD40.

The maximum residual stress magnitude in both cases was located in the stagnation point as a result of the employed single-jet cooling configuration. Furthermore, similar residual stress patterns in terms of distribution were observed, though different magnitudes were obtained. Figure 2.21 provides a deeper insight into the differences noticed in the residual stress magnitude, as it presents the residual stress distribution along x and y directions.

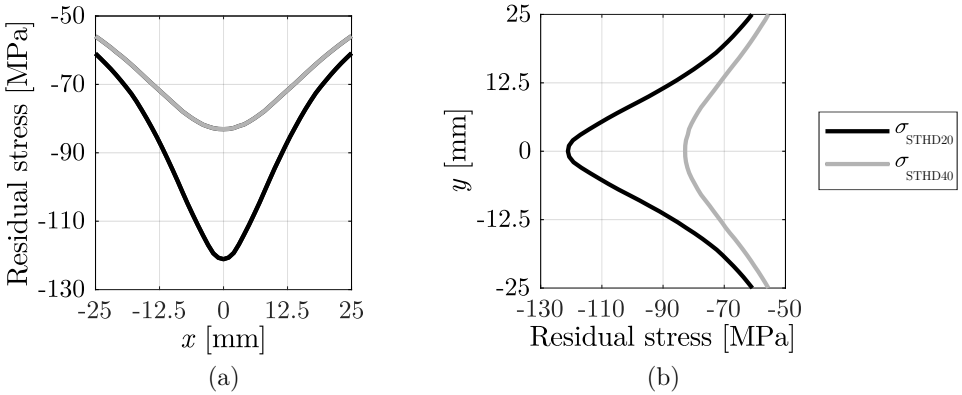

Figure 2.21: Estimated residual stress distributions for the analysed tempered glass configurations: (a) STHD20, and (b) STHD40.

Residual stresses up to 120 MPa and 85 MPa were observed for $H/D = 20$ and $H/D = 40$ configurations, respectively. Differences between the analysed tempering cases tended to decrease as the distance from the stagnation point increased.

Experimental tempering results

With the aim of validating the proposed numerical FSI methodology, glass plates were heat treated under controlled conditions. For this purpose, temperature measurements as well as residual stress measurements were carried out to validate both, the thermofluidic and structural fields of the FSI numerical model. Due to the difficulty to attach thermocouples on the glass surface, a thermographic camera was employed for the thermal validation, whereas a SCALP device was used to measure the residual stress pattern on the surface of the plates.

On the one hand, the temperature variation over time of three samples per each tempering condition was recorded to ensure the repeatability of the performed tests. Figure 2.10 represents the average surface temperature variation over time of each sample for the two analysed tempering configurations.

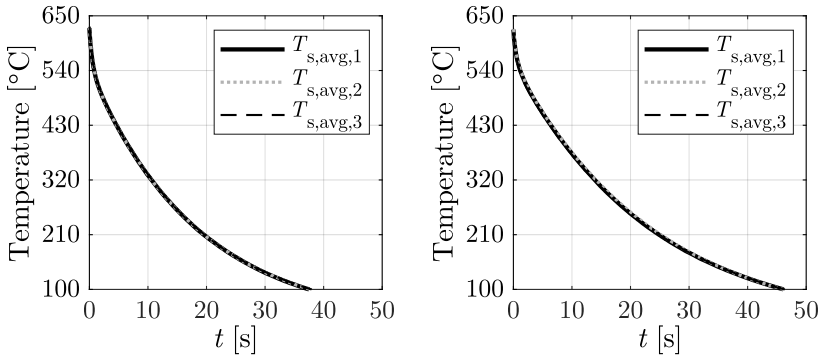

Figure 2.22: Average surface temperature variation over time for the analysed tempered glass configurations: (a) STHD20, and (b) STHD40.

As observed in Figure 2.22, the performed tests overlapped one with each other ensuring the repeatability of the performed heat treatment procedure. In addition, local temperature variations over time were also recorded. Figure 2.23 depicts the temperature variation over time on the local points specified in Table 2.3 for each test configuration.

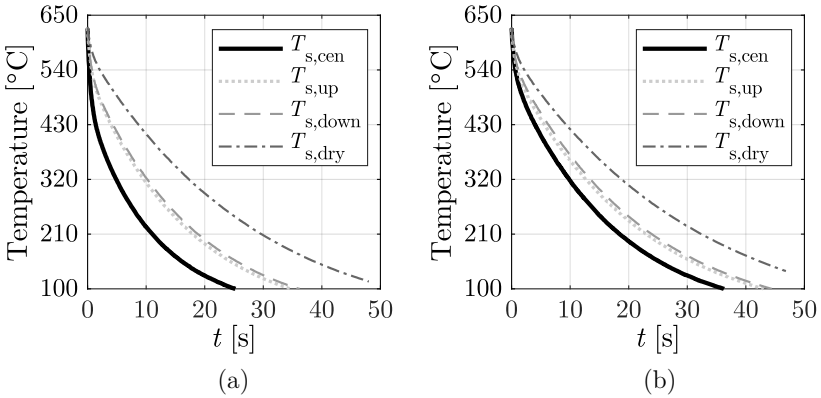

Figure 2.23: Local surface temperature variation over time for the analysed tempering configurations: (a) STHD20, and (b) STHD40.

Following the trends observed in the numerical calculation, larger temperature differences were perceived as the jet-to-plate distance decreased. A shorter distance between the nozzle and the surface led to a larger heat extraction, especially on the stagnation area, and hence, a higher cooling power was achieved.

Once tempered, the surface residual stress distribution on five samples (T1-T5) of each tempering configuration were measured. Figure 2.24 and Figure 2.25 provide the residual stress distributions on the front and rear surfaces of the symmetrically tempered samples at $H/D = 20$.

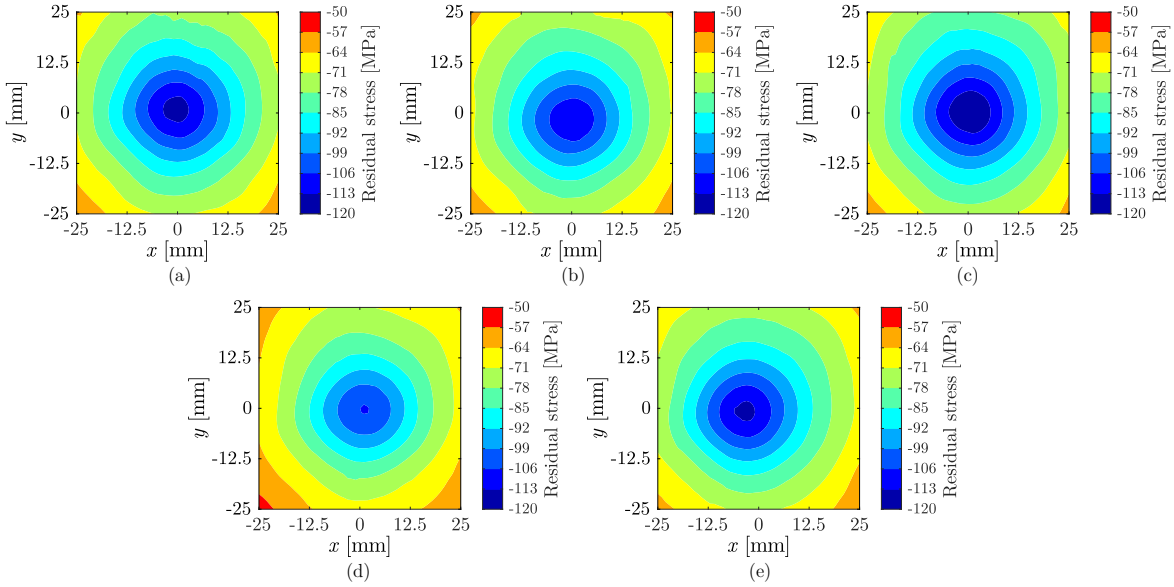

Figure 2.24: Experimental residual stress distribution on the front surface of symmetrically cooled plates at $H/D = 20$: (a) T1, (b) T2, (c) T3, (d) T4, and (e) T5.

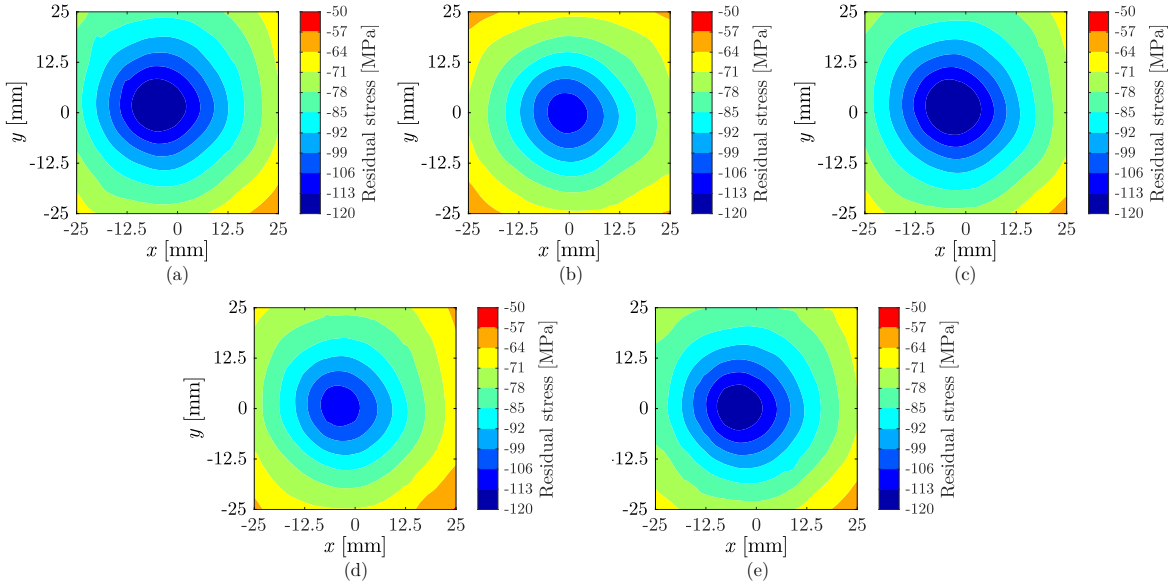

Figure 2.25: Experimental residual stress distribution on the rear surface of symmetrically cooled plates at $H/D = 20$: (a) T1, (b) T2, (c) T3, (d) T4, and (e) T5.

A maximum residual stress magnitude of 120 MPa was located at the stagnation point. All the heat treated samples showed a similar stress pattern; as the flow extended towards the edges of the plate heat extraction decreased and so did residual stresses. A residual stress difference between the stagnation region and the measurement boundary of around 45 MPa was obtained on both surfaces. Additionally, misalignments with respect to the maximum residual stress magnitude location could be observed in Figure 2.24 and Figure 2.25. A better perception about this issue was achieved by looking at the residual stress distribution along x and y directions. Figure 2.26 sets out the measured residual stress distributions on the surface of symmetrically cooled plates at $H/D = 20$.

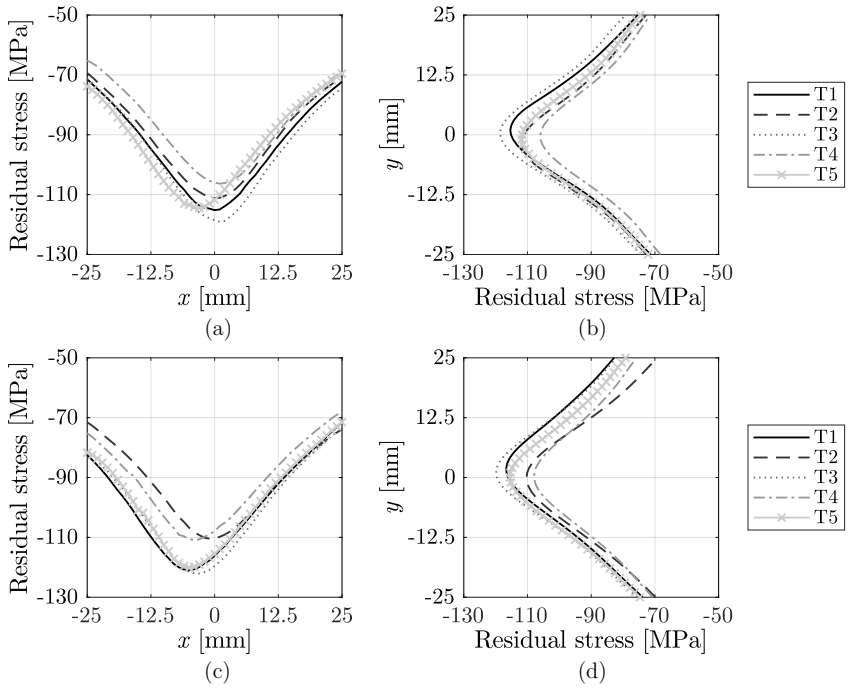

Figure 2.26: Measured experimental residual stress paths of symmetrically cooled plates at $H/D = 20$: (a)-(b) residual stress on the front surface along x and y directions, and (c)-(d) residual stress on the rear surface along x and y directions.

Alignment deviations up to 3 mm and 2 mm were noticed in the residual stress distributions along x and y directions, respectively. As for the rear surface, larger deviations up to 5 mm in x direction and 2 mm in y direction were observed. Furthermore, differences in the residual stress magnitude of around 5 MPa were noticed between the front and rear surfaces. This discrepancy could be related to the previously mentioned misalignments, which may result in different contractions of the front and rear surfaces. Figure 2.27 and Figure 2.28 provide the realigned residual stress distributions on the front and rear surfaces of the symmetrically tempered samples at $H/D = 20$.

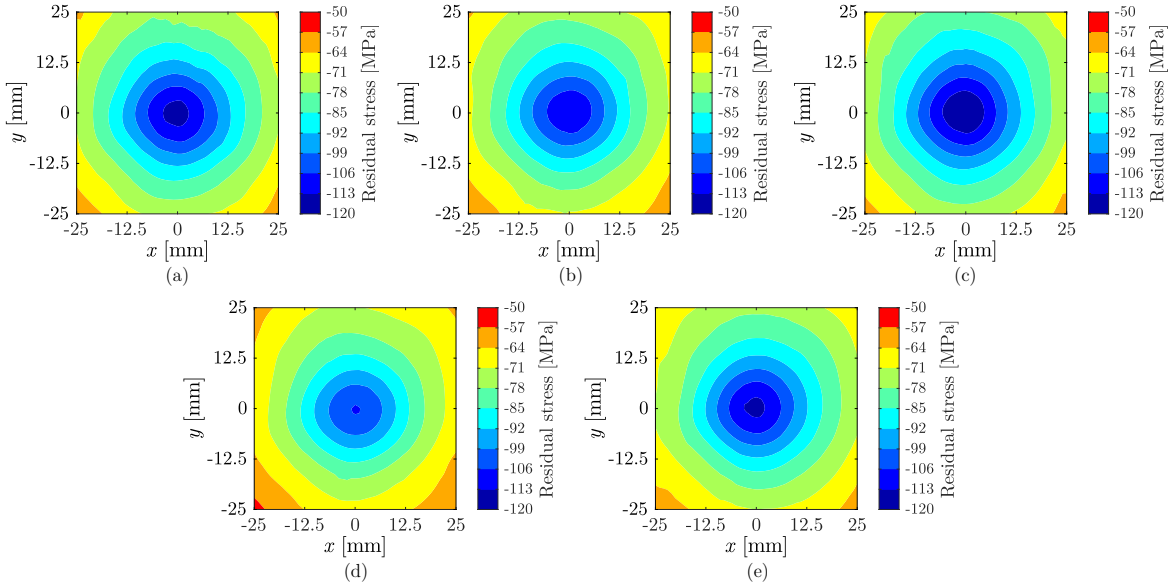

Figure 2.27: Realigned experimental residual stress distribution on the front surface of symmetrically cooled plates at $H/D = 20$: (a) T1, (b) T2, (c) T3, (d) T4, and (e) T5.

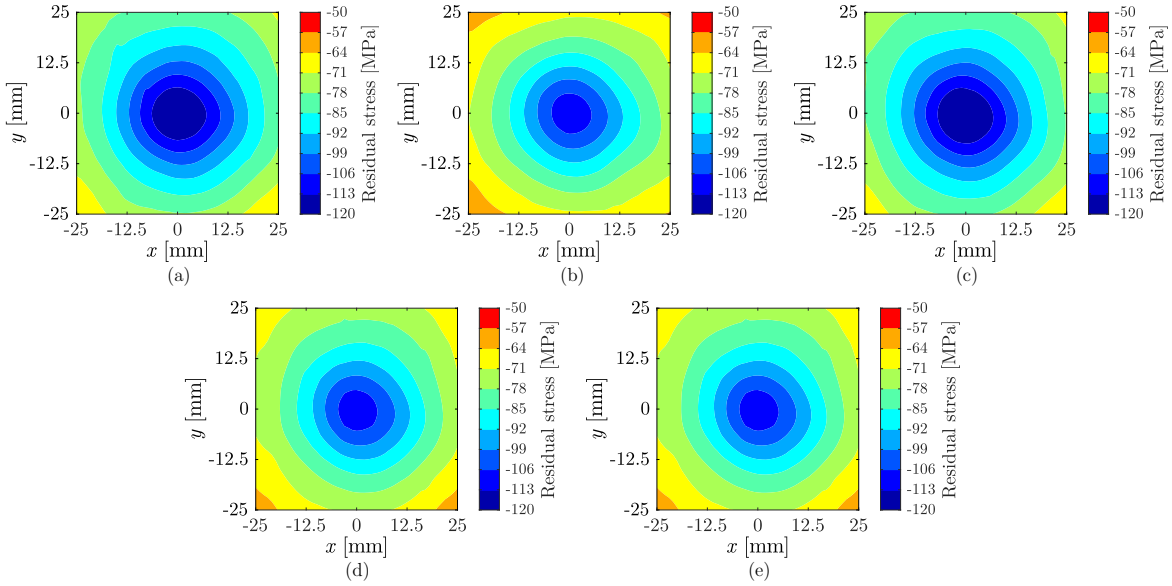

Figure 2.28: Realigned experimental residual stress distribution on the rear surface of symmetrically cooled plates at $H/D = 20$: (a) T1, (b) T2, (c) T3, (d) T4, and (e) T5.

In alike manner, Figure 2.29 shows the residual stress distributions aligned with respect to the the maximum residual stress magnitude, namely, the stagnation point.

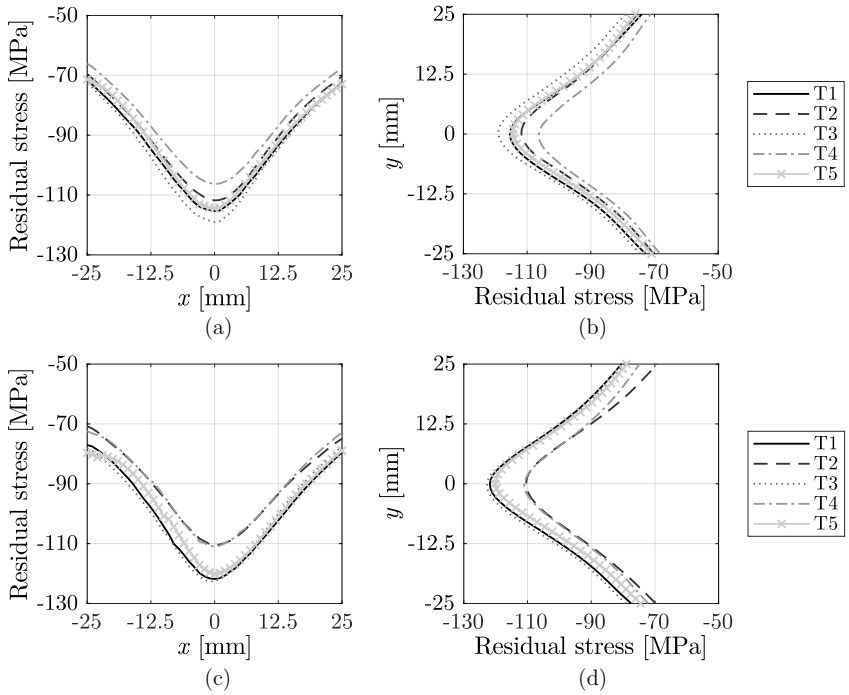

Figure 2.29: Realigned experimental residual stress paths of symmetrically cooled plates at $H/D = 20$: (a)-(b) residual stress on the front surface along x and y directions, and (c)-(d) residual stress on the rear surface along x and y directions.

In this way, the repeatability of the tests was ensured, as differences between measured samples were no greater than 10 MPa. Regarding symmetrically tempered plates at $H/D = 40$, Figure 2.30 and Figure 2.31 present the residual stress distributions on the front and rear surfaces of the plates.

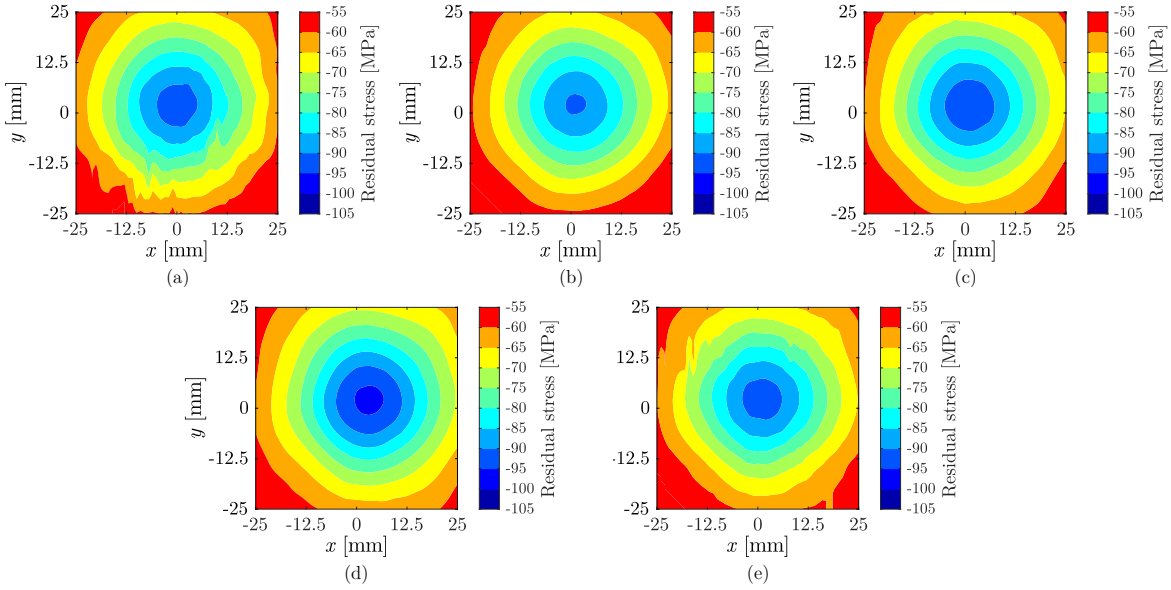

Figure 2.30: Experimental residual stress distribution on the front surface of symmetrically cooled plates at $H/D = 40$: (a) T1, (b) T2, (c) T3, (d) T4, and (e) T5.

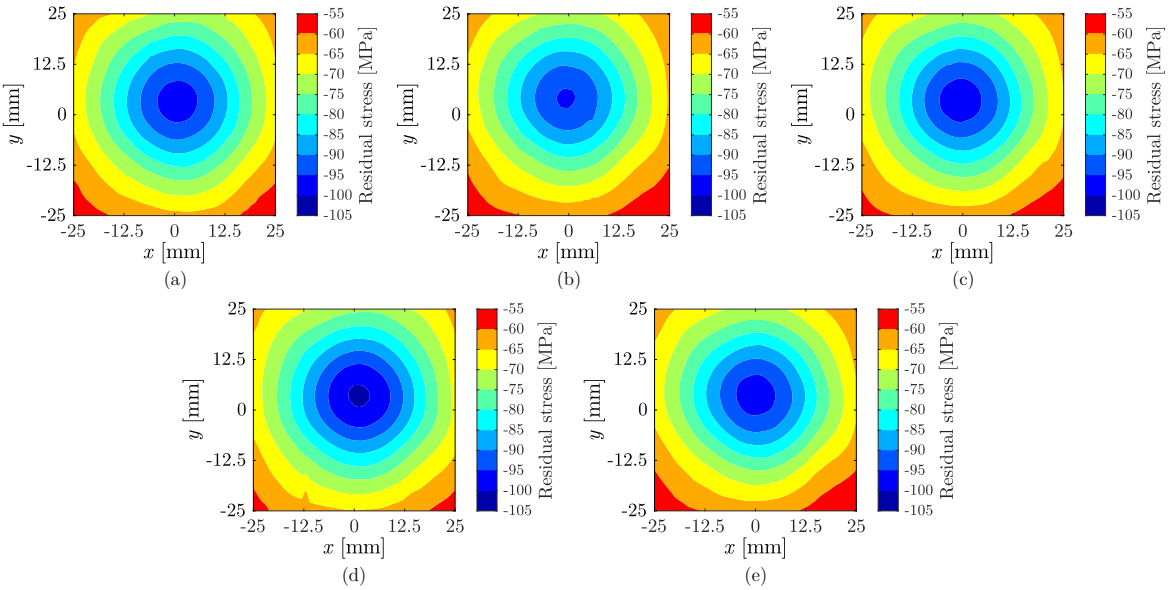

Figure 2.31: Experimental residual stress distribution on the rear surface of symmetrically cooled plates at $H/D = 40$: (a) T1, (b) T2, (c) T3, (d) T4, and (e) T5.

In this case, a lower residual stress magnitudes up to 95 MPa on the front surface and 100 MPa on the rear surface were measured. The reason for this has to do with the lower cooling rate obtained due to the defined larger jet-to-plate distance. Similarly, misalignments with respect to the maximum residual stress magnitude location could be observed. Figure 2.32 sets out the residual stress distribution along x and y directions crossing at the centre of the plates.

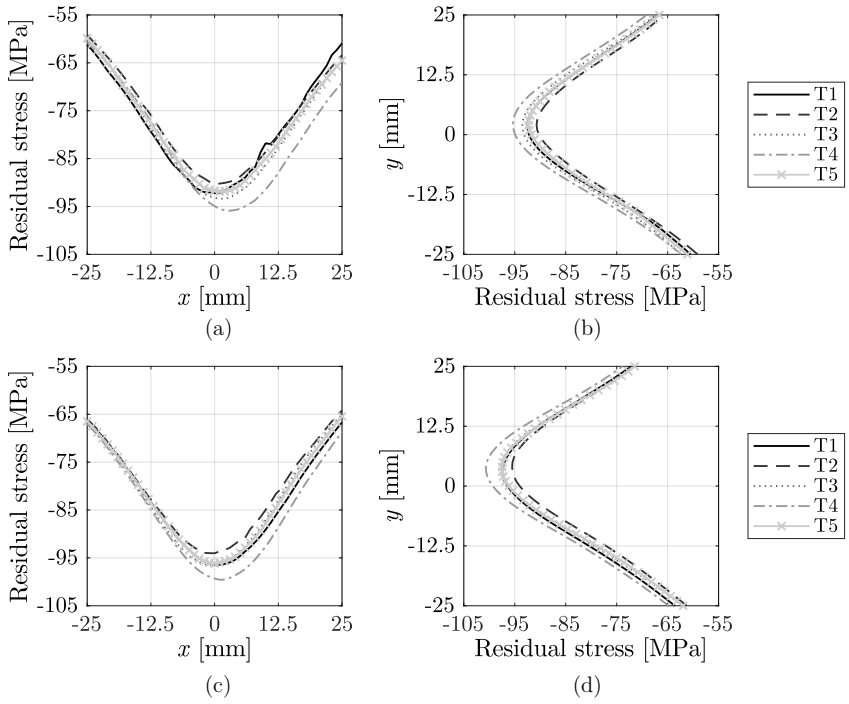

Figure 2.32: Measured experimental residual stress paths of symmetrically cooled plates at $H/D = 40$: (a)-(b) residual stress on the front surface along x and y directions, and (c)-(d) residual stress on the rear surface along x and y directions.

Deviations with respect to the stagnation point up to 4 mm and 3 mm in x and y directions on the front surface were observed. Similar conclusions could be drawn for the rear surface as misalignments up to 2 and 4 mm were encountered. Following the previous realignment procedure, Figure 2.33 and Figure 2.34 illustrate the realigned residual stress distributions on the front and rear surfaces of the symmetrically tempered samples at $H/D = 40$.

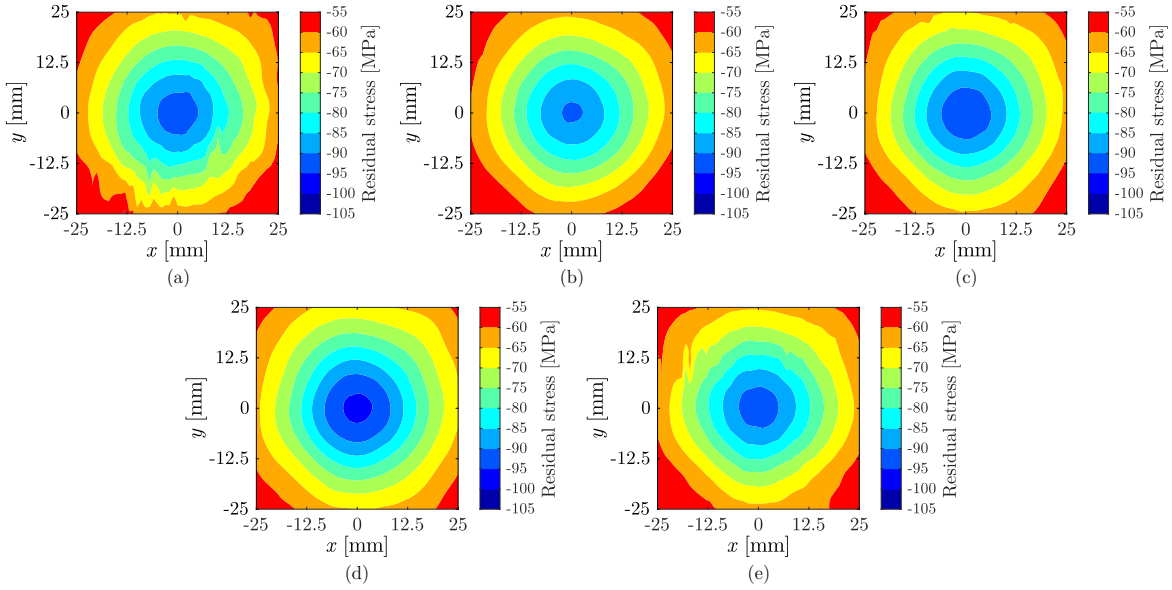

Figure 2.33: Realigned experimental residual stress distribution on the front surface of symmetrically cooled plates at $H/D = 40$: (a) T1, (b) T2, (c) T3, (d) T4, and (e) T5.

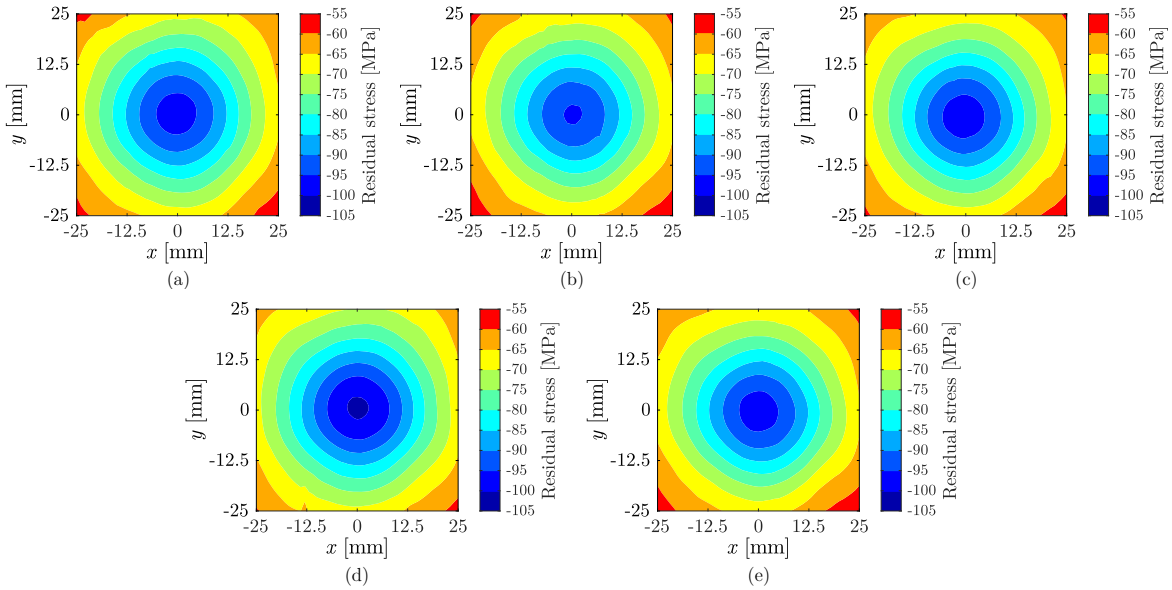

Figure 2.34: Realigned experimental residual stress distribution on the rear surface of symmetrically cooled plates at $H/D = 40$: (a) T1, (b) T2, (c) T3, (d) T4, and (e) T5.

Likewise, Figure 2.35 provides the realigned residual stress paths along x and y directions.

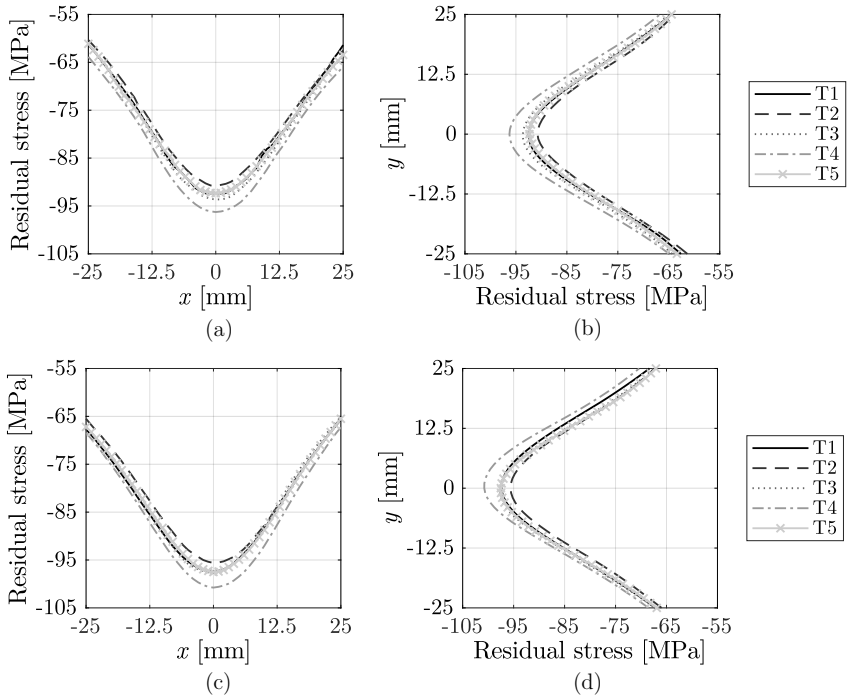

Figure 2.35: Realigned experimental residual stress paths of symmetrically cooled plates at $H/D = 40$: (a)-(b) residual stress on the front surface along x and y directions, and (c)-(d) residual stress on the rear surface along x and y directions.

Differences in residual stress values up to 10 MPa were observed among all measured samples. Consequently, the stress pattern was considered to be repetitive.

In summary, the repeatability of the performed tempering tests was proved and the following part of this section moves on to validate the numerical results by comparing them to the presented experimental measurements.

Validation of the generalised FSI procedure

Firstly, the experimental and numerical temperature variation over the first 15 s of cooling are compared in Figure 2.36.

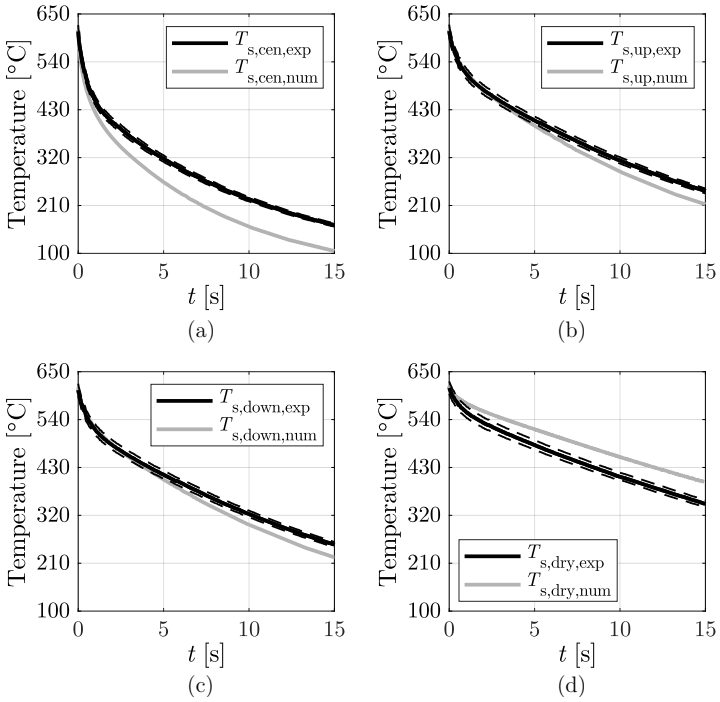

Figure 2.36: Experimental and numerical surface temperature variation over time on STHD20 samples at: (a) central local point, (b) upper local point, (c) lower local point, and (d) dry region.

The emissivity chart of the employed coating stated an uncertainty of 3.5%, and hence, this interval was added to the experimental temperature measurements showed with dashed lines in Figure 2.36. The numerical temperature estimation with respect to experimental data tended to increase as the part was cooled down. When temperature reached 400 °C, relative differences around 9%, 3%, 3.5% and 11% were observed in the central, upper, lower and dry region local points, respectively. Furthermore, the numerically predicted cooling rate on the stagnation region tended to be higher than the experimental measurements. A possible explanation for this might be that flow misalignments could occur during the experimental tests, leading to non-perpendicular flow impinging on the surface. As a result, a lower cooling rate might be achieved and higher temperatures would have been measured. Conversely, the dry region showed an estimated slower temperature drop. This result may suggest that the spreading angle of the employed nozzle was not completely captured. Consequently, a further study with more focus on the internal geometry of the nozzle is suggested.

In like manner, Figure 2.37 depicts the experimental and numerical temperature variation over time of symmetrically tempered plates at $H/D = 40$.

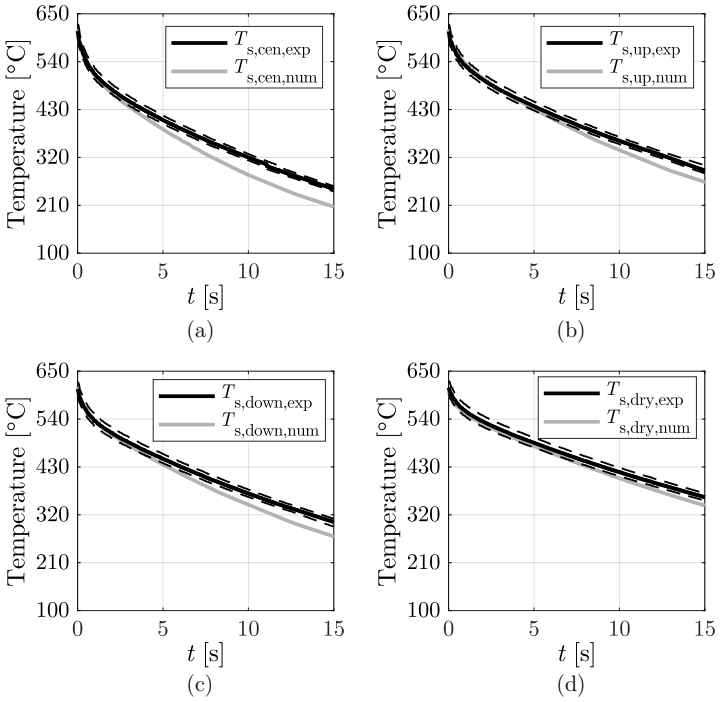

Figure 2.37: Experimental and numerical surface temperature variation over time on STHD40 samples at: (a) central local point, (b) upper local point, (c) lower local point, and (d) dry region.

In this case, even if relative differences seemed smaller, an analogous behaviour was observed as larger differences were noticed when temperature decreased. At 400 °C, relative differences around 6%, 3.5%, 5% and 3.5% were observed in the central, upper, lower and dry region local points, respectively.

Regarding residual stress estimations, Figure 2.38 sets out the average experimental and the numerical residual stress distributions as well as its relative difference for symmetrical tempering plates at $H/D = 20$.

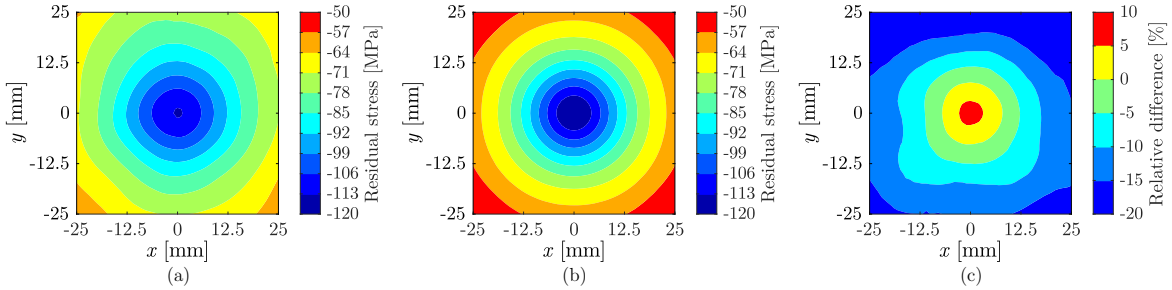

Figure 2.38: Residual stress distribution on the front surface of symmetrically tempered glass samples at $H/D = 20$: (a) experimental average, (b) FSI one-way procedure, and (c) deviation.

Differences with respect to the average experimental contour tended to be smaller within the stagnation region than in the dry regions. Nonetheless, the estimated results were considered to be in agreement due to the scatter that the experimental measurements exhibited as shown in Figure 2.42. A similar conclusion was achieved when the rear surface was analysed in Figure 2.39

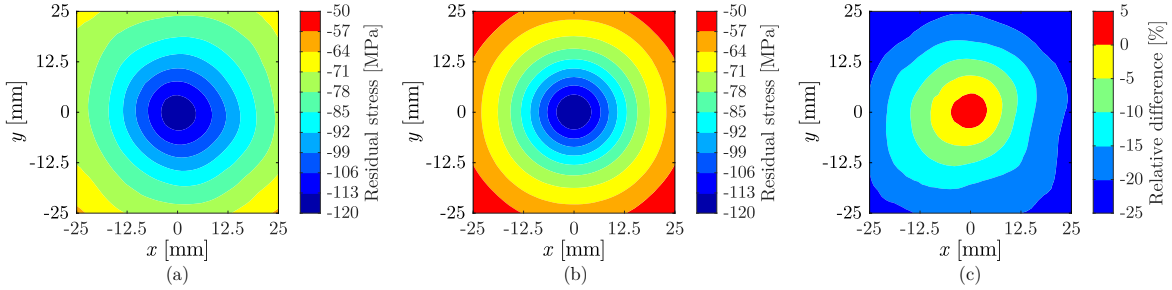

Figure 2.39: Residual stress distribution on the rear surface of symmetrically tempered glass samples at $H/D = 20$: (a) experimental average, (b) FSI one-way procedure, and (c) deviation.

Finally, Figure 2.40 shows the average experimental residual stress, the numerical residual stress and the deviation distributions for symmetrical tempering plates at $H/D = 40$.

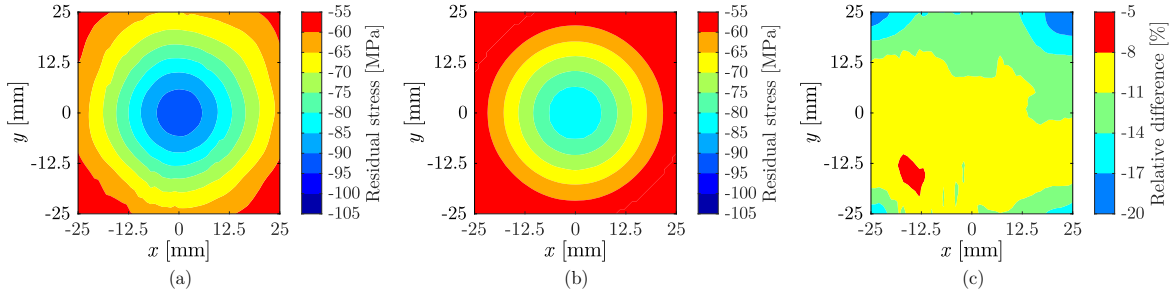

Figure 2.40: Residual stress distribution on the front surface of symmetrically tempered glass samples at $H/D = 40$: (a) experimental average, (b) FSI one-way procedure, and (c) deviation.

In this case the estimated residual stresses were smaller than the experimental average contour and an average deviation of 11% was observed through out the whole surface. Likewise, Figure 2.41 depicts the distributions obtained for the rear surface of the plate.

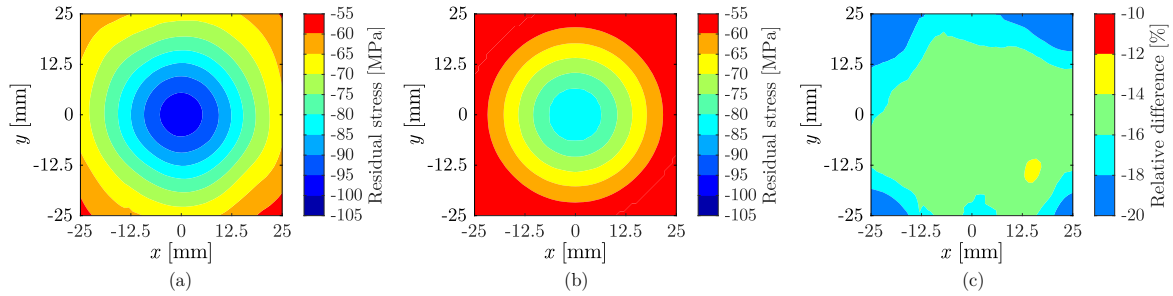

Figure 2.41: Residual stress distribution on the rear surface of symmetrically tempered glass samples at $H/D = 40$: (a) experimental average, (b) FSI one-way procedure, and (c) deviation.

The relative difference found in this area remained around 15%. These deviations came along with the experimental ones observed in Figure 2.43, and hence, were considered appropriate. With the view to analysing not only the residual stress distribution but also the magnitude, Figure 2.42 sets out the predicted stress distribution of symmetrically tempered plates at $H/D = 20$ with respect to the experimental measurement band referring to the five repeatability tests carried out. Likewise, the uncertainty range of 5% of the SCALP was considered.

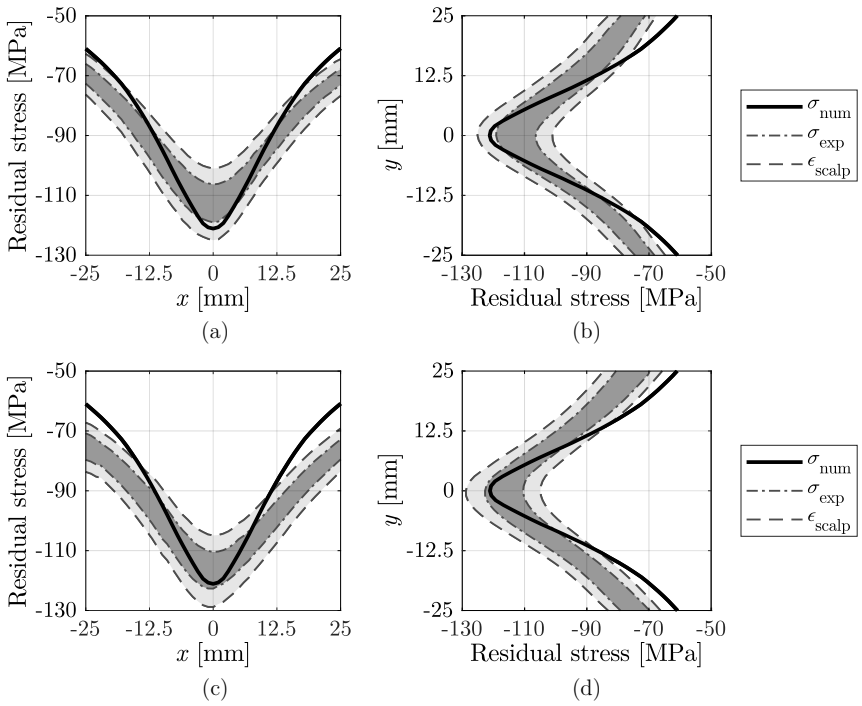

Figure 2.42: Residual stress distribution along x and y directions on the front and rear surfaces of symmetrically tempered glass samples at $H/D = 20$: (a)-(b) residual stress on the front surface along x and y directions, and (c)-(d) residual stress on the rear surface along x and y directions.

The calculated residual stress distributions were found to be in agreement with the experimental measurements in the front and rear surfaces as broadly fell within the specified experimental bands, comprising the five repeatability tests, and the uncertainty band of the SCALP device. Larger differences were perceived in the dry regions of the plate, namely, in the regions where less heat extraction occurred. Figure 2.43 plots the estimated residual stress distribution along x and y directions for symmetrically tempered plates at $H/D = 40$.

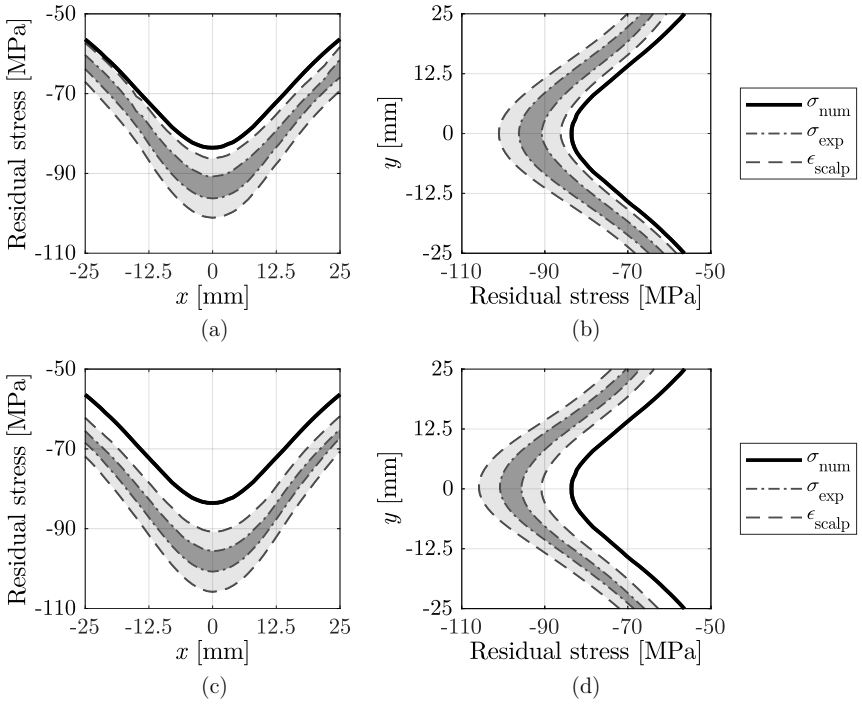

Figure 2.43: Residual stress distribution along x and y directions on the front and rear surfaces of symmetrically tempered glass samples at $H/D = 40$: (a)-(b) residual stress on the front surface along x and y directions, and (c)-(d) residual stress on the rear surface along x and y directions.

In this case, the predicted residual stress distributions remained in the lower limit of the specified experimental bands. A slight asymmetry in the measured residual stresses was also observed between both surfaces, as the compressive layer on the rear surface was found to be around 5% larger than the one in the front. Because of this reason, larger differences in respect to the experimental band were noticeable on the rear surface than on the front surface.

2.5.2 Assessment of computational cost reduction techniques

Hereafter, the analysed computational cost reduction techniques are investigated, namely, the influence of volumetric radiation, the existence of a critical temperature and the influence of assuming a spatially non-uniform time-constant HTC distribution during the tempering process.

Volumetric radiation influence

Firstly, the influence of volumetric radiation on the temperature variation over time of symmetrically tempered plates at $H/D = 20$ and $H/D = 40$ was analysed (see Figure 2.44).

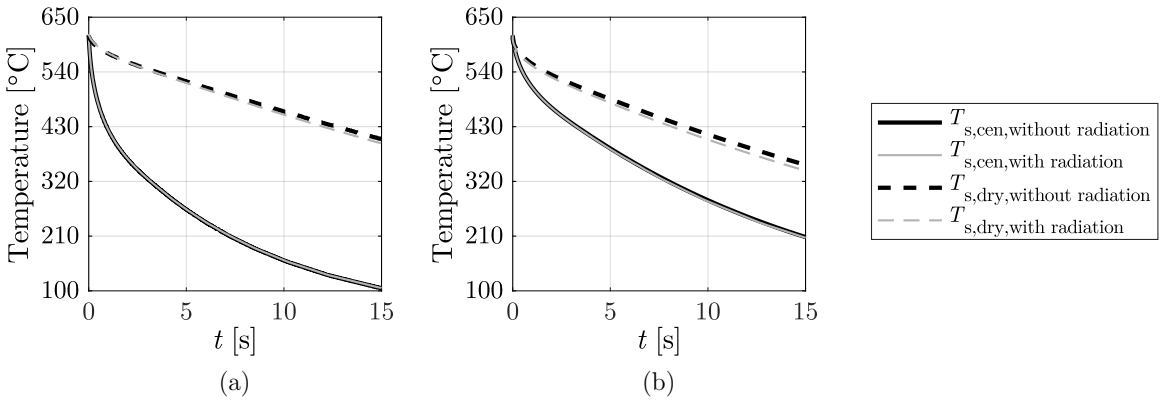

Figure 2.44: Surface temperature variation over time considering and without considering the effect of volumetric radiation for: (a) STHD20, and (b) STHD40.

Taking into account the local points where the highest and lowest cooling rate occured, the relative difference between considering or not considering the effect of radiation remained below 0.3% at the stagnation point and 2.5% in the dry region for both analysed tempering configurations. The reason for this may be the low impact volumetric radiation had during the rapid cooling of the plate. This fact could be better appreciated in Figure 2.45, where the contribution of radiation to the total heat transfer rate for each tempering case is shown.

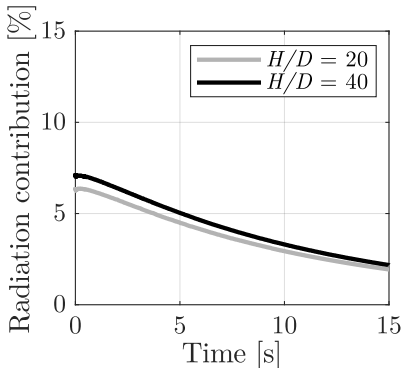

Figure 2.45: Contribution of radiation to the total heat transfer rate for symmetrically tempered plates at $H/D = 20$ and $H/D = 40$.

The contribution of radiation to the total heat transfer rate showed a maximum of 7.2% and 6% at the beginning of the cooling process for the short and large distance symmetrical tempering, respectively. After this maximum, the influence of radiation tended to decrease as the plate temperature dropped. Even though, radiation tended to homogenise the temperature pattern through the material as shown in Figure 2.46.

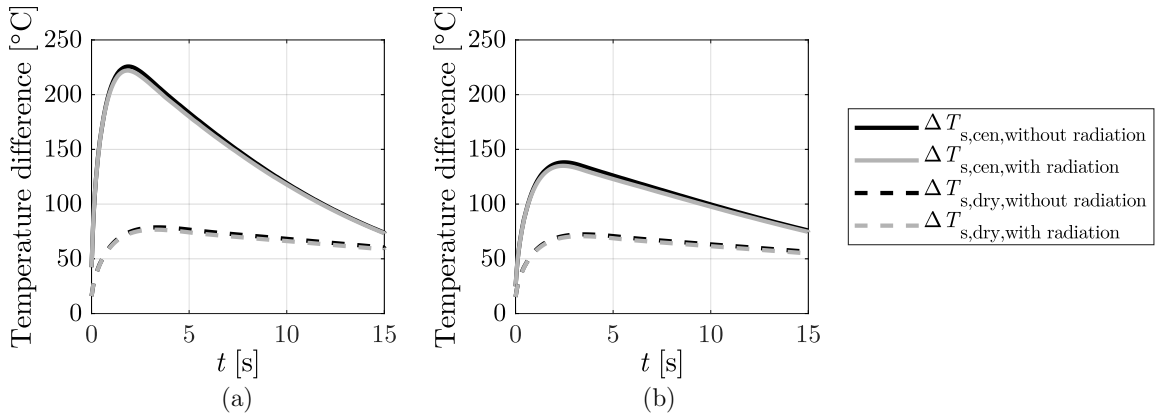

Figure 2.46: Volumetric radiation influence on the temperature difference between the surface and the core of the plate in the stagnation and dry regions for both analysed tempering conditions: (a) STHD20, and (b) STHD40.

The temperature difference increased until a maximum difference of 225 °C was reached in the stagnation region and 80 °C in the dry region for the STHD20 configuration, whereas 135 °C and 70 °C were reached for STHD40. Radiation reduced the temperature difference by 2.2% in the jet facing area and 2.4% in the dry region. These low differences may stem from the applied high cooling rate and low thickness of the material. On the question of residual stress development, Figure 2.47 provides the influence of radiation on the residual stress pattern.

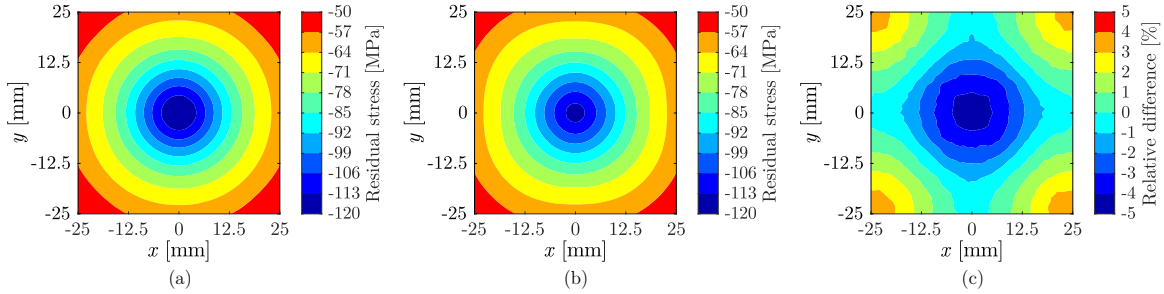

Figure 2.47: Volumetric radiation influence on the estimated surface residual stresses for symmetrically tempered plates at $H/D = 20$: (a) considering radiation, (b) without considering radiation, and (c) deviation.

Deviations in residual stress distributions between considering or not considering the effect of radiation were low. The reason for this may have to do with the short period of time that the components remained at high temperature. Nevertheless, larger differences were noticed as compared to the ones observed in Figure 2.44. As a result, thermal differences cannot be extrapolated to residual stress deviations, and thus, a precise representation of the thermal history was considered critical to accurately calculate residual stresses. Figure 2.48 shows the residual stress paths along x and y directions crossing at the centre of the plate.

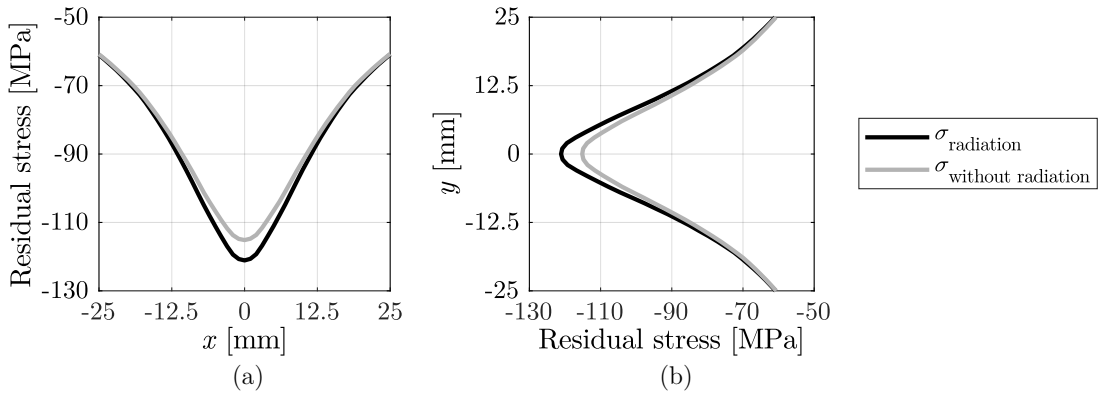

Figure 2.48: Volumetric radiation influence on the surface residual stress paths for symmetrically tempered plates at $H/D = 20$ along: (a) x direction, and (b) y direction.

Similarly, Figure 2.49 illustrates the residual stress contour plots accounting for radiation and neglecting it, as well as, the corresponding deviation for the symmetrical $H/D = 40$ tempering configuration.

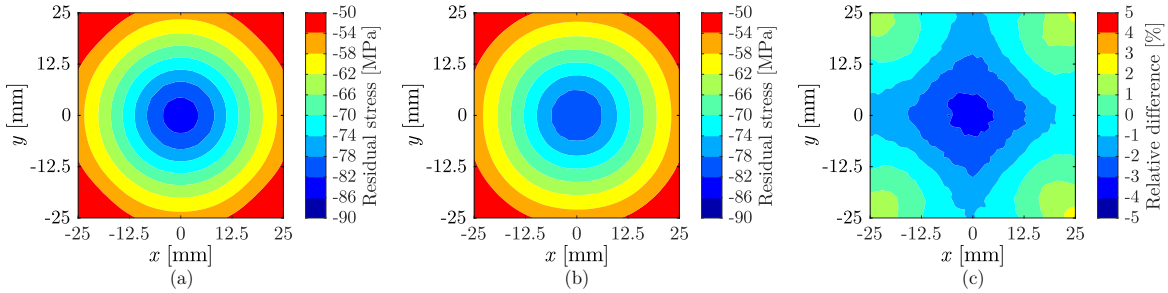

Figure 2.49: Volumetric radiation influence on the estimated surface residual stresses for symmetrically tempered plates at $H/D = 40$: (a) considering radiation, (b) without considering radiation, and (c) deviation.

Analogous to the previous case study, low deviations were observed between both approaches. Figure 2.50 shows the influence of volumetric radiation on the residual stress paths along x and y directions crossing at the centre of the plate.

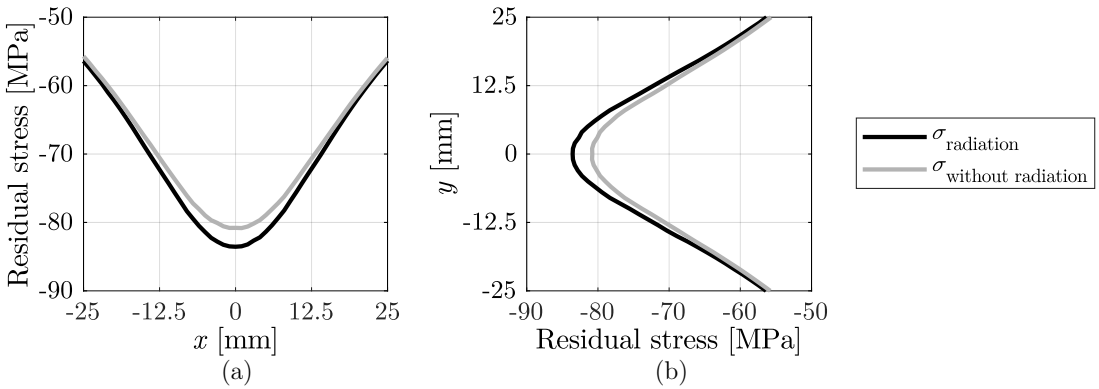

Figure 2.50: Volumetric radiation influence on the surface residual stress paths for symmetrically tempered plates at $H/D = 40$: (a) along x direction, and (b) along y direction.

In both tempering configurations, the residual stress magnitude was around 5% larger when accounting for volumetric radiation. Nevertheless, lower residual stress magnitudes are to be expected when taking volumetric radiation into account due to the temperature homogenisation in the material. The reason for observing larger stresses may have something to do with the dissimilar cooling that the jet facing area and the dry regions exhibited. During the conventional tempering process, multiple jets covering the whole glass surface are employed. Therefore, the cooling and contractions of the stagnation and dry regions broadly happen at the same instant in the whole plate. In this case though, a single jet at each side of the plate was used to perform the tempering tests, meaning that the dry regions cooled down in a slower pace than the stagnation area. During the tempering process, the colder stagnation area, would tend to contract earlier than the warmer dry region. When the dry region tried to contract, the already cold stagnation region restrained this contraction. When radiation is considered, the thermal history of the component varied, especially the warmer regions of the material, i.e. the core of the dry regions. Consequently, different contractions might occurred in the material resulting in a higher compression in the centre of the plate.

In summary, even if differences in temperature variation showed a huge similarity, the deviations in residual stress magnitudes were observe to be higher. Consequently, the assessment of volumetric radiation should be done based on both, temperature and residual stress calculations. Notwithstanding, the maximum deviation observed in terms of residual stress remained below 5%. Thus, radiation can be disregarded when low thickness glass is subjected to large heat extractions. For thicker components though, volumetric radiation might have a larger influence on the residual stress development and additional investigations may be required.

Critical temperature assessment

With the aim of finding the critical temperature, at which residual stresses are no longer influenced by the cooling rate, the computational sequence presented in Figure 2.9 was adopted. Volumetric radiation was shown to have little influence on the residual stress magnitude and distribution, and hence, it was not considered within this analysis.

The CFD calculation was performed until the hottest point, namely the core in the dry region, was at 400 °C. Thus, transient and spatially non-uniform HTCs were considered during the first stage of the cooling process. Once the critical temperature instant was reached, the fluidic and thermal computation could be interrupted and a purely thermal calculation based on a spatially uniform and constant in time HTC was performed. Thereby, different HTC resembling natural and forced convections were defined in order to verify the cooling rate independence, more specifically, 20 W/m^{2}K, 500 W/m^{2}K and 1000 W/m^{2}K. Figure 2.51 provides the residual stress distribution when the CFD calculation was interrupted at a core temperature of 400 °C and subsequently, different uniform and constant HTC were applied. Similarly, the residual stress distribution obtained by the FSI one-way procedure without considering radiation is presented.

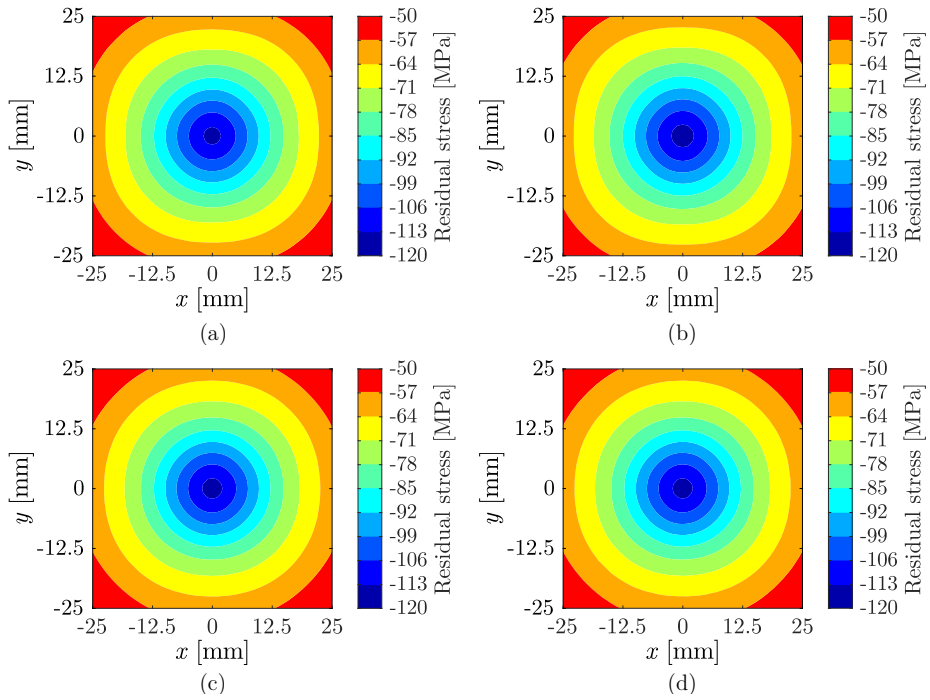

Figure 2.51: Estimated surface residual stress pattern for STHD20 based on: (a) the FSI one-way procedure without considering radiation, and (b)-(d) the proposed procedure based on CFD analysis without radiation until a critical temperature of 400 °C is achieved, followed by a thermo-mechanical calculation considering different HTC values: (b) 20 W/m^{2}K, (c) 500 W/m^{2}K, and (d) 1000 W/m^{2}K.

Despite the HTC variation from 20 to 1000 W/m^{2}K, the obtained final residual stress distribution did not vary with respect to the reference case as the maximum difference remained below 1%. The most interesting aspect of these results was that the same residual stress magnitude and distribution was obtained even if below 400 °C each case showed a different thermal history. Figure 2.52 shows the residual stress distribution of each case along x and y directions.

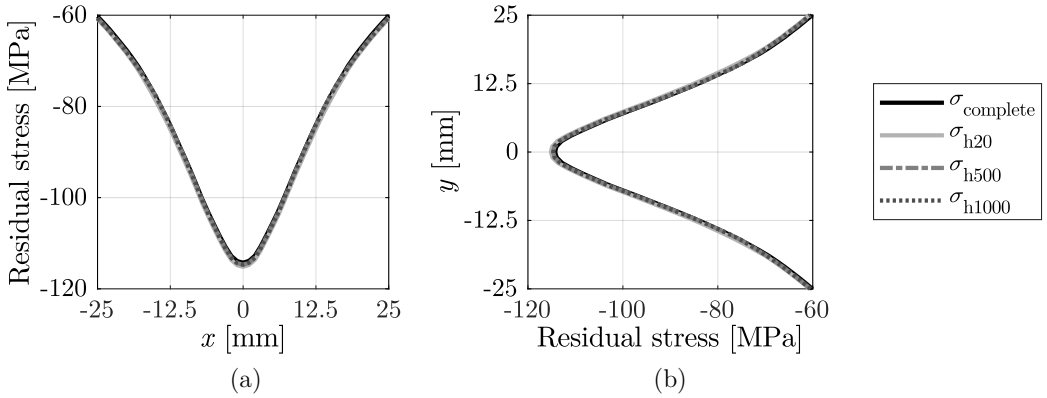

Figure 2.52: Residual stress paths along x and y directions for STHD20 based on the FSI one-way procedure without considering radiation and the proposed procedure based on different HTC values below 400 °C: 20 W/m^{2}K, 500 W/m^{2}K, and 1000 W/m^{2}K.

As observed in Figure 2.51 and Figure 2.52, all the estimations led to a similar residual stress pattern. The reason for this has to do with the volumetric expansion of glass. When the hottest point of the plate was at 400 °C, the critical temperature was reached and the contribution of volumetric expansion phenomenon was almost completely vanished as evidenced in Figure 2.4. As a result, the subsequent cooling technique was no longer influential on the residual stress development and it became cooling rate independent within the range from natural to forced convection cooling. If the critical temperature was not reached though, residual stresses became cooling rate dependent and its final magnitude and distribution varied as a function of the adopted cooling technique. Overall, a residual stress deviation below 1% with regard to the reference model was obtained. The same conclusions were obtained for the symmetrically tempering case at $H/D = 40$.

What stands out from this analysis is the large computational cost that radiation implied on the total calculation time. Simulations were run in parallel with 8 cores on a desktop computer (Intel(R) Xeon(R) Gold 6140 CPU 2.30GHz 2.29 GHz and 256 GB RAM) and the heaviest ones took up to 4 months for completion. This unique assumption led to a reduction of 75% of the total computational time. Furthermore, if the CFD calculation was interrupted, an additional saving of 50% was obtained, which brought about a total decline around 87% of the computational time in respect to the initially proposed procedure.

Spatially non-uniform steady HTC

Finally, the consideration of time-constant but spatially different HTC distributions to calculate residual stresses was analysed. This approximation could lead to a further reduction of the calculation time, as a steady HTC distribution calculated at the beginning of the process could replace the transient flow simulation and its associated larger computational cost.

Figure 2.53 depicts the transient and steady HTC distributions at the critical time instant, namely, when the critical temperature of 400 °C was attained, as well as the deviation between both approaches. The steady HTC pattern calculated at the onset of cooling was maintained constant through out the

cooling process, whereas the transient HTC approach updated the fluid domain, and hence, the HTC distribution, every time step.

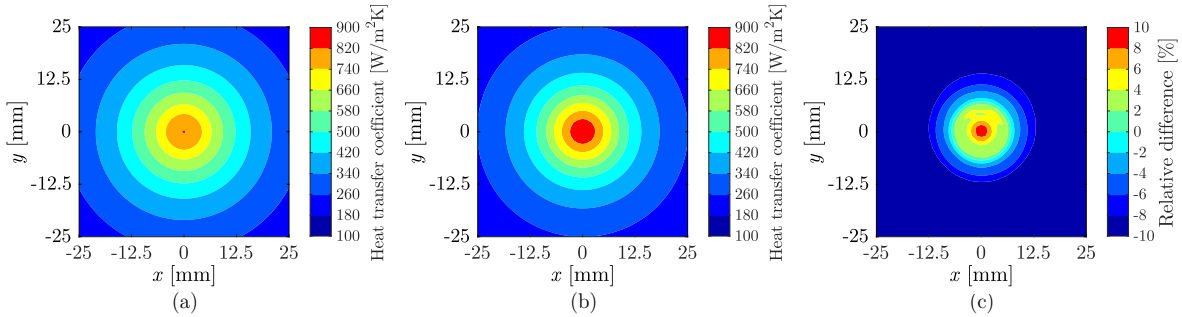

Figure 2.53: HTC distribution at critical temperature ($T_{\text{cri}} = 400$ °C) of symmetrically tempered plates at $H/D = 20$: (a) transient HTC; (b) steady HTC, and (c) deviation.

The transient HTC magnitude in the stagnation point decreased over time whilst the heat extraction in the dry region increased. The latter phenomenon was better appreciated by the negative sign in the deviation contour plot. The relative difference remained about 10%. Likewise Figure 2.54 sets out the transient and steady HTC distributions when symmetrically tempered glass at $H/D = 40$ reached 400 °C.

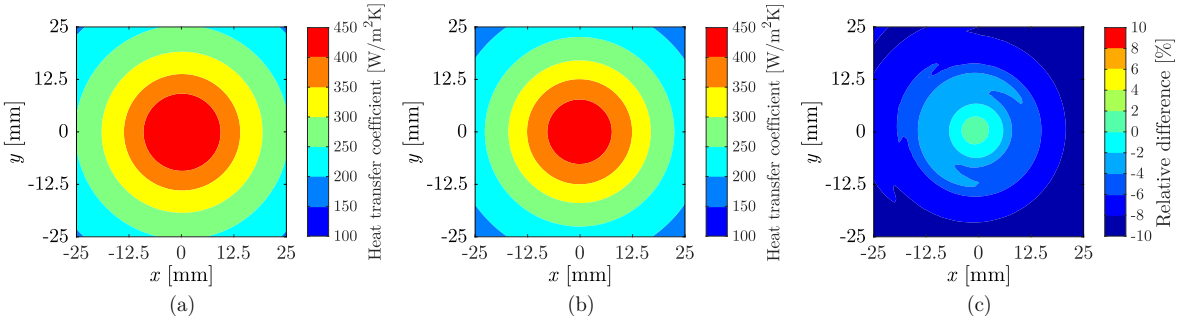

Figure 2.54: HTC distribution at critical temperature ($T_{\text{cri}} = 400$ °C) of symmetrically tempered plates at $H/D = 40$: (a) transient HTC, (b) steady HTC, and (c) deviation.

In this case, a similar behaviour was observed. The HTC in the jet facing area showed a deviation of 2% whereas a larger relative difference up to 10% in the dry region was observed. As for residual stresses, Figure 2.55 presents the final residual stress distribution for STHD20 estimated by considering transient or steady HTC patterns.

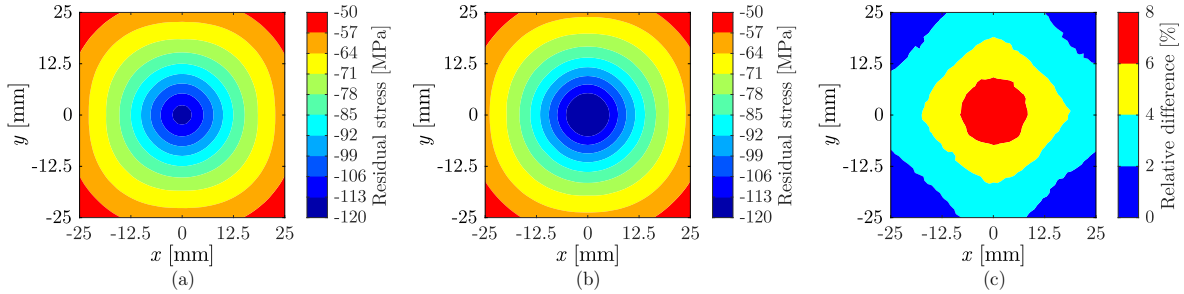

Figure 2.55: Final residual stress distribution on the surface of symmetrically tempered plates at $H/D = 20$ based on: (a) transient HTC, (b) steady HTC, and (c) deviation.

Likewise, Figure 2.56 presents the final residual stress distribution for the large jet-to-plate distance tempering case ($H/D = 40$) considering both, transient and steady HTC distributions.

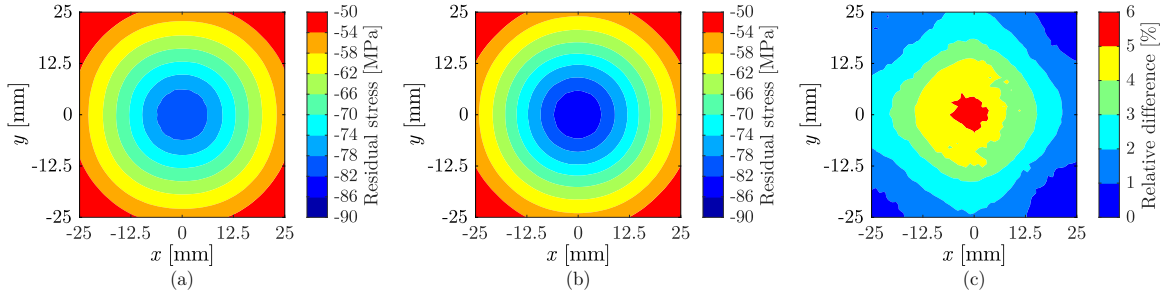

Figure 2.56: Final residual stress distribution on the surface of symmetrically tempered plates at $H/D = 40$ based on: (a) transient HTC, (b) steady HTC, and (c) deviation.

Analysing the residual stress results of both tempering configurations, differences up to 8% in the stagnation region and about 1% in the dry regions were perceived. This aspect might be explained by the contraction of the dry region. By the use of a single jet on each side of the plates, the dry regions exhibited differences in terms of heat extraction between considering steady or transient HTC distributions. Regarding residual stresses though, when assuming a steady HTC, the different heat extraction in the dry region may have a direct effect on the contraction of the stagnation region resulting in larger compressive stresses. Consequently, even if differences remained below 10% and an extra reduction of 70% of the computational time could be achieved, this aspect should be investigated to a greater extent in an industrial case study, where multiple jets are generally employed.

2.5.3 Validation of the modified procedure

Here, the validation of the proposed modified procedure to model low thickness quenching processes is presented. The procedure encompasses both, a CFD model without volumetric radiation to capture the transient local flow phenomena until the critical temperature is attained, and a thermal model where a constant in time and spatially uniform HTC is applied.

Figure 2.57 illustrates the contour plots of the average experimental and the numerical residual stresses, and the relative difference distribution for symmetrical tempering plates at $H/D = 20$.

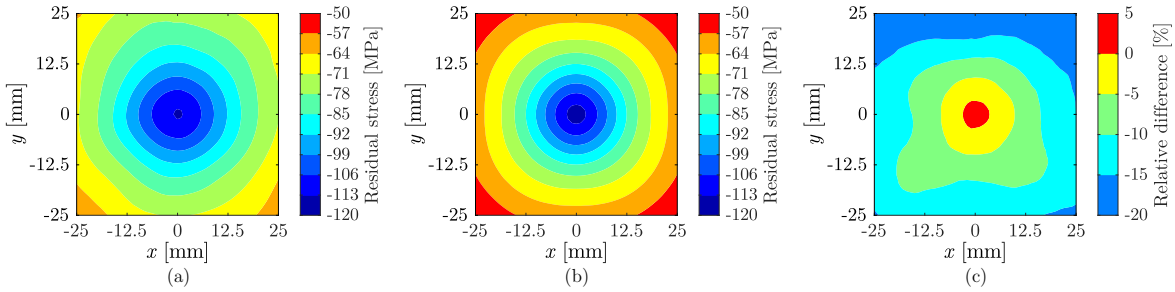

Figure 2.57: Residual stress distribution on the front surface of symmetrically tempered glass samples at $H/D = 20$: (a) experimental average, (b) modified procedure, and (c) deviation.

Differences with respect to the average experimental contour up to 5% and 20% in the stagnation and dry regions were observed, respectively. A similar conclusion was achieved when the rear surface was analysed in Figure 2.58.

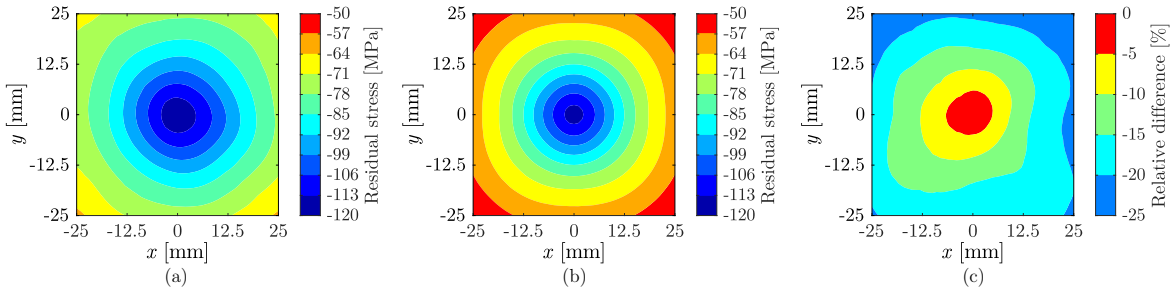

Figure 2.58: Residual stress distribution on the rear surface of symmetrically tempered glass samples at $H/D = 20$: (a) experimental average, (b) modified procedure, and (c) deviation.

Figure 2.59 shows the average experimental residual stress, the numerical residual stress and the deviation distributions for symmetrical tempering plates at $H/D = 40$.

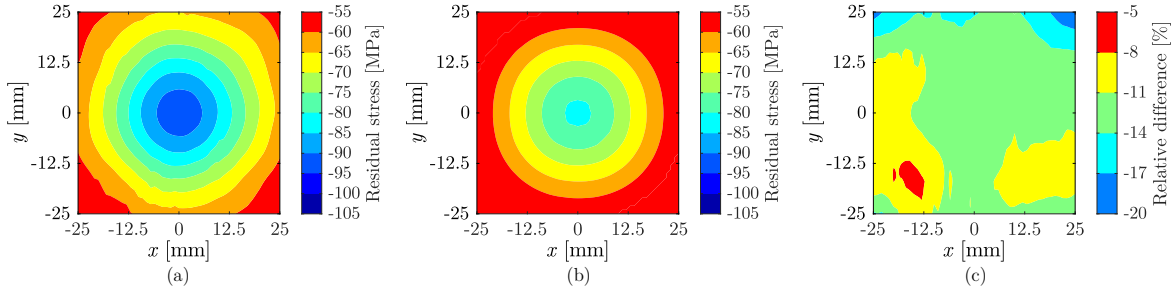

Figure 2.59: Residual stress distribution on the front surface of symmetrically tempered glass samples at $H/D = 40$: (a) experimental average, (b) modified procedure, and (c) deviation.

In this case an homogeneous average deviation around 12% was observed. Likewise, Figure 2.60 sets out the distributions obtained for the rear surface of the plate.

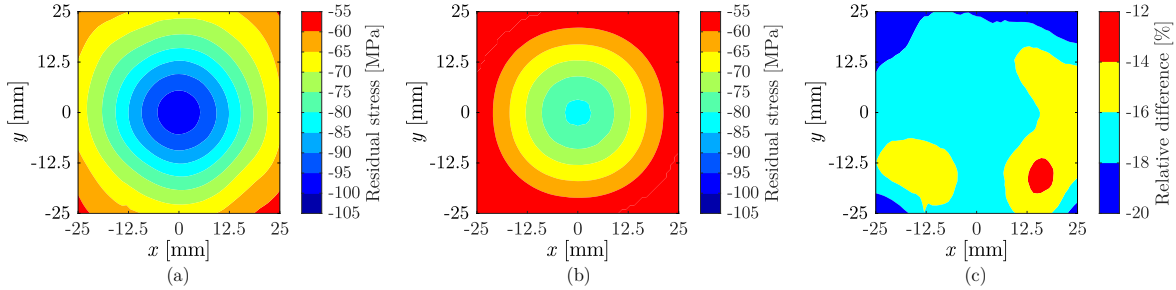

Figure 2.60: Residual stress distribution on the rear surface of symmetrically tempered glass samples at $H/D = 40$: (a) experimental average, (b) modified procedure, and (c) deviation.

The relative difference found in this area remained broadly uniform around 16%. With the view to analysing not only the residual stress distribution but also the magnitude, Figure 2.61 plots the calculated stress in symmetrically tempered plates at $H/D = 20$. In like manner, the experimental measurement band enveloping the performed repeatability tests and the uncertainty range of 5% of SCALP are provided.

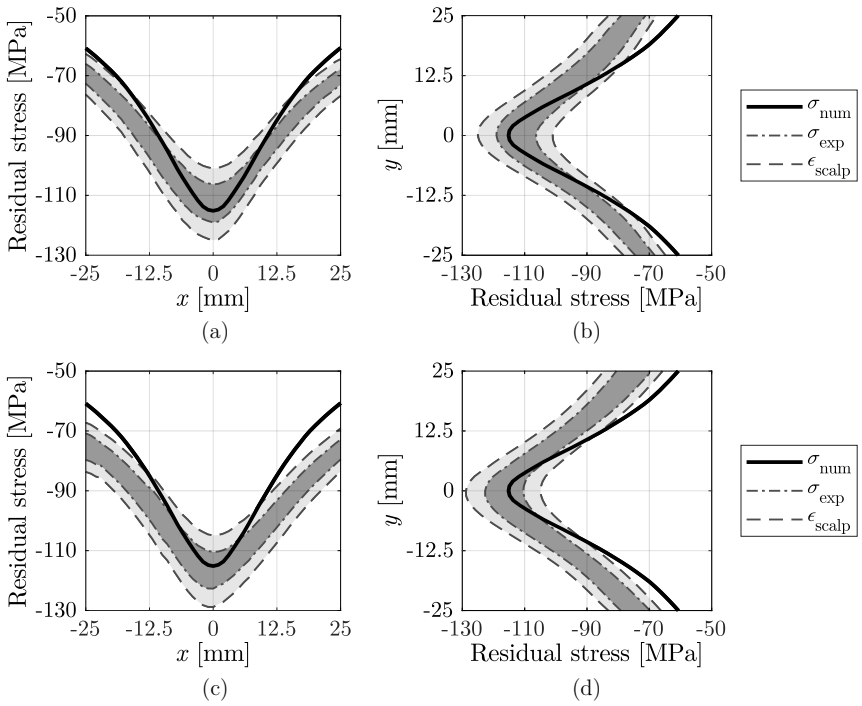

Figure 2.61: Residual stress distribution along x and y directions on the front and rear surfaces of symmetrically tempered glass samples at $H/D = 20$: (a)-(b) residual stress on the front surface along x and y directions, (c)-(d) residual stress at the rear surface along x and y directions.

The predicted residual stress distributions were found to be in agreement with the experimental measurements on the front and rear surfaces as broadly fell within the specified bands. Larger differences were perceived in the dry regions of the plate, namely, in the regions where less heat extraction occurred. Figure 2.62 presents the estimated residual stress distribution along x and y directions for symmetrically tempered plates at $H/D = 40$.

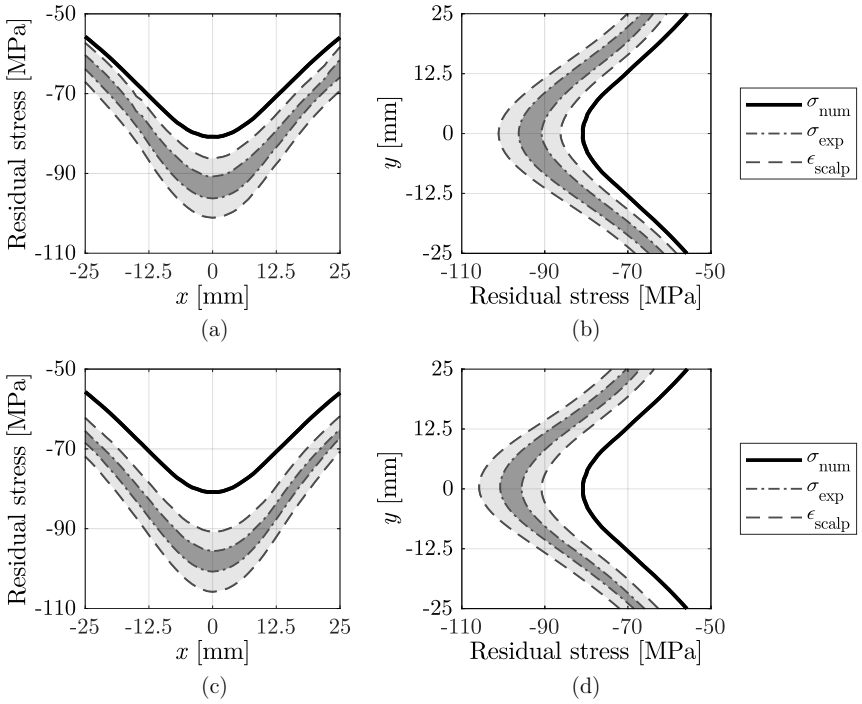

Figure 2.62: Residual stress distribution along x and y directions on the front and rear surfaces of symmetrically tempered glass samples at $H/D = 40$: (a)-(b) residual stress on the front surface along x and y directions, (c)-(d) residual stress at the rear surface along x and y directions.

In this case, the predicted residual stress distributions remained in the lower limit of the specified experimental bands. Due to the asymmetry in the measured residual stresses between the front and rear surfaces, larger differences between the estimated and experimental residual stresses were perceived on the rear surface. These differences could be explained in part by possible uncertainties regarding the modelling of turbulent flow at large jet-to-plate distances. Additionally, volumetric radiation gained more significance and might play a role in the wall temperature and its interaction with the fluid flow. Thus, the next section of this chapter will move on to analyse the sensitivity of specific parameters involved with the proposed numerical procedure.

Despite these discrepancies, the evidence from this study suggested that the proposed modified procedure enabled the calculation of representative residual stress distributions in tempered glass components, as it came along with the results observed in Section 2.5.1.

2.5.4 Sensitivity analysis

In this section, the influence of initial temperature of glass, the defined jet velocity and the selection of the turbulence model on the developed residual stresses is addressed. To this end, the proposed modified procedure is used and the symmetrical tempering configuration at $H/D = 20$ was analysed.

Influence of initial temperature

Experimental parameters, such as the quench delay and the emissivity of the black coating employed to measure the temperature of the plates, can result in distinct initial quenching temperatures and an exact value cannot be guaranteed. Therefore, three different initial temperatures were defined to study its influence on the residual stress development: 600 °C, 610 °C and 625 °C. Figure 2.63 sets out the residual stress distribution along x and y directions crossing at the centre of the plate.

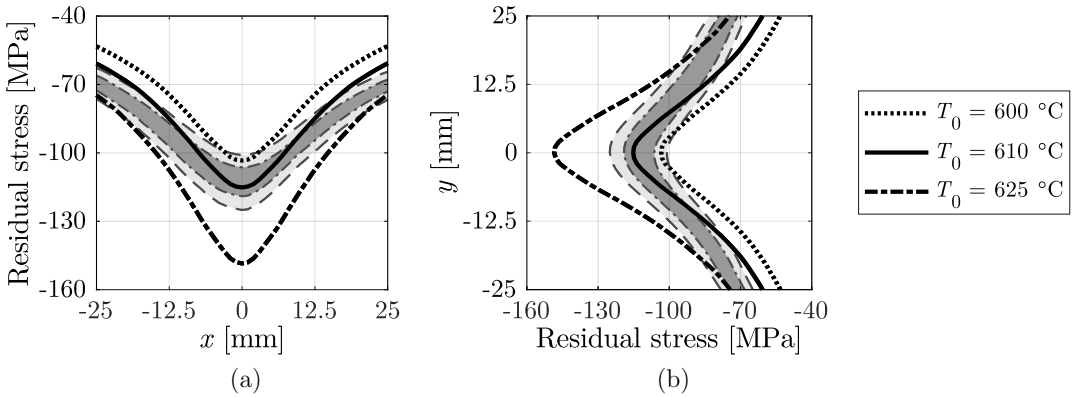

Figure 2.63: Influence of initial glass temperature on the residual stress distribution along: (a) x direction and (b) y direction.

The higher the initial temperature of glass, the larger the developed compressive layer. This process parameter was found to have a significant influence on residual stress magnitude as an increased of 30% was noticed for an initial temperature of 625 °C with respect to 610 °C.

Influence of jet velocity

Once the influence of initial quenching temperature was evaluated, the residual stress dependency on the jet velocity was studied. In this case, the initial temperature distribution in the plate referred again to the one described in Figure 2.18. Based on the pressure measurements taken, a jet inlet-velocity of 200 m/s was defined to estimate residual stresses. With the aim of assessing its impact on the residual stress development, a variation of ± 10 % was defined (see Figure 2.64).

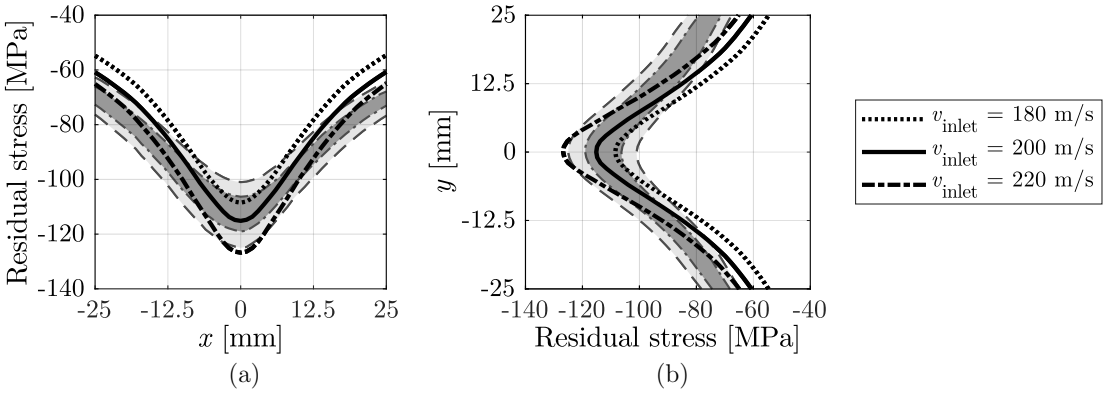

Figure 2.64: Influence of jet velocity on the residual stress distribution along: (a) x direction and (b) y direction.

The influence of the jet velocity on the residual stress magnitude was lower than the one of the initial temperature of glass. Here, differences with respect to the reference velocity of 200 m/s remained below 10%. However, an accurate characterisation of the flow velocity becomes a paramount matter to predict representative residual stresses.

Influence of turbulence model selection

Finally, the influence of turbulence modelling on residual stress development was assessed. For this purpose, the $k-\omega$ SST model, the GEKO model and the GEKO model with Intermittency Transition model with Kato-Launder production limiter are analysed. Figure 2.65 shows the residual stress distribution along x and y directions for each turbulence modelling technique.

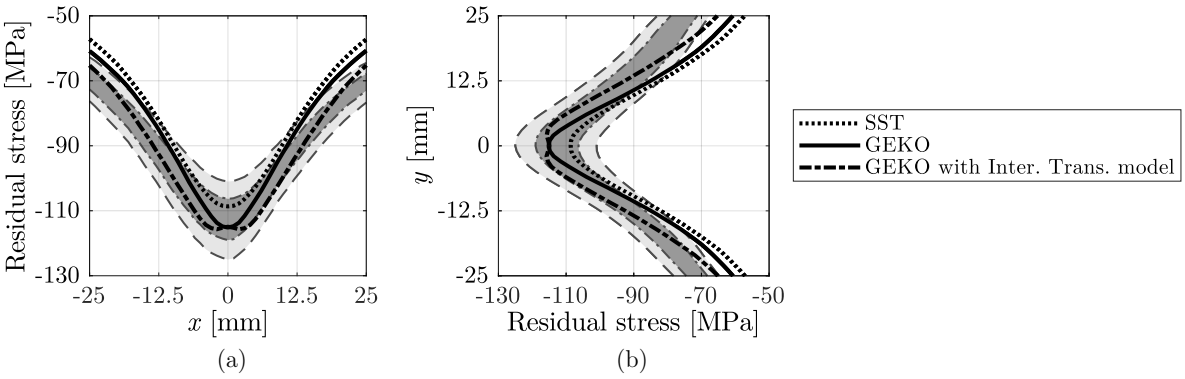

Figure 2.65: Influence of jet velocity on the residual stress distribution along: (a) x direction and (b) y direction.

When the $k-\omega$ SST model was defined, a relative difference of 7% in terms of residual stress magnitude was observed as compared to the GEKO turbulence model. The same residual stress magnitude was attained by the GEKO with Intermittency Transition model with Kato-Launder production limiter, though it tended to excessively flatten the residual stress prediction in the stagnation region. This discrepancy is thought to be related to the large jet-to-plate distance of $H/D = 20$ defined in the current tempering configuration. Underprediction of heat transfer in the stagnation region by the use of Kato-Launder limiter for cases involving $H/D > 10$ was also reported in the literature [108]. In addition to the stagnation region, differences in the residual stress distribution because of the jet spreading could be perceived. Thus, the use of the Kato-Launder production limiter should be checked and verified, especially for case studies defined by $H/D > 10$.

In summary, the current data highlight the importance of accurately characterising the analysed process parameters and modelling techniques since their influence on residual stress development can be significant. As a consequence, the proposed methodology was considered to be representative of the presented laboratory case studies, and hence, the following section aims to validate the procedure in a more complex case study, namely, an industrial tempering unit.

2.6 Application of the FSI numerical method to industrial case study

In this section, the validity of the performed investigation on a industrial environment is checked. Firstly, the description of the industrial case study is performed. Then, multi-nozzle array model, the followed post-processing procedure and a mesh sensitivity study are introduced. When the numerical model and grid are established, as the tempering configuration and thickness of the component differ from the ones of the laboratory case studies, the different computational cost reduction techniques are again evaluated to prove their validity in more complex scenarios. More specifically, the influence of volumetric radiation on the non-uniform residual stress distribution of tempered glass plates, the existence of a critical temperature and the influence of considering a spatially non-uniform steady HTC are investigated. Finally, the calculations made by the proposed procedure are validated.

2.6.1 Industrial case study

The analysed case study alluded to the work presented by Chen et al. in which they measured the residual stress distribution after tempering flat glass specimens of 6 mm thickness [56]. According to this investigation, an industrial tempering unit of the Canadian company, PRELCO Inc., was employed to carry out the tempering tests.

Even if the specimens had a dimension of 300 x 300 x 6 mm, the analysis of the results was limited to a representative area of 28 x 56 mm composed of a centred and its four neighbouring jets (see Figure 2.66).

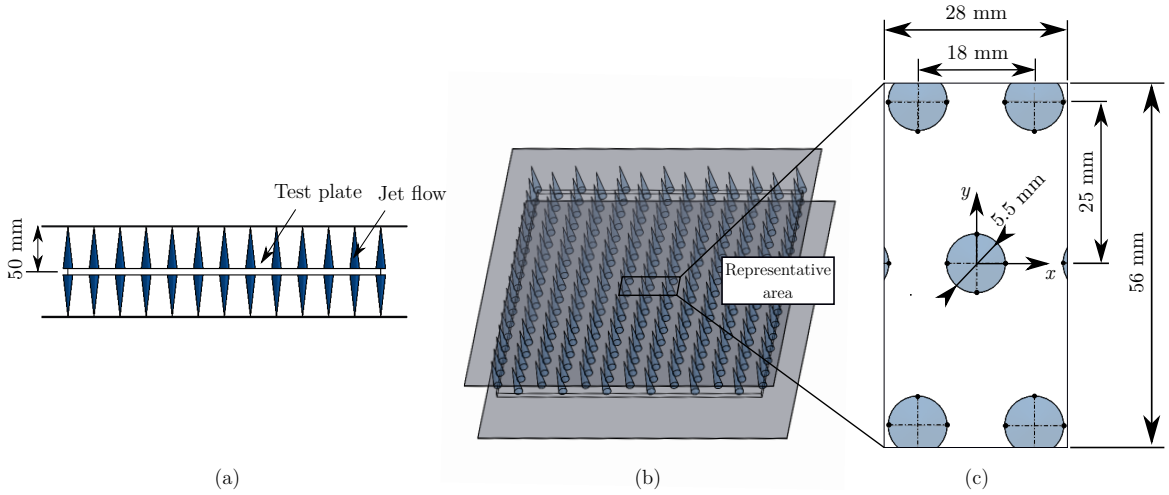

Figure 2.66: Cooling unit over the glass plate and the area of interest: (a) side view; (b) isometric view; and (c) detail of the area of interest.

The cooling jets consisted of perforated plates symmetrically located at both sides of the plate. The holes in the plate had a diameter of 5.5 mm. The distance between adjacent jet columns and rows were 18 mm and 25 mm, respectively. Regarding the nozzle-to-plate distance, it was defined at 50 mm, hence, $H/D \approx 9$. In this way, the numerical model was further extended from laboratory tests to a real tempering case.

2.6.2 Numerical model of the industrial case study

In this section, first the computational fluidic and structural domains are described. Subsequently, the followed post-processing procedure is explained. And finally, a mesh sensitivity analysis to check the mesh suitability is performed.

Multi-nozzle array model set-up

Figure 2.67 illustrates the computational domain composed of the glass plate and the fluid domain. The nozzle arrangement and its dimensions, as well as the process parameters were based on the work of Chen et al. [56]. To reduce the computational time, a 1/8 model was defined by the use of three symmetry planes. Likewise, the computational grid was extended sufficiently far to the sides in order to led the nozzle array flow to develop before reaching the outlet boundary condition.

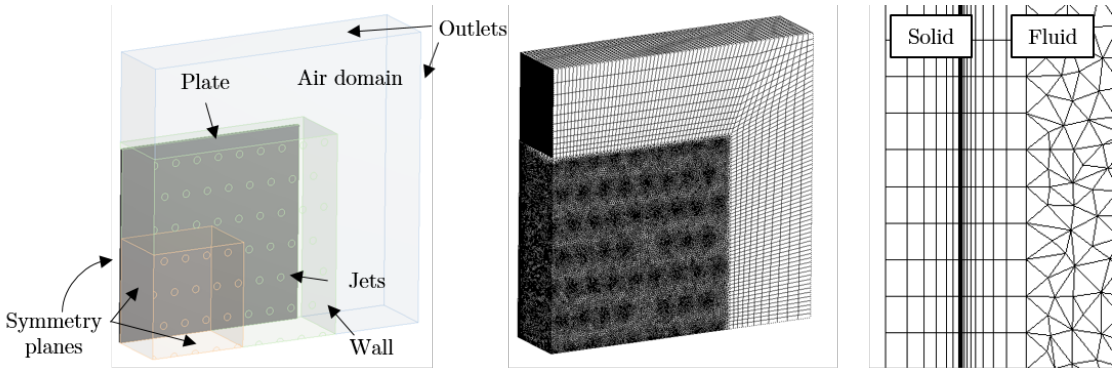

Figure 2.67: Three dimensional symmetric model used in the numerical calculation: (a) 1/8 symmetry computational domain; (b) mesh discretisation; and (c) detail of the near wall mesh.

The central fluid region in contact with the glass plate was discretised with a finer mesh than the surrounding fluid volume to make the calculation more efficient. Six hexahedral elements were defined through half the thickness of the plate and a bias factor of four was used to better capture the thermal gradients developed on the surface. Tetrahedrons were used to mesh the air domain and 14 inflation layers with a first layer thickness of 10 μm were defined near the glass wall to obtain a wall y^+ value in the order of unity. This y^+ value is the recommended one to correctly model the boundary layer when the $k-\omega$ turbulence model is used.

The GEKO turbulence model, which is recommended for modelling jet impingement applications, was employed [104]. As a $H/D \approx 9$ was defined in the industrial tempering unit, the Intermittency Transition model with Kato-Launder production limiter was also considered.

Regarding the solver, a pressure-based solver was employed as the defined flows were subsonic. The SIMPLE algorithm was used to solve the pressure and velocity fields and the second order upwind discretisation scheme was selected. A root mean square residual value below 10^{-4} was considered for convergence of the momentum, continuity, and turbulent equations, whereas a value below 10^{-6} was defined for the energy and radiation calculations.

Each jet was modelled by circular inlet conditions. Here, uniform velocity boundary conditions were imposed while pressure outlet boundary conditions were defined at the outflow boundaries. Two air flow velocities were analysed as stated in the experimental work in literature, namely, 100 m/s and 200 m/s. Likewise, to assess the influence of volumetric radiation, the Discrete Ordinates Method (DOM) was used.

Structural domain of the industrial case study

After the CFD calculation was carried out, a structural analysis was performed. In this case, the fluid domain was removed and the numerical model was only composed of the solid glass plate. The mesh consisted of 60000 quadratic full-integration hexahedral elements, composed of six elements through half the thickness.

Post-processing procedure for the industrial case study

Next, the followed post-processing procedure for analysing the plate tempered in an industrial tempering unit is summarised. As presented in Figure 2.68, the result discussion was limited to the largest stress gradient area, composed of a centred and its four neighbouring jets. This analysis area was also the one defined by previous experimental investigations for measuring the residual stress magnitude on the surface of the components [56]. Therefore, the obtained residual stress results were restricted to this area.

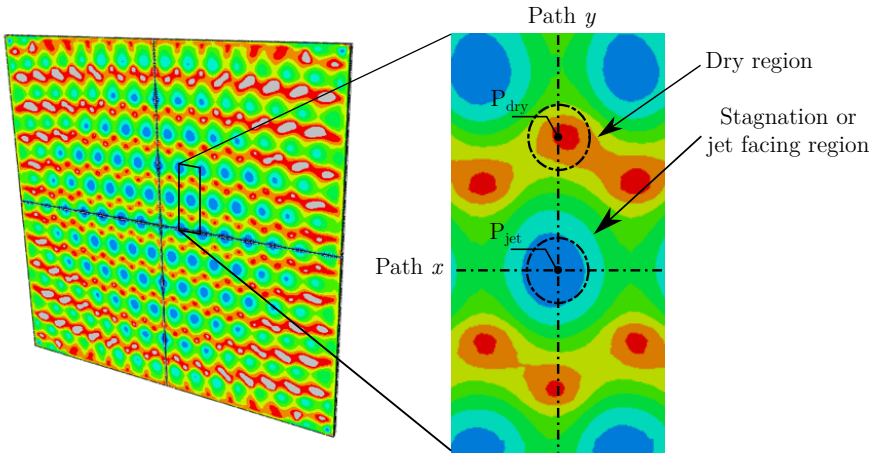

Figure 2.68: Residual stress pattern on the complete glass surface and the area of interest, in which the jet and dry regions and the x and y paths for performing subsequent experimental validations are defined.

Once the analysis area was defined, the following post-processing features were proposed for analysing the results:

- Absolute maximum principal stress contours were plotted in the area of analysis to identify the tensile and compressive regions.
- Two control points located in the dry region, P_{dry}, and jet facing area, P_{jet}, were defined to analyse the residual stress variation over time on both, the surface, $(\bullet)_s$ and the core, $(\bullet)_c$, of the component. The dry region refers to the area between jets, $(\bullet)_{dry}$, whereas the jet region to the stagnation or jet facing area $(\bullet)_{jet}$.
- Two paths along the x and y directions were defined to validate the obtained residual stress magnitudes against experimental measurements.

Mesh sensitivity analysis

Subsequently, a mesh sensitivity analysis was performed to assess the dependency rate of the numerical results with respect to the defined mesh. For this reason, the size and density of the grid cells related to the air domain were varied until mesh independent results were achieved. Element sizes of 2.25, 1.5 and 1.125 mm for the plate and air domain were defined. As a result, a coarse mesh made out of 960935 elements (mesh 1), an intermediate mesh of 3,671,976 (mesh 2) and a fine mesh of 4,851,349 (mesh 3) were studied. Figure 2.69 compares the residual stress variation over time on the surface and core of the jet and dry regions, when a 100 m/s air flow was applied.

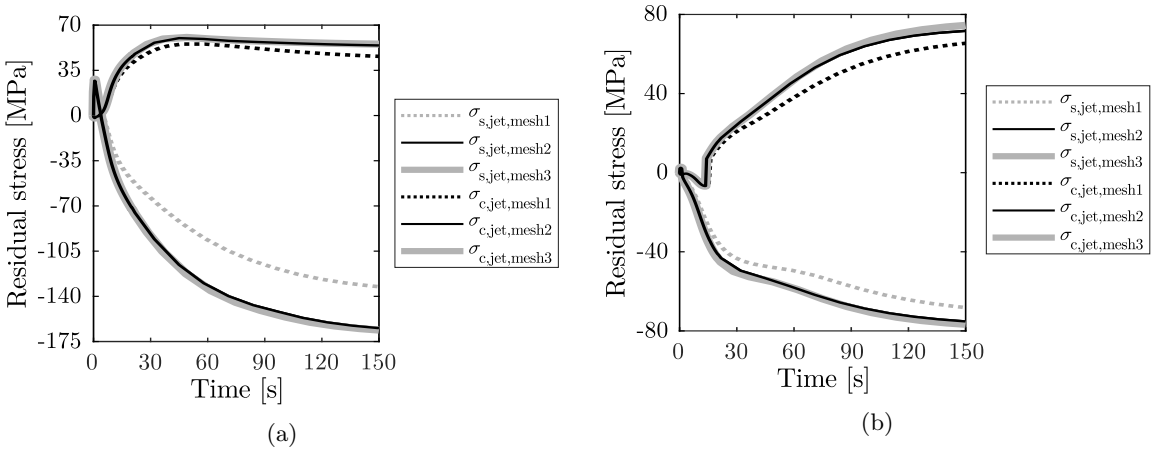

Figure 2.69: Influence of mesh refinement on the residual stress variation over time on the surface and the core of the glass plate in the: (a) jet facing area; (b) dry region.

The coarser grid showed a deviation up to 20%, whereas a deviation of 4% was obtained comparing the finer meshes. Hence, the grid configuration with 3,671,976 cells was selected for the following calculations.

2.6.3 Assessment of computational cost reduction techniques

In this section, the computational cost reduction techniques are again evaluated to confirm their validity in a more complex tempering configuration. More specifically, the influence of volumetric radiation, the existence of a critical temperature and the assumption of a spatially non-uniform time-constant HTC distribution during the tempering process are investigated.

Influence of volumetric radiation in industrial case study

As compared to the performed laboratory case studies, in the presented industrial case study thicker plates of 6 mm were considered, hence, the influence of volumetric radiation needed to be addressed. To this end, even if the initial temperature distribution of the plate after the heating process can play an important role in the residual stress development, due to the lack of information regarding the

thermal history of the components, a uniform initial temperature of 650 °C was assumed. Figure 2.70 sets out the numerically calculated residual stress patterns corresponding to an air velocity of 100 m/s and 200 m/s at the cooling jet exit considering and neglecting radiation phenomenon. The proposed jet velocities were defined according to the experimental work in literature [56].

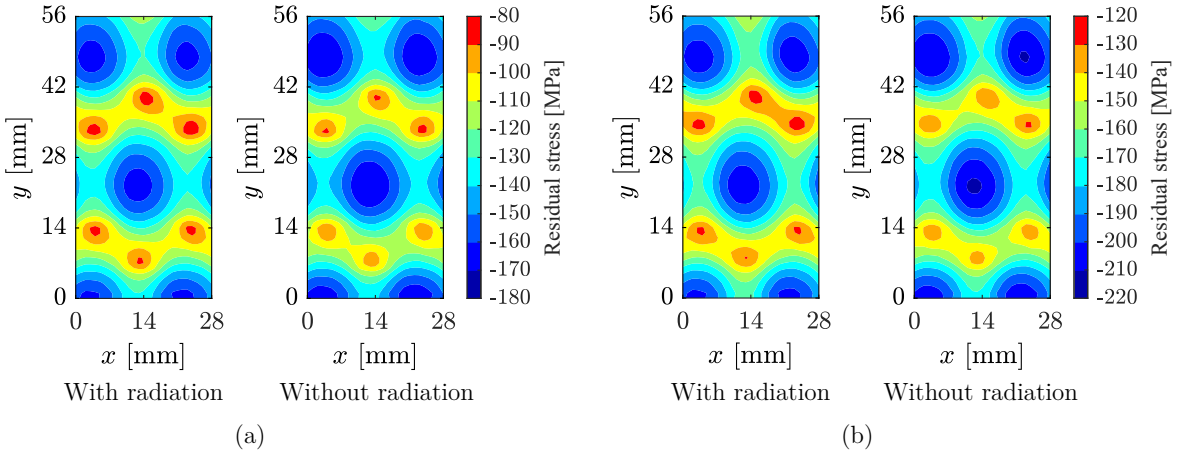

Figure 2.70: Volumetric radiation influence on the estimated surface residual stresses for both analysed jet velocities: (a) $v = 100$ m/s, and (b) $v = 200$ m/s.

The observed large stress variations arose due to the lack of horizontal movement of the plate during the cooling down process [56]. Similarly, higher compressive stresses were observed in the locations where the cooling jets were defined. This fact might be explained by the different thermal gradients developed in the plate. Figure 2.71 provides the temperature difference between the surface and the core of the jet facing area and dry region.

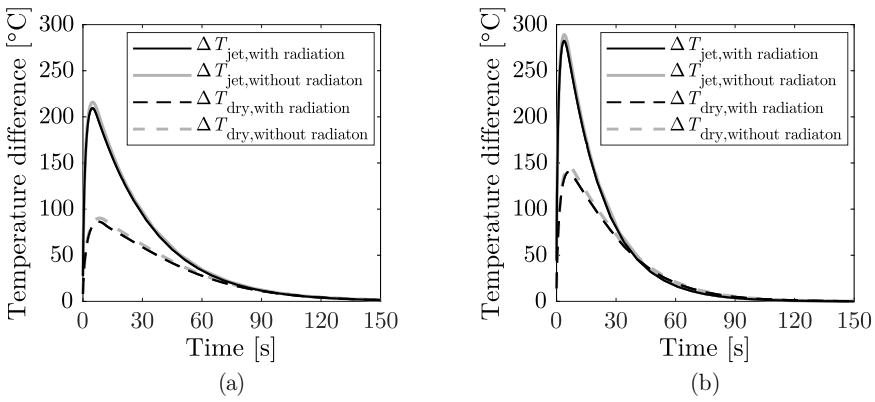

Figure 2.71: Volumetric radiation influence on the temperature difference between the surface and the core of the plate in the jet facing and dry regions for both analysed air velocities: (a) $v = 100$ m/s, and (b) $v = 200$ m/s.

At first instance, the surface cooled more rapidly because of the intense jet flow convection. Nevertheless, the low conductivity of glass hindered a rapid response of the core leading to a large temperature difference at the beginning of the process. The difference increased until a maximum was reached. This maximum point referred to the onset of cooling of the core. A maximum difference of 210 °C was reached in the jet facing area and 85 °C in the dry regions for the 100 m/s air flow, whereas 280 °C and 140 °C were reached for the 200 m/s air flow. As a result, heat extraction was significantly larger in the stagnation area of the jet than in the outer regions, which gave rise to the development of hot spots in the areas between jets, the so-called dry regions. Moreover, at small jet-to-jet distances ($x_{\text{jet}}/D < 4$) and large jet-to-plate lengths ($H/D > 6$), two neighbouring jets may collide turning the flow away from the wall into a 'fountain' shape [100]. The fountain effect reduced the heat transfer rate in this region, fostering the development of dry regions (see Figure 2.72).

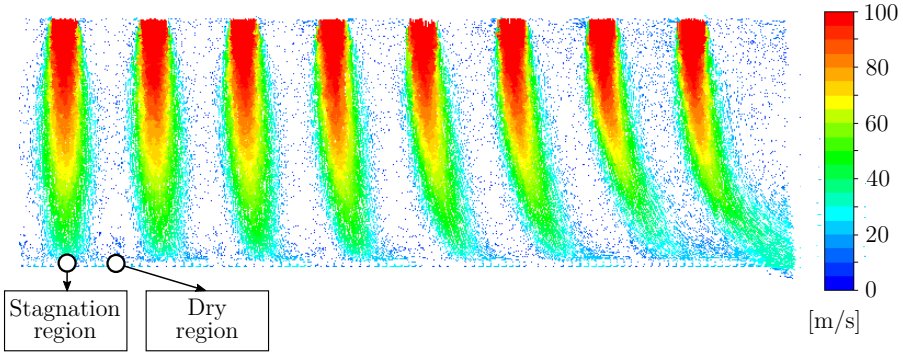

Figure 2.72: Velocity vector contour showing the fountain effect and the defection of flow in the vicinity of the edges along x direction.

The deflection of the outer jets due to the aerodynamic action of the evacuating flow can also be perceived. Similarly, being the jet-to-jet distance larger in y direction, the development of turbulent flow was not hampered by adjacent flow streams. For this reason, larger velocity magnitudes were observed and clearer fountain effects were perceived (see Figure 2.73).

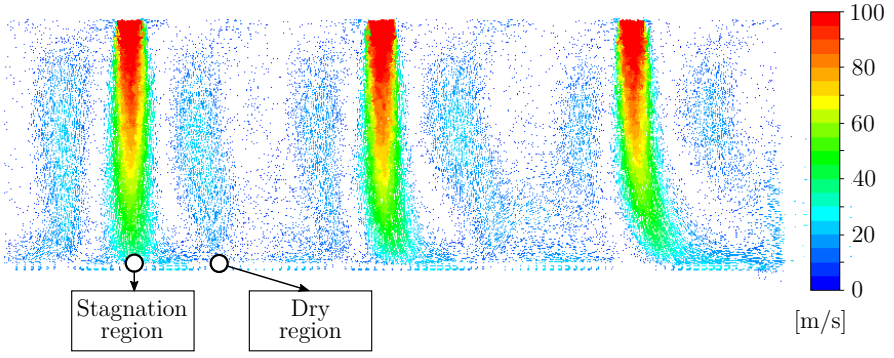

Figure 2.73: Velocity vector contour showing the fountain effect and the defection of flow in the vicinity of the edges along y direction.

These simultaneous phenomena resulted in a non-homogeneous temperature distribution on the surface of the plate, which seemed to be directly related to the non-uniform nature of the residual stress distribution during air jet cooling.

Overall, the influence of volumetric radiation on the final residual stress distribution was low as residual stresses shared a similar pattern (see Figure 2.70). In the case of 100 m/s air flow, the final residual stress magnitudes differed up to 3% in the jet facing area and 5% in the dry region. Similar to the conclusions drawn in the laboratory case studies, as cooling rate increases, the influence of radiation became smaller as these differences decreased down to 2% and 4% with an air velocity of 200 m/s. Figure 2.74 provides a deeper insight by comparing the effect of radiation on the stress prediction along the x and y directions.

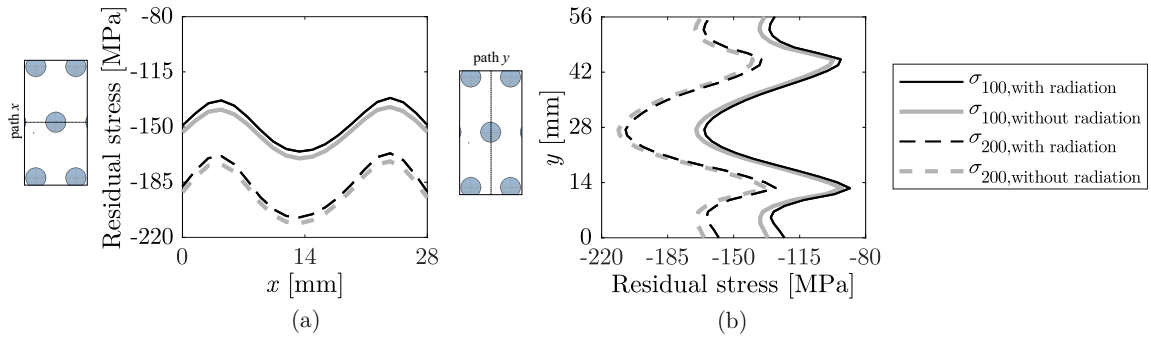

Figure 2.74: Influence of volumetric radiation on the distribution of residual stresses on the surface of the plate when subjected to 100 m/s and 200 m/s air flows. The stress distribution is shown along: (a) path x; (b) path y.

Interestingly, the influence of radiation resulted in a decrease of residual stresses by offsetting its magnitude along the x and y directions. This decrease however, might be considered as negligible as it remained below 5% for both analysed flows. The reason for this may have to do with the short period of time that the components remained at high temperature. The contribution of radiation to the total heat transfer rate showed a maximum of 6% and 4% at the beginning of the cooling process for an air velocity of 100 m/s and 200 m/s, respectively. Additionally, once these maximums were reached, they decreased as temperature did so as seen in Figure 2.75.

Consequently, the higher the air jet velocity, the lower the effect of radiation on the residual stress pattern. In summary, the obtained residual stress distribution considering and without considering radiation showed a huge similarity. The evidence shown here became also reasonable for any plate thickness up to 6 mm. As radiation losses relevance with increasing cooling rate or decreasing thickness, values lower than 6 mm are bound to lead to similar conclusions. For thicker components though, volumetric radiation might play a relevant role in the thermal distribution within the material and a more thorough analysis may be required. Notwithstanding, this was a remarkable outcome regarding the main drawback of the FSI one-way procedure, namely, the computational cost. Taking into account the small differences observed on the final residual stress pattern, radiation can be disregarded when low thickness glass is subjected to large heat extractions, such as during the tempering process.

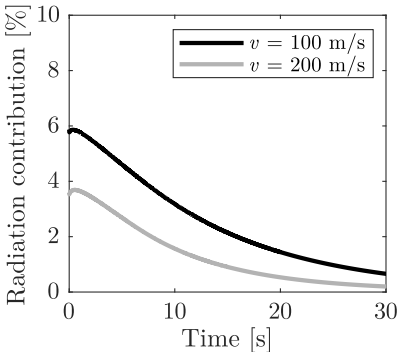

Figure 2.75: Contribution of radiation to the total heat transfer rate during air jet cooling by 100 m/s and 200 m/s.

Critical temperature assessment in industrial case study

With the aim of proving the validity of the critical temperature approach into the industrial case study, once the hottest point of the plate was at 400 °C, different HTC resembling natural and forced convections were defined: 20 W/m^{2}K, 500 W/m^{2}K and 1000 W/m^{2}K. Figure 2.76 depicts the residual stress distribution when the CFD calculation was interrupted at a core temperature of 400 °C and subsequently, different uniform and constant HTC were applied. Similarly, the residual stress distribution obtained by the FSI one-way procedure without considering radiation is presented.

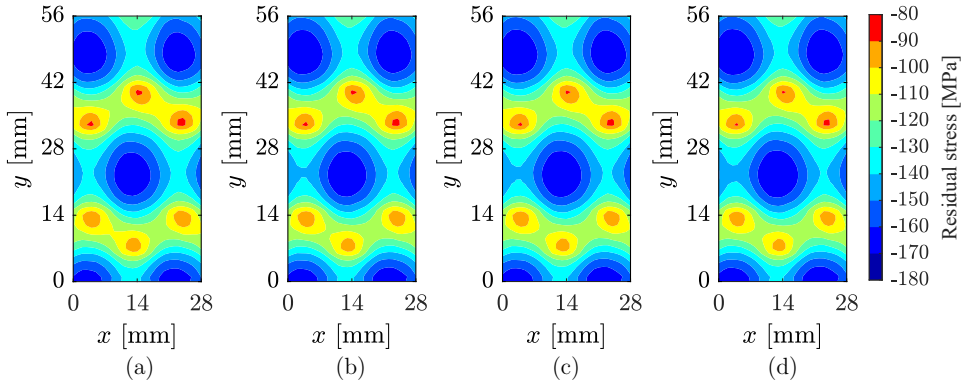

Figure 2.76: Estimated surface residual stress pattern for a 100 m/s air flow based on: (a) the FSI one-way procedure without considering radiation, and (b)-(d) the proposed procedure based on CFD analysis until a critical temperature of 400 °C is achieved, followed then by a thermo-mechanical calculation considering different HTC values: (b) 20 W/m^{2}K; (c) 500 W/m^{2}K; (d) 1000 W/m^{2}K.

Despite the HTC variation from 20 to 1000 W/m^{2}K, the obtained final residual stress distribution did not vary with respect to the reference case as the maximum difference remained below 2%. The most interesting aspect of these results was that the same residual stress magnitude and distribution was obtained even if each case showed a different thermal history and residual stress variation over time. This is observed in Figure 2.77, where the first 150 s of the cooling process are shown.

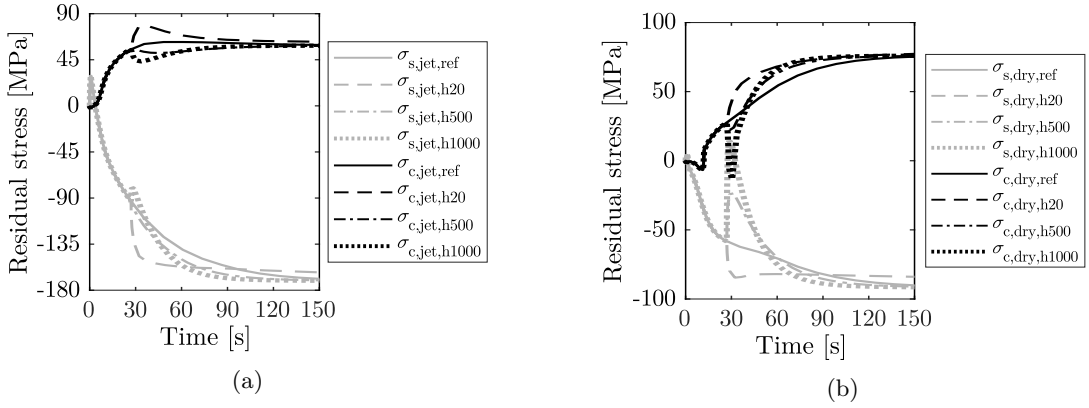

Figure 2.77: Variation of residual stresses over time on the surface and the core of the plate in the: (a) jet facing area; and (b) dry region. Results are shown for a 100 m/s air flow and the calculation is based on the proposed procedure, which relied on different HTC values: 20 W/m^{2}K, 500 W/m^{2}K, and 1000 W/m^{2}K.

Once the critical temperature at 400 °C was reached, the contribution of volumetric expansion phenomenon to the residual stress development diminished as presented in Figure 2.4. Thus, permanent residual stresses were already developed and the subsequent cooling technique was no longer influential on them. In this way, the existence of the critical temperature in complex tempering cofigurations was also confirmed, as residual stress deviations below 2% were noticed. Regarding the case of 200 m/s air flow, the same conclusions were drawn.

As previously mentioned in Section 2.5.2, the confirmation of the low influence of volumetric radiation and the existence of a critical temperature brought about a total decline of around 87% of the computational time in respect to the initially proposed procedure.

Spatially non-uniform steady HTC in industrial case study

Ultimately, the consideration of time-constant but spatially different HTC distributions to calculate residual stresses in an industrial tempering unit was analysed. This approximation could replace the transient flow calculation and its associated larger computational cost.

Figure 2.78 highlights the variation of the HTC distribution over time for a 100 m/s air flow until the maximum temperature of the plate was below 400 °C. At this instant, the critical time was reached, being in this case $t_{cri} = 25$ s. In this way, the variation of transient and steady HTCs over time in the control points P_{jet} and P_{dry}, which are illustrated in Figure 2.68, were monitored.

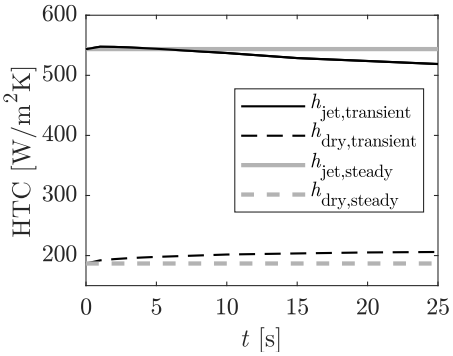

Figure 2.78: HTC magnitude as a function of time in the jet facing and dry regions considering transient and steady HTC.

The HTC magnitude in the stagnation point tended to decrease as time went by, whereas the one in the dry region increased as compared to a steady HTC distribution. With the aim of discussing this fact, the time-constant and transient HTC distributions on the representative analysed area were compared. For the transient calculation, the HTC distribution referring to the critical time instant was adopted. Figure 2.79 shows the transient and steady HTC distributions on the quenched plate and the deviation between both approaches.

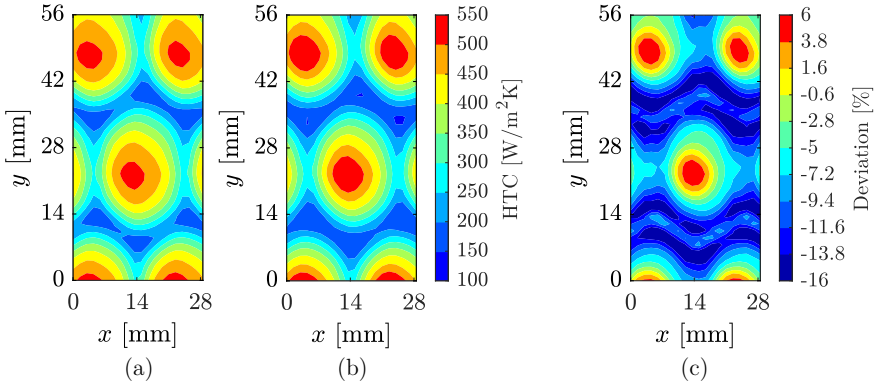

Figure 2.79: HTC distribution at t_{cri} instant ($t = 25s$): (a) transient HTC, (b) steady HTC, and (c) deviation.

When a spatially different and time-constant HTC distribution was adopted, differences up to 16% in the dry regions were appreciated. Contrarily, differences up to 6% in the stagnation areas were observed. With regard to residual stresses, Figure 2.80 presents the final residual stress results in the area of interest.

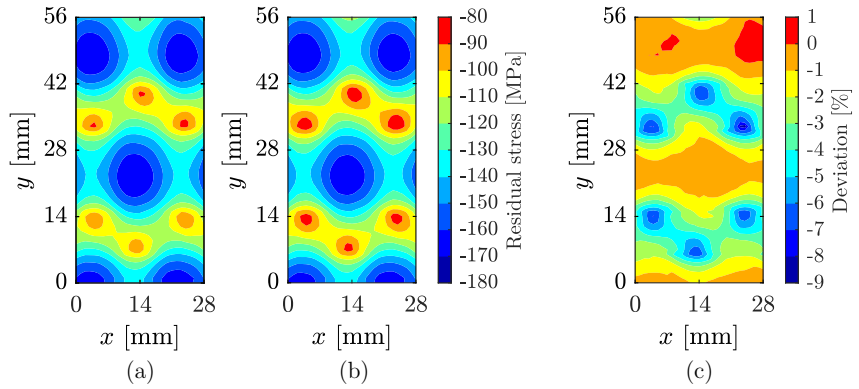

Figure 2.80: Final residual stress distribution on the surface: (a) based on transient HTC, (b) based on steady HTC, and (c) deviation.

Differences up to 1% in the stagnation area and up to 9% in the dry region were found. Similar to the HTC distribution analysis, larger variations were observed in the dry regions. Thus, the residual stress behaviour concurred with the one shown by the HTC.

Furthermore, widening the current analysis to a 1/8 of the geometry, a deeper insight into the obtained results was given. In this case, a 1/8 representation of the model enabled the view of the edges of the plate, making it easier to notice the main differences between these two analysed approaches. Figure 2.81 includes the contour plots of the HTC on a 1/8 of the geometry at t_{cri} instant. In the same manner, the deviation contour plot is shown.

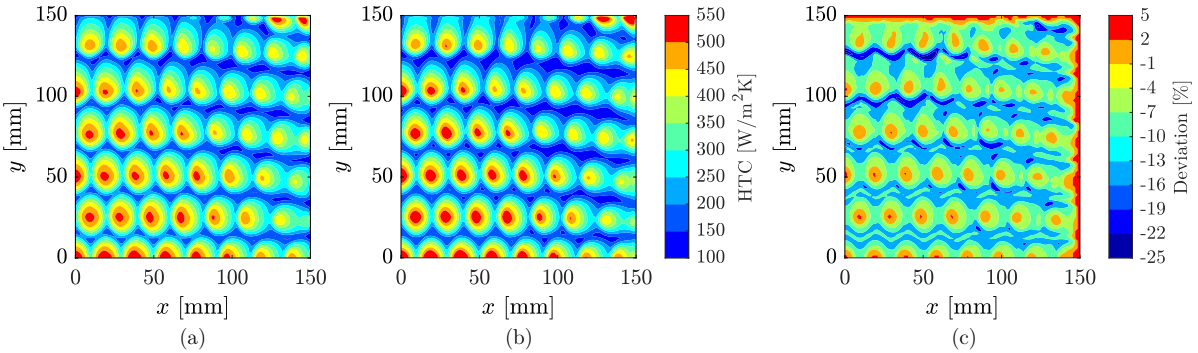

Figure 2.81: HTC distribution on the surface at t_{cri} instant ($t = 25s$): (a) transient HTC, (b) steady HTC, and (c) deviation.

HTC deviations up to 25% were observed in the dry regions while lower deviations up to 6% were observed in stagnation points. In addition, crossflow effects were appreciated close to the flow evacuation areas. This phenomenon distorted the jet pattern on the glass surface and tended to increase the deviations towards the edges of the plate. With regard to residual stresses, Figure 2.82 depicts the final residual stress pattern on the 1/8 representation of the model considering steady HTC, transient HTC and the residual stress deviation between both approaches.

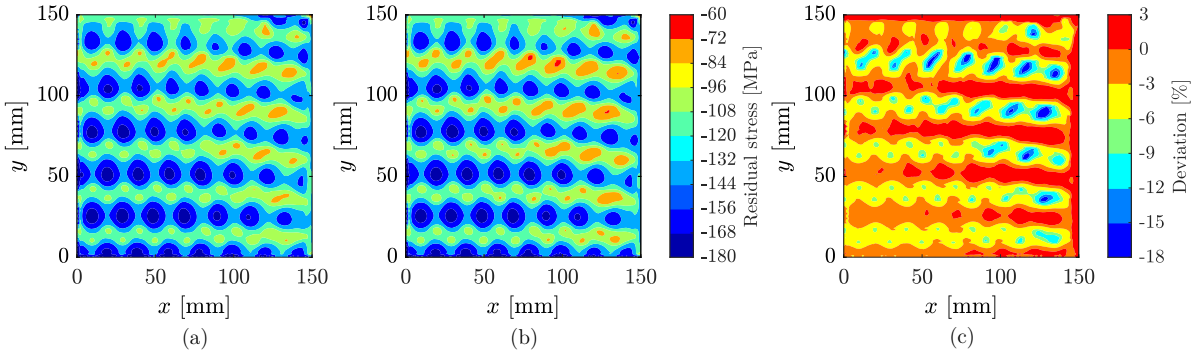

Figure 2.82: Final residual stress distribution on the surface: (a) based on transient HTC, (b) based on steady HTC, and (c) deviation.

Deviations in residual stresses up to 3% and 17% were perceived in the jet facing and dry regions, respectively. Thus, as in the above-mentioned HTC analysis, higher deviations were observed in the dry regions. Correspondingly, differences tended to increase towards the edges of the plate due to the effect of crossflow.

The results in this section indicate that both approaches showed low differences in the stagnation points of the nozzle array. However, higher differences in the HTC and residual stress patterns were observed in the dry regions. Thus, even if the air speed through the perforated metal sheet was constant, due to the large temperature drop of the plate during the tempering process, a variation of the temperature difference between the target surface and the impinging air over time also occurred. Consequently, the thermophysical properties of air also varied having a direct impact on the interacting jet flow regime and the resultant convective HTC.

In summary, an efficient modified procedure to model low thickness quenching processes was proposed. The procedure encompasses both, a CFD model without volumetric radiation to capture the transient local flow phenomena until the critical temperature is attained, and a thermal model where a constant in time and spatially uniform HTC is applied.

2.6.4 Validation of the industrial case study

This section moves on to validate the proposed modified numerical methodology applied in an industrial case study. Nonetheless, no initial temperature specification was made on the experimental work from the literature. The initial quenching temperature was shown to have a large influence on residual stress development (see Section 2.5.4). In this regard, a sensitivity analysis varying the initial temperature from 600 to 650 °C was performed.

Turning now to the experimental measurements, Chen et al. measured the final residual stress distributions by SCALP [56]. Because of this reason, the performed validation made reference to the final residual stress distribution developed on the glass surface. Figure 2.83 sets out the experimental measurements and predicted residual stress distribution for varying initial temperatures along the x and y axes for a jet velocity of 100 m/s and 200 m/s.

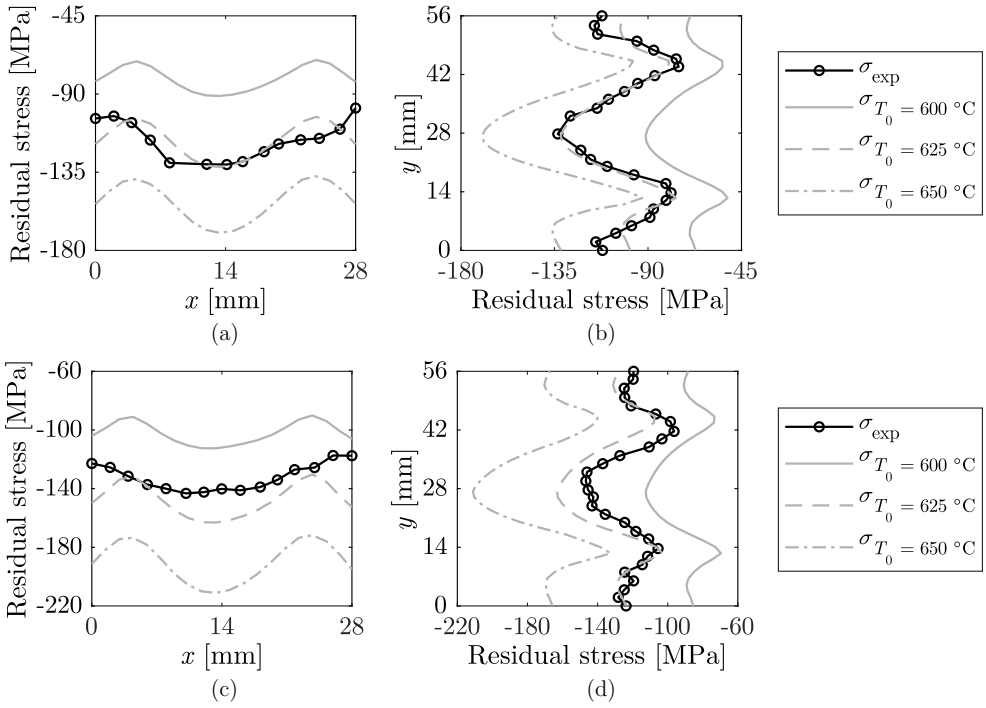

Figure 2.83: Distribution of residual stresses against experimental data for different glass initial temperatures: 600 °C, 625 °C and 650 °C, along: (a) path x with $v = 100$ m/s air flow; (b) path y with $v = 100$ m/s air flow; (c) path x with $v = 200$ m/s air flow; (d) path y with $v = 200$ m/s air flow.

Both, the numerical results and the experimental measurements shared the same trend, as it was able to capture the peaks and troughs caused by the jet pattern in both directions. The difference between the stress amplitudes obtained in the x and y directions may arise from the non-homogeneous heat transfer that occurred on the surface as a result of the defined jet-to-jet distances. The defined jet pitch in x direction made the jet flows to overlap, whereas the larger pitch in the y direction brought about a lower heat extraction between jets, causing the already mentioned dry regions. As a result, the large difference in cooling rate between the jet facing and dry regions led to a large variation in the developed residual stresses between these areas. In both analysed jet velocity cases, the initial temperature of 625 °C seemed to be in better agreement with the experimental results. Not surprisingly, this magnitude is considered a common initial temperature value within the glass tempering process [18, 22, 89].

The results in this chapter indicate that the proposed modified methodology based on FSI was appropriate to represent the residual stress distributions in laboratory case studies as well as in an industrial case study.

2.7 Conclusions

A new numerical methodology to calculate residual stresses in glass plates subjected to non-uniform cooling during the tempering process was presented and validated in single and multiple jet configurations. The significant conclusions are:

- A generalised FSI numerical procedure to predict non-uniform residual stress distributions in glass subjected to single and multiple nozzle or jet arrays was successfully implemented and validated with laboratory experimental measurements and data from the literature. The results showed that local flow phenomena during heat treatment process played a vital role in the residual stress development in glass plates.

- With the aim of seeking a commitment between accuracy and efficiency, different computational cost reduction techniques were assessed. Firstly, the consideration of volumetric radiation tended to homogenise the temperature of the plate, as the temperature difference through the thickness was decreased up to 6% for all the analysed cases. However, no significant differences were observed in the final residual stress pattern nor in their variation over time. The reason for this may have to do with the short period of time that the components remained at high temperature. Additionally, it involved a relatively high computational cost. Hence, volumetric radiation can be disregarded throughout the tempering process. However, a more thorough study needs to be carried out when thicker components or lower heat extractions are considered.

- Secondly, the existence of a critical temperature during the tempering process was confirmed. Once the hottest point of the plate was at 400 °C, the subsequent cooling magnitude and distribution was no longer influential and the residual stress development became cooling rate independent within the range from natural to forced convection cooling. In addition, the cooling stage from the critical to room temperature referred to the longest time period of the tempering process, as cooling rate decreases over time. For this reason, the use of a purely thermal model below the critical temperature was proposed to reduce the high computational cost that the CFD calculation entails. To this end, data was transferred to the thermal model where a spatially homogeneous and constant in time HTC was defined.

- Likewise, the influence of considering steady and transient HTC on the residual stress pattern was analysed. According to the performed single jet tempering tests, differences in terms of HTC up to 10% in the dry region were perceived. Regarding residual stresses though, differences up to 8% and 1% in the stagnation and dry regions were noticed, respectively. The larger differences in terms of HTC observed in the dry region, did not lead to large deviations in residual stresses in the same region. In this case, residual stresses showed larger differences in the stagnation area. These results are likely to be related to the use of a single jet on each side of the plate during tempering, which brought about a characteristic contraction of the plate due to the dissimilar cooling of the dry regions with respect to the stagnation area. Contrary to the single jet configuration, the analysed industrial case study showed deviations in HTC and residual stresses up to 16% and 9%, respectively, in the representative area. As a result, the approach of considering a steady HTC might be a cost-effective solution when crossflow phenomena became negligible. However, differences up to 25% in terms of HTC and 17% in the residual stress magnitudes were observed in the outer area of the plate where crossflow phenomena gained importance. Therefore, the

approximation of steady and constant HTC cannot be directly extended to other quenching case studies as the influence of the flow nature should be first evaluated.

- Based on the conclusions of the computational cost reduction analysis, a modified procedure to model low thickness quenching processes seeking a commitment between accuracy and efficiency was proposed. The modified procedure consisted of a transient CFD simulation without volumetric radiation and a purely thermal model once the part was below the critical temperature. These findings facilitated a decrease of around 87% of the computational time with respect to the initially proposed procedure. In this way, the feasibility and reliability of the proposed modified methodology into industrial environments was verified.
- It can be concluded that residual stress development during tempering is highly sensitive to the definition of process parameters as well as to modelling configurations. Among them, the initial temperature of glass was proved to have a significant impact on the residual stress magnitude as differences up to 30% were observed.
- Finally, the proposed generalised numerical methodology enabled the calculation of non-uniform residual stress distributions. More importantly, it provided an efficient tool for understanding the involved multiphysic phenomena, making it possible to extend its applicability to novel processes such as pulsed jet cooling or interrupt quenching strategies.

Chapter 3

Probabilistic assessment of glass fracture considering residual stresses

3.1 Introduction

The strength of glass is heavily influenced by the presence of micro-cracks on the glass surface and the residual stress state [128]. Several approaches can be found in the literature to determine the influence of surface quality on the strength of glass. On the one hand, certain design guides or standards base their calculations on allowable stresses or safety factors [41, 42]. Nevertheless, the comparison between the calculated design strength and an allowable stress value might not result in accurate predictions, especially if safety applications are of concern. On the other hand, numerical models based on FEM or XFEM to model surface defects become unfeasible if the whole population of microscopic flaws on the glass surface are to be considered. Thus, a probabilistic assessment of glass strength could be considered an appropriate method to account for the randomly distributed microcracks [43]. In this context, the Weibull distribution is reported to be the most widely used statistical approach for representing the fracture strength of brittle materials [44, 45]. Some works however, have performed direct statistical assessment of annealed and tempered glass panes but the results obtained are only representative for the specific geometry or load type analysed in the investigation [11, 46, 47]. Taking into account that large-scale experimental programs are essential for obtaining reliable cumulative distribution functions, this procedure might not be feasible if numerous features are to be investigated [48, 129]. Furthermore, if non-uniform residual stresses are to be considered, the total effort required in the laboratory increases significantly. Lastly, a procedure to design the heat treatment process at an early stage of the production cycle, based on both, the operational load distribution and the failure limit specified by the client, remains a challenge.

In this chapter an alternative, cost-effective method to address both, the residual stress pattern and the statistic nature of glass strength is proposed. The following section provides a brief introduction to

the brittle nature of glass, followed by the most common fracture characterisation techniques. Next, different approaches for modelling glass fracture are reviewed. The proposed methodology and the theoretical and experimental procedures are then detailed. The remainder of the chapter is dedicated to a discussion of the results. Here, the numerical analysis and subsequent statistical assessments of the in-service behaviour of glass are validated against experimental data. Finally, the main conclusions of the investigation are presented.

3.2 Literature review

3.2.1 Glass strength

The strength of glass is limited by stress concentrations around minute cracks inherent to the material [13]. Unlike polycrystalline materials where flaws exist throughout the entire volume of the material, it is commonly known that microcracks exist only on the surface of glass [130]. Consequently, the bending strength of glass may be considerably reduced by surface and edge damage. This phenomenon becomes unimportant in ductile materials as they exhibit plastic behaviour allowing them to deform locally around the flaws. Brittle materials however, are unable to redistribute these stresses, resulting in crack growth and propagation until the fracture of the material. Consequently, a surface flaw acts as a stress multiplier for local tensile stresses.

As flaws are randomly distributed, the failure strength tends to show a large scatter. In addition, different flaw populations might be encountered on the surface or edges of glass, leading to different fracture behaviours [131].

Wang et al. performed mechanical tensile testing on float glass specimens at different temperatures up to 400 °C [132]. As temperature dropped, the switch from the viscoelastic behaviour to the brittle behaviour of glass could be easily appreciated. At high temperatures, viscoelastic behaviour gained importance and the scattering remained low. When temperature decreased, the behaviour was dictated by the presence of surface flaws and the dispersion between measured values became wider. This phenomenon could also be perceived in several experimental works, where the ultimate strength of annealed and heat treated samples was studied [133–135].

Thereby, the presence of defects on the surface is highly influential in the practical strength of glass, particularly if the part is subjected to tensile loading.

3.2.2 Fracture testing

Taking into account the brittle nature of glass and the influence of surface defects on its strength, special attention should be paid to prevent the development of any surface damage during the fracture characterisation tests. For this reason, with the aim of avoiding clamping systems such as the one employed in the standard tensile strength tests, four point bending tests are generally performed. During four point bending tests, the specimen is located on two supporting rollers, and two bending rollers are the ones in charge to apply the load. As a result, a constant bending moment on the loading area is sought and a uni-axial stress state is obtained. The European Standard EN 1288-3 specifies the procedure for testing samples by four point bending [136].

Additionally, the Coaxial Double Ring (CDR) test enables the achievement of a uniform rotational tensile stress field that is independent of edge effects [137]. For this reason, this test configuration is one of the most widely used approach for characterising the intrinsic fracture behaviour of a material. The CDR test consists on placing the glass plate on a circular reaction ring and applying on its opposite surface a load transmitted through a loading ring, until failure occurs. As a result, a biaxial stress state is achieved.

According to the UNE-EN 1288-1 and UNE-EN 1288-5 standards [138, 139], the maximum radial and tangential stresses attained during the CDR test are equal and can be calculated by:

$$\sigma_{\mathrm{rad}} = \sigma_{\tan} = \frac{3(1+\upsilon)}{2\pi}\left[\ln\frac{r_2}{r_1} + \frac{(1-\upsilon)}{(1+\upsilon)}\cdot\frac{\left(r_2^2 - r_1^2\right)}{2r_{3,\mathrm{m}}^2}\right]\frac{F_{\max}}{e_{\mathrm{g}}^2}, \tag{3.1}$$

where σ_{rad} and $\sigma_{\tan}$ are the radial and tangential stresses, υ is the Poisson's ratio of glass, $F_{\max}$ the maximum experimental force, e_{g} the thickness of the plate, r_1 the radius of the load ring, r_2 the radius of the support ring and $r_{3,\mathrm{m}}$ is the mean radius of the square shape sample given by:

$$r_{3,\mathrm{m}} = \frac{(1+\sqrt{2})}{2}\cdot\frac{L}{2} = 0.6L, \tag{3.2}$$

where L refers to the length of the plate side. Thus, the above Equation 3.1 can be simplified to:

$$\sigma_{\mathrm{rad}} = \sigma_{\tan} = K_2\frac{F}{e_{\mathrm{g}}^2}, \tag{3.3}$$

where K_2 is a constant to calculate the bending strength of glass.

3.2.3 Fracture modelling

Historically, different approaches have been adopted to model the fracture behaviour of glass. First, simplified approaches in design guides can be found. The German Institute of Construction defines specific values of maximum allowable stresses to verify the structural collapse of glass components [42]. In this context, different allowable stresses depending on the heat treating condition of glass are established. Afterwards, based on the most unfavourable conditions, the characteristic values of the actions are estimated and compared to the defined allowable stress values. In the same manner, the European standard prEN 13474 is based on the definition of maximum allowable stress values for annealed and pre-stressed glass based on characteristic values of their bending strength and safety coefficients [41, 140]. Nevertheless, the comparison between the calculated design strength and an allowable stress value might not result in accurate predictions especially if safety applications are of concern. Moreover, the calculation of the strength of glass by European standards has implied a large controversy, as it is carried out differently among the various European member states [141]. The reason for this is not clear but it may have something to do with the uncertainty related to the ultimate strength of glass and its difficulty to establish a direct relationship with the several parameters affecting it.

Generally, crack sizes and orientations abound on the glass surface. As a result, the randomly distributed microcracks result in a high uncertainty and foster the use of a probabilistic assessment. The Weibull distribution is reported to be the most widely used statistical approach for representing the fracture strength of brittle materials. The three-parametric distribution function of Weibull is given in the following expression:

$$P_{\mathrm{f}} = 1 - \exp\left[-\left(\frac{GP - \lambda}{\delta}\right)^{\beta}\right], \tag{3.4}$$

where P_{f} is the probability of failure, GP refers to the reference or generalised parameter, λ is the location parameter, β is the shape parameter and δ is the scale parameter. Additionally, the bi-parametric model has also been widely adopted for brittle materials in the literature [43, 45]. This model defined $\lambda = 0$ by assuming that a failure probability exists for any stress state. In other words, it assumes the existence of an infinite flaw size at which a minute load can lead to failure. Therefore, the bi-parametric model is considered a more conservative model than the three-parametric one, as the latter one assumes a threshold below which failure never occurs [44, 142]. Nonetheless, some works in the literature neglected the existence of this threshold. This assumption may lead to prediction errors as a certain amount of energy is always required to make cracks propagate as evidenced by experimental testing [46, 47]. Additionally, if the fracture behaviour of a material follows a two-parametric Weibull distribution, the three-parametric Weibull parameter estimation will set the location parameter as zero. Consequently, the three-parametric model was considered to be more appropriate.

Based on a specific failure criteria, the distribution function of a reference parameter, such as the flaw size or stress, can be calculated by carrying out a statistical evaluation. In 1980 Beason proposed the failure prediction model based on the Weibull theory for float glass [143]. This model was further improved in 1998, enabling to determine the thickness of glass panes for specific design loads [144]. The American standard ASTM E1300 presents several tables to define the thickness of glass components based on this model [145]. Here, different factors are used to adjust the load resistance of the employed glass type, namely, annealed, heat-strengthened or fully tempered glass. Interestingly, the American standard ASTM E1300, differently from the European standard, present its calculations based on a statistical basis.

More recently, phenomenological models have gained traction. These models describe the fracture behaviour of the material based on empirical observations. As a result, they are not derived from fundamental theory and thus, it does not shed light upon the particular mechanisms involved in the fracture process. In the contrary, it permits to consider all the variables influencing on the entire flaw population and it becomes an accurate and cost-effective method for encompassing the statistic nature of glass. Up to this point, limitations were encountered in terms of the size effect and the consideration of local value distributions in workpieces. The size effect had to be considered when extrapolating the results from the experimental specimens to real components with different dimensions. Furthermore, the Weibull model assumes a uni-axial and uniform stress acting on the component, whereas, generally, non-uniform loading cases are encountered in real structural components. The Structural Integrity research group of the University of Oviedo has been working in introducing the concept of equivalent size. More specifically, in 2014 Przybilla proposed an enhanced calculation of the equivalent area [131]. In this way, transferability from the laboratory samples to real components was enabled. Based on this approach, Muñiz-Calvente et al. proposed a Generalised Local Model (GLM) to account also for the local values in parts during loading situations [48, 129]. This work established the concept of Primary

Failure Cumulative Distribution Function (PFCDF). As a result, the complete transferability from a laboratory characterisation to the practical design of components was achieved. Different failure criteria based on the choice of the generalised parameter (GP) could also be taken into consideration. Consequently, the calculation of the PFCDF permitted to characterise the failure behaviour of a component and to facilitate the design and recognition of critical regions in parts subjected to specific loading conditions [146]. Similarly, the authors performed additional studies focusing on the joint evaluation of different tests to increase the reliability of the statistical evaluation [142]. Based on diverse data from different annealed glass samples and tests types, the evaluation of a master PFCDF was carried out and the robustness of the method was confirmed.

Another common approach to study the structural integrity of glass components refers to fracture mechanics. As glass exhibits a liner-elastic behaviour, the Linear Elastic Fracture Mechanics (LEFM) approach has been commonly adopted. Spontaneous breakage of glass occurs when local stress concentrations around flaws lead to a critical combination resulting in the onset of fracture. LEFM tends to calculate the amount of energy needed for a crack to grow and propagate. In this context, Irwin identified the so-called Stress Intensity Factor (SIF), K, to characterise the brittleness or fracture toughness of the material [49]. This physical parameter depends on the applied load, flaw size and specimen geometry and describes the stress and displacement fields around a crack. Different K values are observed for each fracture mode, namely, K_{I}, K_{II} and K_{III}. Figure 3.1 illustrates the three basic modes of crack displacement.

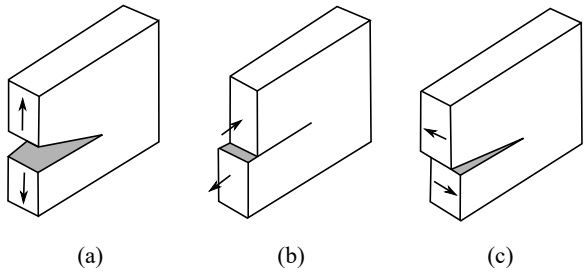

Figure 3.1: Different modes of fracture: (a) opening or mode I, (b) sliding or mode II, and (c) tearing or mode III, adapted from [50].

Mode I corresponds to normal separation of the crack walls under the action of tensile stresses, mode II to longitudinal shearing of the crack walls and mode III to lateral shearing. Of the three modes, the first is the most relevant crack propagation mode in brittle solids [147]. For this reason, the consideration of the fracture toughness in mode I, $K_{\mathrm{I,c}}$, has been a common approach to analyse the fracture behaviour of components. Beyond this threshold, spontaneous fracture of the material occurred. Nonetheless, several failure criteria in mixing mode, that is, considering normal and shearing loads, are well established in the literature [148].

As a result, the influence of cracks under certain load conditions can be investigated by the use of analytical procedures [149, 150]. Lately however, their application to complex problems has been outdated by numerical methods [51]. In this regard, the stress and strain state around the crack front are calculated by means of FEM. A crack though, imply a change in the nominal geometry of the material. Therefore, the finite element mesh needs to be continuously adapting to the crack front and complex meshing techniques are required. Additionally, as the shape functions employed are generally

low-order polynomials, very refined meshes are needed to obtain reliable stress and strain fields around the crack tip. Another option to numerically model cracks is the XFEM. The main advantage of XFEM is that the finite element mesh becomes independent from the crack geometry and advancing front, and the need of remeshing is avoided. Even though, a high discretisation degree is needed in order to accurately represent the stress and displacement distributions around the crack. Pietras et al. performed a numerical analysis in ABAQUS FEA to analyse the strength of a flawed tempered glass [52]. The authors made use of the XFEM to calculate the SIFs. They performed the heat transfer calculation assuming an initial temperature of 670 °C and a constant heat transfer coefficient of 200 W/m^2K for the main surfaces and 100 W/m^2K for the edges. Considering a bending case study, the authors concluded that the defined flaw reduced the load capacity by 32.1%. Nevertheless, this approach required the physical modelling of cracks on the surface. Because of this reason, it becomes unfeasible to discretise the whole population of microcracks on the glass surface by XFEM or FEM. As an alternative, Kinsella et al. presented a numerical method based on Monte Carlo simulation to consider random flaw distributions on the surface of annealed glass, in terms of location, orientation, and size [151]. Even though, when pre-stressed glass has been investigated, the compressive residual stress pattern is usually assumed to be constant and uniform [152, 153]. Nonetheless, the non-uniform temperature distributions developed during the standard cooling process of glass usually lead to stress inhomogeneities on the surface [56].

Another common approach to assess the strength of heat treated glass implies the sum of the compressive prestress magnitude and the lower limit values of the statistical distribution of annealed glass. In this case, the 5% quantile of the distribution is usually considered. Nevertheless, Pisano et al. and Bonati et al, highlighted the fact that the sum of the characteristic bending strength of annealed and heat treated glass was not an appropriate approximation [45, 154]. They argued for the unlikelihood for both material strengths to simultaneously attain their lower values at a given point. Consequently, this approach becomes conservative, as the sum of both characteristic strengths is generally lower than the ones experimentally observed. This fact emphasises the need for a statistical analysis to evaluate the strength of heat treated glass. For this reason, an efficient numerical–statistical model to assess the fracture of glass accounting for residual stresses becomes essential.

Many works performed direct statistical assessment of specimens, and hence, the obtained data only allow reliable prediction of the specific case studied, for instance, specimens exhibiting the same size, shape and being subjected to the same tested loading configuration [11, 45, 47]. In this context, the GLM entailed a valuable contribution as the concept of PFCDF was introduced. Hence, the next section is concerned with the fundamental theory in which the GLM is grounded.

3.2.4 Generalised Local Model (GLM)

Throughout this section, the fundamental theory of the GLM proposed by Muñiz-Calvente et al. is described [48, 155]. The omnipresent statistical scatter of glass strength makes statistical evaluation necessary to analyse its fracture behaviour. For this reason, a brief overview of the weakest link principle and the Weibull model is first carried out, and then, the GLM is described. Finally, the joint assessment procedure is also explained.

Weakest link principle

Fracture of brittle materials mainly occurs due to the pre-existing flaws on its surface. The larger the surface subjected to tensile stresses, the larger the probability of finding a crack to initiate its propagation. The weakest link principle is usually applied to consider this size effect. Based on this theory, the structural component is discretised into smaller elements, that is, individual links, and the survival probability of each of them is calculated. As a result, the weakest link principle establishes that the global survival probability of a component can be calculated as the product of the survival probabilities of each element:

$$P_{\mathrm{s,global}} = \prod_{i=1}^{n} P_{\mathrm{s,link},i}, \tag{3.5}$$

where $P_{\mathrm{s,global}}$ is the survival probability of a component, n refers to the total number of elements and $P_{\mathrm{s,link},i}$ is the survival probability of each element i. Consequently, the global failure probability, $P_{\mathrm{f,global}}$, might be found by:

$$P_{\mathrm{f,global}} = 1 - P_{\mathrm{s,global}}. \tag{3.6}$$

Thus, the failure of one of the discrete elements implies the failure of the complete workpiece.

Weibull model

It is of common practice to consider the Weibull distribution function to statistically analyse the strength of glass based on a certain failure criterion. The obtained cumulative distribution function relates the probability of failure and the selected critical value of the GP. The three-parametric Weibull distribution is given by Equation 3.4. As previously presented, λ is the location parameter, β is the shape parameter and δ is the scale parameter. The shape factor β is related to the scatter. As the sample size reduces, a larger scatter might be observed as the breakage of the component is governed by the largest defect on the surface. As a result, larger variations might be observed when small components are analysed as the location of the largest flaw size is limited into a specific sample. The scale factor δ is related to the specimen size. With regard to the the location parameter λ, it defines the threshold below which failure never occurs. This means that λ is related to the maximum size of the whole crack population on the surface.

Fundamentals of the GLM formulation

The aim of the GLM is to obtain the PFCDF as a material property on the basis of the Experimental Failure Cumulative Distribution Function (EFCDF). The PFCDF permits the transferability of the results from one model to another irrespective of the experimental features employed, namely, load type and the shape and size of the specimens.

To this end, the GLM consists of an iterative process through which the Weibull parameters are fitted within a three-parametric cumulative function. The model is grounded in the three-parametric

Weibull distribution presented in Equation 3.4 and aims to predict the probability of failure, P_{f}. The Weibull distribution characterises the failure of the material considering the area is subjected to a uniform load. However, usual loading configurations show complex non-uniform distributions along parts. As a result, the three-parametric Weibull distribution for calculating the local probability of failure considering an equivalent size, is defined by the following expression:

$$P_{\mathrm{f},S_{\mathrm{eq}}} = 1 - \exp\left[-\frac{S_{\mathrm{eq}}}{S_{\mathrm{ref}}}\left(\frac{GP-\lambda}{\delta}\right)^{\beta}\right]. \tag{3.7}$$

The model is defined by a generalised parameter, GP, which characterises the failure behaviour of the component, uniformly acting on a reference size, S_{ref}. The equivalent size, S_{eq}, refers to the length, area or volume of a sample that subjected to the maximum value of GP, exhibits the same failure probability as compared to the one obtained at the real component subjected to the real GP distribution. In this way, the complex non-uniform distribution along parts can be considered. In addition, it enables the transferability of the results to any other specimen size. Figure 3.2 sets out the real GP distribution on a sample and the constant distribution of the GP on an equivalent size, at which the same probability of failure is attained. It is worth mentioning that the area of both distributions might not coincide one with each other.

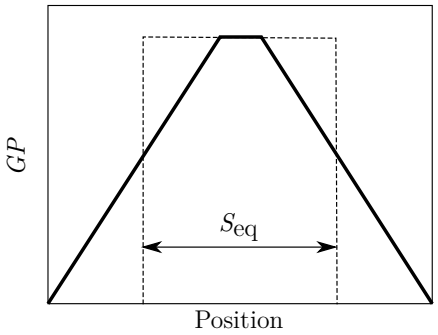

Figure 3.2: Schematic representation of a real GP distribution (bold line) along a real component and the GP distribution on an equivalent size (dashed line) leading to the same probability of failure. Adapted from [155].

The iterative process consisted of different steps. Hereafter, the formulation for fitting the Weibull parameters is delineated.

Firstly, experimental tests for analysing specific sample features were performed. Secondly, a numerical model to reproduce the experimental tests is required. With the aim of performing a reliable statistical fitting, not only the maximum strength value must be known, but also its distribution on the area of analysis. To this end, a FEM based analysis became essential. Once the numerical model was defined, the EFCDF, which relates the probability of failure and the critical value of the generalised parameter, was estimated. This relation is given by a plotting position rule. The critical values of GP_{ij} are sorted in increasing order, where a rank number and a probability of failure are associated to each value [148, 155]. The failure probabilities are assigned by the following equation:

$$P_{\mathrm{f},j} = \frac{K_j - 0.3}{j + 0.4}, \tag{3.8}$$

where K_j ($K_j = 1...j$) refers to the rank order and j the total number of tests per analysed glass type. Subsequently, the global probability of failure must be calculated. Based on the weakest link theory, the global probability of failure depends on the local failure probabilities of the component. Therefore, the global probability of survival refers to the multiplication of the survival probabilities of each link. Considering each link as a finite element, the relation between the local survival probability and the local failure probability is described by:

$$P_{\mathrm{s},S_{\mathrm{eq}},i} = 1 - P_{\mathrm{f},S_{\mathrm{eq}},i}. \tag{3.9}$$

Consequently, the global failure probability $P_{\mathrm{f,global},j}$ of each sample may be found by the combination of the probability of failure of each element:

$$P_{\mathrm{f,global},j} = 1 - \prod_{i=1}^{i_{\mathrm{total}}} (1 - P_{\mathrm{f},S_{\mathrm{eq},i}}) = 1 - \prod_{i=1}^{i_{\mathrm{total}}} \left(\exp \left[-\frac{S_{\mathrm{eq},i}}{S_{\mathrm{ref}}} \left(\frac{GP_{ij} - \lambda}{\delta} \right)^{\beta} \right] \right), \tag{3.10}$$

where $P_{\mathrm{f},S_{\mathrm{eq},i}}$ is the local probability of failure for the element i, $S_{\mathrm{eq},i}$ is the equivalent size of the element and GP_{ij} is the local value of the generalised parameter at the element i of each tested sample. Similarly, the equivalent size of each specimen, $S_{\mathrm{eq},j}$, might be found by:

$$S_{\mathrm{eq},j} = -\log(1 - P_{\mathrm{f,global},j}) S_{\mathrm{ref}} \left(\frac{\delta}{GP_{\mathrm{max},j} - \lambda} \right)^{\beta}. \tag{3.11}$$

Once the equivalent size is calculated, the Weibull parameters are fitted. To this end, the equation of the probability of failure is linearised in the form of $y = Ax + B$, where:

$$y = \log(GP_{\mathrm{max},j} - \lambda), \tag{3.12}$$

$$x = \log(-\log(1 - P_{\mathrm{f,global},j})) \frac{S_{\mathrm{ref}}}{S_{\mathrm{eq},j}}, \tag{3.13}$$

$$A = \frac{1}{\beta}, \tag{3.14}$$

$$B = \log(\delta). \tag{3.15}$$

Finally, the relative difference of the values obtained at the previous iteration (I – 1) with respect to the actual iteration I is calculated by:

$$\frac{|\lambda_I - \lambda_{I-1}|}{\lambda_I} + \frac{|\beta_I - \beta_{I-1}|}{\beta_I} + \frac{|\delta_I - \delta_{I-1}|}{\delta_I} < \varepsilon_{\mathrm{I}}. \tag{3.16}$$

When the iterative relative difference is below $\varepsilon_{\mathrm{I}} < 10^{-9}$ convergence is attained. If not, the iterative process continues and the actual values are transferred to the calculation of the global probability, thus updating the equivalent size calculation and the respective Weibull parameters. In this way, the Weibull parameters of the PFCDF are obtained. As a result, the PFCDF behaves as a material property and it becomes size and shape independent.

The joint test method

The number of specimens tested have a direct impact on the subsequent statistical assessment. Generally, experimental programs are not as large as they should mainly because of lacking resources or time constraints. Likewise, experimental studies usually comprise different parameters of interest making it even more complex to thoroughly analyse each and everyone of them. Owning to these reasons, a joint evaluation of the performed experimental tests becomes a remarkable option to overcome these limitations [142].

The fundamental formulation for the joint evaluation followed a similar trend that the one of the GLM, but slight changes were introduced [155]. Regarding the EFCDF estimation, the local values of the maximum GP of each test type to be merged were already known. Nevertheless, as the maximum GP obtained at each test type may be related to a specific sample size or loading configuration, the initial ranking of all the critical GP values cannot be directly carried out. The reason for this is related to the scale effect. In this context, the probability of failure of a large load referred to a small area might be higher or smaller than a smaller load referred to a large area. For this reason, firstly, the calculation of the global probability of failure of each specimen is addressed by the following expression:

$$P_{\mathrm{f,global},j} = 1 - \prod \left(1 - P_{\mathrm{f},S_{\mathrm{eq},ij}}\right) = 1 - \prod \left(\exp \left[-\frac{S_{\mathrm{eq},ij}}{S_{\mathrm{ref}}} \left(\frac{GP_{ij} - \lambda}{\delta} \right)^{\beta} \right] \right). \tag{3.17}$$

Then, being the reference size related to the scale parameter, δ, the next equation permits the calculation of the equivalent scale parameter, δ_{eq}, for each critical GP value of each sample, $GP_{\mathrm{max},j}$:

$$\delta_{\mathrm{eq},j} = \frac{GP_{\mathrm{max},j} - \lambda}{[-\log(1 - P_{\mathrm{f,global},j})]^{(1/\beta)}}. \tag{3.18}$$

The equivalent scale parameter enables the calculation of the equivalent size. In this way, the conversion of the cumulative damage functions to an equivalent size specimen is performed by the following formulation:

$$S_{\mathrm{eq},j} = \frac{S_{\mathrm{ref}}}{(\delta_{\mathrm{eq},j}/\delta)^{\beta}}. \tag{3.19}$$

As a result, an equivalent size for each sample can be estimated. Once the equivalent size is known, the Weibull parameters are fitted by linear regression following the aforementioned procedure. Lastly, the relative difference between the derived Weibull parameters and the ones obtained at the previous iteration are calculated to check convergence.

3.3 Numerical-probabilistic method to assess glass failure considering residual stresses

The following numerical-probabilistic procedure is grounded on the Generalised Local Model (GLM) presented by Muñiz-Calvente et al. [48, 155]. The GLM accounts for the local values in a workpiece during loading situations. Moreover, the concept of PFCDF enables the complete transferability from a laboratory specimen characterisation to the practical design of components. The model was successfully validated based on annealed glass samples subjected to bending loads. Nevertheless, when structural applications are required, glass is most often heat treated with the view to developing a compressive residual stress layer on the surface. The obtained residual stress pattern hampers crack propagation on the surface, increasing the resistance of glass when subjected to tensile loading. As a result, residual stresses need to be accounted when estimating the failure probability of heat treated glass. With this in mind, the procedure presented in this chapter consists of the following steps:

1. **Non-uniform residual stress prediction:** the residual stress domain after the heat treatment process is predicted by a sequentially coupled FSI approach.
2. **Obtention of the PFCDF:** the final residual stress pattern developed in the heat treatment process is mapped into a structural FEM model. Similarly, an experimental program is carried out to characterise the failure of the material. In this way, the local values of the reference parameter in the specimen at the experimentally determined fracture loads are numerically calculated. The obtained local data is subsequently employed to derive the Primary Failure Cumulative Damage Function by the Generalised Local Model. The PFCDF is based on a three-parameter Weibull function, where the Weibull parameters are iteratively determined. The derived PFCDF permits the evaluation of the probability of failure, being independent from the specimen size, shape and load used in the experimental characterisation.

Figure 3.3 presents the schematic overview of the proposed numerical-statistical procedure for predicting the probability of failure of structural glass components considering the non-uniform residual stress distribution.

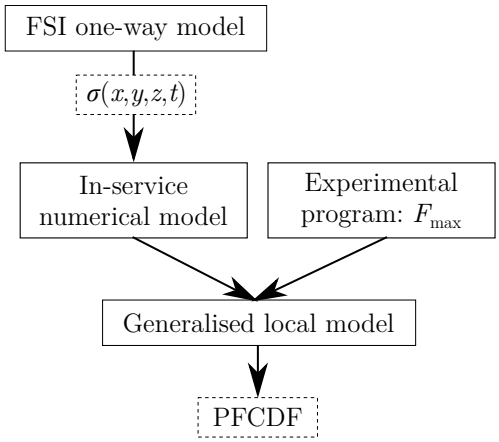

Figure 3.3: Flow chart of the proposed numerical-statistical procedure to predict the probability of failure of pre-stressed structural glass components.

Firstly, following the modelling procedure proposed in Chapter 2, a one-way coupling FSI model consisting of a CFD model and a FEM model was defined to calculate the residual stress distribution after the heat treatment process. The obtained residual stress pattern was mapped into the in-service numerical model, where the local values of the reference parameter, e.g. maximum principal stress, were obtained. At this point, the GLM was used to derive the so-called PFCDF [48]. The aim is not to pinpoint the specific mechanism that contributes to fracture, but to consider all the variables influencing on the entire flaw population. As a result, the PFCDF statistically characterises the material failure based on the three-parametric Weibull model, being size and shape independent with respect to the employed testing sample. Consequently, it makes the transferability of the results from the performed experimental work to the practical design feasible. Finally, glass plates exhibiting different residual stress patterns were used to validate the obtained PFCDF. Therefore, the proposed numerical-statistical procedure becomes an efficient 3D method for predicting the failure probability of glass components, being independent from the inherent residual stress spatial distribution.

Hereafter, the main aspects of the proposed method are delineated.

3.3.1 Case studies

The samples used in this thesis referred to soda-lime square flat plates with a dimension of 90 x 90 x 4 mm. Different glass types were investigated: annealed glass (AA), symmetrically tempered glass (ST) and asymmetrically tempered glass (AT). Figure 3.4 illustrates the asymmetrical tempering glass unit, whereas Figure 2.10 in Chapter 2 depicts the one of symmetrically tempered glass.

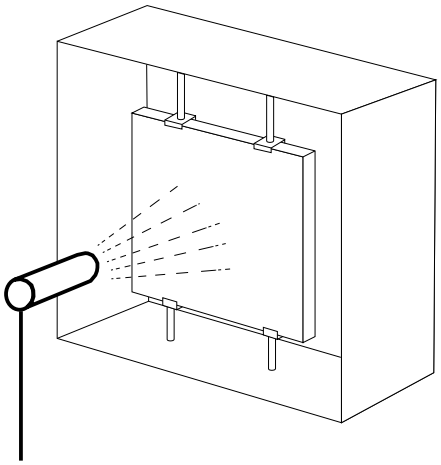

Figure 3.4: Cooling down unit of asymmetrically tempered glass plates.

As aforementioned in Section 2.4.3 of Chapter 2, symmetrical tempering tests with the aim of obtaining samples resembling the conventional residual stress pattern were carried out. Conversely, the asymmetric tempering configuration intended to offer a characteristic case of the tempering process, in which heat extraction by forced convection only occurred from one side of the plate. As a result, an asymmetric residual stress pattern was obtained. The standard tempering process tends to show slight asymmetric residual stress distributions due to the influence of rollers. Even though, differences tends to be small and residual stresses are often considered as symmetrical [156]. Consequently, the asymmetric cooling configuration enabled to consider an extreme case to validate the proposed method.

A radiation furnace NABERTHERM LH60/14 was preheated to 650 °C and after holding each sample for 10 minutes, specimens were transferred to the tempering unit, where jets with an inlet diameter of $D = 3$ mm were used. Similarly, two jet-to-plate distances at $H/D = 20$ and $H/D = 40$ for each tempering configuration were defined.

The brittle nature of glass makes the experimental strength characterisation a cumbersome process due to the exhibited large scatter of the results. With the aim of having a representative amount of samples according to the UNE-EN 1288-1 and UNE-EN 1288-5 standards, a total number of 30 samples were defined for each glass type. Table 3.1 summarises the analysed configurations as well as the corresponding number of samples.

Table 3.1: Overview of the proposed experimental program.

Glass type	H [mm]	H/D	Samples
AA	-	-	30
ST	60	20	30
ST	120	40	30
AT	60	20	30
AT	120	40	30

An important factor to consider during the characterisation of glass strength is the crack orientation on the surface. The number of orientations though, abounds and the testing of an infinite number of samples becomes unfeasible. The use of coaxial double rings enable to assume an equal probability of failure no matter of the orientation of the prevailing crack. For this reason, the mechanical characterisation throughout this thesis consisted on CDR tests at room temperature.

For this purpose, the guidelines stated in the UNE-EN 1288-5 standard were followed [139]. A R30 ring configuration was used; the diameter of the load and support rings was 12 mm and 60 mm, respectively, and the curvature radius of both rings in the contact area referred to 2.5 mm.

3.3.2 Theoretical procedure

Residual stress prediction

A one-way coupling FSI model was defined with the view to calculating the non-uniform residual stress distribution after the heat treatment process. The model intends to capture the non-uniform temperature pattern of cooling techniques and its influence on residual stress development by considering the interaction between the fluidic, thermal and mechanical fields. A detailed description of the model is given in Chapter 2.

In-service numerical model

A numerical model based on the FEM was built to consider the local GP distribution in the part. In other words, the defined numerical model must reliably predict the stress distribution on the part at the breakage load to subsequently feed the GLM and predict the probability of failure.

For this purpose, the commercial software ABAQUS FEA was used. It consisted of the load ring, support ring, the silicon rubber and the glass specimen as shown in Figure 3.5. The support ring was made out of steel and hence, it was considered a rigid body. The load ring was made out of aluminium and it was considered as deformable, as well as the silicon rubber and the glass plate. Table 3.2 sums up the material properties defined for each part based on literature [148].

Table 3.2: General properties of glass, aluminium and silicon rubber at room temperature.

	Soda-lime glass	Aluminium 6000 series	Silicon rubber
Young Modulus [MPa]	70000	70000	20
Poisson coefficient	0.23	0.33	0.47
Density [kg/m^3]	2470	2700	950

Two static general steps were defined. The first referred to an approximation step until the load ring was put in contact with the sample, and the second one, a loading step until the maximum experimental fracture load was attained.

With regard to the interaction between parts, a surface-to-surface contact based on finite sliding formulation was defined between the load ring and the glass plate. The normal behaviour was based on a hard contact configuration without allowing separation after contact, whereas the tangential behaviour was based on the Penalty method assuming a friction coefficient of 0.6 [157, 158]. The contact between the glass plate and the silicon rubber, as well as, the rubber with the support ring were described by a tie constraint. By this constraint, the selected surfaces were assumed to be bonded and the stability of the numerical calculation was ensured.

As for the boundary conditions, the support ring was assumed to be fixed. Once the load ring interacted with the glass plate, a negative displacement based on the experimental tests in z direction was imposed. Likewise, rotations were not hampered but displacements in x and y directions in the central point of the glass plate were impeded until the loading step was initiated. Owning to the small size of the specimens, the bending action due to its own weight was neglected.

A total number of 54077 elements were defined, from which 48600 were associated to the glass specimen. Regarding the element type, quadratic full-integration hexahedral elements were selected. Six elements through the plate thickness were defined (Figure 3.5).

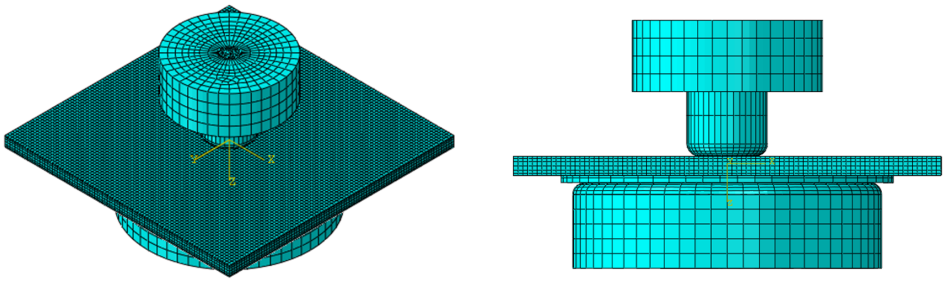

Figure 3.5: Mesh of the in-service model composed of the load ring, support ring, the silicon rubber and the glass specimen.

Finally, the final residual stress pattern obtained during the heat treatment calculation was mapped as an initial condition into the in-service model. In this way, the local values of the generalised parameter, e.g. maximum principal stress, when the part was subjected to the loading configuration were obtained.

Generalised local model (GLM)

Here, the implemented statistical approach based on the GLM proposed by Muñiz-Calvente et al. is detailed [48, 155]. The aim of the GLM is to derive a PFCDF, which permits the transferability of the results from one model to another irrespective of the experimental features employed.

To this aim, the local stress distribution and the element size of the investigated glass conditions were numerically determined. Then, the numerical data was transferred to the GLM, where a reference size of 1 mm^2 was considered. The transferability of the results depends on the appropriate selection of the failure criterion of the component, which is based on the definition of the generalised parameter. Based on the obtained experimental data, it is not obvious which stress or stress combination should be taken as a reference to derive the PFCDF. For this reason, two different criteria, namely, the maximum principal stress, $\sigma_{\max}$, and the Principle of Independent Action (PIA) were analysed [155]:

$$GP = \sigma_{\mathrm{I}} = \sigma_{\max}, \tag{3.20}$$

$$GP = (\sigma_{\mathrm{I}}^{m} + \sigma_{\mathrm{II}}^{m} + \sigma_{\mathrm{III}}^{m})^{(1/m)}. \tag{3.21}$$

Based on literature, a value of $m = 3$ for the PIA criterion is recommended [142]. The maximum principal stress criterion assumes that the material fails when the uniaxial tensile strength of the material is reached. Conversely, the PIA criterion is based on an equivalent stress that accounts for the principal stresses in the three principal directions. In this way, the biaxial loading on the glass surface is considered. As the structural failure of glass commonly stems from the presence of tensile stresses, only the tensile mode of failure are considered, ignoring the influence of compressive stresses. Similarly, the failure mode of the material must be preserved. In this case, breakage is assumed to occur due to same representative defect, more precisely, the largest crack on the surface. As a result, the PFCDF for each glass type could be obtained.

The GLM consists of an iterative process where the Weibull parameters are fitted into the three-parametric Weibull distribution presented in Equation 3.4. In this context, Figure 3.6 shows the flowchart of the iterative process for fitting the three-parametric Weibull distribution.

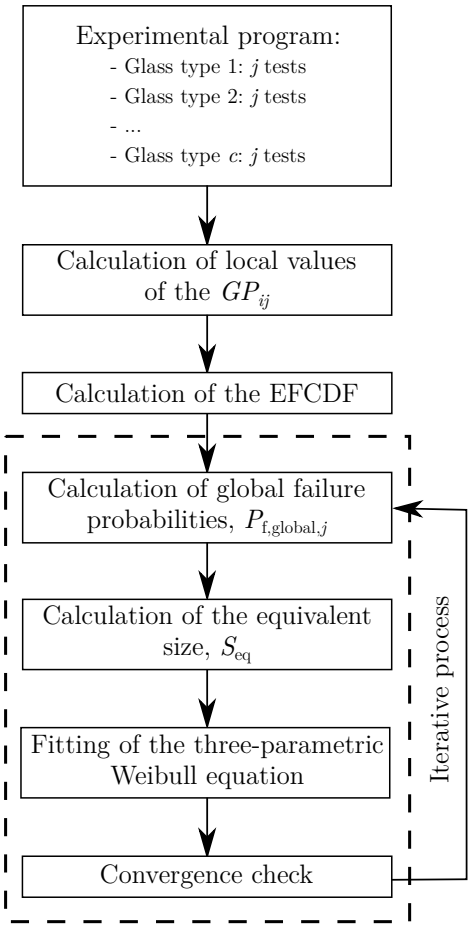

Figure 3.6: Flowchart of the calculation sequence to fit the three-parametric Weibull distribution.

Each step is briefly summarised in the following lines:

1. **Experimental program:** the first step consists on performing j experimental fracture tests for c experimental conditions where specific sample features are analysed. In this investigation, samples of equal size but different residual stress pattern were subjected to the same load conditions. In this way, the fracture loads of the analysed glass types each of them composed by 30 samples were recorded.

2. **Calculation of local values:** the load data obtained during the experimental fracture tests was used to numerically calculate the local distribution of the generalised parameter. Throughout this thesis, the maximum principal stress or an equivalent magnitude in accordance with the PIA criterion was defined as the generalised parameter. In this way, the GP_{ij} distribution on the component at the fracture instant was calculated, where i refers to each element of the numerical model and j to a particular experimental test. Likewise the element size of the defined grid was obtained.

3. **Experimental Failure Cumulative Distribution Function (EFCDF):** the EFCDF represents the relationship between the probability of failure and the critical value of the generalised parameter, namely, the value of GP_{ij} at the instant when each experimental sample collapses. It depends on the test type, applied load and the shape and size of the specimen.

4. **Calculation of global probabilities of failure:** in this step, the global probability of failure is estimated based on each local failure probability of the component.

5. **Calculation of the equivalent size:** the global failure probability, the equivalent size and the Weibull parameters are initially unknown. With the view to starting the iterative process, some initial assumptions are needed. Firstly, the Weibull distribution function was fitted to the EFCDF to determine the initial values of λ, β and δ. Secondly, arbitrary values for the reference size and equivalent size were chosen. For this purpose, a similar size of the analysed case study for the reference size and 80% of the element size for the equivalent size are recommended.

6. **Fitting the three-parametric Weibull distribution:** in this stage, the Weibull parameters are fitted.

7. **Convergence criterion:** finally, the relative difference between the previous iteration and the actual iteration are calculated. When the difference is considered acceptable, the Weibull parameters of the PFCDF are obtained.

The experimental results might show large scattering due to the randomly distributed cracks on the surface. As a result, the calculation of confidence intervals becomes necessary to assess the reliability of the predictions. In fact, certain standards, such as UNE-EN 1288-1, encourage the use of confidence intervals to better represent the statistical uncertainty involved in these experiments [138]. With this in mind, after deriving the PFCDF, the following steps were followed:

- **Relationship between the GP and the failure probability:** firstly, the relation between the critical values of the GP and the failure probability must be defined. To do so, a non-dimensional GP distribution is calculated by dividing the local GP values with the maximum GP value. Assuming a linear relationship between force and stress, the non-dimensional GP distribution is multiplied by an incremental GP value in order to obtain the local GP values at each incremental load. To begin with, the location parameter is set as the initial incremental value, from which the GP will be increased. Once the GP distribution is known, based on the Weibull parameters of the previously derived PFCDF, the failure probability at the corresponding critical GP value can be achieved. Subsequently, an incremental GP value is added and a new failure probability is estimated until a probability of 0.999 is achieved.

The following Figure 3.7 shows the incremental procedure to be followed.

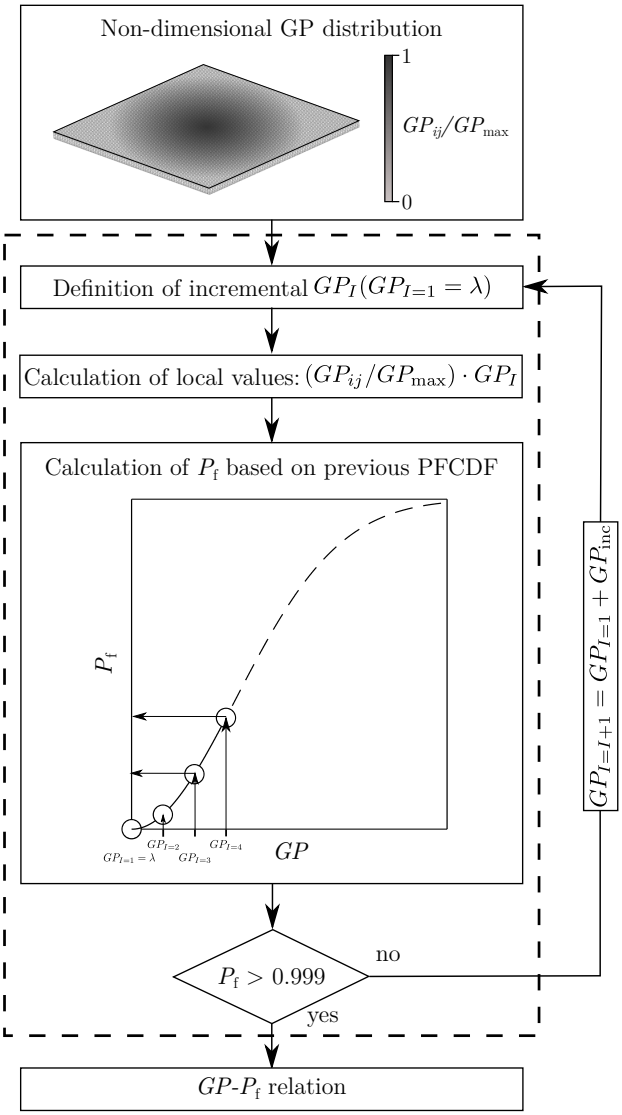

Figure 3.7: Procedure to derive the $GP - P_\mathrm{f}$ relation.

- **Calculation of the PFCDF from simulated experimental program:** here, N fictive PFCDFs that could have been obtained in N experimental programs are calculated. For this purpose, N fictive experimental programs are simulated. Figure 3.8 presents the procedure to estimate the simulated Weibull parameters.

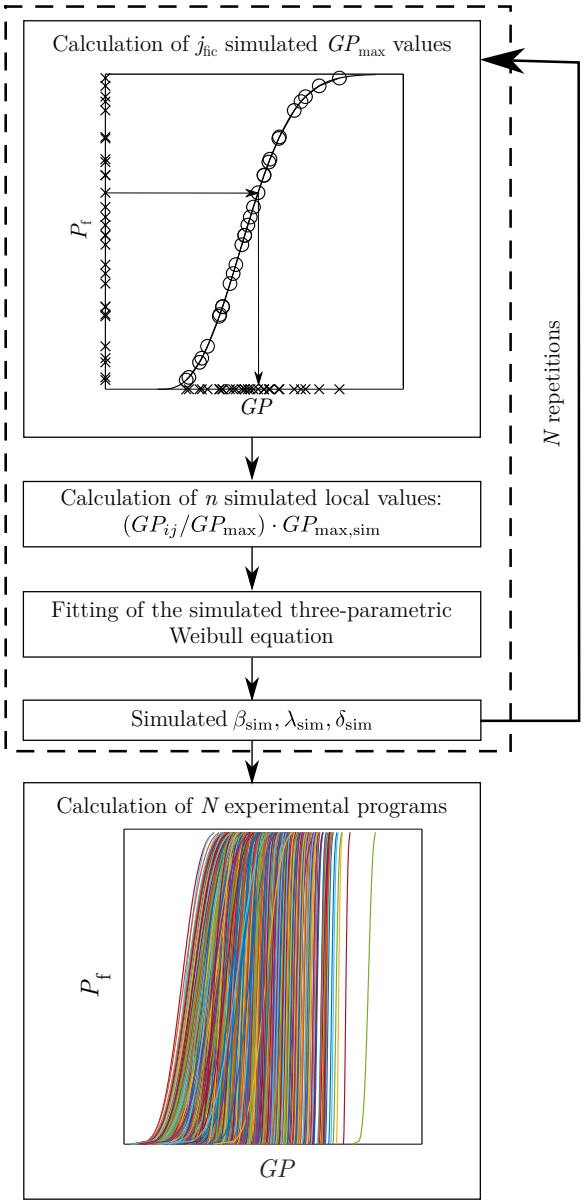

Figure 3.8: Definition of j_{fic} fictive tests to simulate N experimental programs.

After establishing the relation between the GP and failure probability, j_{fic} failure probabilities referring to j_{fic} fictive experimental specimens are defined. In this way, the local values of GP can be obtained by multiplying the maximum GP values by the non-dimensional GP distribution. This results in j_{fic} GP distributions, each referring to a simulated experiment. Lastly, the j_{fic} simulated experimental tests are fitted by the GLM procedure and a new PFCDF is derived. This step is repeated N times, being $N = 1000$ a suitable amount of iterations.

- **Estimating the confidence intervals:** all the PFCDFs are sorted by ascending GP values and the ones corresponding to 5% and 95% of probability are selected. In the case of $N = 1000$, the ones corresponding to 50 and 950 would be selected (see Figure 3.9).

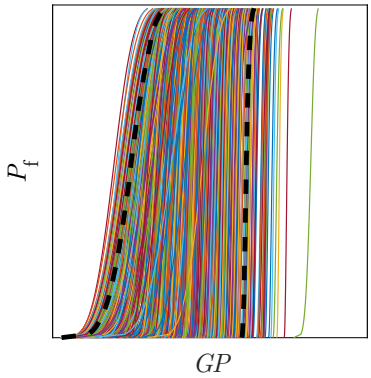

Figure 3.9: 5% and 95% confidence intervals for $N = 1000$ simulated experimental programs.

Ideally, an infinite number of experimental tests would ensure an accurate representation of the PFCDF. Nevertheless, such an effort is not affordable and the confidence intervals allow assessing the reliability of the performed predictions.

Joint method

Based on the GLM, the joint evaluation enables to consider all the experimental case studies as a unique experimental program. As a result, the larger amount of experimental data leads to a more reliable prediction of the probability of fracture. As in the previous single test evaluation, the aim of this evaluation is to derive a PFCDF as material property. Figure 3.10 sets out the flowchart for fitting the three-parametric Weibull distribution based on all the performed experiments.

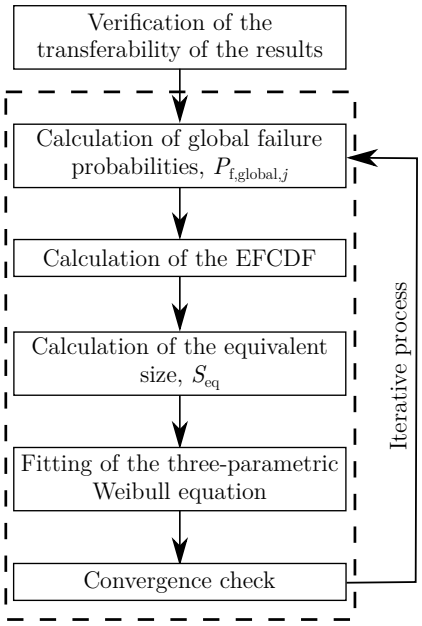

Figure 3.10: Flowchart of the calculation sequence to fit the three-parametric Weibull distribution by the joint test evaluation.

Hereafter, each step is delineated:

1. **Verification of the transferability of the results:** first, the failure criteria and the transferability between the analysed case studies must be checked.
2. **Calculation of the global probabilities of failure:** then, the global probability of failure is calculated. As the joint Weibull parameters in the first iteration are still unknown, the minimum value of λ and the mean values of β and δ of the PFCDFs to be merged are considered. In this way, the global probability of failure for each test at the first iteration was calculated.
3. **Calculation of the EFCDF:** the maximum GP values of each glass type batch are ranked in ascending order and a probability of failure is assigned to each of them using the aforementioned plotting position rule.
4. **Calculation of new equivalent sizes:** an equivalent reference size must be assigned to each GP to carry out the joint assessment. As a result, the GP values of each experimental test are shifted and sorted, giving rise to a unique master curve (see Figure 3.11).

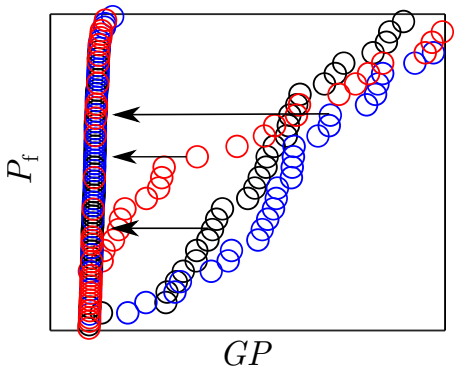

Figure 3.11: Shift of critical GP values to a common cumulative distribution function.

5. **Fitting the three-parametric Weibull parameters:** once the equivalent size is calculated, the Weibull parameters are fitted by linear regression.

6. **Convergence criterion:** if the relative difference is below the defined threshold, the iterative process is brought to an end. If not, the iterative process continues and the actual values are transferred to Step 2. As a result, the Weibull parameters of the joint PFCDF are obtained.

Last but not least, the calculation of confidence intervals aids assessing the reliability of the joint predictions. For this purpose, the aforementioned confidence interval calculation was slightly modified. In the following lines, the step-by-step procedure is explained.

- **Relationship between the GP and the failure probability for each glass type:** firstly, the relation between the GP and the failure probability was defined. In this case, the relationship of each analysed glass type needs to be addressed (see Figure 3.12).

- **Calculation of the PFCDF of j_{fic} simulated experimental tests for each glass type:** afterwards, j_{fic} failure probabilities referring to j_{fic} fictive experimental specimens are randomly estimated. This way, j_{fic} maximum GP values corresponding to each P_{f} and hence, j_{fic} local GP distributions for each analysed glass type are obtained. By the use of the GLM, the Weibull parameters of each glass type are achieved. Until this point, no joint evaluation is performed.

- **Joint evaluation and calculation of the master PFCDF from the simulated experimental program:** here the joint evaluation of all the simulated experimental tests was performed. For example, if the simulated experimental program consisted of 30 experimental tests and five different glass types were considered, 150 simulated tests would be evaluated. As a result, a simulated master PFCDF is obtained.

- **Simulation of N experimental programs:** these steps are iteratively repeated until the desired amount of N experimental programs consisting of c glass types is achieved. This way, N PFCDFs that could have been obtained in N experimental programs were achieved. A summarising scheme of these steps is presented in Figure 3.13.

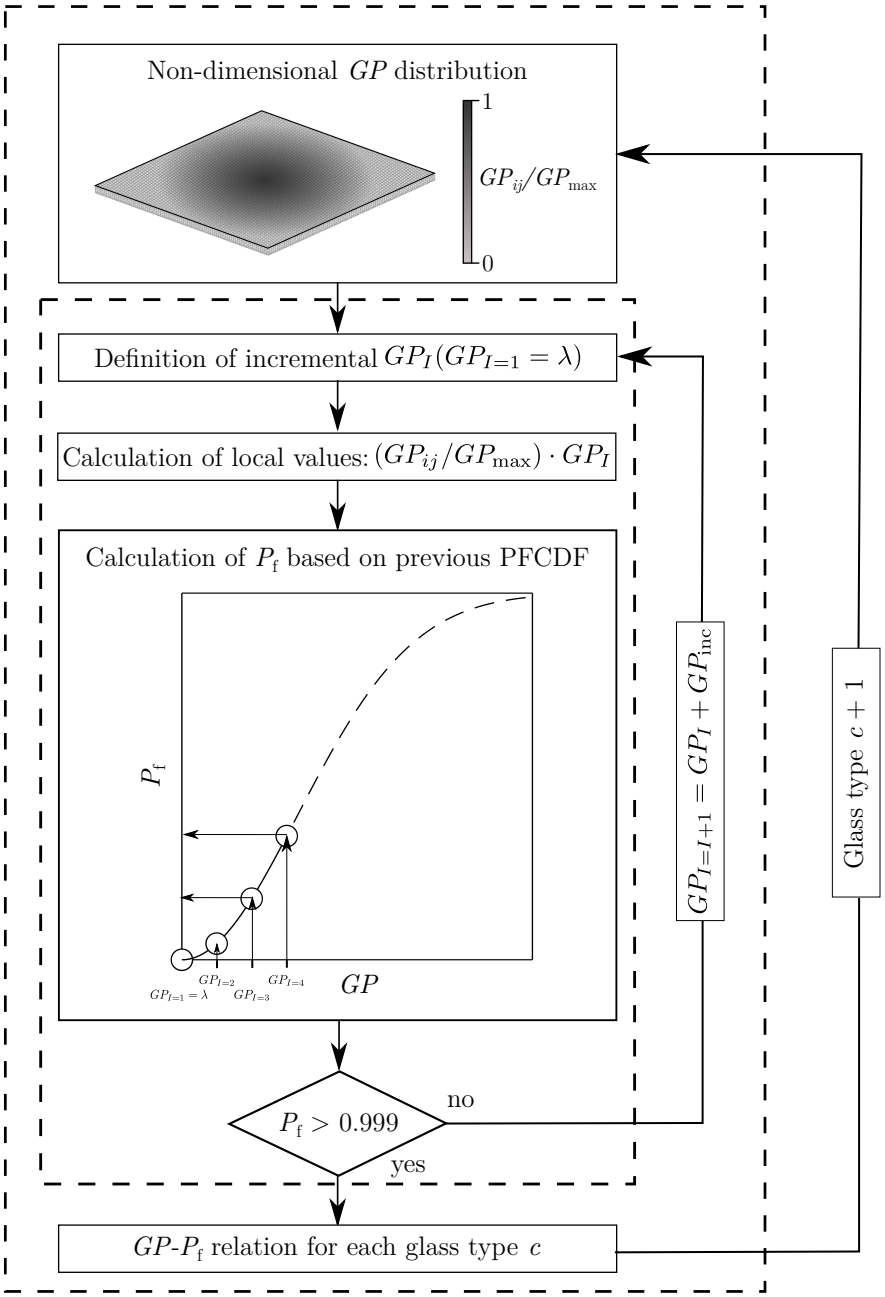

Figure 3.12: Procedure for deriving the $GP - P_\mathrm{f}$ relation for each glass type.

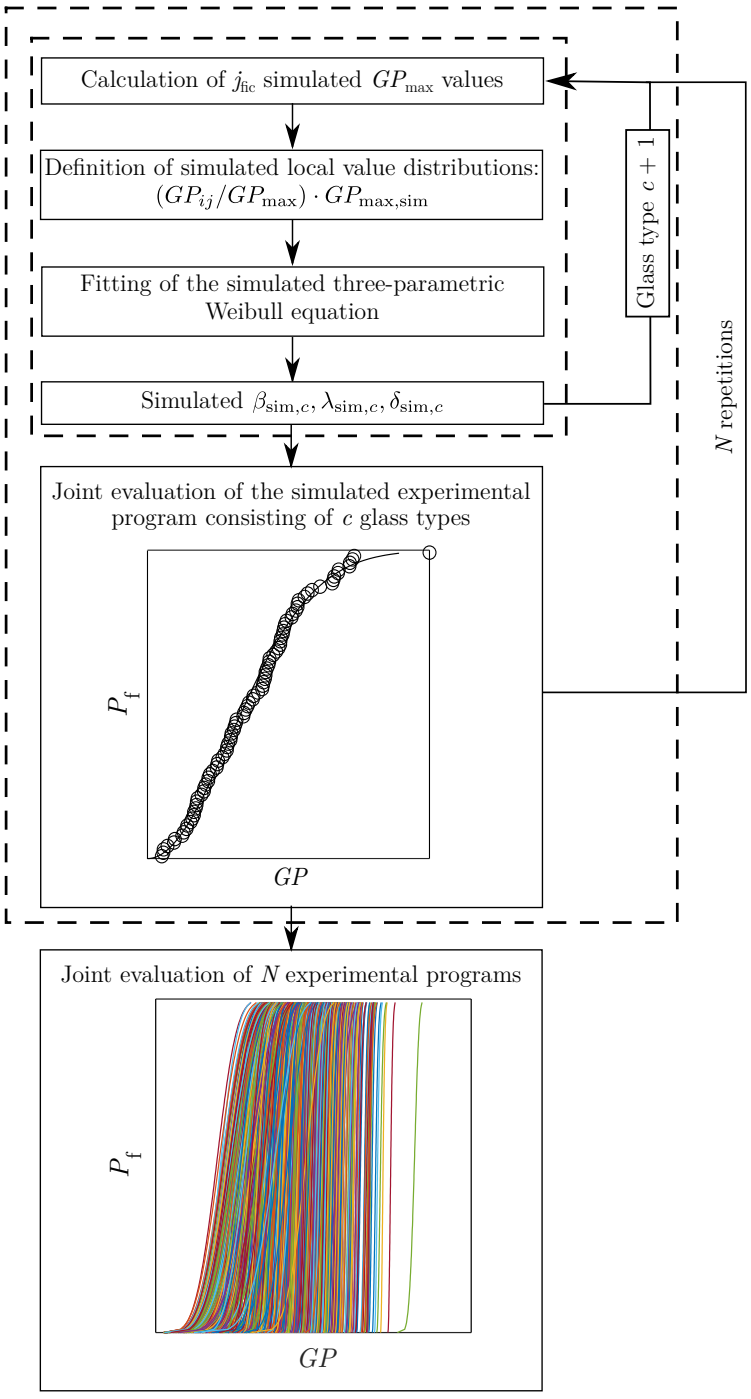

Figure 3.13: Procedure for estimating N joint experimental programs, each consisting of c different glass types and $c \cdot j_{\mathrm{fic}}$ simulated tests.

- **Estimating the confidence intervals:** finally, all the PFCDFs are sorted by ascending GP values and the ones corresponding to 5% and 95% of probability are selected.

  In this case, as a larger amount of experimental points are used to calibrate the master PFCDF, the reliability of the predictions is higher and the confidence intervals will exhibit a narrower band.

3.3.3 Experimental procedure

The experimental procedure consisted of two parts. Firstly, the heat treatment of the samples was carried out and residual stress measurements by means of SCALP were taken. Secondly, bending strength characterisation tests were carried out. In the following lines, the heat treatment and bending test procedures are described.

Heat treated glass samples

As explained in Section 3.3.1, five glass types exhibiting diverse residual stress distributions were analysed: annealed glass (AA), symmetrically tempered plates at $H/D = 20$ (STHD20) and $H/D = 40$ (STHD40), and asymmetrically tempered plates at $H/D = 20$ (ATHD20) and $H/D = 40$ (ATHD40). For this purpose, a radiation furnace NABERTHERM LH60/14 was preheated at 650 °C and glass samples were successively introduced into the furnace. Afterwards, specimens were quenched in the experimental tempering unit. The diameter of the nozzles referred to 3 mm. Finally, residual stress measurements of five heat treated samples by SCALP were performed to ensure the repeatability of the heat treatment process. Here, the experimental procedure delineated in Section 2.4.3 of Chapter 2 was followed.

Coaxial Double Ring (CDR) tests

The UNE-EN 1288-5 standard specifies the procedure and parameters to determine the bending strength of small glass samples by the use of coaxial rings [139]. To this end, a MTS uniaxial testing machine with a 15 kN load cell was employed. Likewise, methacrylate panes were used to ensure the required safety conditions. Figure 3.14 illustrates the defined CDR set-up.

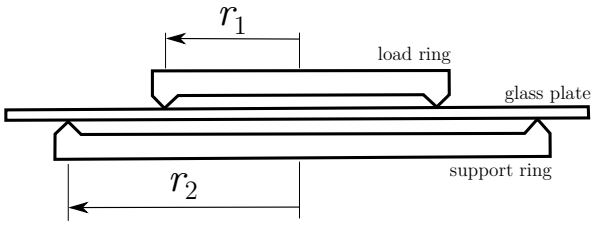

Figure 3.14: CDR set-up consisting of the load and support rings, and the glass plate.

For this purpose, both rings were designed and manufactured in accordance with the specifications given in the UNE-EN 1288-5 standard. Similarly, an additional tool by 3D printing was manufactured to align the samples with respect to the testing machine (see Figure 3.15).

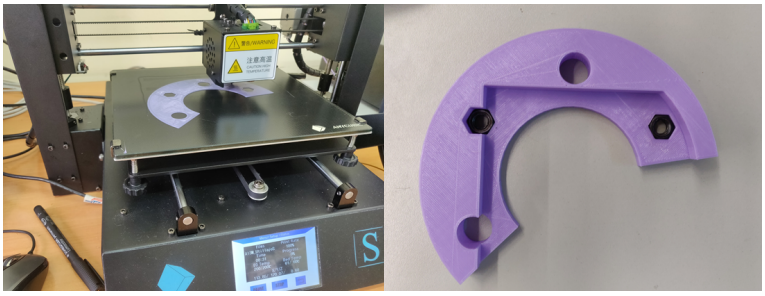

Figure 3.15: Alignment tool manufactured by 3D printing.

A self-adhesive film on the not tested surface was employed as recommended in the UNE-EN 1288-5 standard to ensure that the origin of fracture occurred in the load ring area. In the same manner, a silicon rubber was located between the support ring and the sample. In the case of asymmetrically tempered plates, the downward surface, which would be exposed to tensile stresses during loading, referred to the air-impinged surface, and hence, fracture occurred on this side. A loading rate of 2 MPa/s was defined until the fracture of the specimen occurred (see Figure 3.16).

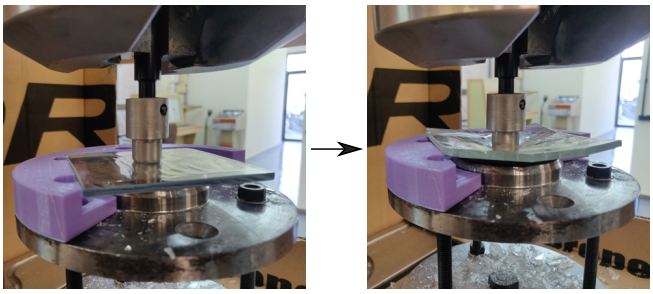

Figure 3.16: Coaxial Double Ring test until fracture of the specimen.

Finally, the vertical displacement field was also investigated by Digital Image Correlation (DIC). Three samples (T1-T3) for each glass type were measured by means of the ARAMIS 3D GOM equipment. An inclined mirror at 45° was used to capture the downside view of the plate and record the displacement field during the tests (see Figure 3.17).

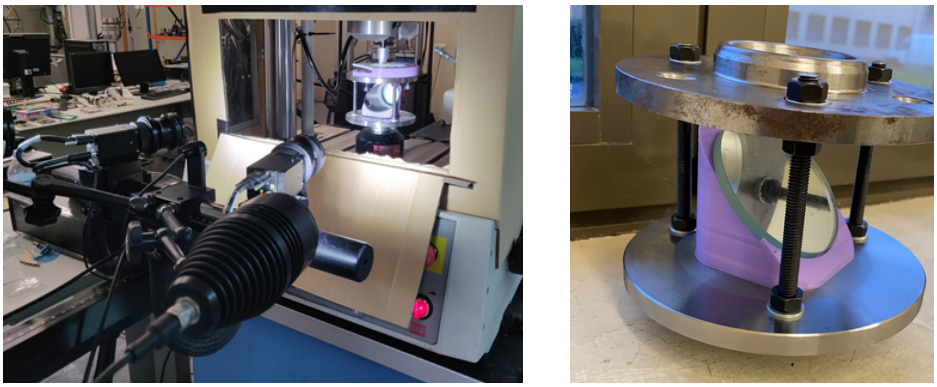

(a) (b)

Figure 3.17: Experimental CDR set-up: (a) ARAMIS 3D GOM equipment, and (b) inclined mirror at 45°.

As a result, the variation of the displacement distribution of each sample during the loading period could be recorded. With the aim of validating the numerical results, an average experimental displacement contour was calculated based on the three samples that were measured for each glass type. Similarly, the vertical displacement distribution along x and y directions was obtained. In this way, a scattering band could be built to compare the numerical calculations to the experimental measurements. Figure 3.18 illustrates the followed post-processing procedure to represent the CDR tests results.

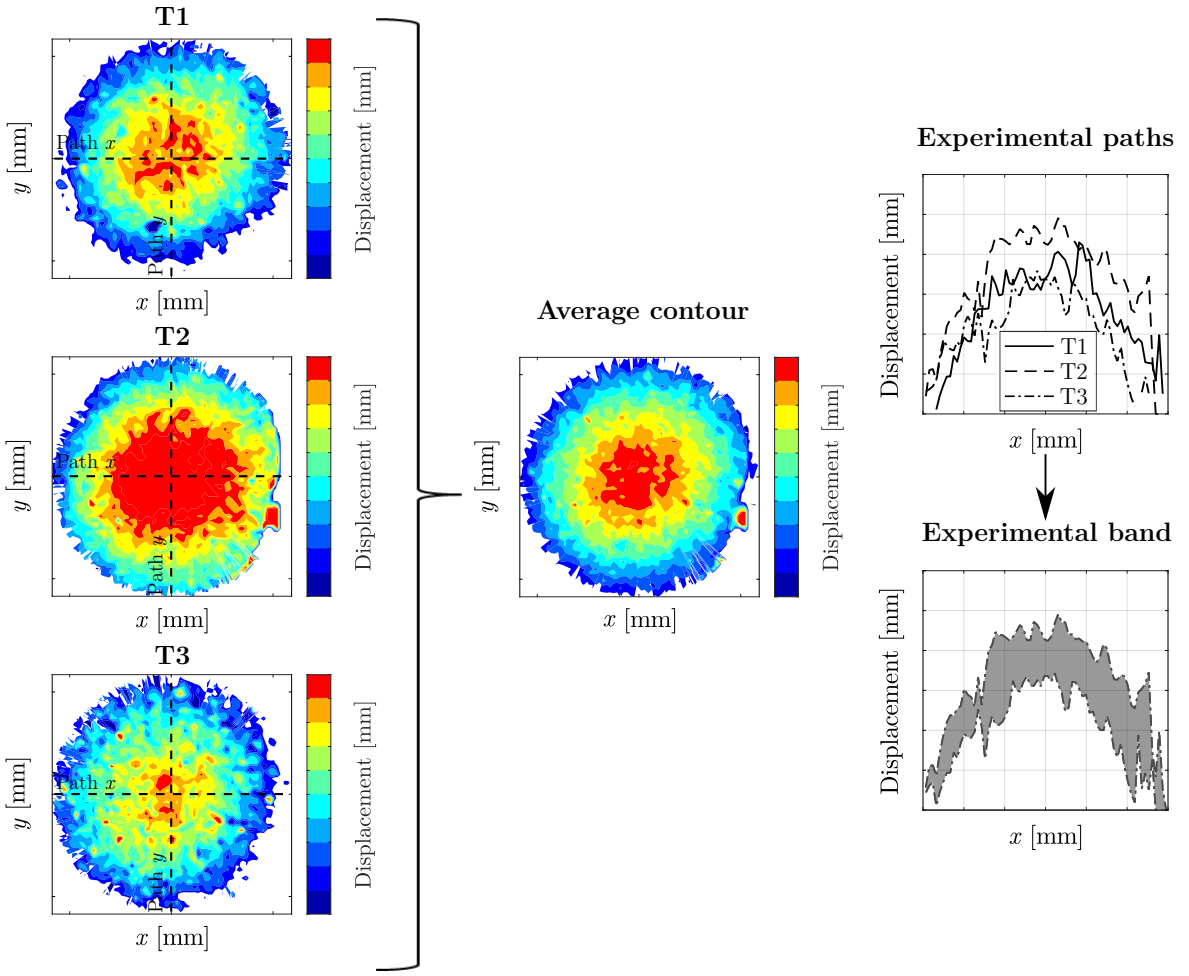

Figure 3.18: Experimental post-processing procedure of the results of the CDR tests.

3.4 Discussion of the results

This section sets out the results of the in-service numerical analysis, the experimental tests and the statistical assessments. Firstly, the numerical model is validated, and the experimental results of the residual stress measurements and the Coaxial Double Ring (CDR) tests are presented. Then, a single test statistical assessment to derive the PFCDF of each glass type is carried out. Two different failure criteria are studied and the failure probabilities of the specimens are predicted, not only based on its own experimental data, but also based on the remaining glass types. In this way, the most suitable failure criterion is selected and the transferability of the results is verified. Finally, a joint assessment of the analysed glass types is performed by merging the data of each glass type as a unique experimental program.

3.4.1 In-service numerical analysis

The Generalised Local Model accounts for the stress distribution of the whole component. For this reason, a numerical model accounting for the residual stress pattern of the glass component was built. In this section, the estimated numerical results are presented. The following analysis was carried out:

- Residual stress distribution of each analysed tempering type was estimated.
- Numerical modelling of the CDR test was done.

Residual stress estimation

The annealed glass specimens were assumed to be stress-free plates during the numerical calculations. With regard to the heat treated plates, the validation of the predicted stress pattern for symmetrically tempered glass was presented in Section 2.5.3 of Chapter 2. Therefore, in the following lines the residual stress development in asymmetrically cooled plates is studied. Figure 3.19 illustrates the contour plots of the numerical residual stresses on the front surface of plates cooled at $H/D = 20$ and $H/D = 40$.

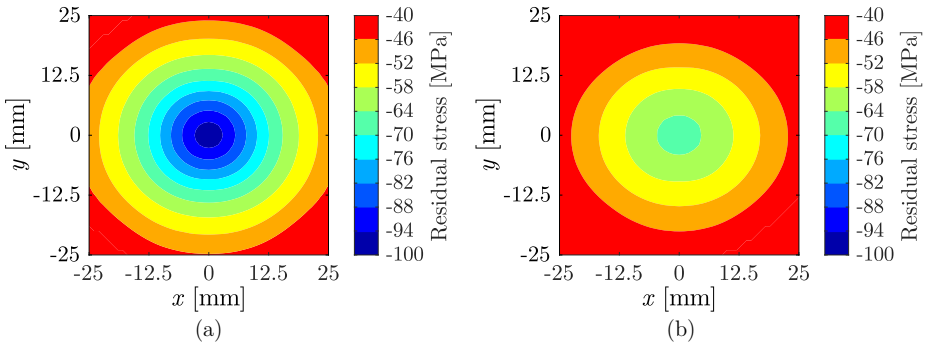

Figure 3.19: Calculated residual stress distributions on the front surface: (a) ATHD20, and (b) ATHD40.

Similarly, Figure 3.20 depicts the residual stress pattern on the rear surface of asymmetrically tempered plates at $H/D = 20$ and $H/D = 40$.

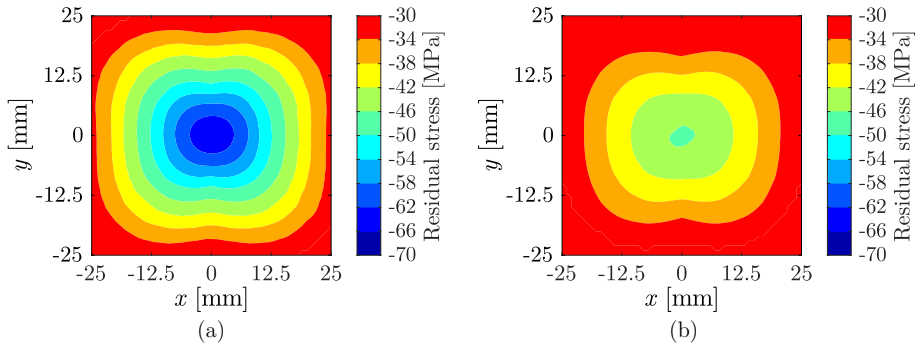

Figure 3.20: Calculated residual stress distributions on the rear surface: (a) ATHD20, and (b) ATHD40.

The maximum residual stress magnitude in the front and rear surfaces for asymmetrically tempered plates was located in the jet facing area. Lower compressive residual stresses were developed on the rear surface, as no forced convection was applied in this area. As observed in the symmetrical tempering case configuration, larger jet-to-plate distances resulted in lower residual stress magnitudes. Figure 3.21 plots the calculated stress distributions along x and y directions on the front and rear surfaces.

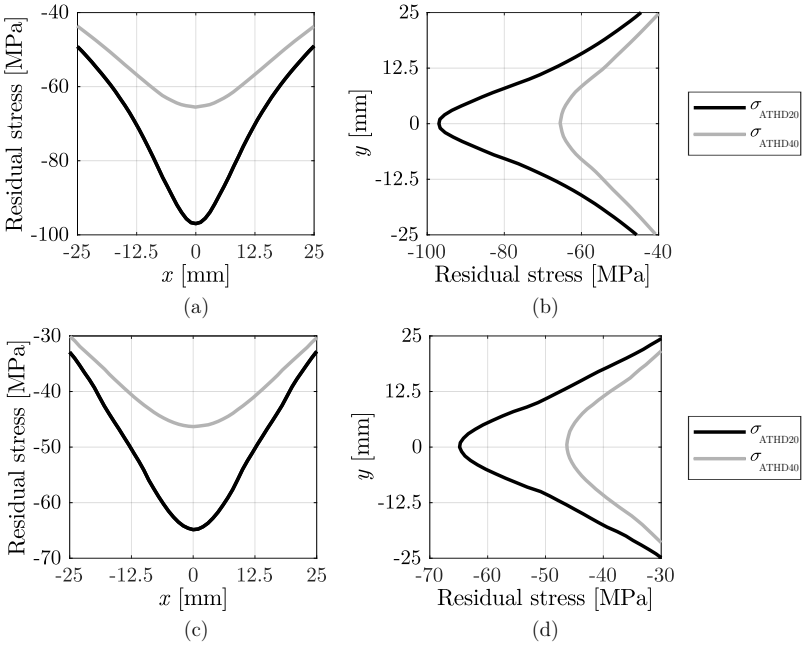

Figure 3.21: Residual stress distributions along x and y directions of asymmetrically tempered glass samples at $H/D = 20$ and $H/D = 40$: (a)-(b) residual stress on the front surface along x and y directions, and (c)-(d) residual stress on the rear surface along x and y directions.

In the case of short jet-to-plate distance tempering tests, residual stresses up to 100 MPa and 65 MPa were observed on the front and rear surfaces, respectively. When the jet-to-plate distance increased to $H/D = 40$, residual stress magnitudes decreased around 65 MPa and 45 MPa on each surface, with the compressive stress always being greater in the jet facing area.

Fracture strength estimation

With the aim of predicting the stress distribution on each sample at the fracture instant, a numerical model of the CDR set-up was built. Likewise, the calculated residual stress distributions were subsequently considered into the in-service numerical analysis. As a result, Figure 3.22 sets out the average, standard deviation and maximum/minimum range of the numerically calculated maximum principal stress at the experimental fracture instant.

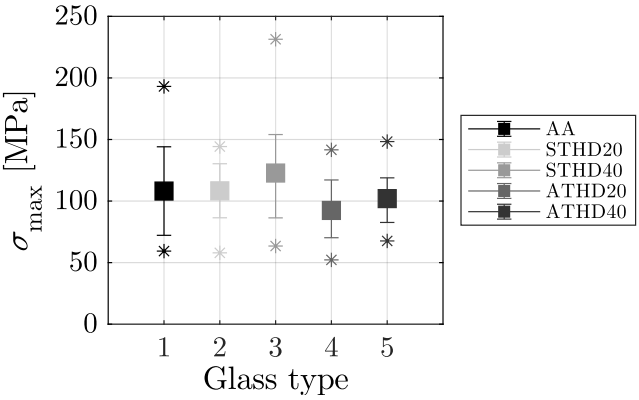

Figure 3.22: Estimated average, standard deviation and maximum/minimum (*) critical stress attained at the experimental fracture instant for each glass type.

Of particular interest was the fact that all glass types presented an average ultimate strength of around 100 MPa. This showed that in spite of the addition of a compressive stress layer on the surface, the material tended to exhibit the same behaviour when fracture occurred. Subsequently, Figure 3.23 shows the stress distribution along the x direction over the loading period for the different glass types.

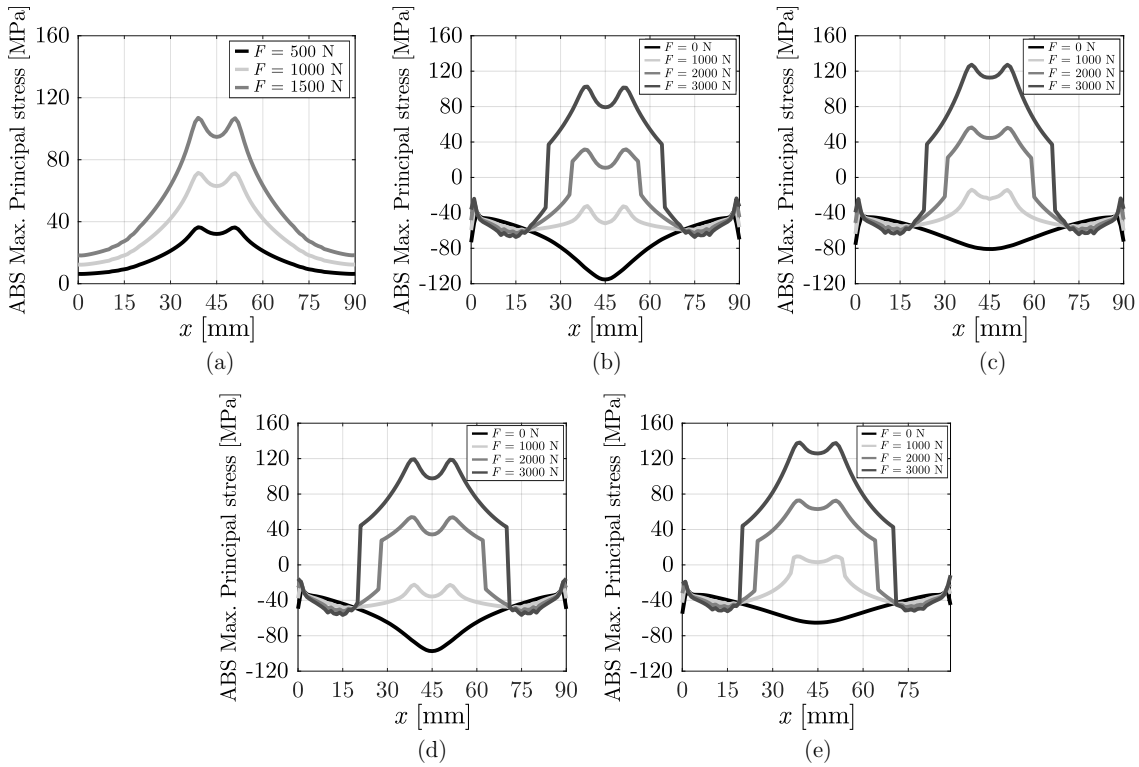

Figure 3.23: Absolute maximum principal stress distribution along x direction during coaxial double ring loading for: (a) AA, (b) STHD20, (c) STHD40, (d) ATHD20 and (e) ATHD40.

The contact areas of the load ring were easily perceived on the stress distributions. Annealed glass plates showed a maximum stress around 100 MPa when a force of 1500 N was applied. Symmetrically and asymmetrically tempered glass tended to exhibit a higher strength due to the initial compressive stress on its surface. In these cases, loads around 3000 N and 2500 N were needed in order to achieve a critical stress value of 100 MPa.

3.4.2 Experimental results

In this section, the residual stress measurements of the heat treated samples and the results of the CDR tests to set-up the Generalised Local Model are presented.

Residual stress measurements

The residual stress measurement results for the symmetrical tempering configuration are presented in Section 2.5.1 of Chapter 2. In line with this approach, here the results of the asymmetrically tempered glass specimens are shown. Five tempering tests (T1-T5) were carried out to ensure the repeatability of the stress patterns, as shown in Figure 3.24 and Figure 3.25.

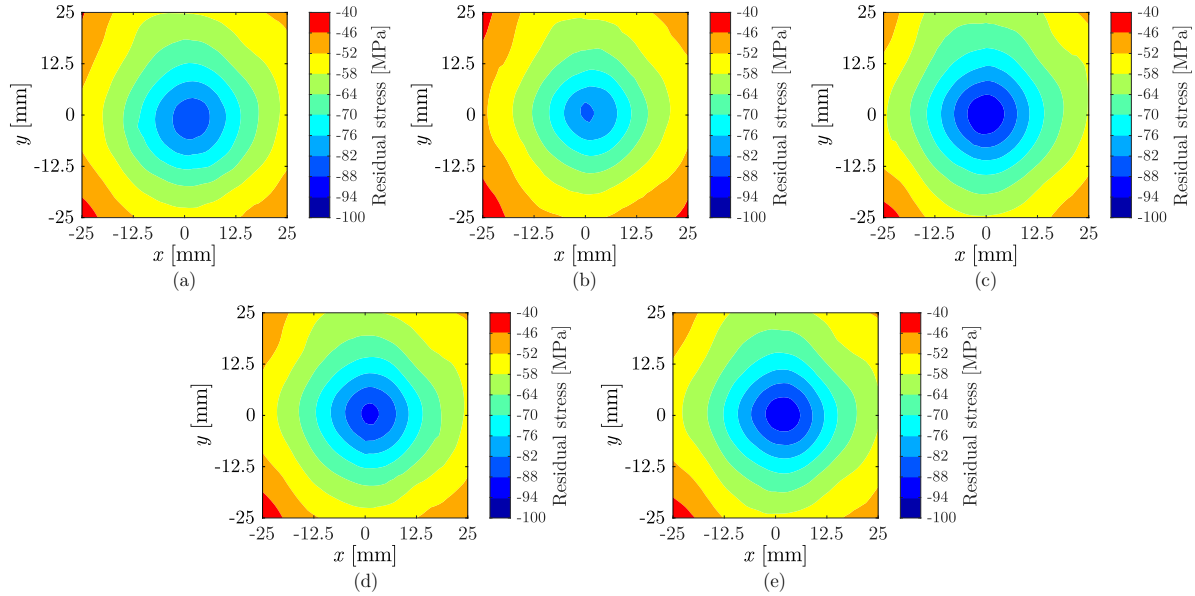

Figure 3.24: Experimental residual stress distribution on the front surface of asymmetrically cooled plates at $H/D = 20$: (a) T1, (b) T2, (c) T3, (d) T4, and (e) T5.

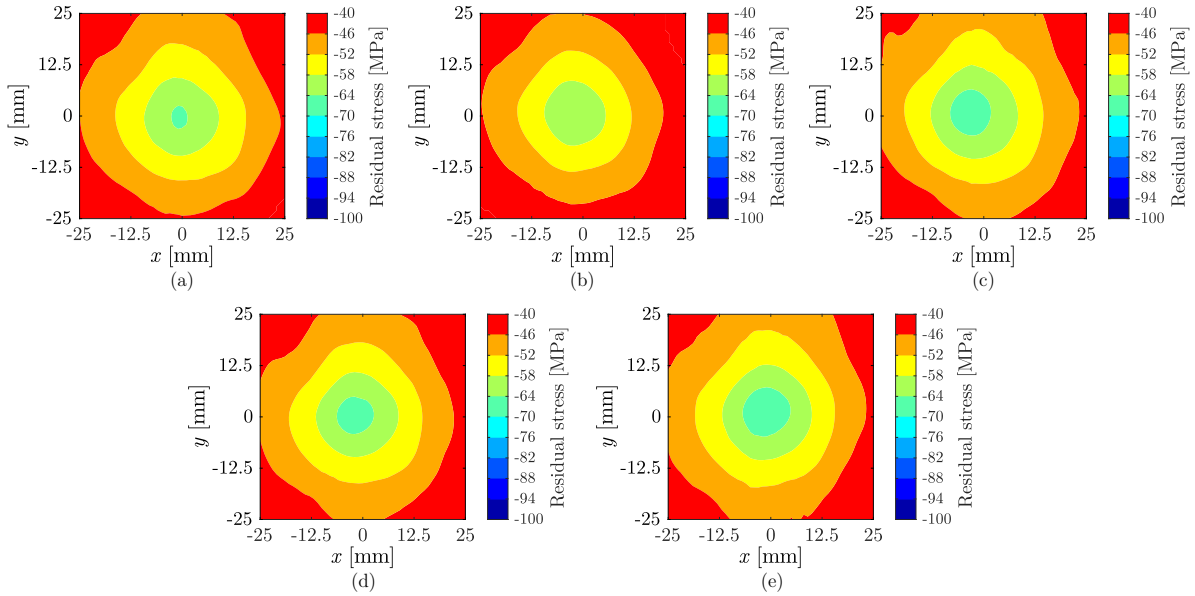

Figure 3.25: Experimental residual stress distribution on the rear surface of asymmetrically cooled plates at $H/D = 20$: (a) T1, (b) T2, (c) T3, (d) T4, and (e) T5.

Residual stress magnitudes up to 90 MPa were perceived on the front surface, where a larger heat extraction occurred. In contrast, residual stress values around 65 MPa were obtained on the rear surface. as observed in Chapter 2, deviations of the stagnation point location, namely, the maximum residual stress area, were observed on both surfaces. Figure 3.26 sets out the residual stress distribution along x and y directions crossing at the centre of asymmetrically cooled plates at $H/D = 20$.

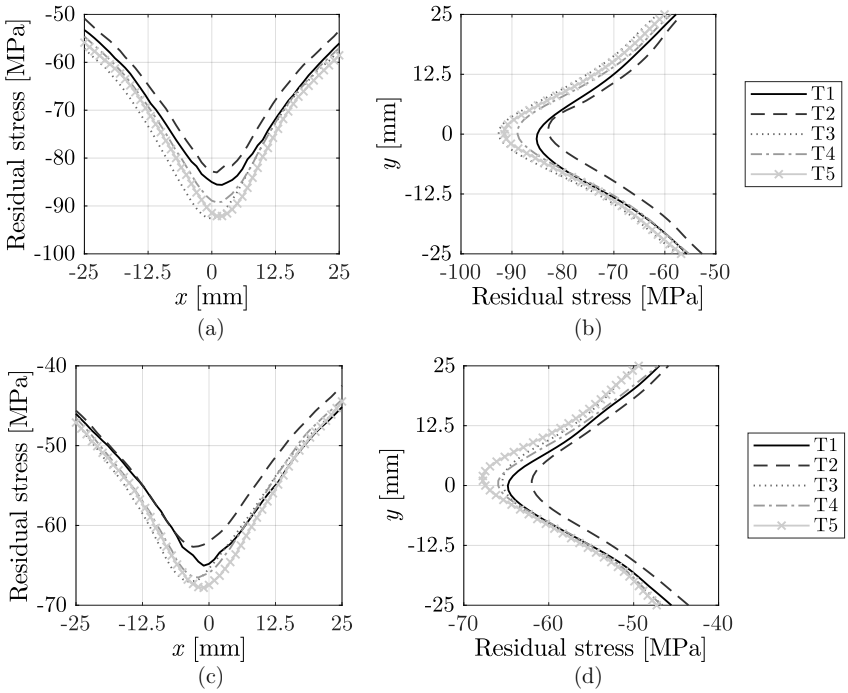

Figure 3.26: Measured experimental residual stress paths of asymmetrically cooled plates at $H/D = 20$: (a)-(b) residual stress on the front surface along x and y directions, and (c)-(d) residual stress on the rear surface along x and y directions.

Misalignments up to 2 mm on the front surface and up to 3 mm on the rear surface were noticed. Not surprisingly, larger residual stress magnitudes were obtained on the front surface, as no forced convection was applied at the back of the plate. For validation purposes, these deviations were corrected and the measured residual stress distributions were realigned in accordance with the maximum residual stress magnitude as shown in Figure 3.27 and Figure 3.28.

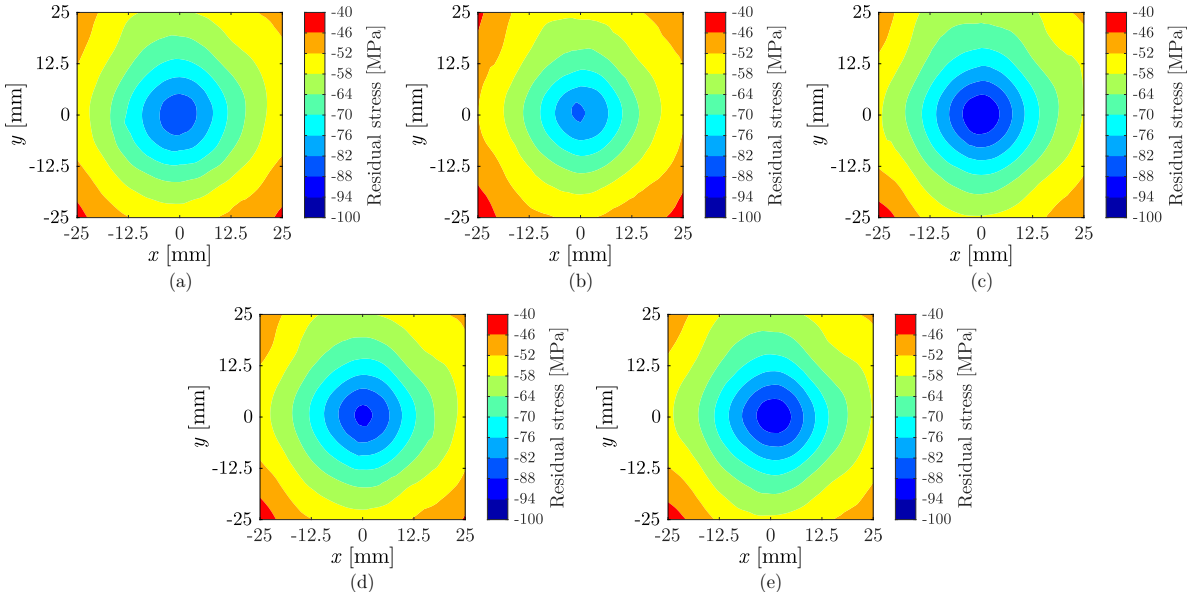

Figure 3.27: Realigned experimental residual stress distribution on the front surface of asymmetrically cooled plates at $H/D = 20$: (a) T1, (b) T2, (c) T3, (d) T4, and (e) T5.

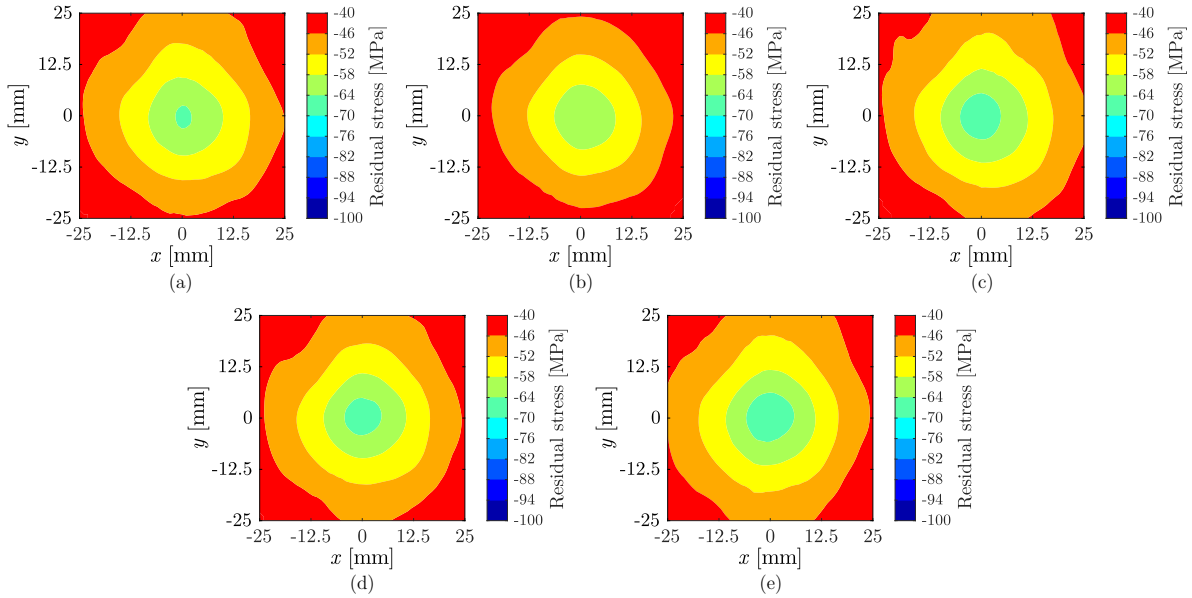

Figure 3.28: Realigned experimental residual stress distribution on the rear surface of asymmetrically cooled plates at $H/D = 20$: (a) T1, (b) T2, (c) T3, (d) T4, and (e) T5.

In the same manner, Figure 3.29 sets out the realigned residual stress distributions along x and y directions on the front and rear surfaces of asymmetrically cooled plates at $H/D = 20$.

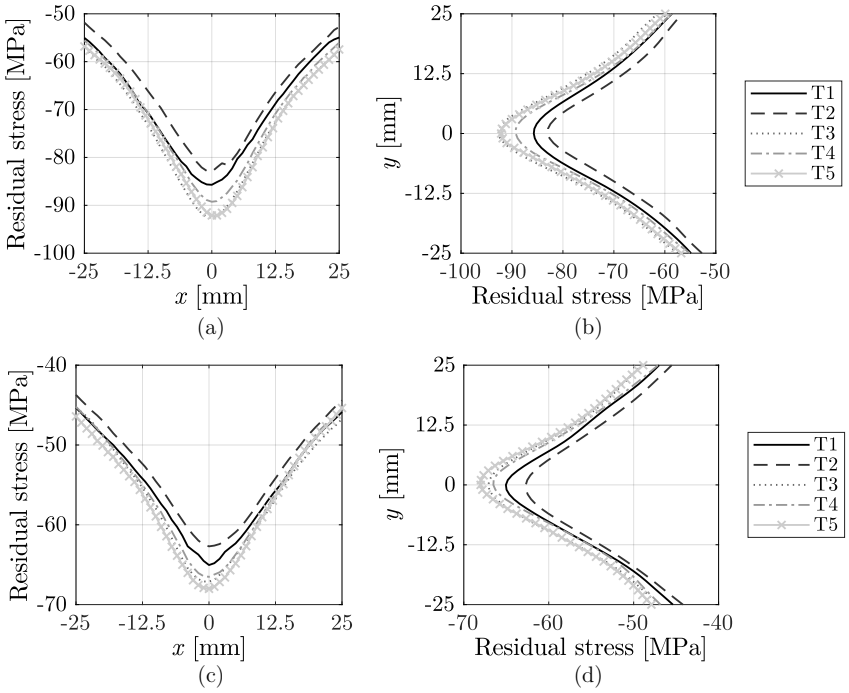

Figure 3.29: Realigned experimental residual stress paths of asymmetrically cooled plates at $H/D = 20$: (a)-(b) residual stress on the front surface along x and y directions, and (c)-(d) residual stress on the rear surface along x and y directions.

Residual stresses in the stagnation area showed its maximum magnitude and decreased towards the edges of the plate. As it can be seen, residual stress profiles kept a similar distribution along both directions, hence, the repeatability of the tests was considered appropriate. Turning now to asymmetrically tempered plates at $H/D = 40$, Figure 3.30 and Figure 3.31 present the residual stress distribution of the five analysed specimens.

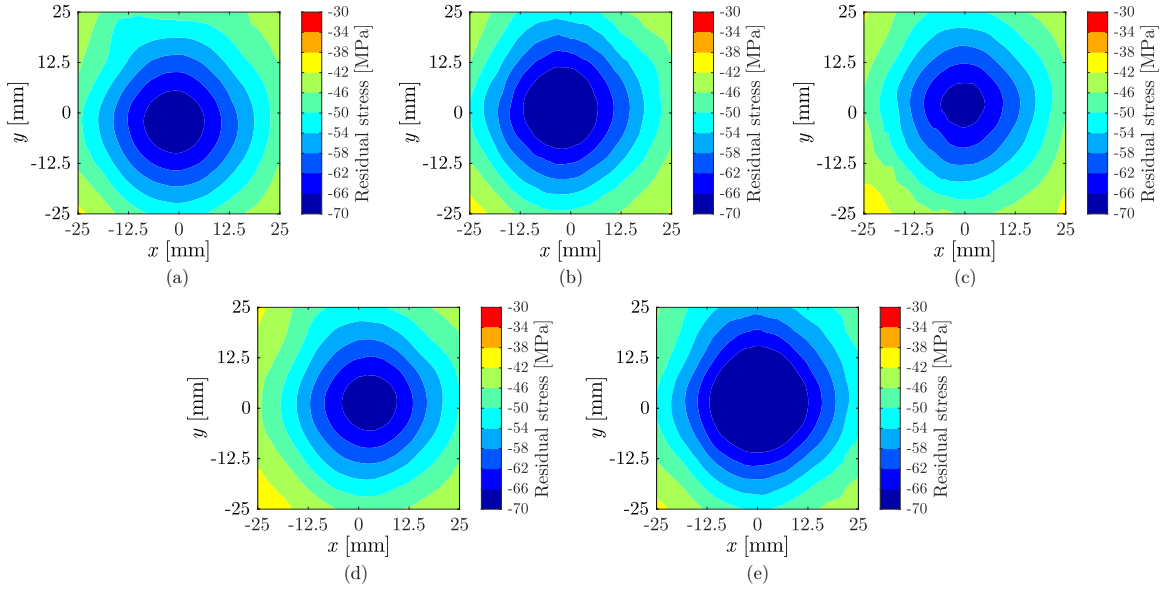

Figure 3.30: Experimental residual stress distribution on the front surface of asymmetrically cooled plates at $H/D = 40$: (a) T1, (b) T2, (c) T3, (d) T4, and (e) T5.

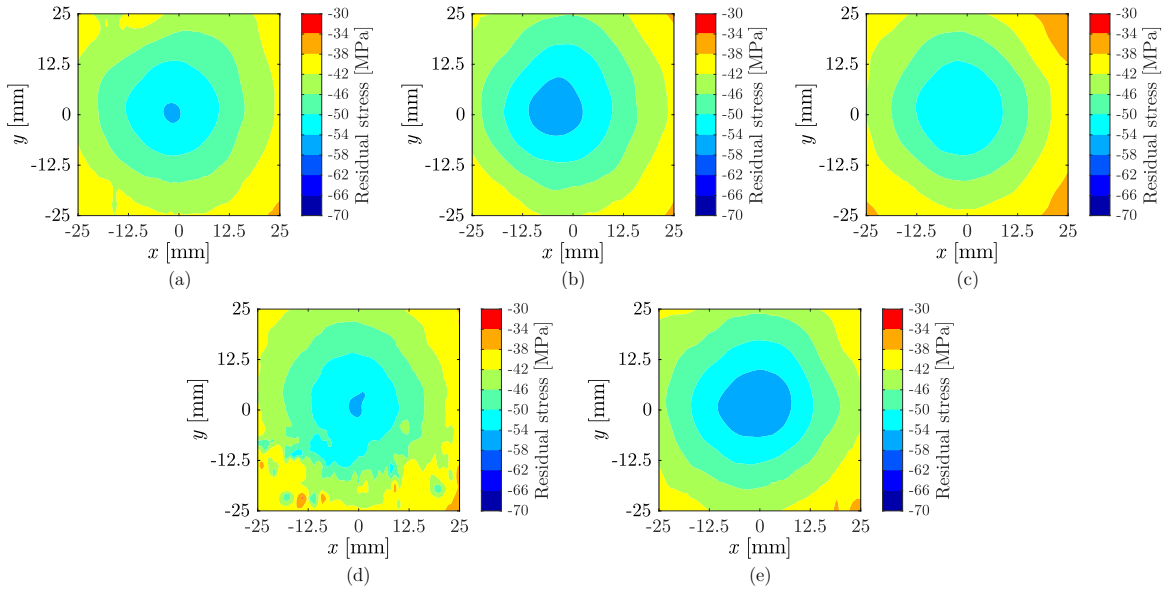

Figure 3.31: Experimental residual stress distribution on the rear surface of asymmetrically cooled plates at $H/D = 40$: (a) T1, (b) T2, (c) T3, (d) T4, and (e) T5.

As the jet-to-plate distance increased to $H/D = 40$, lower residual stress magnitudes were attained. In this case, residual stress around 70 MPa and 55 MPa were perceived on the front and rear surfaces, respectively. Figure 3.32 provides the residual stress distribution along x and y directions crossing at the centre of the plates.

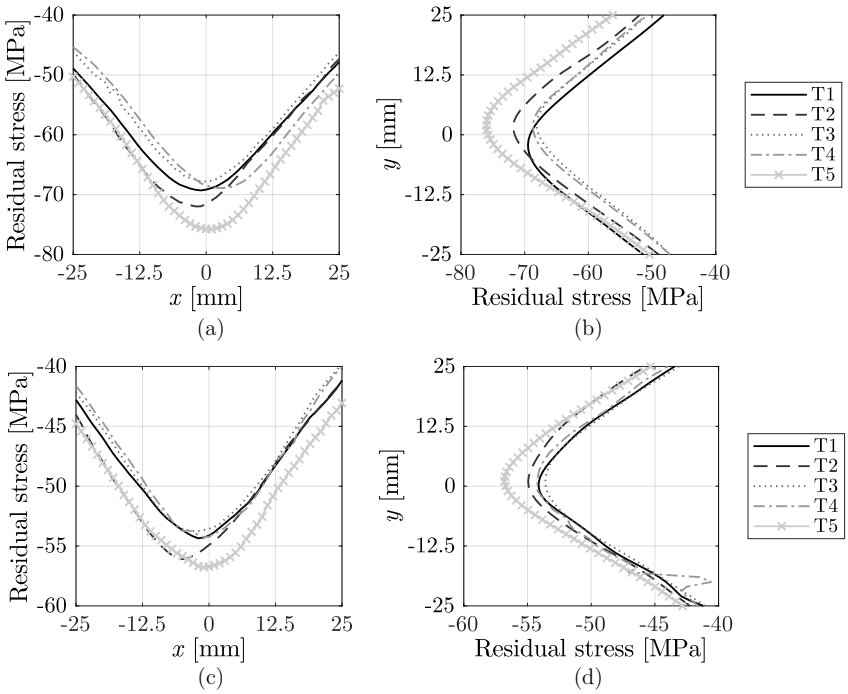

Figure 3.32: Measured experimental residual stress paths of asymmetrically cooled plates at $H/D = 40$: (a)-(b) residual stress on the front surface along x and y directions, and (c)-(d) residual stress on the rear surface along x and y directions.

Misalignments up to 2 mm on the front surface and 5 mm on the rear surface were found. Following the same procedure, the stress distributions were realigned and Figure 3.33 and Figure 3.34 depict the residual stress distributions on the front and rear surfaces of asymmetrically tempered plates at $H/D = 40$.

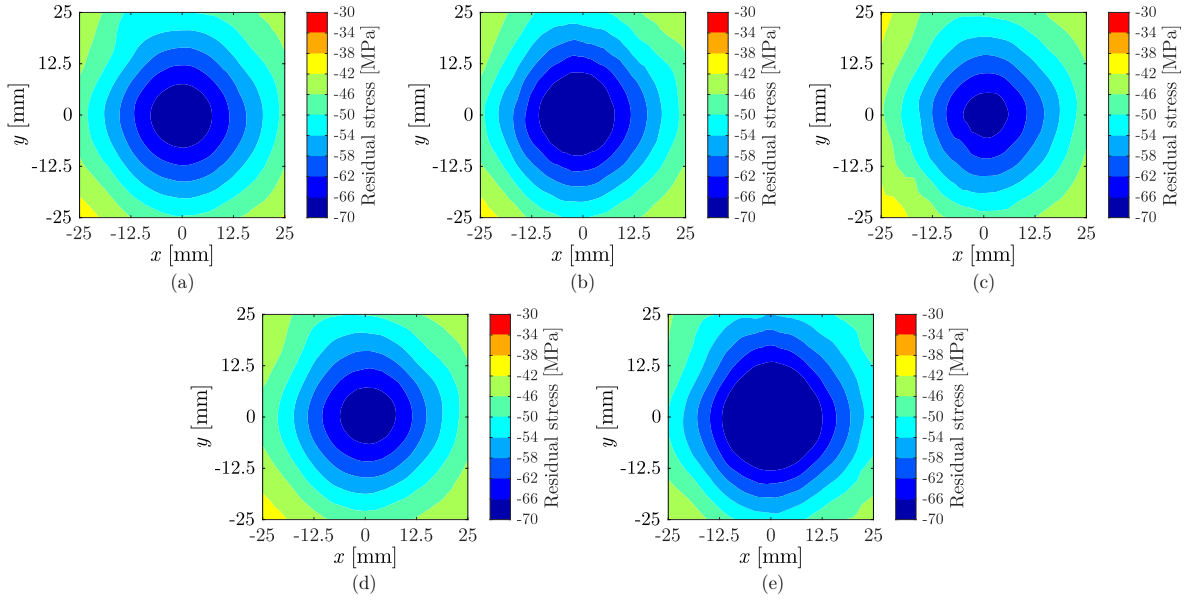

Figure 3.33: Realigned experimental residual stress distribution on the front surface of asymmetrically cooled plates at $H/D = 40$: (a) T1, (b) T2, (c) T3, (d) T4, and (e) T5.

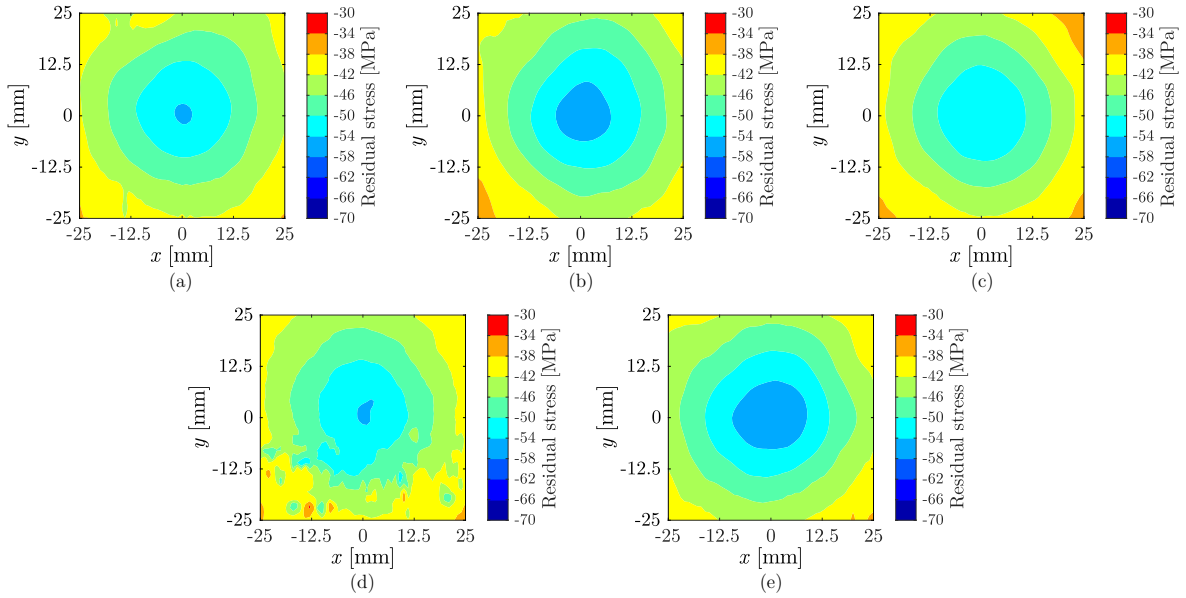

Figure 3.34: Realigned experimental residual stress distribution on the rear surface of asymmetrically cooled plates at $H/D = 40$: (a) T1, (b) T2, (c) T3, (d) T4, and (e) T5.

Likewise, the measured stress paths along x and y directions are presented in Figure 3.35.

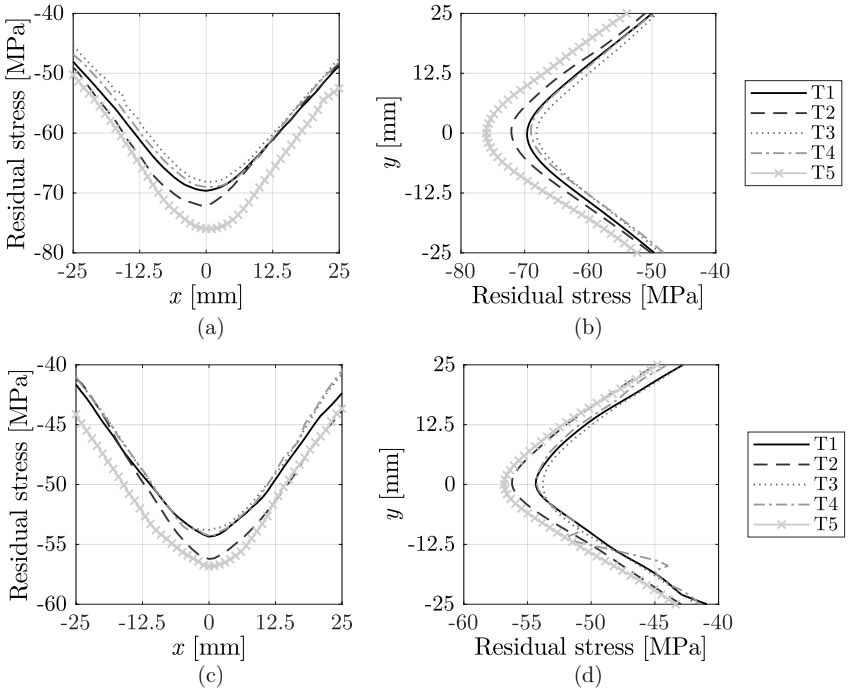

Figure 3.35: Realigned experimental residual stress paths of asymmetrically cooled plates at $H/D = 40$: (a)-(b) residual stress on the front surface along x and y directions, and (c)-(d) residual stress on the rear surface along x and y directions.

The differences in residual stress magnitude among the measured glass plates was found to be less than 10 MPa. Therefore, the repeatability of the experimental tempering tests was verified.

Coaxial Double Ring (CDR) tests

This section sets out the experimental results of the performed CDR bending tests. Firstly, the vertical displacement contours measured by DIC are provided. Then, the ultimate fracture loads of each glass type are shown.

Figure 3.36 and Figure 3.37 present the displacement maps and paths for annealed glass at 500 N and 1000 N.

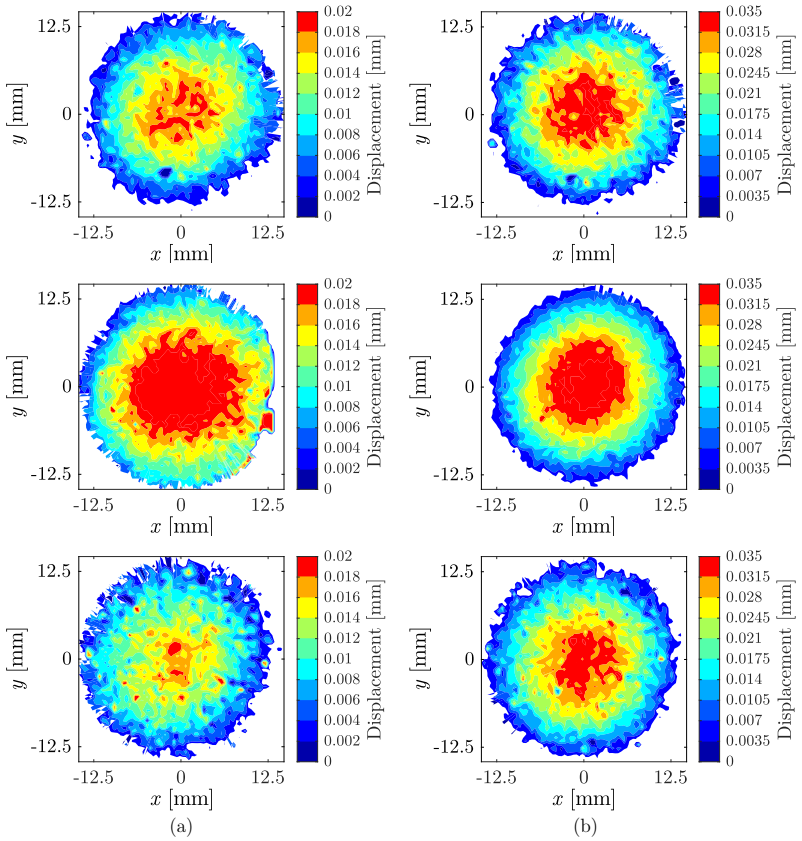

Figure 3.36: Displacement contour of annealed glass samples at: (a) 500 N and (b) 1000 N.

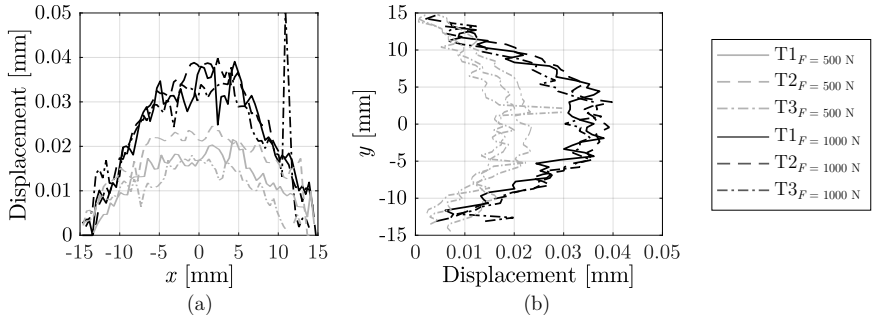

Figure 3.37: Experimental displacement paths in annealed glass samples along: (a) x direction, and (b) y direction.

Figure 3.38 and Figure 3.39 show the displacement patterns and paths for symmetrically tempered glass for a jet-to-plate distance of $H/D = 20$ at 1000, 2000 and 3000 N.

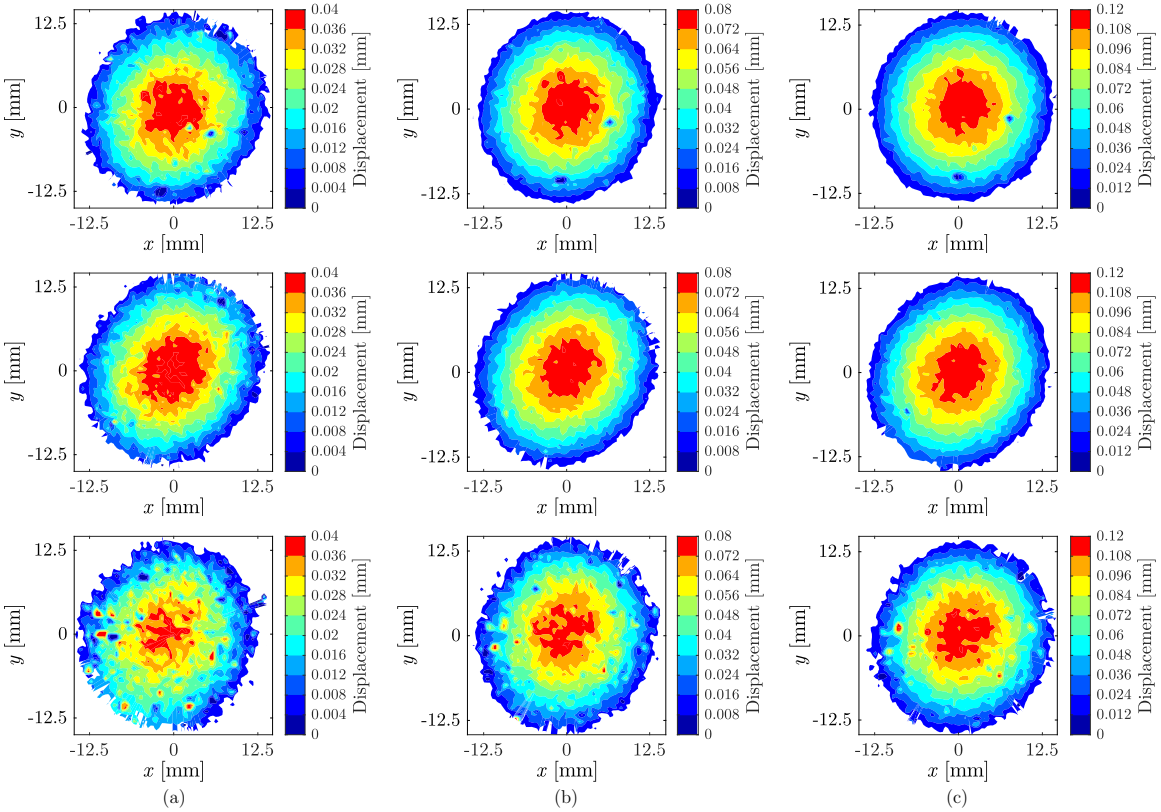

Figure 3.38: Displacement contour of symmetrically tempered glass samples for $H/D = 20$ at: (a) 1000 N, (b) 2000 N and (c) 3000 N.

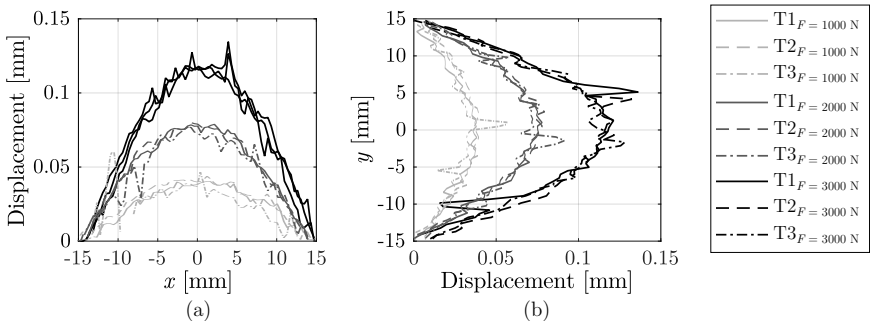

Figure 3.39: Experimental displacement paths in symmetrically tempered glass samples for $H/D = 20$ along: (a) x direction, and (b) y direction.

Figure 3.40 and Figure 3.41 set out the vertical displacement distributions and paths for symmetrically tempered glass for a jet-to-plate distance of $H/D = 40$ and at 1000, 2000 and 3000 N.

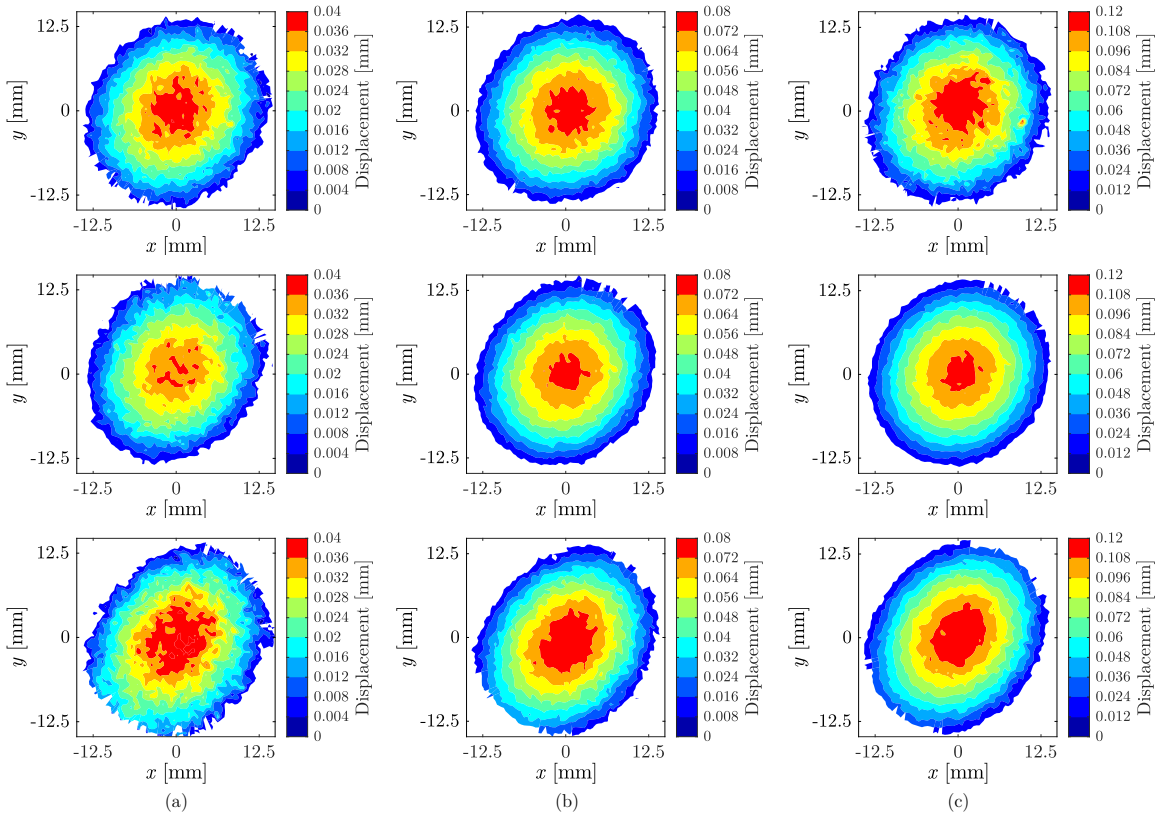

Figure 3.40: Displacement contour of symmetrically tempered glass samples for $H/D = 40$ at: (a) 1000 N, (b) 2000 N and (c) 3000 N.

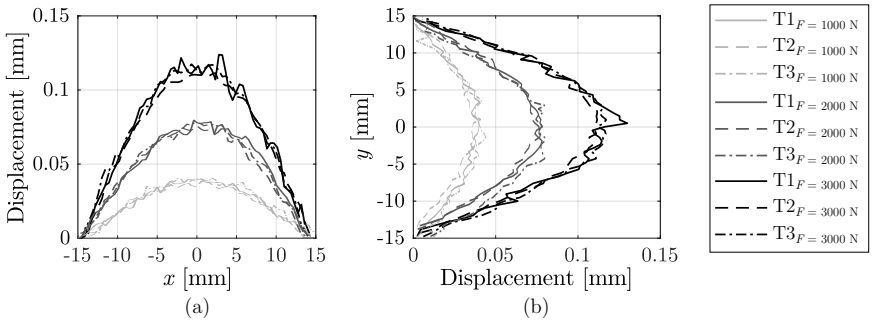

Figure 3.41: Experimental displacement paths in symmetrically tempered glass samples for $H/D = 40$ along: (a) x direction, and (b) y direction.

Figure 3.42 and Figure 3.43 show the displacement patterns and paths for asymmetrically tempered glass for a jet-to-plate distance of $H/D = 20$ at 1500 and 2500 N.

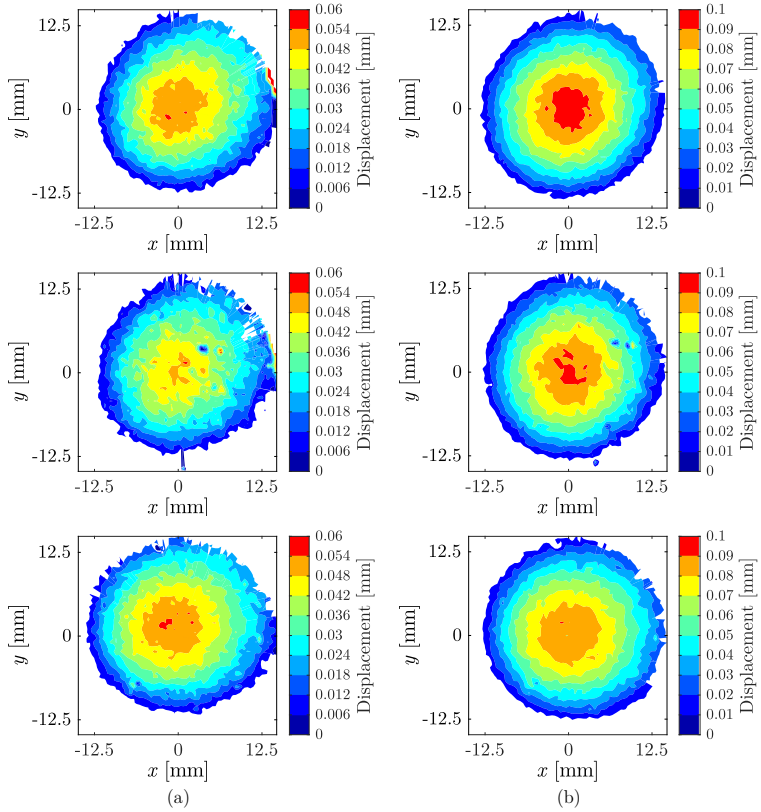

Figure 3.42: Displacement contour of asymmetrically tempered glass samples for $H/D = 20$ at: (a) 1500 N and (b) 2500 N.

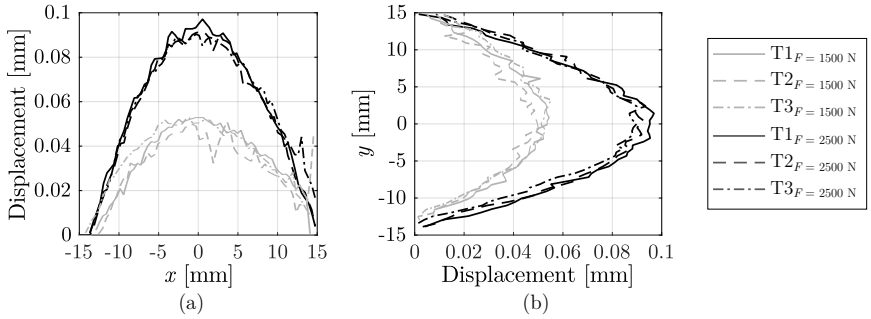

Figure 3.43: Experimental displacement paths in asymmetrically tempered glass samples for $H/D = 20$ along: (a) x direction, and (b) y direction.

Figure 3.44 and Figure 3.45 set out the vertical displacement distribution for asymmetrically tempered glass for a jet-to-plate distance of $H/D = 40$ and at 1500 and 2500 N.

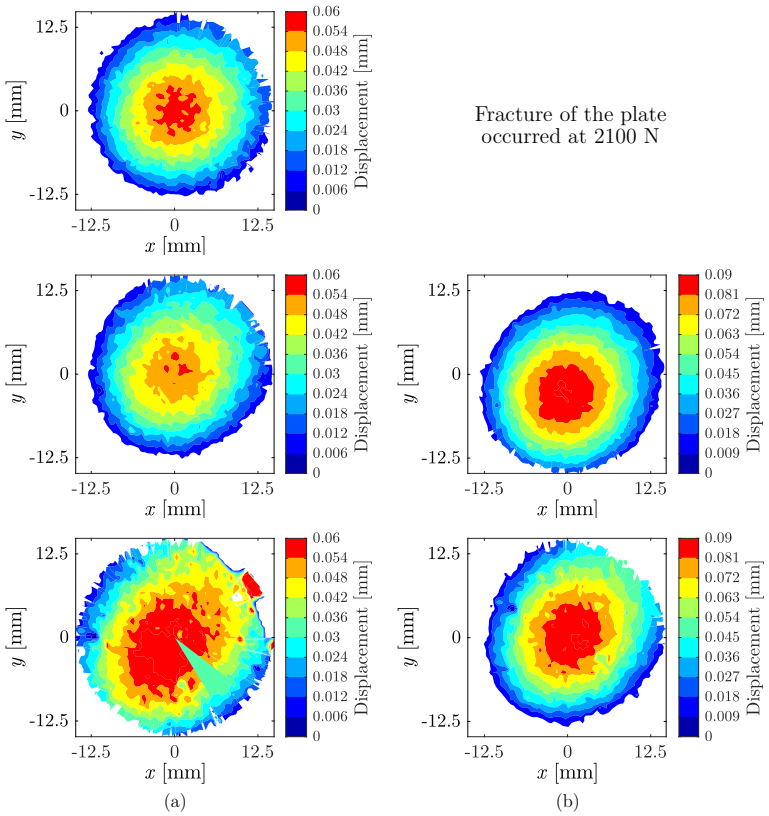

Figure 3.44: Displacement contour of asymmetrically tempered glass samples for $H/D = 40$ at: (a) 1500 N and (b) 2500 N.

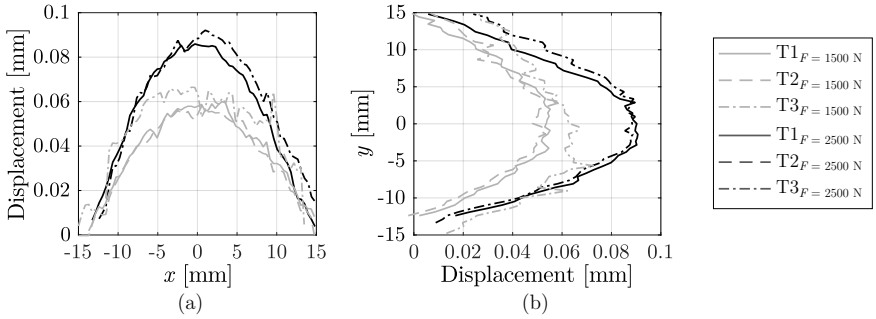

Figure 3.45: Experimental displacement paths in asymmetrically tempered glass samples for $H/D = 40$ along: (a) x direction, and (b) y direction.

The maximum local deformation occurred at the centre of the plate where the load ring was located. Similarly, the displacement tended to increase linearly until fracture took place. Regarding the applied maximum load, Figure 3.46 provide the average, standard deviation and maximum/minimum range of the critical forces corresponding to annealed, symmetrically tempered glass and asymmetrically tempered glass.

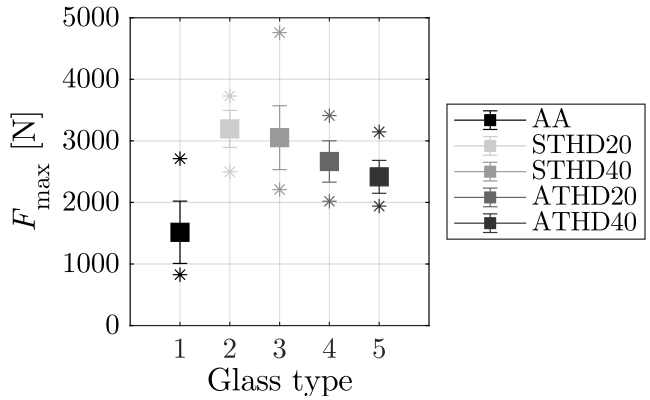

Figure 3.46: Average, standard deviation and maximum/minimum (*) critical force attained at each glass type: (1) AA, (2) STHD20, (3) STHD40, (4) ATHD20, and (5) ATHD40.

The scattering of the results was easily perceived. This scattering stemmed from the flaws existing on the glass surface. Likewise, larger scatter was observed as the jet-to-plate distance increased. In this case, the influence of the glass type on the bearing average maximum force could be noticed, as compared to Figure 3.22, where the ultimate strength among specimens exhibited a similar ultimate strength magnitude around 100 MPa. The average maximum force of annealed glass plates referred to 1515 N. With regard to tempered glass samples, the ultimate average forces increased to 3194 N and 3052 N for symmetrically cooled plates at $H/D = 20$ and $H/D = 40$, and 2665 N and 2416 N for asymmetrically tempered plates at $H/D = 20$ and $H/D = 40$. Nevertheless, even if the initial compressive stress magnitude in plates tempered at $H/D = 20$ were around 20% higher as compared to $H/D = 40$, differences in fracture load magnitudes up to 10% between them were observed for both, symmetrically and asymmetrically tempered samples. This fact may have occurred due to the residual stress misalignments that were perceived with respect to the centre of the plate. In this sense, a small deviation of the stress pattern with respect to the alignment of the rings may have led to similar compressive stress values on both samples, as shown in Figure 3.47.

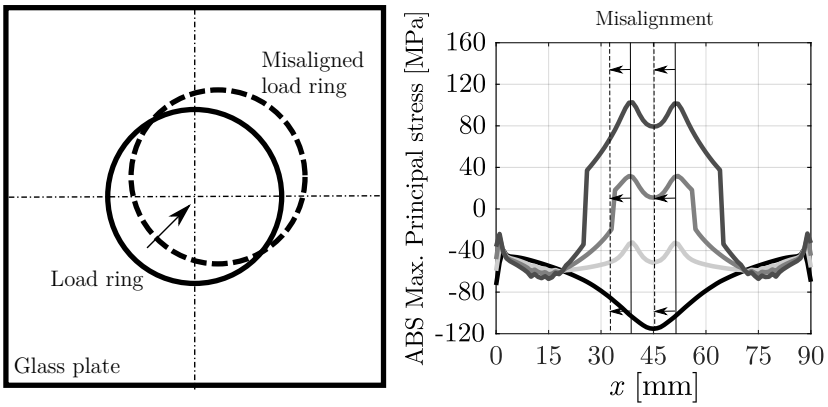

Figure 3.47: Misalignment of the residual stress pattern with respect to the ring axis.

As a unique jet was employed during the quenching process, a significant stress gradient was observed from the stagnation area towards the edges of the plate. Compressive stresses rapidly declined when moving away from the stagnation region. As a result, a small deviation of the stress pattern of a sample tempered at $H/D = 20$ may lead to a similar fracture behaviour of a sample tempered at $H/D = 40$, as compressive stresses could converge to the same values. Being all the experimental results presented, the next section moves on to validate the defined numerical model with the data shown here.

3.4.3 Validation of the in-service numerical model

In this section, the validation of the numerical results is presented. The following validation approaches were carried out:

- Residual stress distribution of each analysed tempering type was validated.
- Experimental and numerical vertical displacements of plates during the tests were compared.
- Experimentally measured and numerically calculated fracture stresses were compared.

Validation of tempering residual stresses

Prior to validating the modelling of the fracture characterisation, the residual stress distribution of each analysed tempering configuration was compared to experimental data. The validation of the numerically predicted stress pattern for symmetrically tempered glass was presented in Section 2.5.3 of Chapter 2, whereas for annealed glass, a stress-free plate was assumed. Therefore, the validation of asymmetrically cooled plates is discussed in this section.

Figure 3.48 depicts the contour plots of the average experimental and the numerical residual stresses, and the relative difference distribution for asymmetrical tempering plates at $H/D = 20$.

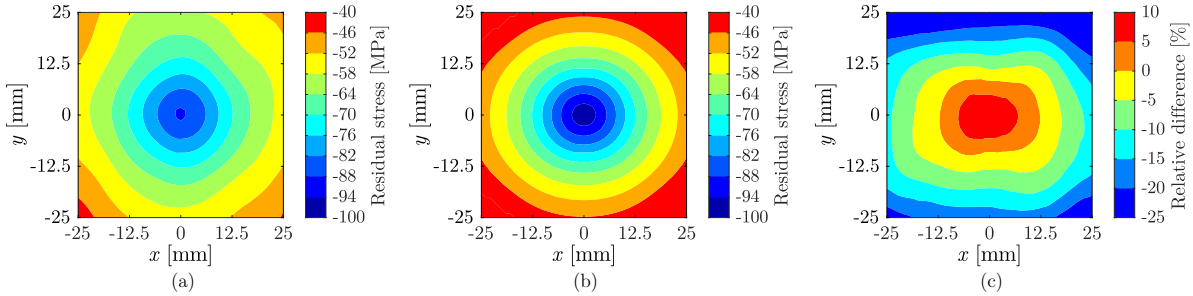

Figure 3.48: Residual stress distribution on the front surface of asymmetrically tempered glass samples at $H/D = 20$: (a) experimental average, (b) modified procedure, and (c) deviation.

Differences in the residual stress distribution up to 10% and 20% in the stagnation and dry regions were perceived, respectively. With regard to the rear surface, differences around 5% and 25% were observed in the same regions (see Figure 3.49).

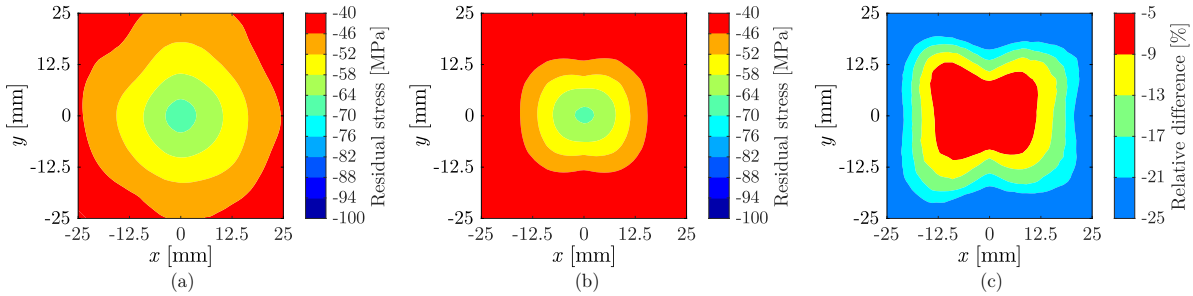

Figure 3.49: Residual stress distribution on the rear surface of asymmetrically tempered glass samples at $H/D = 20$: (a) experimental average, (b) modified procedure, and (c) deviation.

Figure 3.50 presents the average experimental residual stress and the estimated residual stress distributions, as well as the deviation among them for asymmetrical tempering plates at $H/D = 40$.

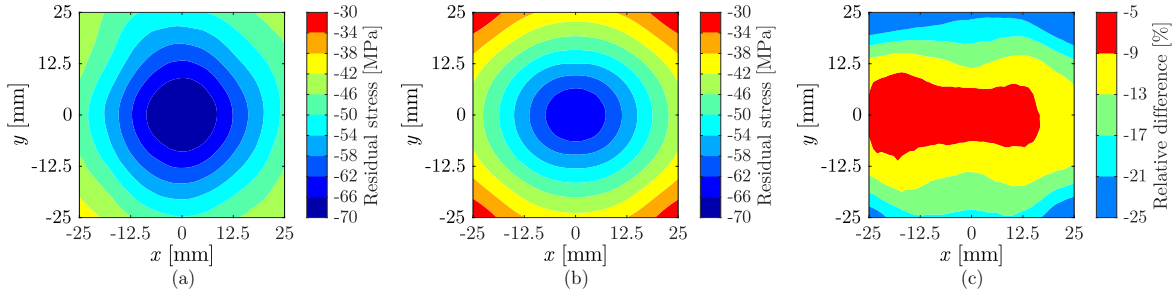

Figure 3.50: Residual stress distribution on the front surface of asymmetrically tempered glass samples at $H/D = 40$: (a) experimental average, (b) modified procedure, and (c) deviation.

Similar conclusions could be drawn in this case, as differences ranged from 5 to 25 % on the surface. Figure 3.51 illustrates the distributions obtained for the rear surface of the plate.

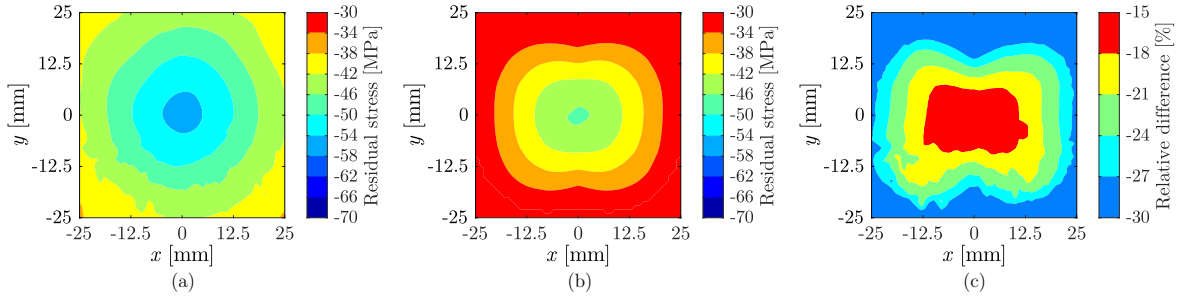

Figure 3.51: Residual stress distribution on the rear surface of asymmetrically tempered glass samples at $H/D = 40$: (a) experimental average, (b) modified procedure, and (c) deviation.

The relative difference in the stagnation area and dry region increased up to 15% and 30% on the rear surface. These discrepancies could be attributed to phenomena related to natural convection on the rear surface. Thus, the proposed modified procedure for modelling low thickness tempering process might encounter limitations when modelling low cooling rate applications. Therefore, if processes involving low cooling rates are to be considered, further study with more focus on the modelling techniques of natural convection cooling is suggested. Even though, the presented FSI methodology continues to be useful to explore this issue as it can account for volumetric radiation or natural convection modelling techniques.

In addition to the residual stress distribution, residual stress paths crossing at the centre of the plates were also investigated. Here, the numerical estimation with respect to the measured experimental band and the uncertainty range of 5% of SCALP was checked. Similarly, shaded areas were introduced with the view to illustrating the diameter of the load ring. As a result, Figure 3.52 sets out residual stress paths along x and y directions of the plates asymmetrically tempered at $H/D = 20$.

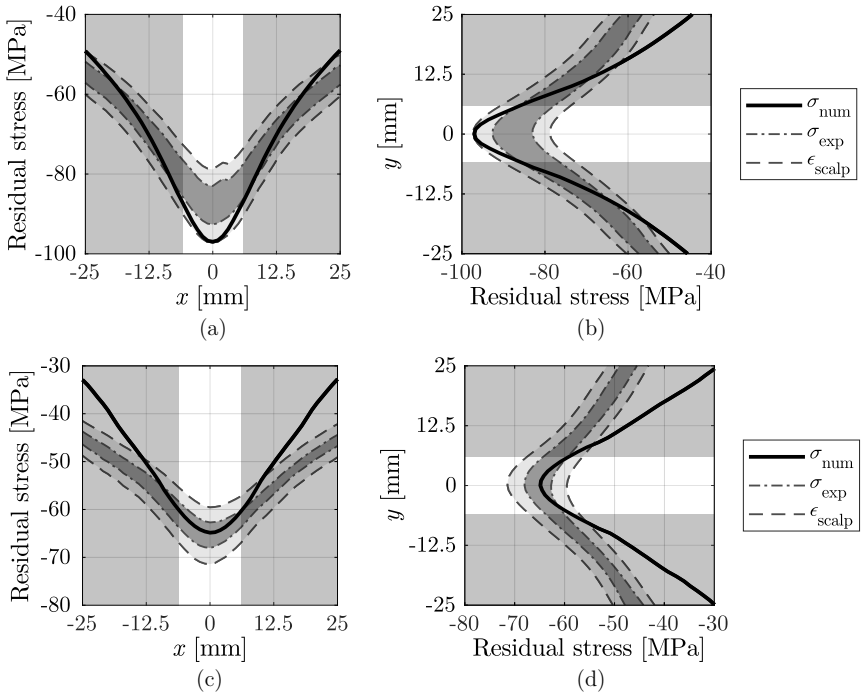

Figure 3.52: Residual stress distribution along x and y directions on the front and rear surfaces of asymmetrically tempered glass samples for $H/D = 20$: (a)-(b) residual stress on the front surface along x and y directions, (c)-(d) residual stress on the rear surface along x and y directions.

The estimated residual stress distributions were considered representative as mostly remained within the specified experimental bands, especially on the front surface where forced convection was applied. Moreover, the stress distribution on the surface area at which the application of the load happened was observed to be representative. Deviations were especially observed towards the dry regions of the plate, where forced convection lost traction. In the same manner, larger differences were noticed on the rear surface, were natural convection cooling prevailed, and thus, radiation could gain importance. These facts came along with the estimated residual stress distribution along x and y directions of samples asymmetrically tempered at $H/D = 40$, as depicted in Figure 3.53.

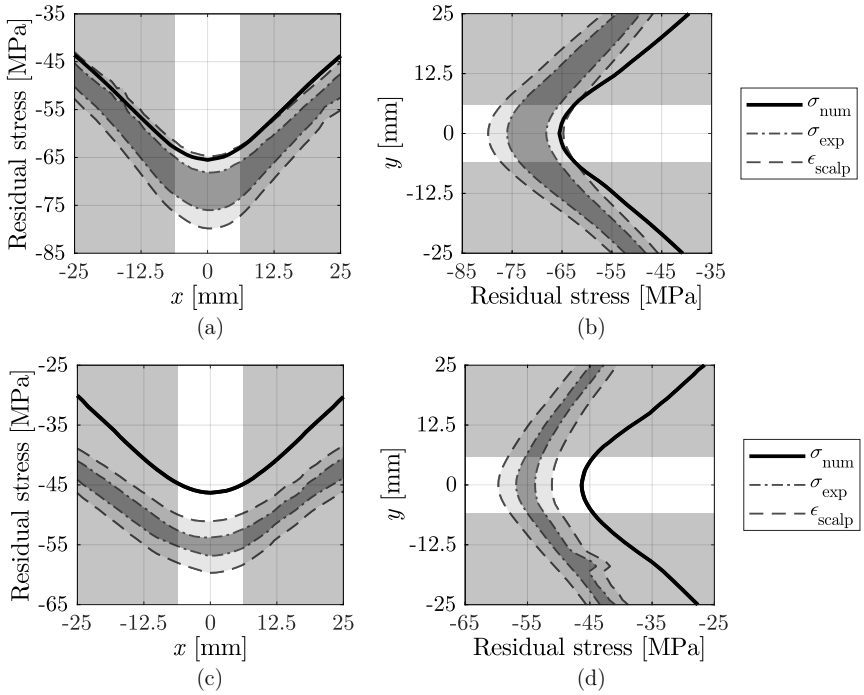

Figure 3.53: Residual stress distribution along x and y directions on the front and rear surfaces of asymmetrically tempered glass samples for $H/D = 40$: (a)-(b) residual stress on the front surface along x and y directions, (c)-(d) residual stress on the rear surface along x and y directions.

As the jet-to-plate distance increased, forced convection became less significant. Likewise, the predicted residual stress on the rear surface showed larger deviations. This aspect evinced the aforementioned relevance of natural convection modelling. Nevertheless, fracture did not occur on the rear surface as the air-impinged surface was the one subjected to tensile stresses during the tests. More importantly, the calculated residual stress distributions on the load application area were within the measured experimental bands. For this reason, the predicted residual stresses were considered representative for this analysis. Notwithstanding, the influence of natural convection cooling and volumetric radiation on residual stress development in glass plates subjected to low cooling rates become an important issue for future research.

Validation of fracture vertical displacement

Once the validation of the developed residual stresses was made, the maximum displacement attained during the fracture characterisation was studied. To this aim, the numerical contour plots of the maximum displacement field and the ones measured by DIC at different time frames were investigated. As three samples were recorded for each glass type, an average experimental displacement distribution was used to validate the results of the numerical calculations. Figure 3.54 presents the displacement fields of annealed glass plates when loads of 500 N and 1000 N were applied.

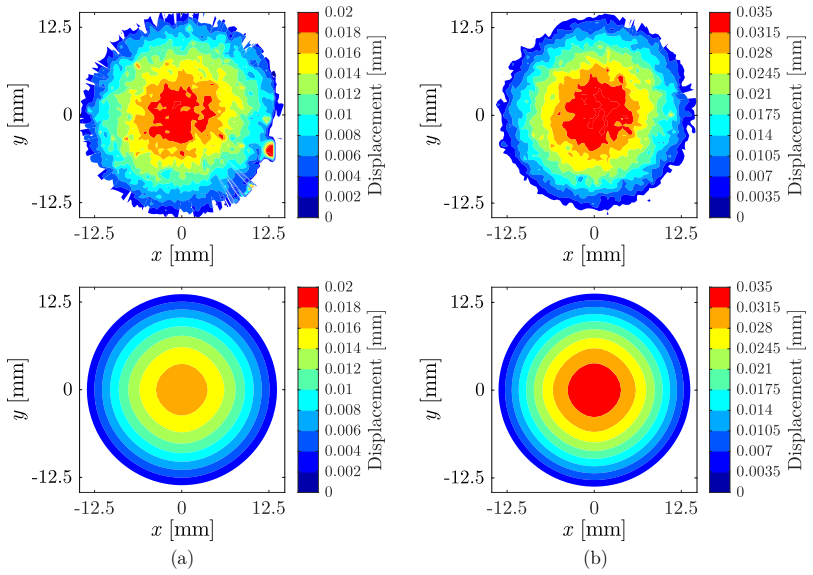

Figure 3.54: Comparison of experimental (above) and numerical (below) displacement distributions of annealed glass at: (a) 500 N and (b) 1000 N.

In alike manner, vertical displacement paths along x and y directions crossing at the centre of the plate were defined. Figure 3.55 sets out the displacement magnitude along both directions for annealed glass at 500 N and 1000 N.

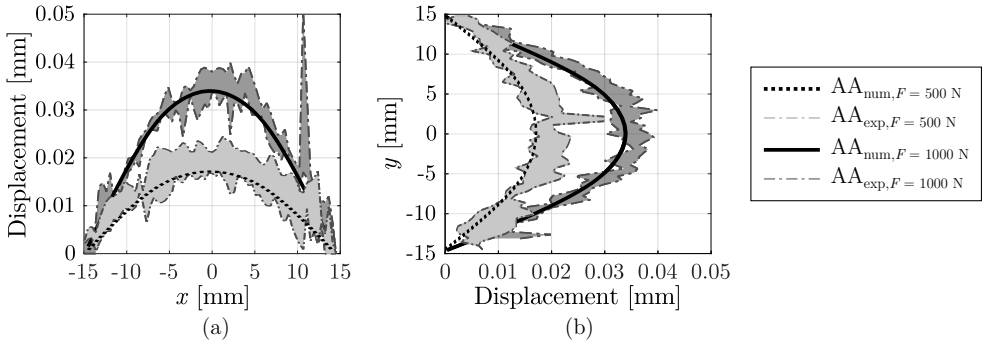

Figure 3.55: Comparison of experimental and numerical displacement paths in annealed glass specimens along: (a) x direction, and (b) y direction.

Figure 3.56 provides the displacement patterns of symmetrically tempered glass for $H/D = 20$ at 1000 N, 2000 N and 3000 N.

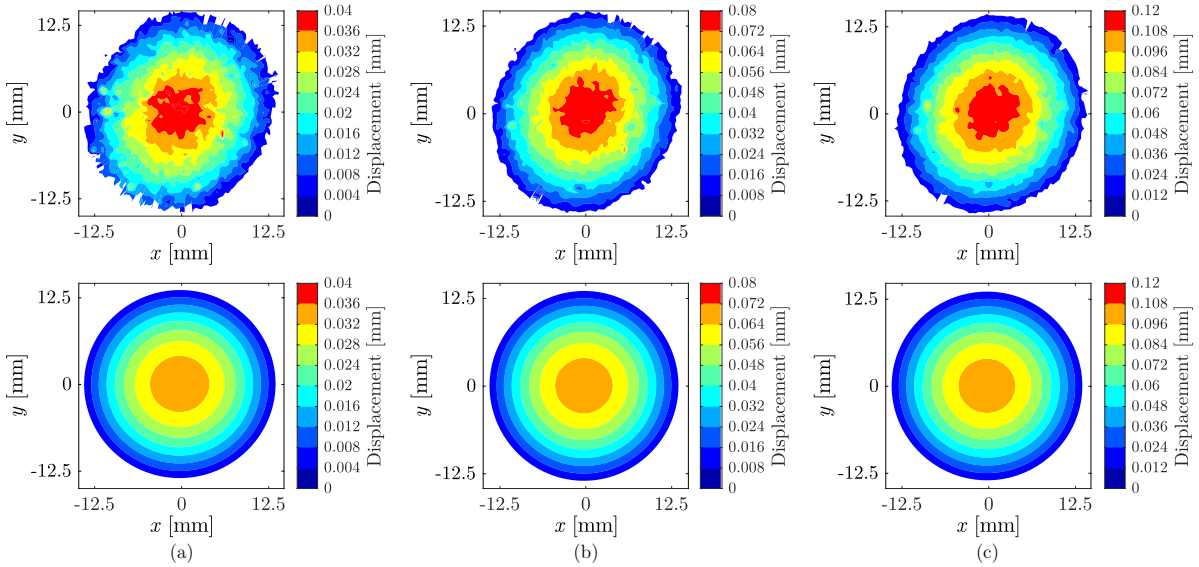

Figure 3.56: Comparison of experimental (above) and numerical (below) displacement distributions of symmetrically tempered glass $H/D = 20$ at: (a) 1000 N, (b) 2000 N, and (c) 3000 N.

Figure 3.57 shows the displacement along the defined paths for symmetrically tempered glass ($H/D = 20$) at 1000, 2000 and 3000 N.

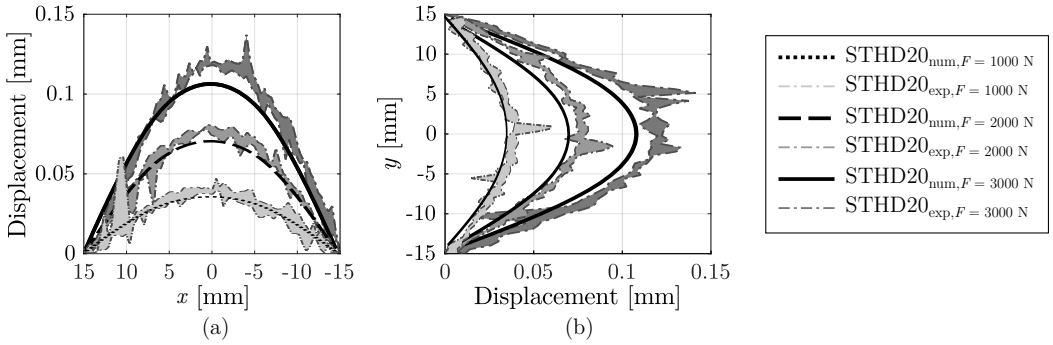

Figure 3.57: Comparison of experimental and numerical displacement paths of symmetrically tempered glass samples for $H/D = 20$ along: (a) x direction, and (b) y direction.

Figure 3.58 provides the displacement distributions of symmetrically tempered glass for $H/D = 40$ at 1000 N, 2000 N and 3000 N.

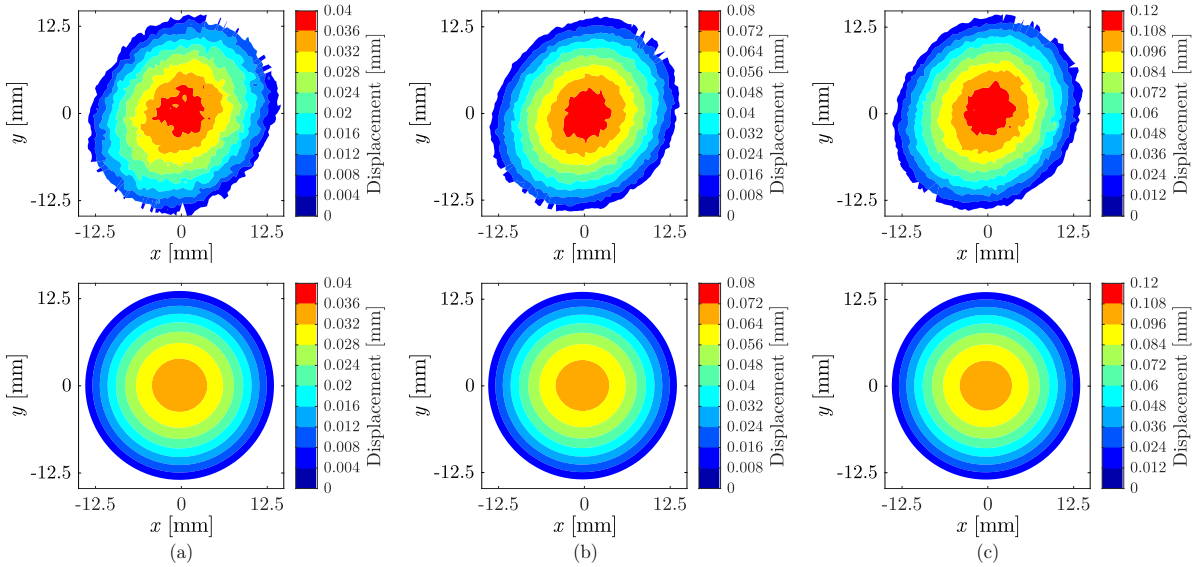

Figure 3.58: Comparison of experimental (above) and numerical (below) displacement distributions of symmetrically tempered glass $H/D = 40$ at: (a) 1000 N, (b) 2000 N, and (c) 3000 N.

Figure 3.59 shows the vertical displacement value along the x and y directions for symmetrically tempered glass ($H/D = 40$) at 1000, 2000 and 3000 N.

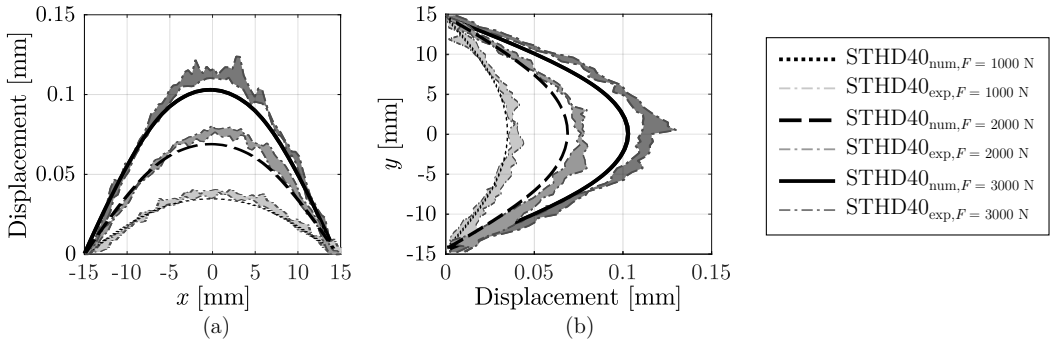

Figure 3.59: Comparison of experimental and numerical displacement paths on symmetrically tempered glass samples for $H/D = 40$ along: (a) x direction, and (b) y direction.

Figure 3.60 presents the displacement distributions of asymmetrically tempered glass for $H/D = 20$ at 1500 N, and 2500 N.

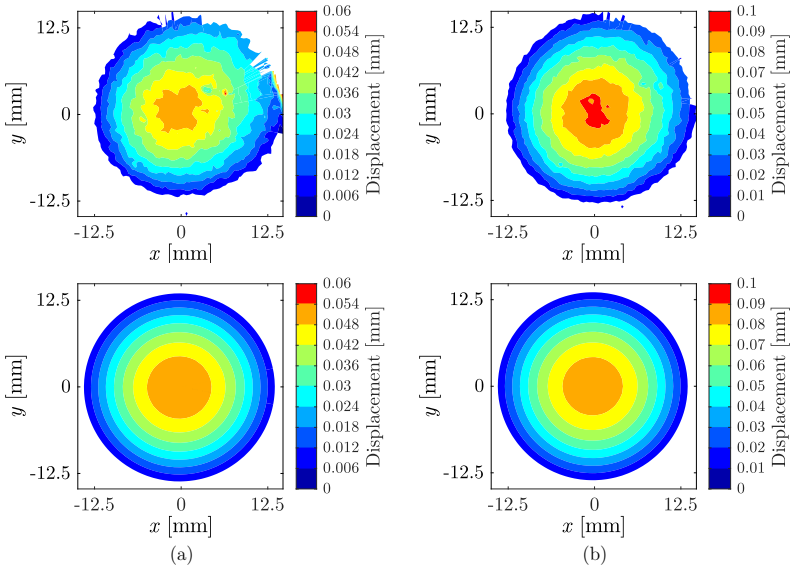

Figure 3.60: Comparison of experimental (above) and numerical (below) displacement distributions of asymmetrically tempered glass $H/D = 20$ at: (a) 1500 N, and (b) 2500 N.

Figure 3.61 sets out the displacement along the defined paths for asymmetrically tempered glass ($H/D = 20$) at 1500 and 2500 N.

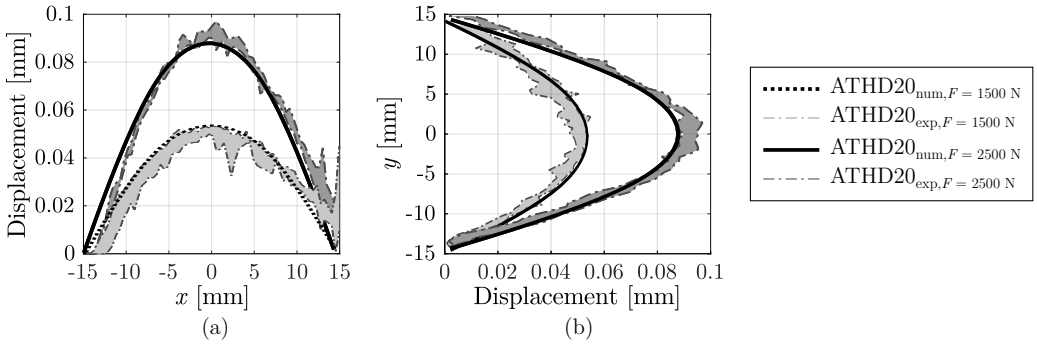

Figure 3.61: Comparison of experimental and numerical displacement paths on asymmetrically tempered glass samples for $H/D = 20$ along: (a) x and (b) y directions.

Finally, Figure 3.62 illustrates the displacement distributions of asymmetrically tempered glass for $H/D = 40$ at 1500 N, and 2500 N.

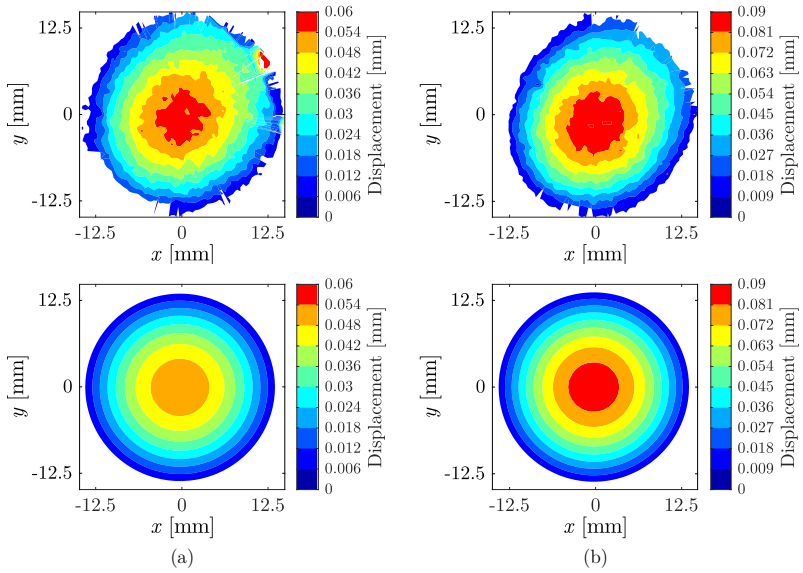

Figure 3.62: Comparison of experimental (above) and numerical (below) displacement distributions of asymmetrically tempered glass $H/D = 40$ at: (a) 1500 N, and (b) 2500 N.

Figure 3.63 shows the vertical displacement value along the x and y directions for asymmetrically tempered glass ($H/D = 40$) at 1500 and 2500 N.

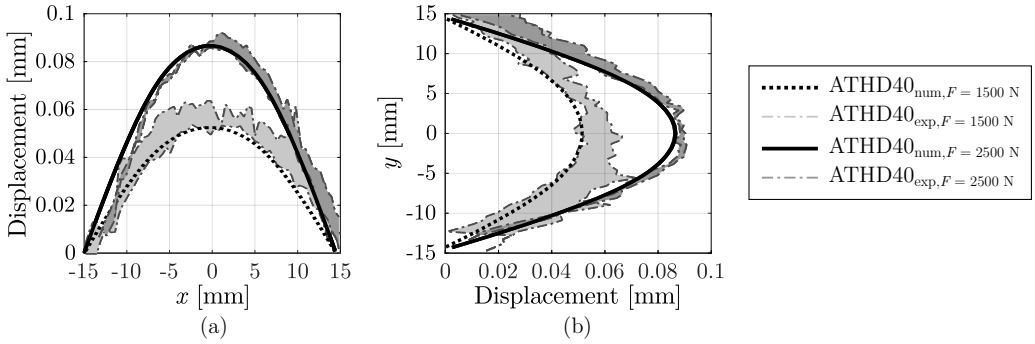

Figure 3.63: Comparison of experimental and numerical displacement paths on asymmetrically tempered glass samples for $H/D = 40$ along: (a) x and (b) y directions.

In summary, the relative error of the numerical model with respect to the experimental results remained below 10% in all the analysed cases.

Validation of fracture strength calculation

Turning to the validation of the predicted maximum stress during the CDR tests, a comparison of the experimentally and numerically calculated strengths was done. By the use of the formulation given in the UNE-EN 1288-1 and UNE-EN 1288-5 standards, the bending radial stress, $\sigma_{\text{rad,exp}}$ was calculated. For this purpose, the value of K_2, which is defined in Equation 3.3, was calculated and set as 1 for the analysed cases. Likewise, the relative difference, ϵ_σ, was calculated based on the following expression:

$$\epsilon_\sigma = \frac{\sigma_{\text{rad,num}} - \sigma_{\text{rad,exp}}}{\sigma_{\text{rad,exp}}} \cdot 100 \tag{3.22}$$

Table 3.3 and Table 3.4 provide the maximum experimental and numerical stresses of annealed, symmetrically tempered and asymmetrically tempered glass plates. The critical stresses were calculated at the corresponding fracture loads ordered in ascending order.

A good agreement between the experimental and numerical values was obtained as differences up to 6% for all the tested specimens were observed.

Table 3.3: Comparison between experimental and numerically estimated fracture strengths at the given fracture loads for annealed (AA) and symmetrically tempered glass at $H/D = 20$ (STHD20) and $H/D = 40$ (STHD40).

AA				STHD20				STHD40			
$F_{\max}$ [N]	$\sigma_{\text{rad,exp}}$	$\sigma_{\text{rad,num}}$	ϵ_σ [%]	$F_{\max}$ [N]	$\sigma_{\text{rad,exp}}$	$\sigma_{\text{rad,num}}$	ϵ_σ [%]	$F_{\max}$ [N]	$\sigma_{\text{rad,exp}}$	$\sigma_{\text{rad,num}}$	ϵ_σ [%]
827	56.97	57.31	0.59	2498	172.08	168.37	-2.21	2210	150.66	146.30	-2.98
948	62.97	65.70	4.15	2632	180.37	177.40	-1.67	2370	162.41	156.89	-3.52
956	63.50	66.25	4.15	2865	194.30	193.10	-0.62	2436	166.07	161.26	-2.98
969	64.37	67.15	4.15	2869	195.58	193.37	-1.14	2542	175.12	168.28	-4.06
1026	68.15	71.10	4.15	2903	199.98	195.66	-2.21	2562	169.31	169.60	0.17
1052	69.88	72.90	4.15	2928	198.57	197.35	-0.62	2675	176.78	177.09	0.17
1096	74.72	75.95	1.63	2975	199.67	200.52	0.42	2737	180.87	181.19	0.17
1103	73.27	76.44	4.15	2977	200.84	200.65	-0.10	2749	181.67	181.98	0.17
1136	75.46	78.72	4.15	3017	206.75	203.35	-1.67	2846	188.08	188.41	0.17
1154	74.72	79.97	6.57	3034	206.83	204.49	-1.14	2862	189.13	189.46	0.17
1161	77.12	80.46	4.15	3050	205.77	205.57	-0.10	2882	190.46	190.79	0.17
1177	78.18	81.57	4.15	3070	210.38	206.92	-1.67	2889	192.90	191.25	-0.86
1254	85.49	86.90	1.63	3162	215.56	213.12	-1.14	2914	195.58	192.91	-1.38
1298	88.49	89.95	1.63	3188	217.33	214.87	-1.14	2917	198.86	193.11	-2.98
1309	89.24	90.71	1.63	3198	216.88	215.55	-0.62	2969	202.40	196.55	-2.98
1317	87.48	91.27	4.15	3228	220.06	217.57	-1.14	2973	197.48	196.81	-0.34
1436	97.89	99.51	1.63	3232	218.05	217.84	-0.10	2977	196.73	197.08	0.17
1580	108.84	109.49	0.59	3258	224.44	219.59	-2.21	2980	196.93	197.28	0.17
1678	111.46	116.29	4.15	3302	221.62	222.55	0.42	3067	204.78	203.04	-0.86
1714	118.08	118.78	0.59	3309	223.24	223.03	-0.10	3108	209.68	205.75	-1.91
1793	123.52	124.25	0.59	3315	223.65	223.43	-0.10	3112	204.60	206.01	0.69
1803	124.21	124.95	0.59	3340	225.33	225.12	-0.10	3247	214.58	214.95	0.17
1945	131.22	134.79	2.65	3351	228.44	225.86	-1.14	3281	224.84	217.20	-3.52
2005	133.18	138.95	4.15	3441	234.58	231.92	-1.14	3288	219.54	217.67	-0.86
2053	139.96	142.27	1.63	3480	232.36	234.55	0.94	3305	221.82	218.79	-1.38
2103	144.87	145.74	0.59	3511	239.35	236.64	-1.14	3425	233.49	226.74	-2.98
2257	154.67	156.41	1.11	3618	241.57	243.85	0.94	3493	230.83	231.24	0.17
2282	155.57	158.14	1.63	3667	249.98	247.16	-1.14	3964	273.08	262.42	-4.06
2319	159.75	160.71	0.59	3679	252.12	247.96	-1.67	4021	265.73	266.19	0.17
2712	186.83	187.94	0.59	3729	251.58	251.33	-0.10	4854	324.10	321.33	-0.86

Table 3.4: Comparison between experimental and numerically estimated fracture strengths at the given fracture loads for asymmetrically tempered glass at $H/D = 20$ (ATHD20) and $H/D = 40$ (ATHD40).

ATHD20				ATHD40			
$F_{\max}$ [N]	$\sigma_{\text{rad,exp}}$	$\sigma_{\text{rad,num}}$	ϵ_σ [%]	$F_{\max}$ [N]	$\sigma_{\text{rad,exp}}$	$\sigma_{\text{rad,num}}$	ϵ_σ [%]
2020	137.71	135.34	-2.21	1941	132.32	127.72	-1.75
2081	137.52	139.427	-1.67	2056	140.16	135.28	1.37
2191	145.54	146.797	-0.62	2096	143.64	137.92	0.86
2253	149.66	150.951	-1.14	2113	143.30	139.04	0.86
2280	150.67	152.76	-2.21	2160	148.80	142.13	1.37
2389	157.88	160.063	-0.62	2220	153.74	146.08	1.37
2406	159.00	161.202	0.42	2237	150.92	147.19	1.37
2430	161.41	162.81	-0.10	2239	152.64	147.33	0.86
2497	164.17	167.299	-1.67	2250	152.59	148.05	1.87
2502	170.56	167.634	-1.14	2278	155.29	149.89	-1.75
2514	171.38	168.438	-0.10	2322	159.12	152.79	-1.75
2521	171.86	168.907	-1.67	2335	160.01	153.64	-1.75
2582	171.51	172.994	-1.14	2350	160.20	154.63	0.86
2626	172.65	175.942	-1.14	2350	157.72	154.63	1.87
2702	179.48	181.034	-0.62	2366	158.80	155.68	0.86
2717	180.48	182.039	-1.14	2387	162.73	157.06	0.86
2743	186.02	183.781	-0.10	2394	163.20	157.53	-1.22
2756	187.88	184.652	-2.21	2398	163.48	157.79	-1.75
2756	183.07	184.652	0.42	2439	166.27	160.49	0.86
2761	183.40	184.987	-0.10	2472	171.19	162.66	0.86
2790	185.33	186.93	-0.10	2475	168.72	162.86	0.86
2822	186.49	189.074	-0.10	2486	166.85	163.58	1.37
2877	189.15	192.759	-1.14	2499	170.36	164.43	1.87
2888	191.84	193.496	-1.14	2526	170.42	166.21	0.86
3002	198.39	201.134	0.94	2707	181.68	178.12	1.37
3031	201.34	203.077	-1.14	2753	187.68	181.15	0.86
3057	202.02	204.819	0.94	2828	192.79	186.08	1.37
3088	204.07	206.896	-1.14	2834	193.20	186.48	1.37
3269	222.85	219.023	-1.67	2834	190.21	186.48	-1.75
3412	226.64	228.604	-0.10	3146	214.47	207.01	0.86

3.4.4 Single test statistical assessment

In this section, a statistical assessment for the fracture characterisation of glass is performed. Firstly, the local stress distribution and the element size of the investigated glass types were numerically determined. Then, the numerical data was transferred to the GLM. Regarding the failure criteria, based on the obtained experimental data, it is not obvious which stress or stress combination should be taken as a reference to derive the PFCDF. For this reason, two different criteria, namely, the maximum principal stress ($\sigma_{\max}$) and the Principle of Independent Action (PIA) were analysed (see Equation 3.20 and Equation 3.21). Table 3.5 summarises the Weibull parameters for the considered glass type and failure criteria.

Table 3.5: Weibull parameters for each analysed glass type based on the maximum principal stress and PIA criteria.

Glass type	PIA			$\sigma_{\max}$		
	β	λ	δ	β	λ	δ
AA	2	42.92	2.28	2	35.17	2.07
STHD20	3.38	42.1	10.7	3.45	33.93	9.99
STHD40	2	66	2.35	2	53.74	2.16
ATHD20	3.01	23.7	9.11	3.05	20.85	8.42
ATHD40	2.16	69	1.76	2.05	57	1.33

Even if differences are perceptible among the calculated Weibull parameters, in the following lines a good correlation between the analysed cases is proved. This seems reasonable as the development of compressive stresses on the surface did not produce any alteration in the material itself. Moreover, with the aim of ensuring the transferability of the results between the investigated glass types, the derivation of the PFCDFs was, not only based on the own experimental results of each glass type, but also on the results of the remainder glass types. In this sense, Figure 3.64 sets out the predicted failure probability of annealed glass with the corresponding confidence intervals of 5% and 95%.

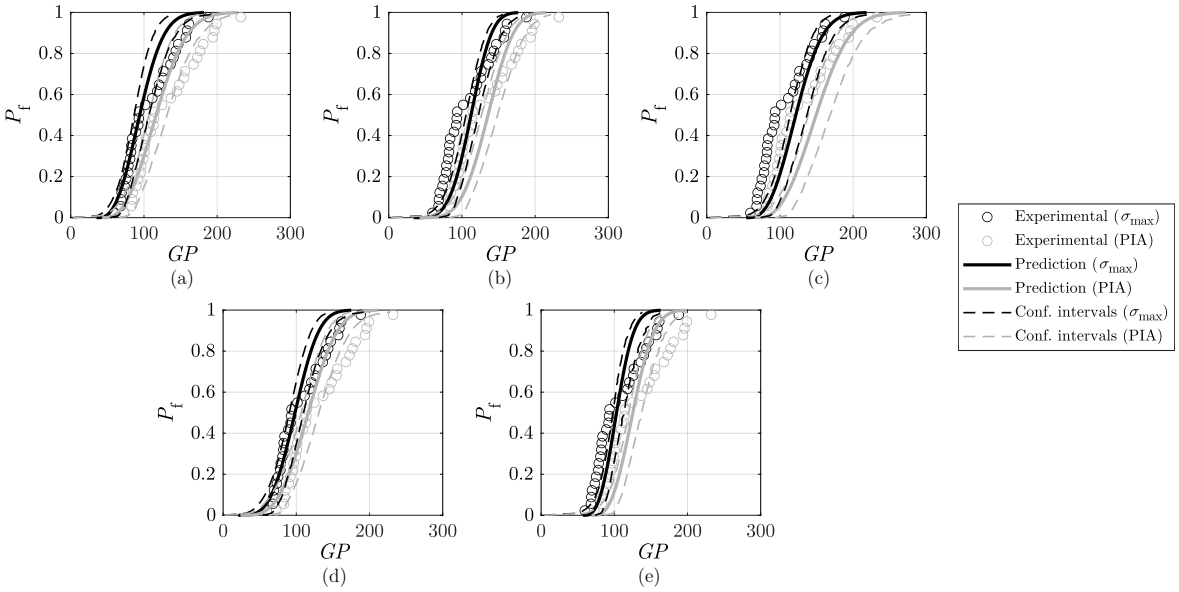

Figure 3.64: Failure probability prediction of annealed glass plates considering the PFCDF based on maximum principal stress and PIA failure criteria and derive from: (a) own experiments, (b) STHD20, (c) STHD40, (d) ATHD20 and (e) ATHD40.

The predictions were based on the Weibull parameters derived from its own experimental data, being in this case annealed glass, and the remainder glass types, i.e. heat treated glass. The predictions were observed to be in good agreement with the annealed glass experimental data. Based on its own experiments, short distance symmetric tempering (STHD20) and asymmetric tempering cases, the relative average error of the predictions remained below 10%. The average deviation increased to 15% for the large distance symmetric tempering case (STHD40). Nonetheless, even if specific regions were found not to be within the reliability intervals, in general the calculated intervals tended to envelop the experimental measurements. The reason for this may be the limited number of the experimental tests that were carried out. Nevertheless, the predictions based on different glass types were observed to behave in a representative manner. Likewise, both failure criteria showed an appropriate representativeness of the experimental results, being the criterion of maximum principal stress the one exhibiting lower deviations. Nevertheless, these differences were considered not significant as they remained below 1% between both failure criteria. Moving forward to the analysis of tempered glass, Figure 3.65 presents the probability prediction as well as the confidence intervals of 5% and 95% for symmetrically tempered glass plates at $H/D = 20$.

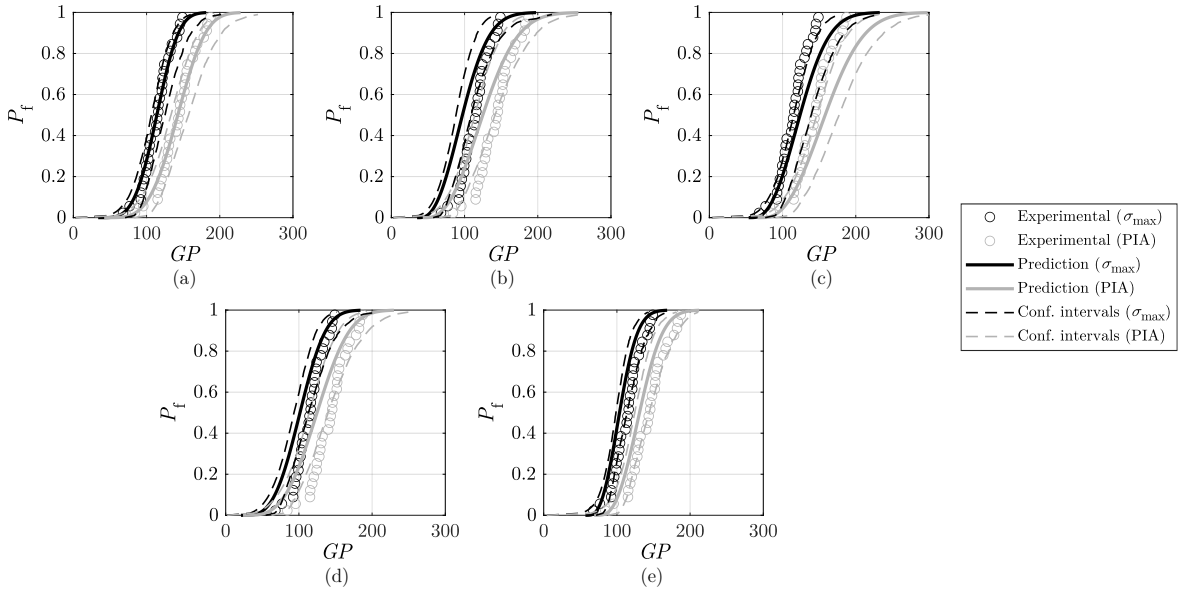

Figure 3.65: Failure probability prediction of symmetrically tempered glass ($H/D = 20$) considering the PFCDF based on maximum principal stress and PIA failure criteria and derive from: (a) own experiments, (b) AA, (c) STHD40, (d) ATHD20 and (e) ATHD40.

Predictions based on its own data were found to be in agreement with experimental data as differences up to 5% were observed. In this case, the maximum average difference increased to 12%. Likewise, the experimental results were for the most part within the confidence intervals. Figure 3.66 plots the prediction of symmetrically tempered glass plates at $H/D = 40$ with the corresponding 5%-95% intervals.

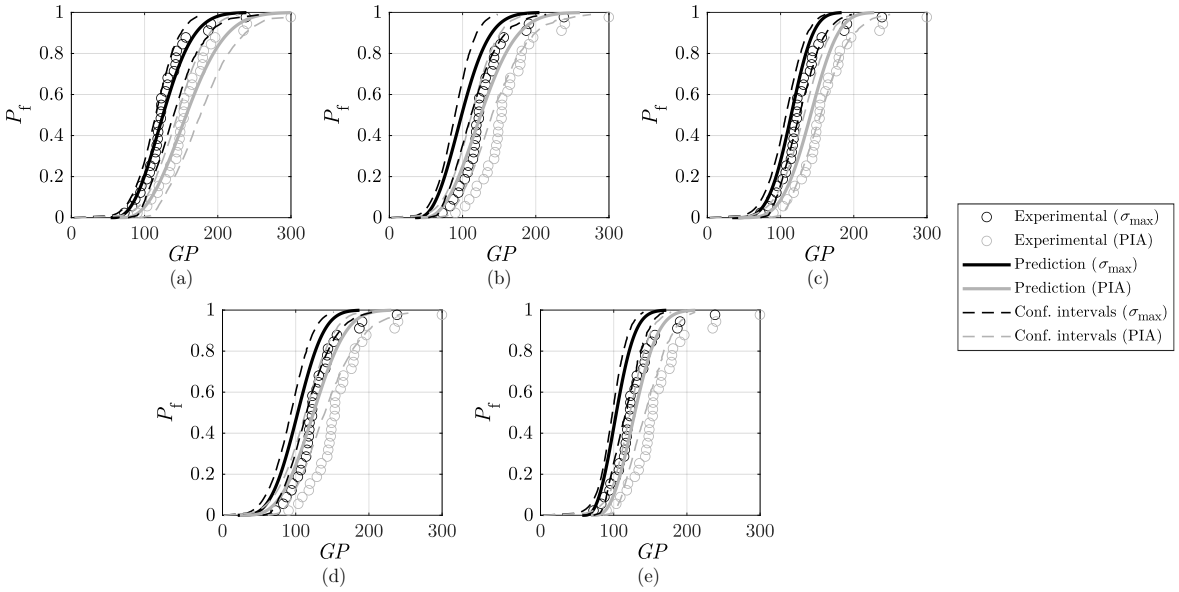

Figure 3.66: Failure probability prediction of symmetrically tempered glass ($H/D = 40$) considering the PFCDF based on maximum principal stress and PIA failure criteria and derive from: (a) own experiments, (b) AA, (c) STHD20, (d) ATHD20 and (e) ATHD40.

In this case, the average deviation between the experimental and predicted values based on their own experiments, annealed glass and short distance symmetric tempering and asymmetrically tempered glass, remained at 5%, 20%, 7%, and 18%, respectively. Similarly, even if the considered failure criteria showed analogous results, the maximum principal stress criterion showed lower variations being the difference as compared to the PIA criterion up to 2%.

Similar conclusions could be drawn for the asymmetrically tempered glass cases. Figure 3.67 sets out the estimated probabilities of failure of asymmetrically tempered glass plates at $H/D = 20$ with the corresponding confidence intervals of 5% and 95%.

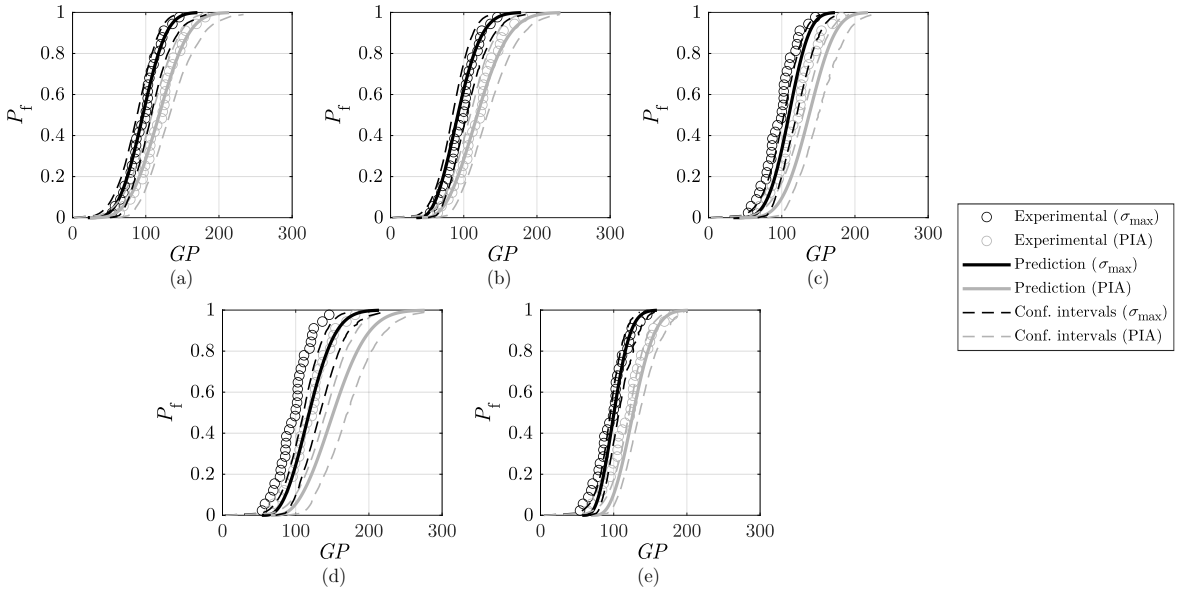

Figure 3.67: Failure probability prediction of asymmetrically tempered glass ($H/D = 20$) considering the PFCDF based on maximum principal stress and PIA failure criteria and derive from: (a) own experiments, (b) AA, (c) STHD20, (d) STHD40 and (e) ATHD40.

Predictions based on annealed or asymmetrically tempered experimental data were observed to be in good agreement as the average differences were below 10%. Based on STHD20 and STHD40 the relative average error increased up to 15% and 25%, respectively. In the same manner, the calculated probabilities of failure of asymmetrically tempered glass plates at $H/D = 40$ are presented in Figure 3.68.

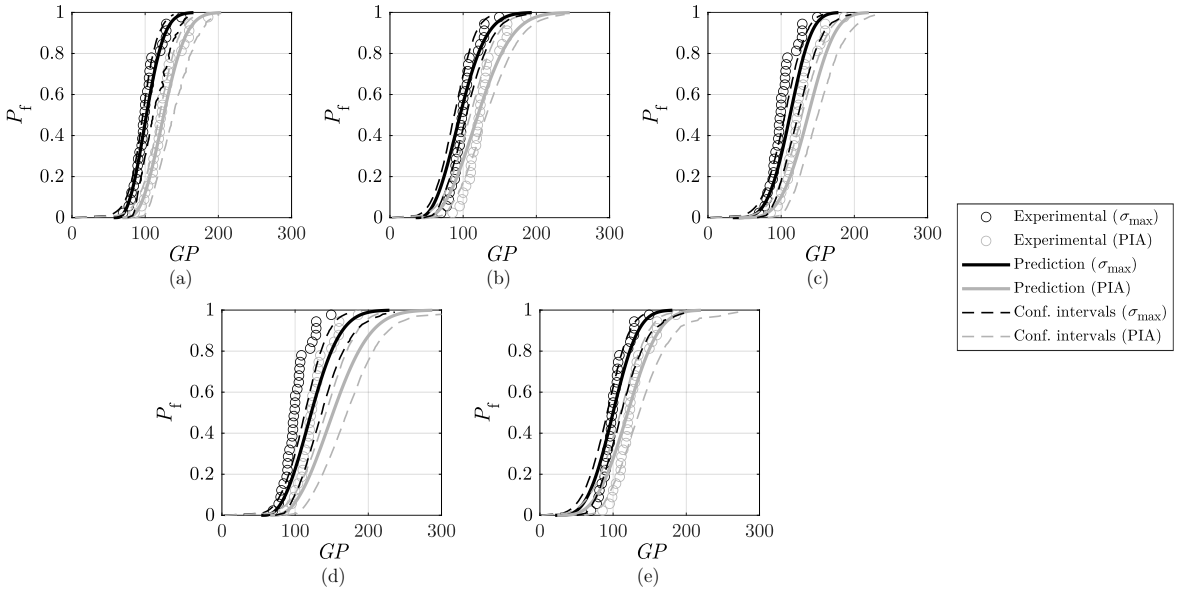

Figure 3.68: Failure probability prediction of asymmetrically tempered glass ($H/D = 40$) considering the PFCDF based on maximum principal stress and PIA failure criteria and derive from: (a) own experiments, (b) AA, (c) STHD20, (d) STHD40 and (e) ATHD20.

Average relative differences up to 10% were observed in the predictions based in annealed, short distance symmetric tempering and asymmetric tempering cases. Larger differences up to 20% in the estimations derived from the large distance symmetrical tempering case were noticed. In this way, the transferability between the cumulative damage functions of annealed and tempered glass was proved. Finally, Figure 3.69 shows the predictions made for tempered glass specimens based on the PFCDF derived from annealed glass experimental data.

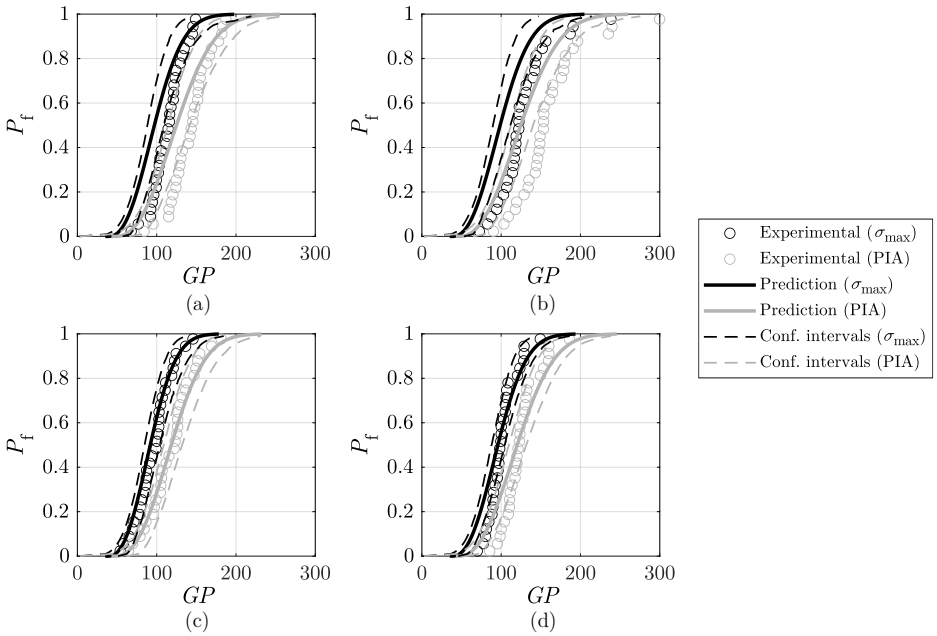

Figure 3.69: Failure probability of tempered glass plates considering the PFCDF based on maximum principal stress and PIA failure criteria and derive from annealed glass experimental data: (a) STHD20, (b) STHD40, (c) ATHD20 and (d) ATHD40.

What is striking about the data in this figure is that the failure characterisation of annealed glass components could enable the estimation of the probability of failure of heat treated glass. As a result, the large experimental work needed for characterising the failure of structural glass components could be simplified due to the versatility that the obtained results exhibited.

In summary, predictions were found to be in good agreement with experimental data as broadly lied within the confidence intervals. Both failure criteria were considered to be representative as the predictability of the probability of failure was found to be analogous. Slightly lower differences were observed with the maximum principal stress criterion, even if it did not account for the biaxial feature of the CDR test. As the maximum principal stress criterion also implied an easier implementation than the PIA, this failure criterion was adopted for the subsequent analysis. Even though, this would be a fruitful area for further work. Finally, transferability of the results from one glass type to another was verified. For this reason, the next section moves on to perform a joint assessment to derive the generalised Weibull parameters, which enabled the calculation of a master PFCDF.

3.4.5 Joint test statistical assessment

Once the transferability from one glass type to another was checked, the joint statistical evaluation of the experimental results was carried out. The aim of this analysis is to obtain a master PFCDF derived by merging different experimental programs, which exhibits a higher level of reliability than the PFCDFs obtained from individual experimental programs. For this purpose, the following joint experimental analyses were proposed:

- Symmetrical tempering tests (ST): symetrically tempered samples STHD20 and STHD40 were considered.
- Asymmetrical tempering tests (AT): asymetrically tempered samples ATHD20 and ATHD40 were considered.
- Short jet-to-plate distance tempering tests (HD20): samples tempered at a jet-to-plate distance $H/D = 20$ were taken into account, namely, STHD20 and ATHD20.
- Large jet-to-plate distance tempering tests (HD40): samples tempered at a jet-to-plate distance $H/D = 40$ were taken into account; STHD40 and ATHD40.
- Merging of all the experimental tests (ALL): all the tested samples were taken into account; AA, STHD20, STHD40, ATHD20 and ATHD40.

First, joint evaluations based on similar tempering features were first addressed; ST, AT, HD20 and HD40. Then, the transferability of the results was verified. As a result, the mode of failure was assumed to be preserved and all the tested samples were employed to carry out a complete joint assessment (ALL). Finally, the effect of increasing the amount of tested samples on the predictions was investigated. Table 3.6 presents the Weibull parameters for the joint assessment based on the maximum principal stress criterion.

Table 3.6: Estimated Weibull parameters based on statistical joint assessment considering the maximum principal stress criterion.

	β	λ	δ
ST	2.25	48.2	3.16
AT	3.52	25.07	10.32
HD20	3.98	14.83	15.82
HD40	2	59.82	1.4
ALL	2.04	41.72	2.33

In this context, Figure 3.70 sets out the comparisons between the predictions of annealed glass failure based on tempered glass data.

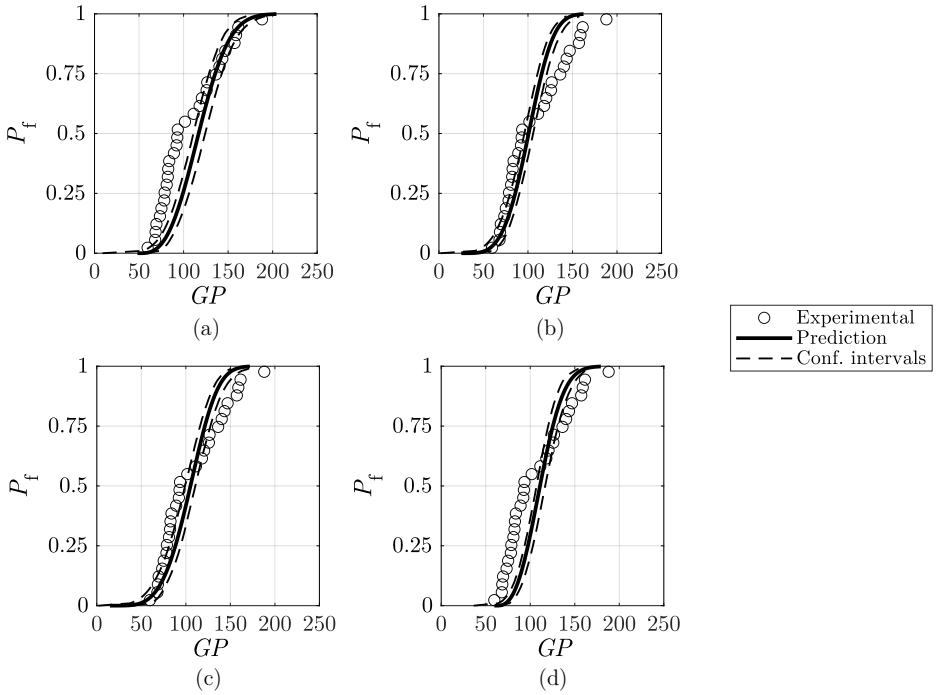

Figure 3.70: Joint evaluation of the failure probability of annealed glass based on the master PFCDF derived from: (a) ST, (b) AT, (c) HD20 and (d) HD40.

As observed, the transferability of the results is maintained. With regard to the relative average difference, it remained below 10%. Similarly, a shrinkage of the confidence intervals occurred due to the larger statistical population employed to derive the PFCDF. Figure 3.71 shows the predicted fracture behaviour of symmetrically tempered glass at $H/D = 20$ based on asymmetrical tempering data and large distance tempering tests.

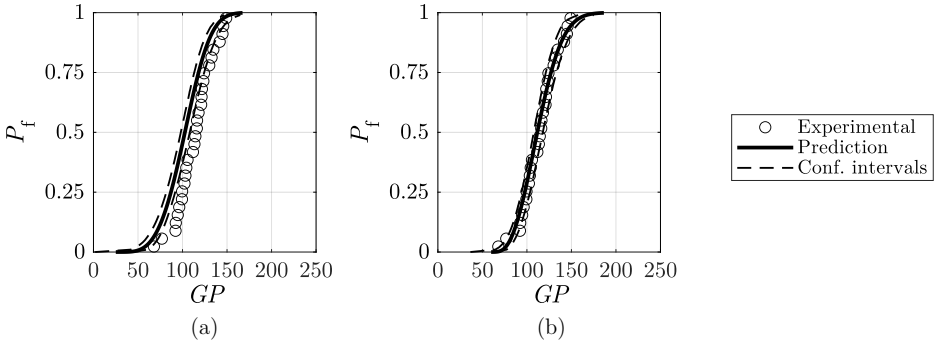

Figure 3.71: Joint evaluation of the failure probability of symmetrically tempered glass ($H/D = 20$) based on the master PFCDF derived from: (a) AT and (b) HD40.

An average relative difference up to 10% was observed for this glass type. Figure 3.72 provides the predicted fracture behaviour of symmetrically tempered glass at $H/D = 40$ based on asymmetrical tempering data and short distance tempering tests.

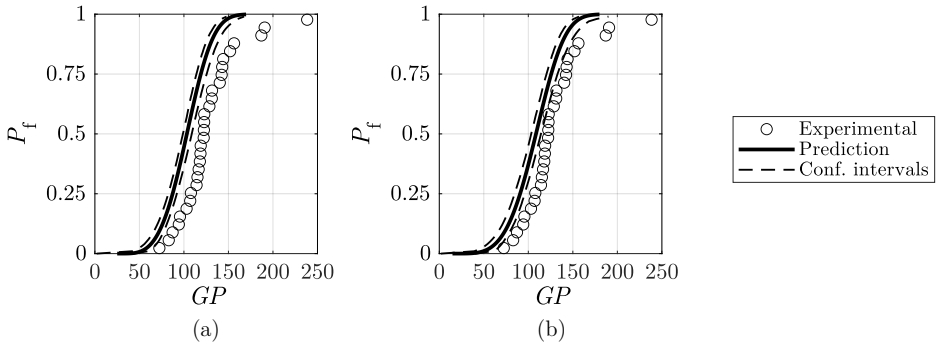

Figure 3.72: Joint evaluation of the failure probability of symmetrically tempered glass ($H/D = 40$) based on the master PFCDF derived from: (a) AT and (b) HD20.

In this case, the maximum average difference remained at 18%. Figure 3.73 presents the estimated probability of failure of asymmetrically tempered glass at $H/D = 20$ based on symmetrical tempering data and large distance tempering tests.

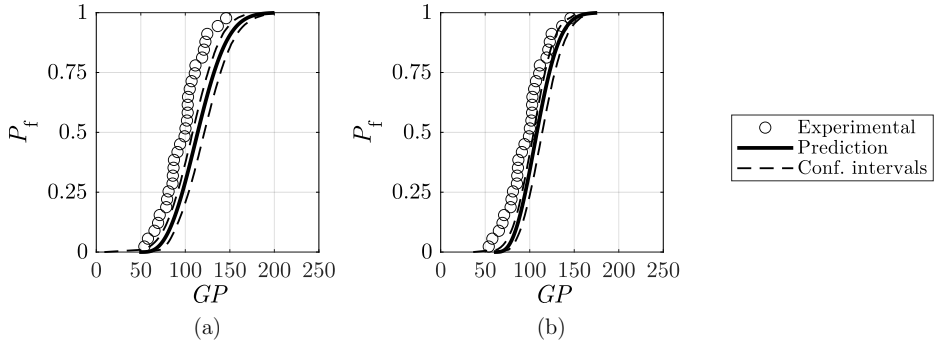

Figure 3.73: Joint evaluation of the failure probability of asymmetrically tempered glass ($H/D = 20$) based on the master PFCDF derived from: (a) ST and (b) HD40.

The estimations based on symmetrical tempering data led to an average difference up to 19%. In the same manner, Figure 3.74 shows the prediction made for asymmetrically tempered glass at $H/D = 40$ based on symmetrical tempering data and short distance tempering tests.

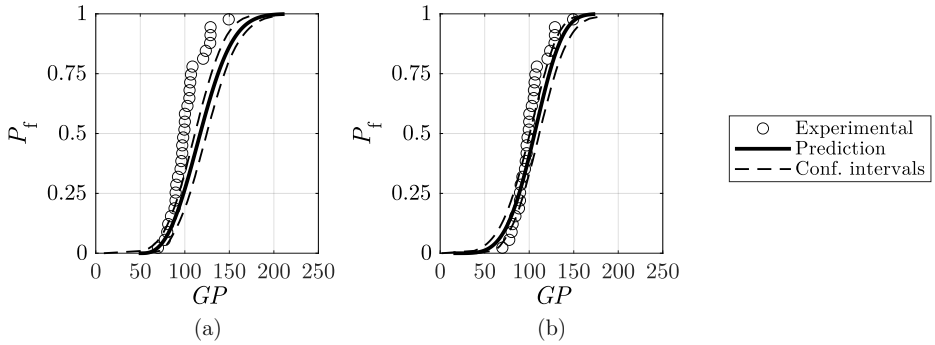

Figure 3.74: Joint evaluation of the failure probability of asymmetrically tempered glass ($H/D = 40$) based on the master PFCDF derived from: (a) ST and (b) HD20.

In this case, the prediction based on symmetrical tempering data performed well in the left-hand tail region but exhibited larger deviations at larger probabilities of failure. Altogether, the maximum average error referred to 15%. Finally, Figure 3.75 sets out the comparisons between the predictions and the experimental data of each analysed glass type based on the joining of all the experimental batches.

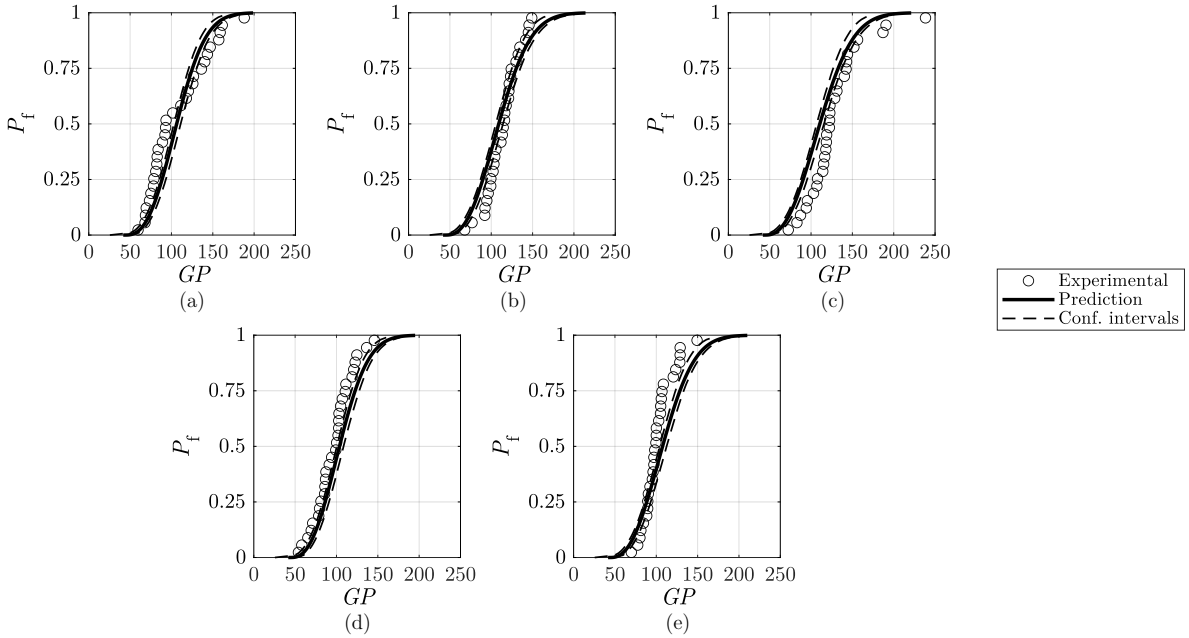

Figure 3.75: Joint evaluation based on the merging of all the experimental tests to predict the failure probability of: (a) AA, (b) STHD20, (c) STHD40, (d) ATHD20, and (e) ATHD40.

As observed, the derived master PFCDF permitted to reliably represent the probability of failure of all the investigated glass types. In this case, the predicted failure probabilities showed an average

error up to 10% as compared to experimental measurements. Additionally, experimental data broadly fell within the confidence intervals meaning that reliable predictions were obtained. Thus, the derived PFCDF was considered appropriate to predict the fracture behaviour of annealed and tempered glass.

Taken together, the derived master PFCDFs permitted a more reliable representation of the probability of failure of the investigated glass types due to the larger data points employed. Additionally, the average relative difference remained about 10%. Consequently, the versatility of the procedure for predicting the fracture behaviour of annealed and tempered glass was verified.

3.5 Conclusions

A methodology to assess the failure of pre-stressed glass components has been presented and validated in this chapter. The main conclusions are set out below:

- A statistical-numerical model to evaluate the fracture probability of tempered glass components was presented. The model accounts for any non-uniform residual stress distribution that may arise during the manufacturing or heat treatment process of glass. The model is able to predict the probability of failure of a component considering the local stress distribution when an external bending load is applied. This model makes the ad hoc design of heat treatment processes early in the production cycle possible, based on both, the operational load distribution and the required failure probability specified by the client.
- The transferability between the failure cumulative functions of annealed and tempered glass exhibiting different residual stress patterns was confirmed. As a result, a PFCDF independent from the experimental sample shape, size and load was derived by means of the GLM. Therefore, the failure characterisation of annealed or tempered plates was proved to be valid to assess the fracture design of either glass type. This meant that for the analysed case studies, the failure mode remained unaltered irrespective of the initial residual stress distribution. Consequently, the need for resource-heavy large-scale experimental programs is reduced, which was previously the main drawback of assessing the in-service behaviour of pre-stressed glass.
- Once the transferability from one glass type to another was confirmed, all the experimental tests were merged by means of the joint statistical evaluation. As a result, a master Primary Failure Cumulative Damage Function (PFCDF) was calculated. The joint assessment facilitated a more reliable prediction of the fracture behaviour of annealed and tempered glass. Overall, average relative differences between the predicted and experimental data were below 10%. Thus, the versatility of the procedure was verified.
- Regarding failure criteria, different approaches were adopted, namely, the maximum principal stress and the PIA criteria. Both showed analogous predictive behaviour for the analysed case studies, with differences between them below 2%. The maximum principal stress criterion was therefore selected due to its easier implementation. Nonetheless, further efforts might be needed to obtain more in-depth knowledge about the influence of the failure criterion selection when considering residual stresses.
- Of particular note was the scatter band of the experimental results. Fracture strength data ranged from 50 and 250 MPa, resulting in a dispersion of 200 MPa. Thus, an enhancement of

the model could be expected if the number of tested samples was increased. This great variation in glass strength would suggest that statistical evaluation should be a mandatory step in the design and assessment of structural pre-stressed components.

Chapter 4

Conclusions and future work

The main objective of this study was to provide a numerical methodology to predict the in-service behaviour of glass plates subjected to bending loads considering the residual stresses developed during the glass cooling process. Two main contributions were developed in the course of the research::

- A sequentially coupled FSI numerical methodology for calculating residual stresses in glass plates subjected to non-uniform cooling during the tempering process.
- A probabilistic methodology to assess the in-service behaviour of heat treated glass components considering the residual stress pattern.

Hereafter, the general conclusions of the thesis are presented together with insights for future work.

4.1 Conclusions

A one-way coupling FSI model consisting of a CFD model and a FEM model was defined with the view to calculating residual stress distributions after the heat treatment process. It was found that local flow phenomena during heat treatment process play a vital role in residual stress development in glass plates. Therefore, non-uniform cooling techniques need to be considered to obtain representative residual stress distributions. In addition, the proposed numerical FSI procedure was validated in both, single jet cooling laboratory tests and an industrial case study composed by a multiple-nozzle array.

Subsequently, several computational cost reduction techniques were evaluated to optimise the efficiency of the methodology. Firstly, the influence of volumetric radiation on residual stresses was studied. As the air jet velocity was increased or the thickness of the parts decreased, the cooling rate increased and the effect of radiation on the residual stress pattern lessened. For this reason, the analysed case studies showed a similar residual stress pattern when radiation was disregarded. Nevertheless, these findings cannot be extrapolated to all tempering case studies, as discrepancies might appear when lower air flow velocities or higher thickness are defined. These results do, however, provide support for the hypothesis that radiation could be disregarded when low thickness glass is subjected to large heat extractions. In

the present study, this was true for any plate thickness of up to 6 mm. For thicker components though, volumetric radiation might play an important role in thermal distribution within the material and a more thorough analysis may be required. Notwithstanding, the presented FSI methodology continues to be useful for analysing thicker components or low cooling rate applications as it can account for volumetric radiation. Nonetheless, following the proposed hypothesis of disregarding radiation for large cooling rate situations, a reduction of 75% of the total computational time was achieved. This is a significant outcome, considering that the main drawback of the FSI one-way procedure, is the computational cost.

Secondly, the existence of a critical temperature was verified. The influence of structural relaxation on the volumetric expansion of glass lost traction at 400 °C. Thus, when the hottest point of the plate attained this temperature, the critical temperature was reached and the subsequent cooling technique no longer influenced residual stress development. In other words, residual stresses became cooling rate independent within the range from natural to forced convection cooling. This hypothesis resulted in an additional saving of 50% of the computational cost, bringing about a total reduction of around 87% of the computational time as compared to the initially proposed procedure.

The assumption of considering steady or transient HTC introduced a larger discrepancy into the analysis. The approach could be valid in particular areas of interest, as differences in specific locations of the quenched part remained low. However, greater differences in the HTC and residual stress patterns were observed in the regions where crossflow was observed, namely, the dry regions. Even if the air speed through the perforated metal sheet was constant, the large drop in temperature of the plate during the tempering process caused a variation in the temperature difference between the target surface and the impinging air over time. Consequently, the thermophysical properties of air also varied which had a direct impact on the interacting jet flow regime and the resultant convective HTC. In this sense, laboratory tests quenched by a single jet on each side of the specimens could lead to unrepresentative findings as no crossflow phenomena occurred. Hence, the nature of the flow in each particular case should be first addressed.

Accordingly, the proposed numerical procedure encompasses both, a CFD model without volumetric radiation to capture the transient local flow phenomena until the critical temperature is attained, and a thermal model where a constant in time and spatially uniform HTC is applied. As a result, the procedure was found to reliably model low thickness quenching processes in both, laboratory and industrial environments.

On the other hand, a probabilistic assessment of the risk of failure of tempered glass components subjected to bending loads was carried out. For this purpose, dissimilar non-uniform residual stress patterns developed during the heat treatment process were taken into account.

The GLM was used to derive the corresponding PFCDFs. The aim was not to pinpoint the specific mechanism that contributes to fracture, but to consider all the variables influencing the entire flaw population. In this way, the transferability of the results based on annealed and tempered glass exhibiting different residual stress patterns was verified. This is a noteworthy outcome, as it eliminates the need for the characterisation of each type of glass. As a result, the total experimental effort required, as well as the involved economic cost, can be significantly reduced.

Similarly, the joint assessment of the performed experimental work permitted the calculation of master PFCDFs, which led to a more reliable prediction of the fracture behaviour of annealed and tempered glass. Overall, average relative differences of below 10% were observed between the predicted and

experimental data. The wide scatter bands exhibited by the experimental results highlight the need to test a representative amount of samples to assess glass fracture. It was proved that, if the fracture mode and failure criterion remained unaltered, the joint assessment could reduce the amount of tests required for a specific glass type by merging diverse experimental data from already performed tests. In this way, the versatility of the procedure was confirmed. Thus, the insights gained from this study can contribute to the development of a data-base, which becomes more reliable as the stored data grows.

In summary, the results demonstrate that the presented methodology can predict the in-service behaviour of glass components from an early stage of the manufacturing process, namely, the design stage. Representative residual stress distributions developed during the tempering process of low thickness parts were also successfully obtained. Similarly, the risk of failure for different tempering scenarios was also estimated by means of statistical assessment. The use of this methodology can therefore assist designers in defining efficient heat treatment procedures to obtain the required tempering state based on ad hoc in-service conditions. Consequently, the proposed numerical methodology can minimise the need for the design, manufacturing and testing of prototypes, which would result in a significant reduction in manufacturing costs and cycle time.

4.2 Future Work

The present research has contributed to enhancing the understanding of residual stress development during the tempering process and highlighted its importance for subsequent failure assessment. Nevertheless, this research has opened up many issues for further investigation.

With regard to the numerical FSI model, turbulence is known to have a great influence on the heat transfer performance of jet impingement applications. With this in mind, continued efforts should be made to further calibrate the RANS turbulence models that have been employed. Additionally, numerical solutions, such as those based on LES, should be tested. Such methods require fine grids, and thus, low time step sizes, to solve the scales of turbulence of the flow. Consequently, they involve a high computational cost. Nevertheless, its impact on the residual stress development during heat treatment process could be worthy of exploration.

Additionally, further research should be undertaken to explore the feasibility of diverse cooling strategies for industrial applications. Cooling techniques involving spray mist cooling or steam on moving glass plates could result in effective tempering results on even thinner glass plates, due to the high latent heat of vaporisation of water droplets. Likewise, the design of cooling strategies encompassing pulsed jets, swirling jets, or interrupt quenching techniques could be of great interest. More importantly, the consideration of local flow phenomena might prove effective in the prediction of in-process breakage of components during cooling.

In the assessment of failure of pre-stressed glass, bending loads were considered to be the main loads acting on glass components. Nevertheless, a natural progression of this work would be to extend the analysis to fatigue, thermal shock, and impact loading configurations. Similarly, damage to the glass surface might result from many factors, such as, inappropriate usage, cleaning of building façades or solar panels, unexpected impacts, or the erosive action of natural weathering. This damage usually results in surface scratches, which may have a direct effect on the structural performance of components. Further investigation in this field could greatly assist the development of predictive models to determine

the in-service behaviour of tempered glass with noticeable surface damage. In this way, the structural integrity of tempered glass, which plays a vital role in the daily life of people, could be further assessed.

Finally, this methodology can be applicable for not only the glass industry, but also the heat-treating industry as a whole. There are a significant number of processes in which residual stresses and workpiece distortion are a concern for subsequent in-service analysis. Thus, the expected benefits from the implementation of this methodology include higher part quality, increased productivity, the elimination or decrease of scrap, and the removal of costly trial-and-error prototype testing or heat treatment operations. In the same vein, many engineering problems are focused on predicting microstructural distributions in heat treated parts, which in fact, is strongly linked to thermal history and local temperature distribution. Thus, microstructural variation within the part after the heat treatment process could be an additional implementation. Taken together, these are important issues for future research.

4.3 Scientific contributions

A. Iglesias, M. Martinez-Agirre, I. Torca, I. Llavori, and J.A. Esnaola. "Numerical methodology based on fluid-structure interaction to predict the residual stress distribution in glass tempering considering non-uniform cooling". In: *Computers & Structures* 264, 2022.

Bibliography

[1] Glaston Corporation. *Capital Markets Day 2021*. Tech. rep. August. 2021. URL: https://glaston.net/reports-and-presentations/#reports-and-presentations.

[2] F. Oikonomopoulou, T. Bristogianni, L. Barou, F. A. Veer, and R. Nijsse. "The potential of cast glass in structural applications. Lessons learned from large-scale castings and state-of-the art load-bearing cast glass in architecture." In: *Journal of Building Engineering* 20.June (2018), pp. 213–234. ISSN: 23527102. DOI: 10.1016/j.jobe.2018.07.014.

[3] F. Bos and C. Louter. "Structural Glass in Architecture." In: *Encyclopedia of Glass Science, Technology, History, and Culture*. Ed. by P. Richet, R. Conradt, A. Takada, and J. Dyon. Vol. II. 2021, pp. 1071–1090. DOI: 10.1002/9781118801017.ch9.1.

[4] S. J. Brown, K. L. Bratton, P. S. L. Ngankeu, and P. Stargardter. *Cooling tube nozzle for a post-manufacture glass container thermal strengthening station*. 2014.

[5] F. A. Veer. "The strength of glass, a nontransparent value." In: *Heron* 52.1-2 (2007), pp. 87–104. ISSN: 00467316.

[6] R. A. McMaster. "Flat Glass Tempering - How It Works." In: *Glass Industry* (1989), pp. 10–15.

[7] A. K. Varshneya. "Chemical Strengthening of Glass: Lessons Learned and Yet To Be Learned." In: *International Journal of Applied Glass Science* 1 (2010), pp. 131–142. ISSN: 20411286. DOI: 10.1111/j.2041-1294.2010.00010.x. arXiv: arXiv:1011.1669v3.

[8] S. Karlsson, B. Jonson, and C. Stålhandske. "The technology of chemical glass strengthening - A review." In: *Glass Technology: European Journal of Glass Science and Technology Part A* 51.2 (2010), pp. 41–54. ISSN: 00171050. DOI: 10.1128/MCB.23.4.1181-1195.2003.

[9] A. Berenjian and G. Whittleston. "History and manufacturing of glass Title History and manufacturing of glass History and Manufacturing of Glass." In: *American Journal of Materials Science* 1 (2017), pp. 18–24. ISSN: 2162-8424. DOI: 10.5923/j.materials.20170701.03.

[10] R. Hess. "Material Glass." In: *Structural Engineering International: Journal of the International Association for Bridge and Structural Engineering (IABSE)* 14.2 (2004), pp. 76–79.

[11] K. C. Datsiou and M. Overend. "The strength of aged glass." In: *Glass Structures & Engineering* 2.2 (2017), pp. 105–120. ISSN: 2363-5142. DOI: 10.1007/s40940-017-0045-6. URL: http://link.springer.com/10.1007/s40940-017-0045-6.

[12] R. Gy. "Ion exchange for glass strengthening." In: *Materials Science and Engineering B: Solid-State Materials for Advanced Technology* 149.2 (2008), pp. 159–165. ISSN: 09215107. DOI: 10.1016/j.mseb.2007.11.029.

[13] R. Gardon. "Thermal Tempering of Glass." In: *Glass Science and Technology*. Ed. by D.R. Uhlmann and N.J. Kreidl. Academic Press, Inc., 1980, pp. 145–216. ISBN: 0927-4472. DOI: 10.1016/B978-0-12-706705-6.50010-2.

[14] P. J. Lezzi, R. O. Maschmeyer, J. C. Thomas, and K. L. Wasson. *Thermally tempered glass and methods and apparatuses for thermal tempering of glass*. 2016.

[15] L. H. Adams and E. D. Williamson. "The annealing of glass." In: *Journal of the Franklin Institute* 190.5 (1920), pp. 597–631. ISSN: 00160032. DOI: 10.1016/S0016-0032(10)91090-9.

[16] E. H. Lee, T. G. Rogers, and T. C. Woo. "Residual Stresses in a Glass Plate Cooled Symmetrically from Both Surfaces." In: *Journal of the American Ceramic Society* 48.9 (1965), pp. 480–487. ISSN: 15512916. DOI: 10.1111/j.1151-2916.1965.tb14805.x.

[17] O. S. Narayanaswamy. "Model of Structural Relaxation in Glass." In: *Journal of the American Ceramic Society* 54.10 (1971), pp. 491–498. DOI: 10.1111/j.1151-2916.1971.tb12186.x.

[18] O. S. Narayanaswamy. "Stress and structural relaxation in tempering glass." In: *Journal of the American Ceramic Society* 61.3-4 (1978), pp. 146–152.

[19] H. Carre and L. Daudeville. "Numerical Simulation of Soda-Lime Silicate Glass Tempering." In: *Journal de Physique IV* 6 (1996), pp. 175–185.

[20] K. Agboka, F. Béchet, N. Siedow, and D. Lochegnies. "Influence of radiative heat transfer model on the computation of residual stresses in glass tempering process." In: *International Journal of Applied Glass Science* 9.2 (2018), pp. 235–251. ISSN: 20411294. DOI: 10.1111/ijag.12335.

[21] F. P. Incropera, D. P. Dewitt, T. L. Bergman, and A. S. Lavine. *Fundamentals of heat and mass transfer*. Sixth edit. 1986. John Wiley & Sons, 2007, p. 1070. ISBN: 9780471457282. DOI: 10.1109/TKDE.2004.30. arXiv: 1105-.

[22] L. Daudeville and H. Carré. "Thermal tempering simulation of glass plates: Inner and edge residual stresses." In: *Journal of Thermal Stresses* 21.6 (1998), pp. 667–689. ISSN: 1521074X. DOI: 10.1080/01495739808956168.

[23] J. H. Nielsen, J. F. Olesen, P. N. Poulsen, and H. Stang. "Simulation of residual stresses at holes in tempered glass: A parametric study." In: *Materials and Structures/Materiaux et Constructions* 43.7 (2010), pp. 947–961. ISSN: 13595997. DOI: 10.1617/s11527-009-9558-z.

[24] N. Pourmoghaddam, J. H. Nielsen, and J. Schneider. "Numerical simulation of residual stresses at holes near edges and corners in tempered glass: A parametric study." In: *Engineered Transparency*. Ed. by Jens; Schneider and Bernhard; Weller. Wiley, 2016.

[25] N. Pourmoghaddam and J. Schneider. "Finite-element analysis of the residual stresses in tempered glass plates with holes or cut-outs." In: *Glass Structures & Engineering* February (2018). ISSN: 2363-5142. DOI: 10.1007/s40940-018-0055-z.

[26] A. Mikkonen, A. Aronen, M. Rantala, and R. Karvinen. "Effects of non-uniform heat transfer in a tempering process on glass quality." In: *Glass Performance Days GDP 2017*. 2017.

[27] M. Reich, S. Schöne, O. Kessler, M. Nowak, O. Grydin, F. Nürnberger, and M. Schaper. "Simulation of Gas and Spray Quenching during Extrusion of Aluminium Alloys." In: *Key Engineering Materials* 424 (2010), pp. 57–64. DOI: 10.4028/www.scientific.net/kem.424.57.

[28] D. D. Hall and I. Mudawar. "Experimental and numerical study of quenching complex-shaped metallic alloys with multiple, overlapping sprays." In: *International Journal of Heat and Mass Transfer* 38.7 (1995), pp. 1201–1216. ISSN: 00179310. DOI: 10.1016/0017-9310(94)00244-P.

[29] D. D. Hall and I. Mudawar. "Optimization of quench history of aluminum parts for superior mechanical properties." In: *International Journal of Heat and Mass Transfer* 39.1 (1996), pp. 81–95. ISSN: 00179310. DOI: 10.1016/S0017-9310(96)85008-3.

[30] D. D. Hall, I. Mudawar, R. E. Morgan, and S. L. Ehlers. "Validation of a systematic approach to modeling spray quenching of aluminum alloy extrusions, composites, and continuous castings." In: *Journal of Materials Engineering and Performance* 6.1 (1997), pp. 77–92. ISSN: 10599495. DOI: 10.1007/s11665-997-0036-x.

[31] S. Schüttenberg, J. Lütjens, M. Hunkel, and U. Fritsching. "Adapted spray quenching for distortion control." In: *Materialwissenschaft und Werkstofftechnik* 43.1-2 (2012), pp. 99–104. ISSN: 09335137. DOI: 10.1002/mawe.201100895.

[32] M. Brzoza, E. Specht, J. Ohland, O. Belkessam, T. Lübben, and U. Fritsching. "Minimizing stress and distortion for shafts and discs by controlled quenching in a field of nozzles." In: *Materialwissenschaft und Werkstofftechnik* 37.1 (2006), pp. 97–102. ISSN: 09335137. DOI: 10.1002/mawe.200500970.

[33] M. Soltani, A. Pola, and G. M. La Vecchia. "Computational Model For Spray Quenching Of A Heavy Forging." In: *Proceedings 28th European Conference on Modelling and Simulation*. Brescia, Italy, 2014. ISBN: 9780956494481. DOI: 10.7148/2014-0292.

[34] F. Monnoyer and D. Lochegnies. "Heat transfer and flow characteristics of the cooling system of an industrial glass tempering unit." In: *Applied Thermal Engineering* 28.17-18 (2008), pp. 2167–2177. ISSN: 13594311. DOI: 10.1016/j.applthermaleng.2007.12.014.

[35] J. H. Nielsen, J. F. Olesen, and H. Stang. "Characterization of the Residual Stress State in Commercially Fully Toughened Glass." In: *Journal of Materials in Civil Engineering* 22.2 (2010), pp. 179–185. ISSN: 0899-1561. DOI: 10.1061/(asce)0899-1561(2010)22:2(179).

[36] J. Anton, A. Errapart, M. Paemurru, D. Lochegnies, S. Hödemann, and H. Aben. "On the inhomogeneity of residual stresses in tempered glass panels." In: *Estonian Journal of Engineering* 18.1 (2012), p. 3. ISSN: 1736-6038. DOI: 10.3176/eng.2012.1.01.

[37] K. H. Lee and R. Viskanta. "Quenching of flat glass by impinging air jets." In: *Numerical Heat Transfer; Part A: Applications* 33.1 (1998), pp. 5–22. ISSN: 15210634. DOI: 10.1080/10407789808913925.

[38] M. F. Modest. *Radiative Heat Transfer*. 2nd. Academic Press, Inc., 2003. ISBN: 0125031637.

[39] R. Siegel. "Transient Thermal Effects of Radiant Energy In Semitransparent Materials." In: *Journal of Heat Transfer* 120 (1998), pp. 4–23. ISSN: 0887-8722. DOI: 10.2514/1.16842.

[40] N. Siedow, D. Lochegnies, F. Béchet, P. Moreau, H. Wakatsuki, and N. Inoue. "Axisymmetric modeling of the thermal cooling, including radiation, of a circular glass disk." In: *International Journal of Heat and Mass Transfer* 89 (2015), pp. 414–424. ISSN: 00179310. DOI: 10.1016/j.ijheatmasstransfer.2015.04.091.

[41] CEN. *prEN 13474-1. Glass in building – Design of glass panes – Part 1: General basis of design*. 1999.

[42] Deutsches Institut für Bautechnik (DIBt). *TRAV - Technische Regeln für die Verwendung von absturzsichernden Verglasungen*. 2003.

[43] M. Overend, G. A. R. Parke, and D. Buhagiar. "Predicting Failure in Glass—A General Crack Growth Model." In: *Journal of Structural Engineering* 133.8 (2007). ISSN: 0733-9445. DOI: 10.1061/(ASCE)0733-9445(2007)133:8(1146).

[44] A. Ramos, M. Muniz-Calvente, P. Fernández, A. Fernández-Canteli, and M. J. Lamela. "Análisis probabilístico de elementos de vidrio recocido mediante una distribución triparamétrica Weibull." In: *Boletin de la Sociedad Espanola de Ceramica y Vidrio* 54.4 (2015), pp. 153–158. ISSN: 21730431. DOI: 10.1016/j.bsecv.2015.06.002.

[45] G. Pisano and G. R. Carfagni. "Statistical interference of material strength and surface prestress in heat-treated glass." In: *Journal of the American Ceramic Society* 100.3 (2017), pp. 954–967. ISSN: 15512916. DOI: 10.1111/jace.14608.

[46] J. Belis S. Schula, J. Schneider, M. Vandebroek. "Fracture strength of glass, engineering testing methods and estimation of characteristic values." In: *COST Action TU0905, Mid-term Conference on Structural Glass*. Porec, Croatia, 2013, pp. 223–234.

[47] G. Castori and E. Speranzini. "Fracture strength prediction of float glass: The Coaxial Double Ring test method." In: *Construction and Building Materials* 225 (2019), pp. 1064–1076. ISSN: 09500618. DOI: 10.1016/j.conbuildmat.2019.07.264.

[48] M. Muniz-Calvente, A. M.P. de Jesus, J. A.F.O. Correia, and A. Fernández-Canteli. "A methodology for probabilistic prediction of fatigue crack initiation taking into account the scale effect." In: *Engineering Fracture Mechanics* 185 (2017), pp. 101–113. ISSN: 00137944. DOI: 10.1016/j.engfracmech.2017.04.014. URL: https://doi.org/10.1016/j.engfracmech.2017.04.014.

[49] S. W. Freiman. "Fracture Mechanics of Glass." In: *Glass Science and Technology*. Ed. by D.R. Uhlmann and N.J. Kreidl. Vol. 5. Academic Press, Inc., 1980, pp. 21–78. ISBN: 9780127067056. DOI: 10.1016/B978-0-12-706705-6.50007-2.

[50] S. Mohammadi. *Extended Finite Element Analysis*. Blackwell Publishing Ltd, 2008, p. 277. ISBN: 9781405170604. DOI: 10.1002/9780470697795.

[51] I. Llavori, J. A. Esnaola, A. Zabala, M. Larrañaga, and X. Gomez. "Fretting: Review on the Numerical Simulation and Modeling of Wear, Fatigue and Fracture." In: *Contact and Fracture Mechanics* (2017). DOI: http://dx.doi.org/10.5772/46845.

[52] D. Pietras, T. Sadowski, and L. Wójcik. "Impact of Exploitation Flaws on Load Capacity of Tempered Glass Stairs Assessed by Numerical Analysis with XFEM." In: *7th International Conference on Advanced Materials and Structures - AMS 2018*. Vol. 416. 2018. DOI: 10.1088/1757-899X/416/1/012085.

[53] B. Egboiyi, R. Mattey, S. Konica, P. Nikam, S. Ghosh, and T. Sain. "Mechanistic understanding of the fracture toughening in chemically strengthened glass—experiments and phase-field fracture modeling." In: *International Journal of Solids and Structures* 238.111374 (2022). ISSN: 00207683. DOI: 10.1016/j.ijsolstr.2021.111374.

[54] R. Karvinen and A. Aronen. "Influence of Cooling Jets on Stress Pattern and Anisotropy in Tempered Glass." In: *Glass Performance Days GPD 2019*. 2019.

[55] J. Barr. *The Glass Tempering Handbook - Understanding the Glass Tempering Process*. 2015. URL: http://www.lambertgtservices.co.uk/book/TheGlassTemperingHandbook.pdf.

[56] Y. Chen, D. Lochegnies, R. Defontaine, J. Anton, H. Aben, and R. Langlais. "Measuring the 2D residual surface stress mapping in tempered glass under the cooling jets: The influence of process parameters on the stress homogeneity and isotropy." In: *Strain* 49.1 (2013), pp. 60–67. ISSN: 00392103. DOI: 10.1111/str.12013.

[57] M. Illguth, C. Schuler, and Bucak. "The effect of optical anisotropies on building glass façades and its measurement methods." In: *Frontiers of Architectural Research* 4.2 (2015), pp. 119–126. ISSN: 20952635. DOI: 10.1016/j.foar.2015.01.004. URL: http://dx.doi.org/10.1016/j.foar.2015.01.004.

[58] M. Zaccaria and M. Overend. "Nondestructive Safety Evaluation of Thermally Tempered Glass." In: *Journal of Materials in Civil Engineering* 32.4 (2020). ISSN: 0899-1561. DOI: 10.1061/(asce)mt.1943-5533.0003086.

[59] M. Zier, P. Stenzel, L. Kotzur, and D. Stolten. "A review of decarbonization options for the glass industry." In: *Energy Conversion and Management: X* 10.February (2021). ISSN: 25901745. DOI: 10.1016/j.ecmx.2021.100083.

[60] K. Leitch. "Structural Glass Technology : Systems and Applications." PhD thesis. Massachusetts Institute of Technology, 2005.

[61] M. Hasanuzzaman, A. Rafferty, M. Sajjia, and A.-G. Olabi. "Properties of Glass Materials." In: *Reference Module in Materials Science and Materials Engineering* (2016), pp. 1–12. DOI: 10.1016/B978-0-12-803581-8.03998-9.

[62] M. F. Ashby. "Material profiles." In: *Materials and the Environment*. 2nd. 2013. Chap. 15, pp. 459–595. DOI: 10.1016/B978-0-12-385971-6.00001-4.

[63] S. R. Ledbetter, A. R. Walker, and A. P. Keiller. "Structural Use of Glass." In: *Journal of Architectural Engineering* 12.3 (2006), pp. 137–149. ISSN: 1076-0431. DOI: 10.1061/(ASCE)1076-0431(2006)12:3(137).

[64] S. M. Rekhson. "Viscoelasticity of glass." In: *Glass: Science and Technology - Viscosity and Relaxation*. Ed. by D.R. Uhlmann and N.J. Kreidl. Vol. 3. Academic Press, Inc., 1986. ISBN: 0444997210. DOI: 10.1097/00000433-198206000-00020. arXiv: arXiv:1011.1669v3.

[65] S. Costa, M. Miranda, H. Varum, and F. Teixeira Dias. "On the Evaluation of the Mechanical Behaviour of Structural Glass Elements." In: *Materials Science Forum* 514-516 (2006), pp. 799–803. ISSN: 1662-9752. DOI: 10.4028/www.scientific.net/MSF.514-516.799.

[66] H. S. Norville and E. J. Conrath. "Considerations for blast resistant glazing design." In: *Journal of Architectural Engineering* September (2001), pp. 80–86.

[67] ASTM. *ASTM Standard C1048 - Heat Treated Flat Glass*. 2004th ed. West Conshohocken, PA: ASTM International, 2004, p. 7. URL: www.astm.org.

[68] D. Delincé and D. Callewaert. "Post-breakage behaviour of laminated glass in structural applications." In: *Challenging Glass: Conference on Architectural and Structural Applications of Glass*. Ed. by Freek; Bos, Christian; Louter, and Fred; Veer. IOS Press, 2008, pp. 459–467.

[69] C. Schuler, Ö. Bucak, V. Sackmann, H. Gräf, and G. Albrecht. "Time and temperature dependent mechanical behaviour and durability of laminated safety glass." In: *Structural Engineering International: Journal of the International Association for Bridge and Structural Engineering (IABSE)* 14.2 (2004), pp. 80–83. ISSN: 10168664. DOI: 10.2749/101686604777964026.

[70] R. Gardon. "Calculation of Temperature Distributions in Glass Plates Undergoing Heat-Treatment." In: *Journal of the American Ceramic Society* 41.6 (1958), pp. 200–209. ISSN: 15512916. DOI: 10.1111/j.1151-2916.1958.tb13541.x.

[71] Antti Aronen and Reijo Karvinen. "Effect of glass temperature before cooling and cooling rate on residual stresses in tempering." In: *Glass Structures and Engineering* 3.1 (2018), pp. 3–15. ISSN: 23635150. DOI: 10.1007/s40940-017-0053-6.

[72] ASM. *ASM Handbook: Volume 04 Heat treating*. Ed. by ASM International. 10th ed. 1991. ISBN: 978-0871703798.

[73] B. Liscic, H. M. Tensi, L. C. F. Canale, and G. E. Totten. *Quenching Theory and Technology*. 2010. ISBN: 9780849392795.

[74] E. W. Starr. *Method and apparatus for producing heat-strengthened glass sheets having improved break patterns*. 1983.

[75] D. Colmon and B. Letemps. *Quenching or tempering by means of a two-phase jet*. 1986.

[76] S. Aratani and T. Muramoto. *Method of tempering glass sheet by air quenching*. 1988. DOI: 10.1007/s11113-013-9277-6. arXiv: arXiv:1710.00875v1.

[77] B. J. Thomas, J. Artama, and J. Klemola. *Tempering of glass*. 2005.

[78] S. J. Brown, T. A. Ringuette, K. L. Brathon, S. J. Pinkerton, and M. R. Hyre. *Post-manufacture glass container thermal strengthening method*. 2011. DOI: 10.1037/t24245-000. arXiv: 0403007 [arXiv:physics].

[79] M. Rantala. "Heat Transfer Phenomena in Float Glass Heat Treatment Processes." PhD thesis. Tampere University of Technology, 2015, p. 154. ISBN: 9789521536465.

[80] H. Ohkubo and S. Nishio. "Mist Cooling for Thermal Tempering Glass." In: *JSME International Journal* 31.3 (1988), pp. 444–450.

[81] B. Hinrichs, N. Hornig, S. Schüttenberg, and U. Fritsching. "Controlled spray quenching in heat treatment process." In: *12th Triennial International Conference on Liquid Atomization and Spray Systems*. Heidelberg, Germany, 2012.

[82] C. J. Garciamoreno, D. A. Everest, and A. Atreya. "Heat Transfer in Glass Quenching for Glass Tempering." In: *75th Conference on Glass Problems*. Ed. by S. K. Sundaram. Columbus, Ohio: The American Ceramic Society, 2015, pp. 235–252.

[83] G. Liang and I. Mudawar. "Review of spray cooling – Part 2: High temperature boiling regimes and quenching applications." In: *International Journal of Heat and Mass Transfer* 115 (2017), pp. 1206–1222. ISSN: 00179310. DOI: 10.1016/j.ijheatmasstransfer.2017.06.022.

[84] O.S. Narayanaswamy. "Annealing of glass." In: *Glass: Science and Technology - Viscosity and Relaxation*. Ed. by D.R. Uhlmann and N.J. Kreidl. Academic Press, Inc., 1986, pp. 275–318.

[85] J. H. Nielsen. "Tempered Glass: -Bolted Connections and Related Problems." PhD thesis. Technical University of Denmark, 2009, p. 78. ISBN: 9788778772824. DOI: 10.1016/j.carres.2009.08.031.

[86] A. Q. Tool. "Relation Between Inelastic Deformability and Thermal Expansion of Glass in Its Annealing Range." In: *Journal of the American Ceramic Society* 29.9 (1946), pp. 240–253. ISSN: 15512916. DOI: 10.1111/j.1151-2916.1946.tb11592.x.

[87] C. Guillemet. "Annealing and tempering of glass." In: *Journal of Non-Crystalline Solids* 123 (1990), pp. 415–426.

[88] O. S. Narayanaswamy and R. Gardon. "Calculation of Residual Stresses in Glass." In: *Journal of the American Ceramic Society* 52.10 (1969), pp. 554–558. ISSN: 15512916. DOI: 10.1111/j.1151-2916.1969.tb09163.x.

[89] J. H. Nielsen, J. F. Olesen, P. N. Poulsen, and H. Stang. "Finite element implementation of a glass tempering model in three dimensions." In: *Computers and Structures* 88.17-18 (2010), pp. 963–972. ISSN: 00457949. DOI: 10.1016/j.compstruc.2010.05.004.

[90] F. Bernard, R. Gy, and L. Daudeville. "Finite element computation of residual stresses near holes in tempered glass plates." In: *XIX Int. Congr. Glass*. Vol. 43C. Edinburgh, 2002, pp. 290–295. DOI: 10.4028/www.scientific.net/MSF.404-407.43.

[91] F. Bernard and L. Daudeville. "Point fixings in annealed and tempered glass structures: Modeling and optimization of bolted connections." In: *Engineering Structures* 31.4 (2009), pp. 946–955. ISSN: 01410296. DOI: 10.1016/j.engstruct.2008.12.004.

[92] N. Pourmoghaddam and J. Schneider. "Determination of the engine power for quenching of glass by forced convection : simplified model and experimental validation of residual stress levels." In: *Glass Structures & Engineering* (2018). ISSN: 2363-5150. DOI: 10.1007/s40940-018-0078-5.

[93] Z. X. Wen, Y. L. He, X. W. Cao, and C. Yan. "Numerical study of impinging jets heat transfer with different nozzle geometries and arrangements for a ground fast cooling simulation device." In: *International Journal of Heat and Mass Transfer* 95 (2016), pp. 321–335. ISSN: 00179310. DOI: 10.1016/j.ijheatmasstransfer.2015.12.022.

[94] B. Weigand and S. Spring. "Multiple jet impingement - A review." In: *Int. Symp. on Heat Transfer in Gas Turbine Systems*. Vol. 42. 2. Antalya, Turkey, 2009, pp. 101–142. DOI: 10.1615/HeatTransRes.v42.i2.30.

[95] G. Liang and I. Mudawar. "Review of spray cooling – Part 1: Single-phase and nucleate boiling regimes, and critical heat flux." In: *International Journal of Heat and Mass Transfer* 115 (2017), pp. 1174–1205. ISSN: 00179310. DOI: 10.1016/j.ijheatmasstransfer.2017.06.029.

[96] R. Gardon and J. C. Akfirat. "Heat Transfer Characteristics of Impinging Two-Dimensional Air Jets." In: *Journal of Heat Transfer* 88 (1966), pp. 101–107. ISSN: 00221481. DOI: 10.1115/1.3691449.

[97] F. Cirillo and G. M. Isopi. "Glass tempering heat transfer coefficient evaluation and air jets parameter optimization." In: *Applied Thermal Engineering* 29.5-6 (2009), pp. 1173–1179. ISSN: 13594311. DOI: 10.1016/j.applthermaleng.2008.06.005.

[98] Y. Yamane, Y. Ichikawa, M. Yamamoto, and S. Honami. "Effect of injection parameters on jet array impingement heat transfer." In: *International Journal of Gas Turbine, Propulsion and Power Systems* 4.1 (2012), pp. 27–34. ISSN: 18825079.

[99] A. Schroder, S. Ou, and U. Ghia. "Experimental Study of an Impingement Cooling-Jet Array Using an Infrared Thermography Technique." In: *Journal of Thermophysics and Heat Transfer* 26.4 (2012), pp. 590–597. ISSN: 0887-8722. DOI: 10.2514/1.60244.

[100] N. Zuckerman and N. Lior. "Jet impingement heat transfer: Physics, correlations, and numerical modeling." In: *Advances in Heat Transfer* 39.C (2006), pp. 565–631. ISSN: 00652717. DOI: 10.1016/S0065-2717(06)39006-5.

[101] M. Wannassi and F. Monnoyer. "Fluid flow and convective heat transfer of combined swirling and straight impinging jet arrays." In: *Applied Thermal Engineering* 78 (2015), pp. 62–73. ISSN: 13594311. DOI: 10.1016/j.applthermaleng.2014.12.043.

[102] N. Sozbir and S. C. Yao. "Spray mist cooling heat transfer in glass tempering process." In: *Heat and Mass Transfer* 53.5 (2017), pp. 1699–1711. ISSN: 14321181. DOI: 10.1007/s00231-016-1930-2.

[103] F. J. Granados-Ortiz and J. Ortega-Casanova. "Avances en la simulación de la transferencia de calor mediante mecanismos de impacto de chorro." In: *Técnica Industrial* 330 (2021), pp. 46–59. DOI: 10.23800/10.513.

[104] ANSYS Inc. *ANSYS FLUENT Theory Guide Release 18.2*. Canonsburg, PA, 2017. DOI: 10.1016/0140-3664(87)90311-2. arXiv: ArXivID.

[105] K. Petera and M. Dostál. "Heat transfer measurements and CFD simulations of an impinging jet." In: *EPJ Web of Conferences* 114 (2016). DOI: 10.1051/epjconf/201611402091.

[106] F. J. Granados-Ortiz, J. Ortega-Casanova, and C. H. Lai. "Two-step numerical simulation of the heat transfer from a flat plate to a swirling jet flow from a rotating pipe." In: *International Journal of Numerical Methods for Heat and Fluid Flow* 30.1 (2019), pp. 143–175. ISSN: 09615539. DOI: 10.1108/HFF-04-2019-0343.

[107] S. Gurgul, T. Kura, and E. Fornalik-Wajs. "Numerical analysis of turbulent heat transfer in the case of minijets array." In: *Symmetry* 12.1785 (2020), pp. 1–19. ISSN: 20738994. DOI: 10.3390/sym12111785.

[108] J. Wienand, A. Riedelsheimer, and B. Weigand. "Numerical study of a turbulent impinging jet for different jet-to-plate distances using two-equation turbulence models." In: *Open Archives of the 16th International Symposium on Transport Phenomena and Dynamics of Rotating Machinery, ISROMAC 2016*. Honolulu. Hawaii, 2016, pp. 1–9.

[109] N. Siedow, T. Grosan, D. Lochegnies, and E. Romero. "Application of a new method for radiative heat transfer to flat glass tempering." In: *Journal of the American Ceramic Society* 88.8 (2005), pp. 2181–2187. ISSN: 00027820. DOI: 10.1111/j.1551-2916.2005.00402.x.

[110] K. H. Lee and R. Viskanta. "Two dimensional combined conduction and radiation heat transfer: comparison of the discrete ordinates method and the diffusion approximation methods." In: *Numerical Heat Transfer* 39 (2001), pp. 205–225.

[111] European Standard. *EN 12150-1: Glass in building - Thermally toughened soda lime silicate safety glass. Part 1: Definition and description*. Brussels, 2015.

[112] H. Aben, J. Anton, A. Errapart, S. Hödemann, J. Kikas, H. Klaassen, and M. Lamp. "On non-destructive residual stress measurement in glass panels." In: *Estonian Journal of Engineering* 16.2 (2010), p. 150. ISSN: 1736-6038. DOI: 10.3176/eng.2010.2.04.

[113] H. Lee, S. Cho, K. Yoon, and J. Lee. "Glass Thickness and Fragmentation Behavior in Stressed Glasses." In: *New Journal of Glass and Ceramics* 02.04 (2012), pp. 116–121. ISSN: 2161-7554. DOI: 10.4236/njgc.2012.24020.

[114] M. Akcay. "Experimental investigation of the relationship between heat transfer rate and number of broken glass particles in tempering process of glass plates." In: *Experimental Thermal and Fluid Science* 83 (2017), pp. 260–270. ISSN: 08941777. DOI: 10.1016/j.expthermflusci.2017.01.013.

[115] N. Pourmoghaddam and J. Schneider. "Experimental investigation into the fragment size of tempered glass." In: *Glass Structures & Engineering* 3.2 (2018), pp. 167–181. ISSN: 2363-5142. DOI: 10.1007/s40940-018-0062-0. URL: http://link.springer.com/10.1007/s40940-018-0062-0.

[116] H. Aben and C. Guillemet. *Photoelasticity of Glass*. 1993. ISBN: 978-3-642-50073-2. DOI: 10.1007/978-3-642-50071-8. URL: http://link.springer.com/10.1007/978-3-642-50071-8.

[117] R. Gardon. "Variation of Densities and Refractive Indices in Tempered Glass." In: *Journal of the American Ceramic Society* 61.3-4 (1978), pp. 143–146. ISSN: 15512916. DOI: 10.1111/j.1151-2916.1978.tb09258.x.

[118] F. Bernard and L. Daudeville. "Is prestressing control possible for tempered glass structures?" In: *Research in Architectural Engineering Series* 1 (2007), pp. 1–6. ISSN: 18736033 18798225.

[119] K. Lohr and B. Weller. "Residual stress distribution in tempered glass with reground edges." In: *Glass Structures & Engineering* (2018). ISSN: 2363-5142. DOI: 10.1007/s40940-018-0084-7.

[120] K. Ramesh and V. Ramakrishnan. "Digital photoelasticity of glass: A comprehensive review." In: *Optics and Lasers in Engineering* 87 (2016), pp. 59–74. ISSN: 01438166. DOI: 10.1016/j.optlaseng.2016.03.017.

[121] J. Anton. *Scattered light polariscope SCALP User's Manual (Version 5.8.2)*. Tech. rep. Tallinn, Estonia: GlasStress Ltd, 2019. URL: https://www.glasstress.com/web/.

[122] H. Aben, A. Errapart, and J. Anton. "Measuring residual stresses in homogeneous and composite glass materials using photoelastic techniques." In: *Residual Stresses in Composite Materials* (2014), pp. 152–172. DOI: 10.1533/9780857098597.1.152.

[123] F. Soulié, N. Siedow, J. Anton, and D. Lochegnies. "Numerical and Experimental Investigations on the Residual Stresses at the Centre of Flat Glass Disks After Thermal Tempering." In: *Advanced Materials Research* 39-40 (2008), pp. 553–558. ISSN: 1662-8985. DOI: 10.4028/www.scientific.net/AMR.39-40.553.

[124] B. A. Balan and M. Achintha. "Assessment of Stresses in Float and Tempered Glass Using Eigenstrains." In: *Experimental Mechanics* 55.7 (2015), pp. 1301–1315. ISSN: 17412765. DOI: 10.1007/s11340-015-0036-y.

[125] V. Nicolau and F. P. Maluf. "Determination of radiative properties of commercial glass." In: *The 18th Conference on Passive and Low Energy Architecture* November (2001), p. 5.

[126] Y. Cengel and M. Boles. "Appendix 1: Property tables and charts." In: *Heat and Mass Transfer*. Ed. by McGraw Hill. 4th. Mexico, 2011, p. 884. ISBN: 0072458933.

[127] A. Markovsky and T. F. Soules. "An Efficient and Stable Algorithm for Calculating Fictive Temperatures." In: *Communications of the American Ceramic Society* (1984), pp. 56–57.

[128] J. Neugebauer, I. Kasumovic, and I. Blazevic. "Influence of Distribution of Residual Stress on Strength Tests." In: *Glass Performance Days GDP 2017*. 2017.

[129] M. Muniz-Calvente, A. Ramos, P. Fernández, M. J. Lamela, A. Álvarez, and A. Fernández-Canteli. "Probabilistic failure analysis for real glass components under general loading conditions." In: *Fatigue and Fracture of Engineering Materials and Structures* 42.6 (2019), pp. 1283–1291. ISSN: 14602695. DOI: 10.1111/ffe.13011.

[130] F. M. Ernsberger. "Techniques of Strengthening Glasses." In: *Glass Science and Technology*. Ed. by D.R. Uhlmann and N.J. Kreidl. Vol. 5. Academic Press, Inc., 1980, pp. 133–144. ISBN: 0127067051.

[131] C Przybilla. "Mechanical characterization of materials in fracture and fatigue focussed on the size effect." PhD thesis. Universidad de Oviedo, 2014.

[132] Y. Wang, Q. Wang, G. Shao, H. Chen, J. Sun, L. He, and K. M. Liew. "Experimental study on critical breaking stress of float glass under elevated temperature." In: *Materials and Design* 60 (2014), pp. 41–49. ISSN: 18734197. DOI: 10.1016/j.matdes.2014.03.038.

[133] F. A. Veer, P. C. Louter, and F. P. Bos. "The strength of annealed, heat-strengthened and fully tempered float glass." In: *Fatigue and Fracture of Engineering Materials and Structures* 32.1 (2009), pp. 18–25. ISSN: 8756758X. DOI: 10.1111/j.1460-2695.2008.01308.x.

[134] F.A. Veer, F. Oikonomopoulou, A.C. Riemslag, P. Carvalho, P.J.S. Cruz, Y. M. Rodichev, and H. Soroka. "Consistency of pre-stress and bending strength of annealed, heat stressed and tempered glass." In: *Proceedings 13th International Conference Glass Performance Days*. Finland, 2013, pp. 538–544.

[135] Y. M. Rodichev, F. A. Veer, O. B. Soroka, and O. A. Shabetya. "Structural Strength of Heat-Strengthened Glass." In: *Strength of Materials* 50.4 (2018), pp. 584–596. ISSN: 15739325. DOI: 10.1007/s11223-018-0004-8.

[136] European Standard. *EN 1288-3: Glass in building - Determination of the bending strength of glass. Part 3: Test with specimen supported at two point (four point bending)*. Brussels, 2000.

[137] M. J. Meyland, J. H. Nielsen, and C. Kocer. "Tensile behaviour of soda-lime-silica glass and the significance of load duration – A literature review." In: *Journal of Building Engineering* 44.102966 (2021). ISSN: 23527102. DOI: 10.1016/j.jobe.2021.102966.

[138] European Standard. *EN 1288-1: Glass in building - Determination of the bending strength of glass. Part 1: Fundamentals of testing glass*. Brussels, 2000.

[139] European Standard. *EN 1288-5: Glass in building - Determination of the bending strength of glass. Part 5: Coaxial double ring test on flat specimens with small test surface areas*. Brussels, 2000.

[140] M. Haldimann. "Fracture strength of structural glass elements - analytical and numerical modelling , testing and design." PhD thesis. École Polytechnique Fédérale de Lausanne, 2006, p. 222.

[141] M. Feldmann, R. Kaspar, B. Abeln, A. Gessler, K. Langosch, J. Beyer, J. Schneider, S. Schula, G. Siebert, A. Haese, F. Wellershoff, P. Cruz, J. Belis, J. Colvin, T. Morgan, F. Ensslen, M. Eliasova, Z. Šulcová, G. Royer-Carfagni, L. Galuppi, C. Grenier, H. Hoegner, R. Kruijs, C. Louter, G. Manara, J. Neugebauer, V. Rajcic, and R. Zarnic. *Guidance for European Structural Design of Glass Components*. Tech. rep. Luxembourg, 2014. DOI: 10.2788/5523.

[142] M. Muniz-Calvente, A. Ramos, F. Pelayo, M. J. Lamela, and A. Fernández-Canteli. "Statistical joint evaluation of fracture results from distinct experimental programs: An application to annealed glass." In: *Theoretical and Applied Fracture Mechanics* 85 (2016), pp. 149–157. ISSN: 01678442. DOI: 10.1016/j.tafmec.2016.08.009. URL: http://dx.doi.org/10.1016/j.tafmec.2016.08.009.

[143] W. L. Beason. "A failure prediction model for window glass." PhD thesis. Texas Tech University, 1980.

[144] W.L. Beason, T.L. Kohutek, and J.M. Bracci. "Basis for ASTM E 1300 annealed glass thickness selection charts." In: *Journal of Structural Engineering* 142.2 (1998), pp. 215–221.

[145] ASTM. *ASTM Standard E1300 - Determining load resistance of glass in buildings*. 2003rd ed. West Conshohocken, PA: ASTM International, 2003, p. 58. DOI: 10.1520/E1300-12A.1.7. URL: www.astm.org.

[146] M. Muñiz-Calvente, A. Ramos, V. Shlyannikov, M. J. Lamela, and A. Fernández-Canteli. "Hazard maps and global probability as a way to transfer standard fracture results to reliable design of real components." In: *Engineering Failure Analysis* 69 (2016), pp. 135–146. ISSN: 13506307. DOI: 10.1016/j.engfailanal.2016.02.004. URL: http://dx.doi.org/10.1016/j.engfailanal.2016.02.004.

[147] B. Lawn. *Fracture of brittle solids*. Ed. by E. A. Davis and I. M. Ward. 2nd. Press Syndicate of the University of Cambridge, 1993. ISBN: 0-521-40972-1.

[148] A. Ramos. "Modelo probabilístico para el dimensionamiento de elementos de vidrio estructural bajo solicitación estática y dinámica." PhD thesis. Universidad de Oviedo, 2017.

[149] H. Tada, P. C. Paris, and G. R. Irwin. *The Stress Analysis of Cracks Handbook*. Third. New York: The American Society of Mechanical Engineers, 2000. ISBN: 0-7918-0153-5.

[150] C. Przybilla, A. Fernández-Canteli, and E Castillo. "Deriving the primary cumulative distribution function of fracture stress for brittle materials from 3-and 4-point bending tests." In: *Journal of the European Ceramic Society* 31.4 (2011), pp. 451–460.

[151] D. T. Kinsella and K. Persson. "A numerical method for analysis of fracture statistics of glass and simulations of a double ring bending test." In: *Glass Structures and Engineering* 3.2 (2018), pp. 139–152. ISSN: 23635150. DOI: 10.1007/s40940-018-0063-z.

[152] F. A. Veer and Y. M. Rodichev. "Improving the engineering strength of heat strengthened glass." In: *Heron* 61.2 (2016), pp. 121–138. ISSN: 15744078.

[153] G. Pisano, G. Royer Carfagni, and J. Schneider. "Open issues in the calibration of partial safety factors for heat-treated glass." In: *Structural Safety* 79 (2019), pp. 1–11. ISSN: 01674730. DOI: 10.1016/j.strusafe.2019.01.002.

[154] A. Bonati, A. Occhiuzzi, G. Pisano, and G. Royer-Carfagni. "A micro-mechanically motivated model for the strength of heat-treated glass." In: *Glass Structures and Engineering* 3.2 (2018), pp. 153–166. ISSN: 23635150. DOI: 10.1007/s40940-018-0071-z.

[155] M. Muñiz-Calvente. "The generalized local model: A methodology for probabilistic assessment of fracture under different failure criteria." PhD thesis. Universidad de Oviedo, 2017.

[156] J. H. Nielsen, K. Thiele, J. Schneider, and M. J. Meyland. "Compressive zone depth of thermally tempered glass." In: *Construction and Building Materials* 310.125238 (2021). ISSN: 09500618. DOI: 10.1016/j.conbuildmat.2021.125238.

[157] M.M. Mahmoud. "Frictional Behavior of Different Glove Materials Sliding Against Glass Sheet." In: *Journal of Applied Sciences* 16.10 (2016), pp. 491–495. ISSN: 18125654. DOI: 10.3923/jas.2016.491.495.

[158] M. F. Ashby, H. Shercliff, and D Cebon. "Friction and wear." In: *Materials: engineering, science, processing and design*. Fourth Edi. Butterworth-Heinemann, 2019. ISBN: 978-0-08-102376-1.